CONF-9605 13--

NREL Preprints for the Photovoltaic Specialists Conference of

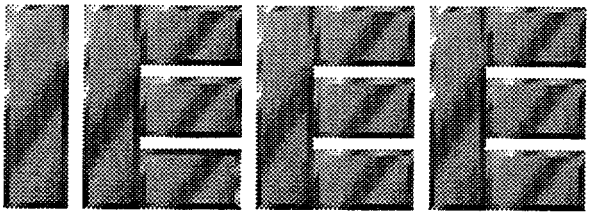

Twenty-Five

Don Gwinner, Editor

May 1996
NREL/TP-410-21091
UC Category: 1250

Center for Photovoltaics and Electronic Materials

Center for Performance Engineering, Qualification, and Reliability

Center for Measurements and Characterization

Center for Basic Science and Advanced Concepts

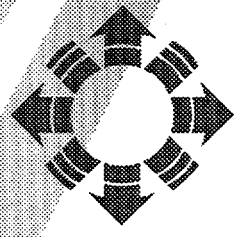

National Renewable Energy Laboratory

1617 Cole Blvd.
Golden, CO 80401-3393

Prepared under
Task No. PV610107

Notice

Printed in the United States of America

Available to DOE and DOE contractors from:
Office of Scientific and Technical Information (OSTI)
P.O. Box 62
Oak Ridge, TN 37831
Prices available by calling (615) 576-8401

Available from:
National Technical Information Service
U.S. Department of Commerce
5285 Port Royal Road
Springfield, VA 22161
(703) 487-4650

Information pertaining to the pricing codes can be found in the current issue of the following publications which are generally available in most libraries: Government Reports Announcements and Index (GRA andI); Scientific and Technical Abstract Reports (STAR); and publication NTIS-PR-360 available from NTIS at the above address.

Printed with a renewable source ink on paper containing at least 50% wastepaper and 10% postconsumer waste

Preface

This document contains preprints of 40 papers prepared by photovoltaics researchers at the National Renewable Energy Laboratory (NREL) and collaborating researchers for the 25th IEEE Photovoltaic Specialists Conference. The conference was held May 13–17, 1996, in Washington, D.C. Most of the NREL work described here was funded by the U.S. Department of Energy under contract No. DE-AC36-83CH10093.

Approved for the
National Renewable Energy Laboratory

John Benner
Director, Center for Photovoltaics and Electronic Materials

Roland Hulstrom
Director, Center for Performance Engineering, Qualification, and Reliability

Larry Kazmerski
Director, Center for Measurements and Characterization

Satyen Deb
Director, Center for Basic Science and Advanced Concepts

Contents

The 40 papers in this document are listed in alphabetical order according to the first author's last name. One paper (Levi et al.) was not available at the time of this printing; therefore, only an abstract is included here.

OPTICAL PROPERTIES AND DEFECT LEVELS IN A SURFACE LAYER FOUND ON $CuInSe_2$ THIN FILMS

F. Abulfotuh, T. Wangensteen, R. Ahrenkiel, and L.L. Kazmerski
National Renewable Energy Laboratory, Golden, Colorado, USA

ABSTRACT

In this paper we have used photoluminescence (PL) and wavelength scanning ellipsometry (WSE) to clarify the relationship among the electro-optical properties of copper indium diselenide (CIS) thin films, the type and origin of dominant defect states, and device performance. The PL study has revealed several shallow acceptor and donor levels dominating the semiconductor. PL emission from points at different depths from the surface of the CIS sample has been obtained by changing the angle of incidence of the excitation laser beam. The resulting data were used to determine the dominant defect states as a function of composition gradient at the surface of the chalcopyrite compound. The significance of this type of measurement is that it allowed the detection of a very thin layer with a larger bandgap (1.15-1.26 eV) than the CIS present on the surface of the CIS thin films. The presence of this layer has been correlated by several groups to improvement of the CIS cell performance. An important need that results from detecting this layer on the surface of the CIS semiconductor is the determination of its thickness and optical constants (n, k) as a function of wavelength. The thickness of this surface layer is about 500 Å.

INTRODUCTION

The performance of the copper indium diselenide (CIS) polycrystalline thin film devices has evolved to the point where total-area device efficiency of 17.1% [1] and modules with demonstrated stability and conversion efficiencies exceeding 11 % have been reported [2]. However, an explanation of the observed variable behavior of this material, including the dependence of the device's performance on the junction and material quality, has not yet been established. Therefore, numerous investigations [e.g., Refs. 3-5] have focused on the structure and chemistry of the chalcopyrite compound.

The improved device performance has been attributed to the formation of a surface layer on the CIS film [6,7], often called an ordered-vacancy compound (OVC) or chalcopyrite defect compound (CDC), resulting from optimized material processing. Detection and determination of the electro-optical properties of this very thin (≈500-A thick) layer is extremely important for understanding and modeling of device performance.

In this paper, the photoluminescence (PL) technique has been used to study the effect of this layer on the emission from CIS when this layer exists. To characterize the material further to understand its effect on the device behavior, the optical constants of the solar-cell components (including window layers) as a function of wavelength have been measured using wavelength scanning ellipsometry (WSE). These data are essential for modeling the behavior of such a component and to ascertain the influence of composition and processing steps on the fundamental properties of materials.

EXPERIMENTAL METHODS

The PL measurements were taken on the bare surfaces of both thin films and single crystals (after Se diffusion) of CIS samples and through the window layer deposited on the absorber surface. WSE was used to monitor both the surface layer of the thin film and the interfacial layer between the window and the absorber of the complete device. PL emission from points at different depths from the surface of the CIS sample were obtained by changing the angle of incidence of the excitation laser beam. The resulting data were then used to determine the dominant defect states as a function of composition gradient of the chalcopyrite compound. The significance of the type of measurement is that it allowed the detection of the CDC layer if present on the surface of the CIS films.

The design of the WSE is based on a unique approach that consists of a stepper-motor-controlled rotating polarizer-fixed analyzer with an ac detection system to ensure accurate measurements of the ellipsometric parameters Ψ and Δ in a wide range of wavelengths. This approach exhibits several advantages over the commonly used rotating analyzer-fixed polarizer system. The rotating prism assembly is driven with a small flexible chain by a high-resolution stepper motor (12,800 steps per revolution). This allows precise positioning of the polarizer plate via an ES732 interface for integrated measurements. An optical encoder provides an "absolute" position reference. To carry out ellipsometric measurements, a light from a 100-W tungsten-halogen lamp is polarized by a rotating prism after being collimated. After reflection from the surface of

the sample under investigation, the polarized beam is directed to the fixed analyzer, and then to the monochromator. In this configuration, the system is able to collect an average of 24,000 data points at each wavelength, perform a Fourier analysis on the resulting intensity curves, and present a real-time plot in less than 20 s. The Fourier coefficients are then used to calculate Ψ and Δ.

RESULTS

The data resulting from PL emission from points at different depths below the surface of the CIS sample were used to determine the dominant defect states as a function of composition gradient at the surface of the chalcopyrite compound. The PL emission from the In-rich sample as shown by Fig. 1 demonstrates the emission from the top surface CIS layer of this sample. It is clear that the spectrum is dominated by three emissions of 1.26 eV, 1.22 eV, and 1.15 eV. The origin the emission peaks was determined from observing the change in the PL peak position and intensity with excitation power and the temperature at which measurements are carried out. These three peaks demonstrated a blue shift and an increase in intensity with increasing temperature and excitation power respectively. Therefore, they are identified as resulting from band-to-band recombination.

The detection of three band gaps suggests that the In-rich layer, formed on the surface of the CIS film by the defect compound $Cu_1In_3Se_5$, has a graded composition where the Cu content varies with depth. A donor-acceptor recombination peak at 1160 nm was also detected. The low-energy emission from deeper regions, measured at a slightly larger angle, shows the typical emission from a bulk CIS film that is attributed mainly to donor-acceptor recombination. The location and relative concentration of these states depend not only on the chemical composition, but also on the processing steps and conditions.

An important need resulting from detecting the $Cu_1In_3Se_5$ layer on the surface of the CIS semiconductor is the determination of its thickness and optical constants (n, k) as a function of wavelength. Careful ellipsometric measurements using WSE have shown that the average value of k, from measurements on CIS film that has this layer, is 1.2-1.4 times the value measured from the bulk of the CIS absorber film. The total thickness of this surface layer is about 250 Å. Figs. 2 and 3 show a comparison between Ψ (Fig. 1) and Δ (Fig. 2) measured on two CIS films with and without the top layer (chalcopyrite defect compound). Measurements on a synthesized $Cu_1In_3Se_5$ thin-film compound were also carried out, and the data are shown by Figs. 2 and 3.

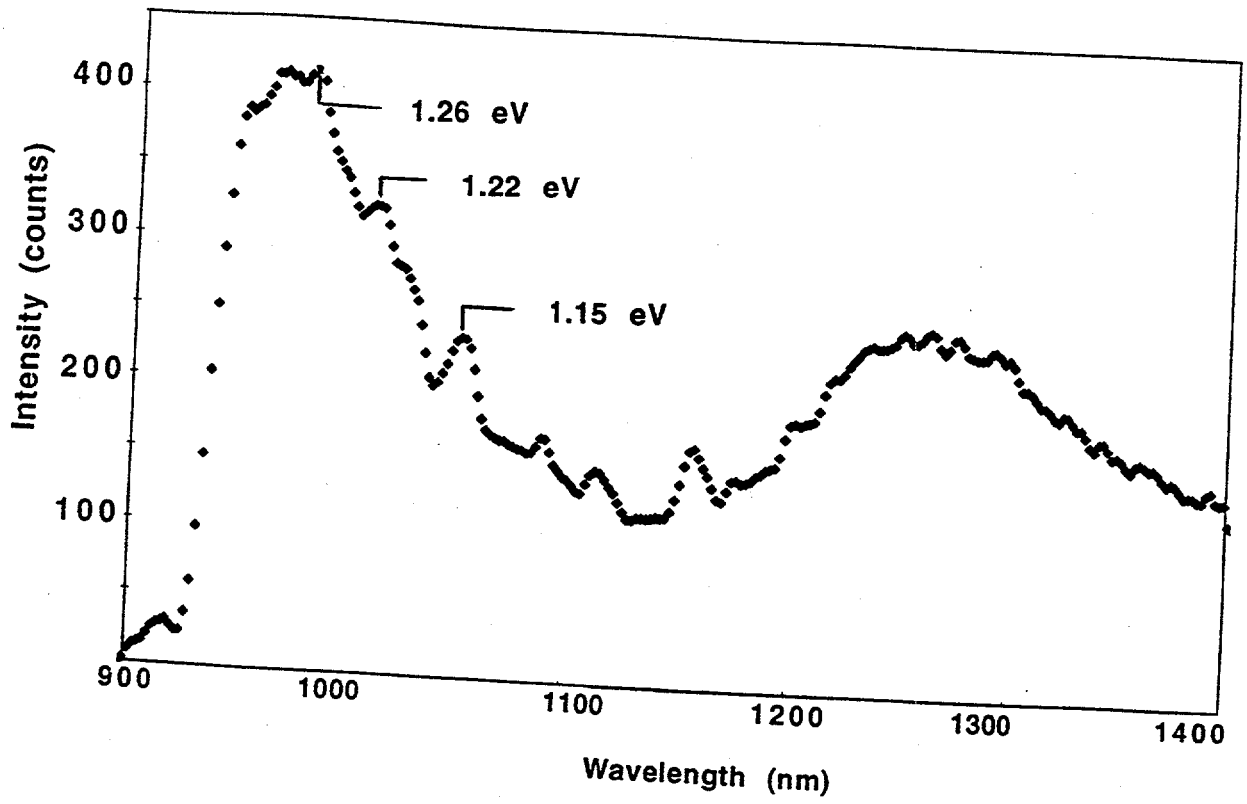

Fig. 1. PL emission spectrum of an In-rich CIS film measured at 4 K.

Determining the optical constants of the individual components of the CIS absorbing film as a function of wavelength is essential for modeling the behavior of such a component and for ascertaining the influence of composition on the fundamental properties of materials. The effective optical constants of the synthesized $Cu_1In_3Se_5$ layer are 1.7 and 0.55 for n and K, respectively. The actual composition of this layer as determined from electron microprobe analysis is $Cu_{10.46}In_{34.3}Se_{55.2}$, which has a slight Cu and In deficiency as compared to the ideal composition. Therefore, the lattice parameters are expected to shrink with respect to the ideal compound, and consequently the absorption will start at longer wavelengths [8].

In an actual device, the CDC layer is segregated at the surface of the CIS absorber [9]. However, an abrupt change of composition is highly unlikely. The gradual change in composition from $CuInSe_2$ to $Cu_1In_3Se_5$ will result in a gradual change in the optical properties even within the defect-compound layer itself. Figs. 4 and 5 show the fitted curves between the calculated values of Ψ and Δ of the assumed multilayer graded composition as compared to the experimental values obtained from the ellipsometric measurements. Modeling of the ellipsometric data has led to an estimated thickness of the CDC layer, formed at the surface of the CIS absorber, that ranges between 200 and 300 Å.

This layer consists of at least three intermediate regions or sublayers. The top sublayer represents the closest composition and optical properties of the $Cu_1In_3Se_5$ compound. The optical absorption of this layer is at least 20% higher than the effective absorption of the CDC layer The optical constants of the two sublayers beneath this layer change gradually as we go deeper below the surface. The bottom layer of this stack has the same value of n as the bulk CIS film and a much lower value of k (about 0.2 to 0.4). This result indicates that the formation of the defect compound starts with a composition having a very low Cu content.

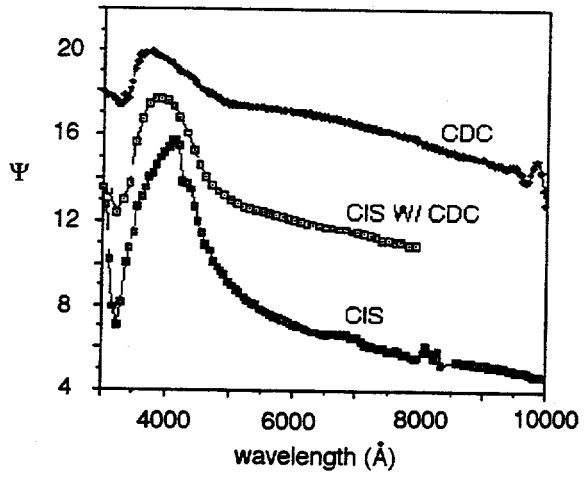

Fig. 2. Ellipsometric parameter Ψ as a function of Wavelength for CIS films with and without the chalcopyrite defect compound and a synthesized $Cu_1In_3Se_5$ thin film.

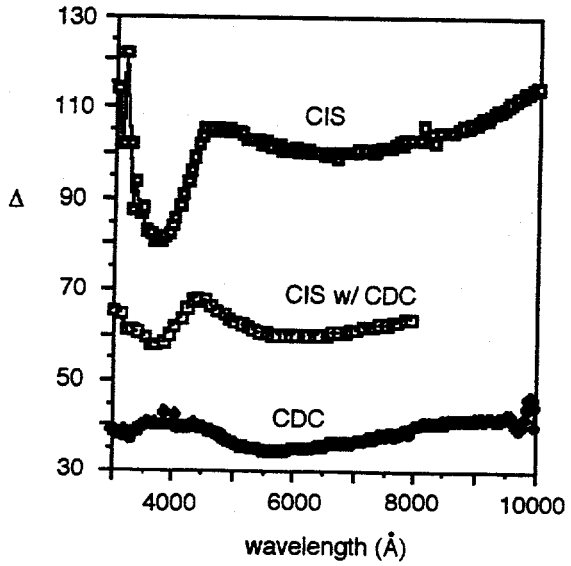

Fig. 3. Ellipsometric parameter Δ as a function of Wavelength for CIS films with and without the chalcopyrite defect compound and synthesized $Cu_1In_3Se_5$ thin film.

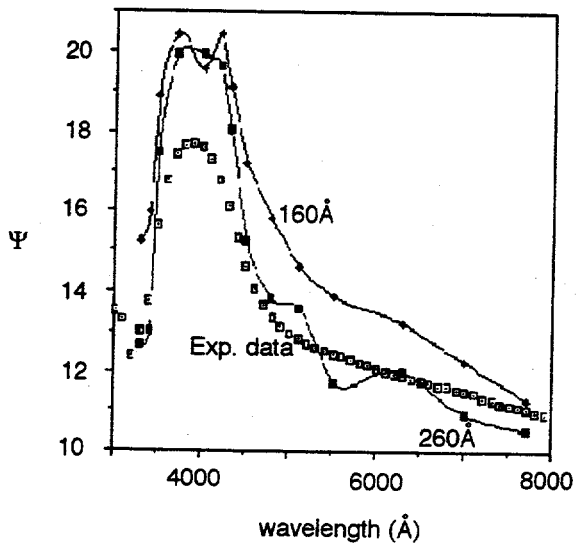

Fig. 4. Comparison of the experimental and calculated values of Ψ.

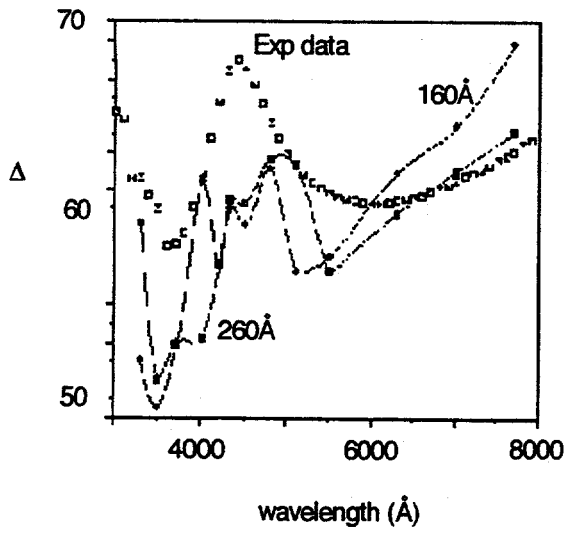

Fig. 5. Comparison of the experimental and calculated values of Δ.

CONCLUSIONS

The defect states and optical properties of the In-rich CDC layer, which is usually segregated on the surface of the absorber of high-quality CIS devices, are determined using both PL and WSE. Careful ellipsometric measurements using WSE have shown that the average value of k, from measurements on CIS film that has this layer, is 1.2-1.4 times the value measured from the bulk of the CIS absorber film. We also found that the thickness of this layer is about 250Å and it has a gradual change of composition (Cu content) with depth, which results in a gradual change in optical properties. However, three main regions or sublayers are identified and three bandgaps at 1.26 eV, 1.22 eV, and 1.15 eV are reported. The value of k varies from a maximum of 0.62 to a minimum near 0.25.

ACKNOWLEDGMENTS

The authors would like to thank M Contreras for supplying thin-film materials. This work was supported under contract No. DE-AC36-83CH10093 with the U.S. Department of Energy.

REFERENCES

1. J.R. Tuttle, M.A. Contreras, A.M. Gabor, K.R. Ramanathan, A.L. Tennant, D.S. Albin, J. Keane, and R. Noufi, *Prog. in Photovoltaic*, Nov-Dec, 1996 (in press).

2. J. Ermer. R. Gay, D. Pier, and D. Tarrant, *J. Vac. Sci. Technol.* **A11**, (1993), p. 1888.

3. A. Rockett, F. Abul fotuh, D. Albin, M. Bode, J. Ermer, R. Klenk. T. Lommasson, T.W.F. Russel, and R.D. Peterson, *Thin Solid Films* 237, (1994), p.1.

4. R. Schwartz and J. Gray, *Proc. 21st IEEE PV Sc., Kissimmee, FL,May 1990*, (IEEE. New York,1990), p. 570.

5. R. Scheer, C. Knieper, H.J. Lewerenz, M. Bodegard, L. Stolt, *proc. 13th EC PVSEC, Nice, France, Oct. 23-27,1995*, p.1696.

6. D. Schmid, M. Ruckh, F. Grunwald, and H.W. Schock, *J. Appl. Phys.* 73, (1993), p. 2902.

7. R. Scheer and H.J. Lewerenz, *J. Vac. Sci. Techol. A* 13, (1995), p.1924.

8. M. Contreras, H. Wiesner, R. Matson, J. Tuttle, K. Ramanathan, and R. Noufi, Presented at the Material Research Soc. Sprig Meeting, San Francisco, April, 8-12, 1996.

9. J. Kessler, D. Schmid, R. Schaffler, and H. Schock, *Proc. 23rd IEEE PV SC.* (1993), p. 549.

PROPERTIES OF IRON-DOPED MULTICRYSTALLINE SILICON GROWN BY THE FLOAT-ZONE TECHNIQUE

T. F. Ciszek, T. H. Wang, R. K. Ahrenkiel, and R. Matson
National Renewable Energy Laboratory, Golden, CO 80401

ABSTRACT

Multicrystalline Fe-doped Si ingots were float-zoned from high-purity feed rods. Fe was introduced by pill-doping, which gives uniform impurity content for small segregation coefficients ($k \sim 10^{-5}$ for Fe in Si). Fe concentrations were calculated from the initial weight of the Fe pill, the molten zone geometry, and the growth parameters. Values in the range of 10^{12}-10^{16} atoms/cm^3 were targeted. No additional electrically active dopants were introduced. Minority charge carrier lifetime (via YAG-laser-excited, 430-MHz ultra-high-frequency-coupled, photoconductive decay) was measured on the ingots, and wafers were cut to examine grain structure and electron-beam-induced current response of grain boundaries. Observed lifetimes decreased monotonically with increasing Fe content for similar grain sizes (from ~10 μs to 2 μs for < 10^{-3} cm^2 grains, from ~30 μs to 2 μs for ~5 x 10^{-3} cm^2 grains, and from ~300 μs to 2 μs for > 10^{-2} cm^2 grains) as the Fe content increased to 1 x 10^{16} atoms/cm^3.

INTRODUCTION

The float-zone (FZ) method for silicon crystal growth allows a high degree of control over background impurity and defect levels and is an excellent vehicle for controlled studies of deliberately introduced impurities and/or defects. In this investigation, we grew Fe-doped multicrystalline ingots by the FZ method to study Fe effects on minority charge carrier lifetime, grain structure, and electron-beam-induced current characteristics of multicrystalline silicon.

IRON-DOPED SILICON INGOT GROWTH

The 34-mm-diameter, Fe-doped ingots were grown at 4 mm/min. from high-purity polycrystalline Si feed rods in a 99.999% Ar ambient with 2.1 MHz induction heating. We used 2-cm-diameter, polycrystalline seeds that were core-drilled along the diameter of large chemical vapor deposited (CVD) polycrystalline silicon logs. This method yields an initial small multicrystalline grain size, and grains approach 1 mm in size after 3-4 cm of growth [1]. Fe was introduced by the pill-doping method[2], where a piece (or pill) of the dopant is inserted near the beginning of growth and enters the molten zone. The required mass of dopant, m, is given by $m = (W/L_A)(C/k)V$, where W is the atomic weight of the dopant, L_A is Avogadro's number, C is the desired dopant concentration in the ingot, k is the effective segregation coefficient, and V is the volume of the floating zone. We make the assumption that $k \sim 2k_o$, where k_o is the equilibrium segregation coefficient. Because $k_o \sim 1 \times 10^{-5}$ for Fe in Si, the reservoir remains essentially constant and concentrations are uniform along the ingot length. Uncertainties arise in correct values for k and V, as well as in the fact that some Fe may be lost by evaporation from the zone. Nevertheless, a range of Fe concentrations, which we calculate to lie between ~2 x 10^{12} and ~1 x 10^{16} atoms/cm^3, was produced using m values between 0.14 mg and 0.5 g. No additional electrically active dopants were introduced.

MINORITY CARRIER LIFETIME CHARACTERIZATION

Minority carrier lifetime (via YAG-laser-excited, 430-MHz ultra-high-frequency-coupled, photoconductive decay) was measured on the ingots. Observed lifetimes decreased monotonically with increasing Fe content for similar grain sizes (from ~10 μs to 2 μs for < 10^{-3} cm^2 grains, from ~30 μs to 2 μs for ~5 x 10^{-3} cm^2 grains, and from ~300 μs to 2 μs for > 10^{-2} cm^2 grains) as the Fe content increased to 1 x 10^{16} atoms/cm^3. The details are presented in Fig. 1. We had previously observed that grain size alone has a strong effect on lifetime[1].

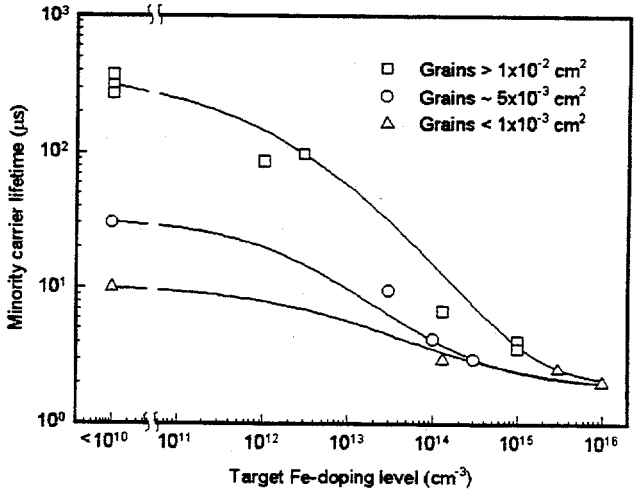

Fig. 1. Measured bulk minority carrier lifetime vs. target Fe-doping level for float-zoned multicrystalline Si ingots with various grain sizes.

GRAIN STRUCTURE AND ELECTRICAL RESPONSE

Wafers were cut to examine grain structure and electron-beam-induced current (EBIC) response of grain boundaries. In the samples with heavy Fe doping (10^{15}-10^{16} atoms/cm^3), nonuniformities in EBIC response were present. These were manifested both as large areas with reduced EBIC signals, extending over numerous grains, and as local areas of reduced response, presumably due to local agglomerations or precipitates of Fe. Fig. 2 is an EBIC photo and Fig. 3 is a scanning electron micrograph of the same area on a sample with targeted doping near 1 x 10^{16} atoms/cm^3. We also observed that the EBIC response was reduced more near the axis of these ingots than at the periphery, perhaps indicating a coring effect in the Fe distribution.

We also saw evidence of constitutional supercooling in the heavily doped samples, with a dramatic accompanying effect on grain structure. This indicates that growth speeds of 4 mm/min., which are routine for dislocation-free, high-purity silicon float zoning, are too fast when significant amounts of Fe are present in the melt. The effect is illustrated in Figs. 4-7, where the grain structure and dislocation distributions of Secco-etched wafers from the seed end and tail end of lightly and heavily Fe-doped ingots are compared. Each photograph shows a 2.5-mm-wide region. Precipitation of Fe is particularly evident in the dislocation etch-pit clusters seen in the tail-end wafer from the heavily doped ingot.

We attempted to estimate actual Fe contents in the ingots from capacitance-voltage measurements coupled with the 0.27 eV (below the conduction band) active Fe

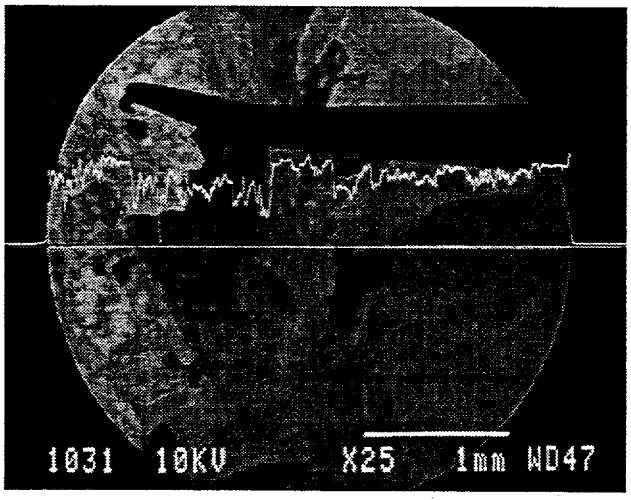

Fig. 2. EBIC photo of a wafer region from an ingot with 1 x 10^{16} atoms/cm^3 target Fe doping concentration

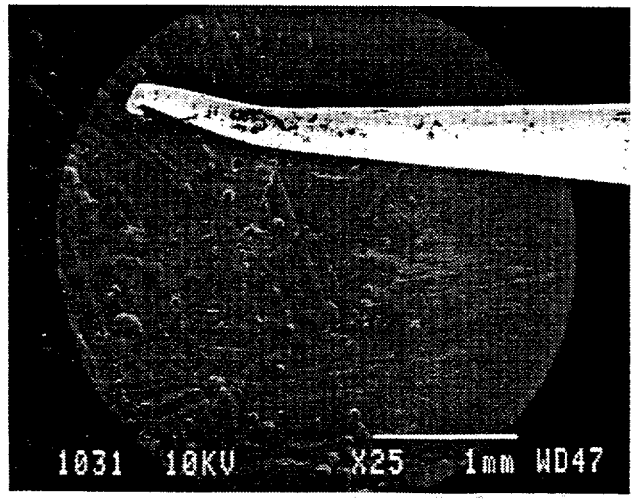

Fig. 3. SEM photo of the same wafer region shown in the EBIC photo of Fig. 2.

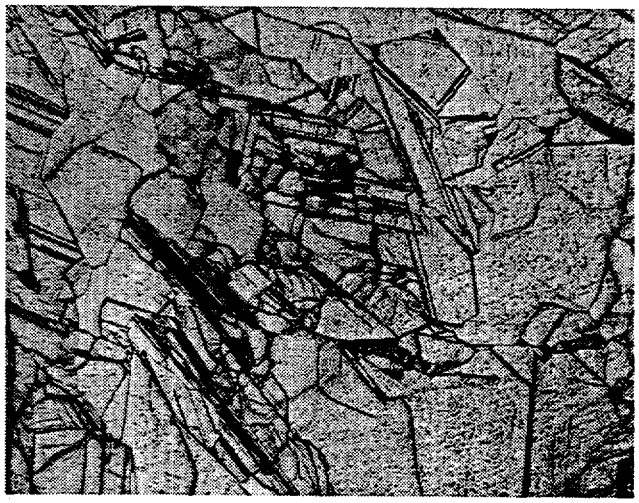

Fig. 4. Seed-end, Secco-etched wafer from an ingot with 3x10^{12} cm^{-3} target Fe doping (2.5-mm-wide region)

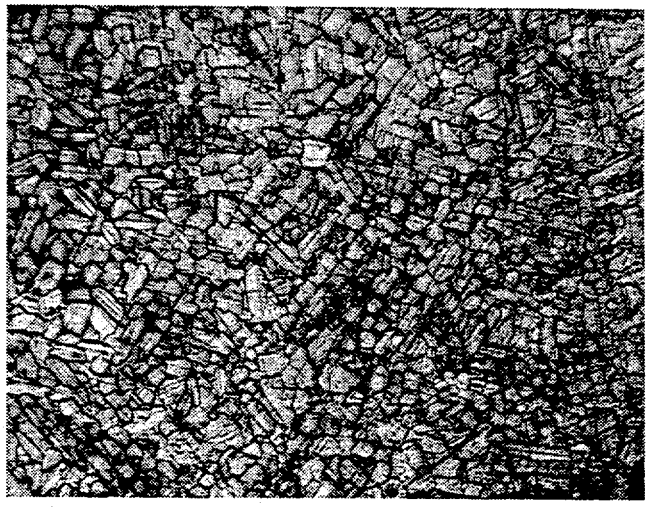

Fig. 5. Seed-end, Secco-etched wafer from an ingot with 1x10^{16} cm^{-3} target Fe doping (2.5-mm-wide region)

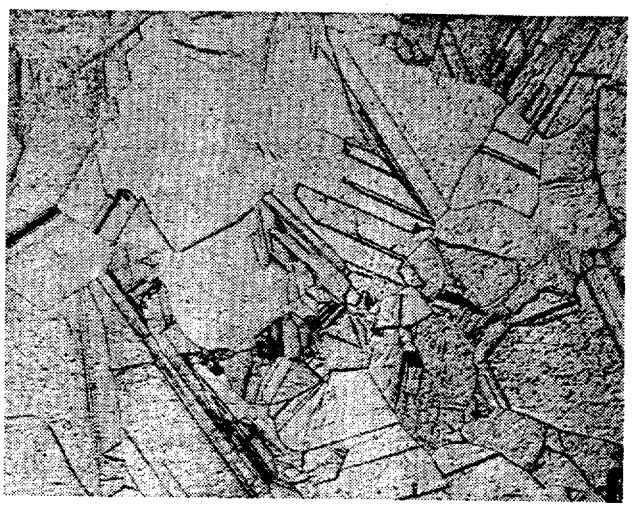

Fig. 6. Tail-end, Secco-etched wafer from an ingot with $3x10^{12}$ cm^{-3} Fe doping (2.5-mm-wide region)

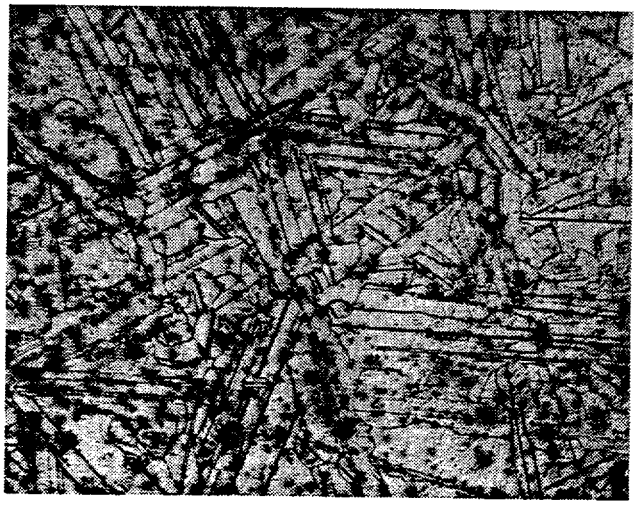

Fig. 7. Tail-end, Secco-etched wafer from an ingot with $1x10^{16}$ cm^{-3} target Fe doping (2.5-mm-wide region)

level. Generally, lower levels of Fe were indicated than the target values. Fourier-transform infrared (FTIR) spectroscopy also could not detect significant Fe in even the heavily doped samples.

DISCUSSION AND SUMMARY

It is difficult to quantify nonuniformities in Fe content from coring, constitutional supercooling, segregation to dislocations and grain boundaries, and formation of precipitates in the intra-grain areas (due to fast diffusivity and low solubility). The measurement of low Fe levels, even if the distribution is uniform, is also challenging, because the effects of Fe on lifetime occur at Fe levels which are below the detection limit for most analytical methods. Some of these effects might be better quantified by studies of Fe-doped single crystals. We performed x-ray topography on a wafer from a <100> dislocation-free crystal doped during growth with Fe at a target level of $1x10^{14}$ cm^{-3} and saw no evidence of Fe precipitates (see Fig. 8).

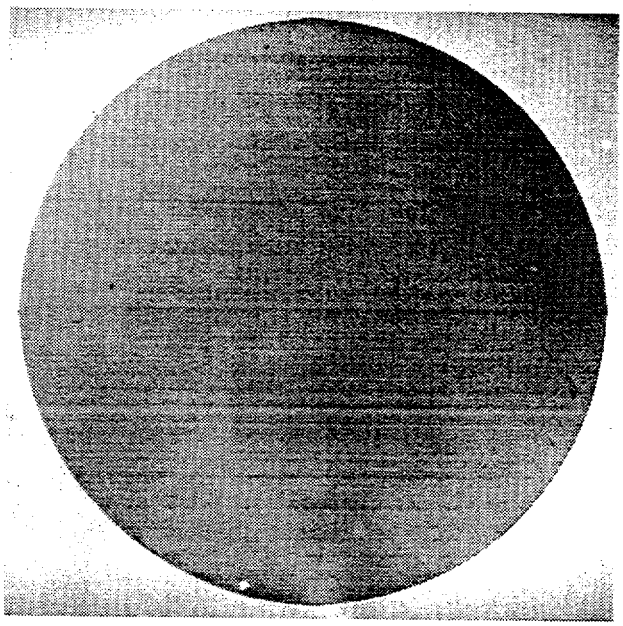

Fig. 8. (022) x-ray topograph of a 33-mm-diameter (100) wafer from a dislocation-free, float-zoned Si ingot doped with Fe during growth to a target level of 1×10^{14} atoms cm^{-3}. The diffraction vector points to the right.

We continue to explore Fe effects with other dopants, Fe effects on solar-cell efficiency, Fe-doped single crystals, and several alternative analysis methods, such as electrical resistivity measurements or photoluminescence, for determining actual Fe concentrations. Uncertainty in actual Fe concentrations is a shortcoming of the work presented here.

REFERENCES

[1.] T. F. Ciszek, T. H. Wang, R. W. Burrows, X. Wu, J. Alleman, Y. S. Tsuo, and T. Bekkedahl, "Grain Boundary and Dislocation Effects on the PV Performance of High-Purity Silicon," *23th IEEE PV Specialists Conf. Record, Louisville, 1993* (IEEE, New York, 1993), p. 101.

[2.] Keller and Muhlbauer, *Floating-Zone Silicon*, Marcel Dekker, Inc.: New York, 1981, pp. 79-82.

ACKNOWLEDGMENTS

We thank John Webb and Martha Symko for attempting FTIR spectroscopy Fe-concentration determinations on the Fe-doped samples. This work was supported by the U.S. Department of Energy under contract No. DE-AC36-83CH10093 to NREL.

DEFECT CHALCOPYRITE $Cu(In_{1-x}Ga_x)_3Se_5$ (0<x<1) MATERIALS AND HIGH-Ga-CONTENT $Cu(In,Ga)Se_2$-BASED SOLAR CELLS

Miguel A. Contreras, H. Wiesner, D. Niles, K. Ramanathan, R. Matson, J. Tuttle, and R. Noufi
National Renewable Energy Laboratory, 1617 Cole Blvd., Golden, CO 80401 USA

ABSTRACT

Crystallographic, optical, and electrical properties of defect chalcopyrite $Cu(In_{1-x}Ga_x)_3Se_5$ (0<x<1) materials in polycrystalline thin-film form are reported. Also, an energy band alignment between such materials and CdS has been calculated from X-ray photoelectron spectroscopy data. A comparison of some properties against published data on similarly prepared chalcopyrite $CuIn_{1-x}Ga_xSe_2$ absorber materials is presented. Considering the chalcopyrite/defect chalcopyrite junction model, we postulate that the traditionally poor device performance of *uniform* high-Ga-content absorbers (x>0.3) is due to a relatively inferior character—both structural and electrical—at the very chalcopyrite/defect chalcopyrite interface. We demonstrate that this situation can be circumvented (for absorbers with x>0.3) by properly engineering such an interface by reducing Ga content in the region near the surface of the absorber.

INTRODUCTION

High-efficiency $CuIn_{1-x}Ga_xSe_2$ (CIGS) solar cells have been shown to contain a thin layer of a "defect chalcopyrite" material—identified as $Cu(In,Ga)_3Se_5$—at the surface of the absorber [1]. This thin surface layer seems to play an essential role in the operation of the CIGS-based solar cell and has led to the development of a chalcopyrite/defect chalcopyrite junction model for such devices. This very significant finding gives much support to earlier observations of a "buried" junction [2] elucidated by electron-beam induced current (EBIC) methods. In that work, the mapping of the space-charge region (by EBIC) showed consistently that the electronic junction did not appear to be at the metallurgical junction between CIGS and CdS but rather somewhere *within* the CIGS absorber. The ramifications of this proposed junction model are numerous, and its concept must be put to a test in structures incorporating Ga. In essence, the chalcopyrite/defect chalcopyrite model tells us that in state-of-the-art devices, ZnO plays no active role in junction formation; rather, ZnO can be viewed merely as an efficient medium to extract current from a given device.

Materials characterization of CIGS absorber materials is quite extensive and can be found in the literature. On the other hand, data on the defect chalcopyrites is rather minimal. Because knowledge of some physical properties of defect chalcopyrite materials may help us better understand the junction phenomena in CIGS-based devices, we present crystallographic data obtained by X-ray diffraction (XRD) methods, an optical characterization, and electrical properties as determined by Hall measurements. An experimentally determined band alignment between CdS and the defect chalcopyrites (as a function of Ga content) is also presented. To elucidate and confirm the findings of electrical properties in the defect chalcopyrites, we perform an EBIC mapping of junction position in solar cells incorporating different Ga contents.

The knowledge gained from the fundamental characterization of defect chalcopyrite materials is put to a test in solar cells incorporating a modified high-Ga-content absorber.

DEFECT CHALCOPYRITE AND ABSORBER MATERIALS

Structural Analysis

First, we must distinguish the crystallographic differences between the "absorber" $Cu(In,Ga)Se_2$ and the defect chalcopyrite $Cu(In,Ga)_3Se_5$ materials. The unit cell of the absorber has been related to an atomic arrangement described by space group $I\bar{4}2d$, whereas experimental XRD data for the defect chalcopyrite [3] have been associated with space group $P\bar{4}2c$. This group belongs to the tetragonal system, but there are reports [4,5] about the existence of a cubic phase in $Cu(In,Ga)_3Se_5$ materials. Our experimental XRD data on such samples show a spectra characteristic only of the tetragonal phase, as indicated by the presence of a 101 diffraction peak at 2θ~17.2°-18.1° (depending on Ga content) that should be absent in a cubic structure.

Polycrystalline $Cu(In,Ga)_3Se_5$ thin films (~0.5 μm thick) have been grown on 7059 Corning glass by coevaporation from the elemental sources and at a fixed substrate temperature of 550°C. After the 10 min. deposition of Cu-In-Ga-Se, a selenization step followed (at 15 Å/s of Se vapor), in which the sample was cooled from 550°C to 350°C in 20 min.

We have calculated lattice parameters for such materials with near-stoichiometry compositions, that is, atomic compositions close to the ideal given by Cu:(In,Ga):Se=11.1:33.3:55.6. XRD spectra have been obtained using Cu Kα radiation (unfiltered). The XRD system has been calibrated with an external standard (Si powder SRM 640) and doublets due to Kα2 radiation are removed from a given spectrum via software. Peak positions have been determined by a Split Pearson curve-fitting routine (at constant Kα1 and Kα2), and lattice parameter calculations for all films have been done using a least-squares refinement of the calculated 2θ values. No corrections of the lattice parameters have been done due to stress or thermal effects. Fig. 1 shows our calculated

lattice parameters for the defect chalcopyrite materials, along with published lattice parameter values for CIGS [6] absorber materials with near-stoichiometry compositions.

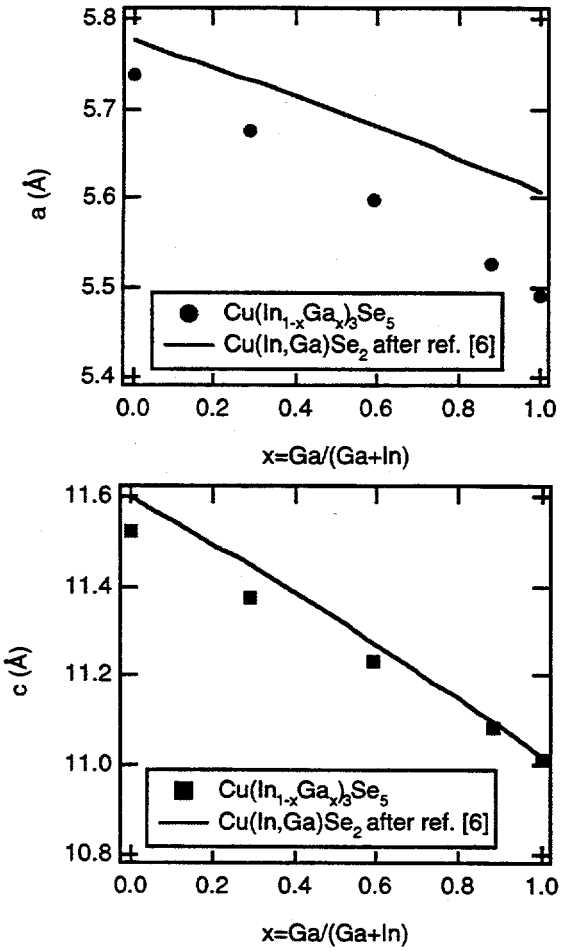

Fig. 1. Lattice parameters comparison between tetragonal near- stoichiometry defect chalcopyrite and near- stoichiometry absorber materials.

From Fig. 1 we see that there is a significant difference in the basal lattice parameters between both crystal structures. Indeed, the lattice mismatch at x~0.3 has been calculated to be near 1% and becomes worse for higher values of x. The lattice parameter "c", on the other hand, shows a maximum mismatch of about 0.7% at x=0. The consequences of lattice mismatch are well understood in other semiconductor systems, and for a p-n junction, mismatch results in an increased density of recombination centers due to point, line, and/or plane defects induced by the mismatch. The question becomes: is the $Cu(In,Ga)Se_2/Cu(In,Ga)_3Se_5$ interface an abrupt interface or a naturally occurring, smooth-graded transition that accommodates and diffuses strains? First, there is the fact that we were able to grow defect chalcopyrite materials in a wide range of deviations from stoichiometry (Cu-rich to Cu-poor) [7]. Second, compositional depth profiles done by X-ray photoemission spectroscopy (XPS) and other methods [8,9] on absorber materials show a smooth decrease in Cu content in the region near the surface of *low-Ga-content* CIGS absorbers. These findings suggest that—at least in the low-Ga-content end, i.e., x<0.3—the interface might accommodate a graded transition from one phase to the other. But this situation may be more difficult to accomplish as Ga is increased (x>0.3) because the lattice mismatch becomes more significant.

Optical and Electrical Analysis

Absorption coefficients have been determined from reflection and transmission data obtained using a Cary 2000 spectrophotometer and applying the approximations given by Pankove [10]. Bandgap calculations on near-stoichiometry samples have been done by extrapolation of $(\alpha)^2$ vs. photon energy, and their relationship to Ga content is shown in Fig. 2. The figure includes a second-degree polynomial curve fit of the calculated bandgap values.

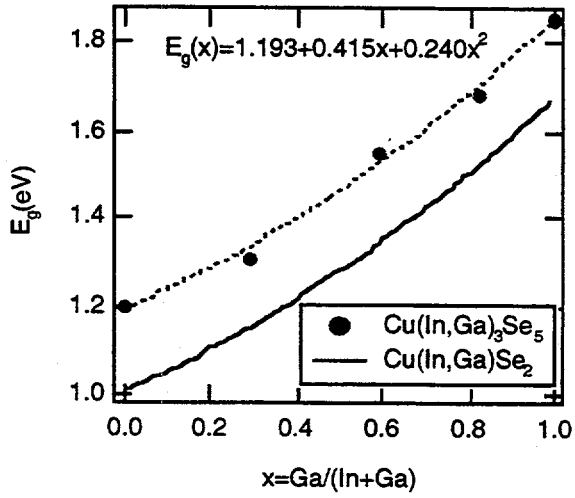

Fig. 2. Optical bandgap for near-stoichiometry defect chalcopyrite and near-stoichiometry absorber materials. Data for $Cu(In,Ga)Se_2$ after Ref. [6]

Fig. 2 also includes the bandgap values for absorber materials (solid line) as reported in Ref. 6. In general, the defect chalcopyrite materials show a bandgap ~180 meV higher than their absorber counterparts with similar Ga contents.

Hall measurements reveal highly resistive materials with rather low mobility and carrier concentrations. There is also an apparent change in conductivity type as Ga is increased. Materials with low Ga content show n-type conductivity, and for high Ga content they turn to p-type conductivity. This change in conductivity type was also observed by testing similar samples with a thermoelectric probe. Table 1 summarizes Hall measurements obtained with a system in compliance to the ASTM F76-1985 standard for obtaining Hall data. Results presented in Table 1 were consistent in the conductivity type; however, mobility and carrier concentrations calculated by the *software* varied as much as one order of magnitude when remeasured.

Even though the table shows a conductivity type, we must emphasize that the low values of carrier concentrations combined with a high resistivity are more indicative of intrinsic-type materials.

Table 1. Room-temperature Hall Measurements for $Cu(In_{1-x}Ga_x)_3Se_5$ (0<x<1) Materials.

x=Ga/(Ga+In)	R (Ω-cm)	Hall mobility (cm^2/V-s)	Carrier density (cm^{-3})	cond. type
0.00	$2.7x10^6$	~10	$~10^{11}$	n
0.29	$3.9x10^6$	~3	$~10^{12}$	n
0.59	$6.9x10^5$	~2	$~10^{12}$	p
0.88	$7.8x10^5$	~6	$~10^{12}$	p
1.00	$8.0x10^6$	~13	$~10^{11}$	p

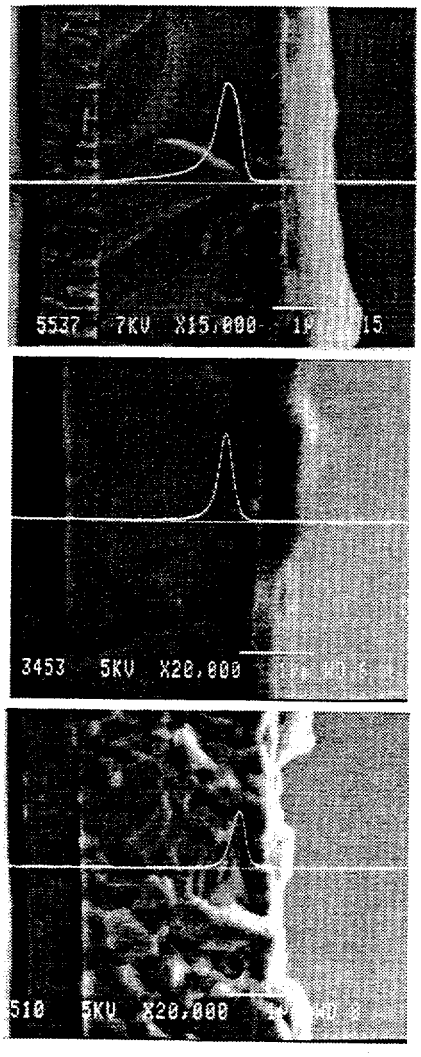

Fig. 3. EBIC scan of ZnO/CdS/$CuIn_{1-x}Ga_xSe_2$/Mo/glass devices with x~0.3 (top), x~0.5 (center), and x~1 (bottom).

However, the electrical implications of such weak conductivity types may have a significant influence on the space-charge distribution (and band alignment) at the very junction when these materials form an interface with the absorber. In effect, EBIC studies done on solar cells with different Ga contents [11] reveal a systematic shift of the junction position with increased Ga content. This situation can be seen in Fig. 3, where the EBIC mapping is shown for three of these cases, namely, $CuIn_{1-x}Ga_xSe_2$ with x~0.3, x~0.5, and x~1.0. Because EBIC maps the junction position, we see that as Ga is increased the structure becomes more and more a true heterojunction, where the CdS/ZnO layers begin to play an influential role in junction formation. This situation agrees with the electrical characterization presented above. If indeed the chalcopyrite/defect chalcopyrite interface loses its p-n character (becoming more a p-p$^+$ type of junction with increased Ga), the junction position can be *expected* to shift toward the metallurgical junction.

On another subject, we have experimentally determined a band alignment between the defect chalcopyrites and CdS using X-ray photoelectron spectroscopy (XPS). Details of this measurement technique can be found in Ref. [12]. The ~500 Å CdS layer has been deposited over the defect chalcopyrite thin films by the standard chemical bath deposition (CBD) technique used in solar-cell fabrication. We find that the valence-band offset (VBO) between CdS and the defect chalcopyrite is rather independent of Ga content and is in the order of ~1.0 eV (see Fig. 4). To calculate the conduction-band offset (CBO) we use the relationship:

$$CBO = E_g(CdS) - E_g(\text{def. chalcop.}) - VBO \qquad (1)$$

In general, the addition of Ga proves beneficial because the larger bandgaps (for x<0.3) in the defect chalcopyrite help reduce the CBO and, furthermore, for x>0.3, the CBO becomes negative. In other words, the band offset at the CdS/defect chalcopyrite interface does not seem to present adverse consequences for optimum PV performance.

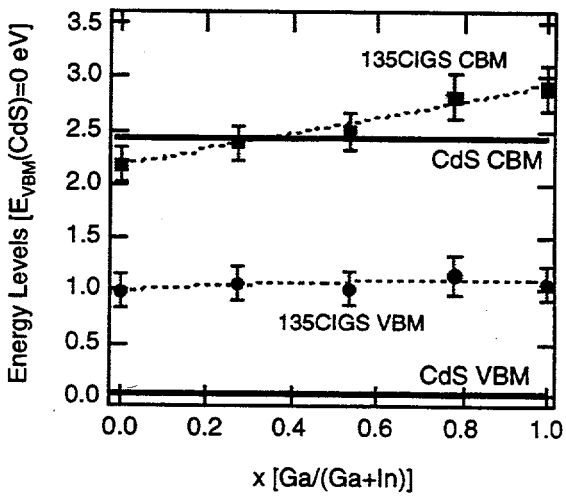

Fig. 4. Band alignment for CdS/$Cu(In_{1-x}Ga_x)_3Se_5$ (0<x<1). CBM and VBM are conduction-band minimum and valence -band maximum, respectively. 135CIGS refers to $Cu(In_{1-x}Ga_x)_3Se_5$ materials.

HIGH-Ga-CONTENT DEVICES

As seen from the data presented above, there seems to be (at least) two detrimental factors in the chalcopyrite/defect chalcopyrite junction of *uniform* high-Ga-content absorbers (x>0.3); namely, the structural and electrical differences between both kind of materials. It follows that both factors could be circumvented by tailoring the very surface of such high-Ga absorber materials (x>0.3) to produce a low-Ga-content (x<0.3) defect chalcopyrite. Because these defect chalcopyrites have been reported to be thin (<500 Å), such proposed grading does not necessarily have to be over a long portion of the absorber; rather, a short and somewhat abrupt transition could suffice. This situation in actuality may be difficult to accomplish considering the high processing temperatures associated with absorber fabrication. We have nevertheless attempted to obtain some grading, but so far this grading is rather coarse and perhaps covers more absorber thickness than it needs to. The compositional depth profile of such an absorber is shown in Fig. 5. The graph clearly shows the intentional low Ga content at the surface and the high Ga content in the bulk of the absorber. A device made from this same material showed 687 mV of open-circuit voltage (V_{oc}); a reduced current density of 23.7 mA/cm^2 (as anticipated due to the shift in bandgap), a fill factor (FF) of ~75%, and a total-area efficiency of 12.2% under AM1. No antireflective coating has been used in such a device.

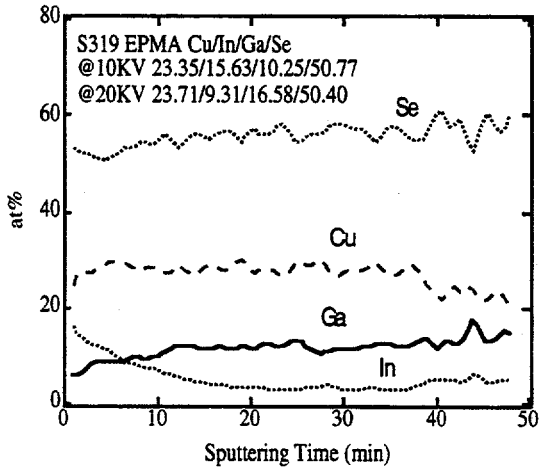

Figure 5. Depth profile of high-Ga absorber with low-Ga $Cu(In,Ga)_3Se_5$ surface layer.

CONCLUSIONS

We have shown that there are significant crystallographic differences between the absorber $Cu(In,Ga)Se_2$ and the defect chalcopyrite $Cu(In_{1-x}Ga_x)_3Se_5$ materials. Lattice mismatch in the basal plane becomes >1% for Ga contents of >30% (relative to In). Also, the n-type conductivity of defect chalcopyrites is found to exist up to x~0.3, and for higher Ga contents it shifts to p-type. Uniform high-Ga-content absorbers are observed to behave more like true heterostructures, where the CdS/ZnO layers begin to play a more active role in junction formation.

Considering the chalcopyrite/defect chalcopyrite junction model, we postulate that the traditionally poor device performance of *uniform* high-Ga-content absorbers (x>0.3) is due to a relatively poorer character—both structural and electrical—at the very chalcopyrite/defect chalcopyrite interface. We have demonstrated that improved efficiencies are attainable in high-Ga-content absorbers by properly grading the very surface of such materials.

REFERENCES

[1] D. Schmid, R. Ruckh, F. Grunwald, and H.W. Schock. *J. Appl. Phys.* **73** (6), 15 March 1993, p. 2902.

[2] R. Matson, R. Noufi, R. Ahrenkiel, and C. Powell, *Solar Cells* **16**, 1986, p. 496.

[3] W. Hönle, G. Kühn, and U. Boehnke, *Cryst. Res. Technol.* **23**, (10/11), 1988, p. 1347.

[4] T. Negami, N. Kohara, M. Nishitani, T. Wada, and T. Hirao. *Appl. Phys. Lett.* **67** (6), 7 August 1995, p. 825.

[5] U.-C. Boehnke, G. Kühn. *J. Materials Science* **22** (1987) p. 1635.

[6] D.S. Albin, J.J. Carapella, J.R.Tuttle, and R. Noufi, *Mat. Res. Soc. Symp. Proc.*, Vol 228, MRS, 1992, p. 267.

[7] M.A. Contreras, H. Wiesner, R. Matson, J. Tuttle, K. Ramanathan, and R. Noufi. *Proceedings of the 1996 Materials Research Society Spring Meeting*, Symposium J, San Francisco, April 8-12 1996 (in press).

[8] A.J. Nelson, A.M. Gabor, M.A. Contreras, J.R. Tuttle, and R. Noufi. *First World Conference on Photovoltaic Energy Conversion*, Dec. 5-9, 1994, Hawaii, Proceedings of the 24th IEEE PVSC-1994, Vol. I, p. 279.

[9] T. Nakada, N. Okano, Y. Tanaka, H. Fukuda, and A. Kunioka. *First World Conference on Photovoltaic Energy Conversion*, Dec. 5-9, 1994, Hawaii, Proceedings of the 24th IEEE PVSC-1994, Vol. I, p. 95.

[10] J.I. Pankove, *Optical Processes in Semiconductors*, Dover Publications, Inc., New York 1971, p. 93.

[11] R. Matson, M. Contreras, and R. Noufi. Proceedings of the *1996 Materials Research Society Spring Meeting*, Symposium J, San Francisco, April 8-12 1996 (in press).

[12] D.W. Niles, M.A. Contreras, K. Ramanathan, and R. Noufi. (these proceedings).

A REVIEW OF RECENT ADVANCES IN THERMOPHOTOVOLTAICS

T. J. Coutts, M. W. Wanlass, J. S. Ward, and S. Johnson*
National Renewable Energy Laboratory, 1617 Cole Blvd., Golden, Colorado 80401
*Independent Consultant

ABSTRACT

Thermophotovoltaic (TPV) generation of electricity is attracting attention because of advances in materials and devices and because of a widening appreciation of the large number of applications thatmay be addressed using TPV-based generators. The attractions include the wide range of fuel sources and the potentially high power density outputs. The two main approaches to TPV generators are (1) broad-band radiators, coupled with converters with bandgaps in the range 0.4-0.7 eV, and (2) narrow-band emitters coupled with lower-cost silicon converters. The key issues in realizing a viable TPV system are the durability, efficiency, and properties of the radiant emitter; the recuperation of sub-bandgap photons; the optimization of the converter performance; and the recuperation of waste heat.

INTRODUCTION

TPV generation of electricity has been researched for more than 20 years , but faded from interest around 1980 because of the lack of a high-efficiency converter. The conventional approach used a high-efficiency PV cell combined with a selective radiator having its emission band near the band-edge of the cell. The cells used were either silicon or germanium, and the performance of these was inadequate, causing interest to decline [1, 2]. There has been a renewal of interest in TPV-based generation of electricity over the course of the last 4 or 5 years, as evidenced by two conferences specifically on the topic [3, 4]. One of the main reasons for the new level of interest is the availability of high-performance cells based on semiconductors from the III-V family. These systems use semiconductors such as InGaAs, stemming from work on high-efficiency tandem solar cells in which III-V materials were the infrared-sensitive, low-bandgap bottom cell [5] .

Figure 1 shows the modelled power density as a function of converter bandgap for various blackbody emitter temperatures [6], showing that cells with bandgaps in the range 0.4-0.7 eV are required. At 1500 K, the electrical power density output from a TPV device operating at 25°C could be as great as 3-4 watts cm^{-2}. Many assumptions are made in this calculation, including a wavelength-independent quantum efficiency of 0.95, an emissivity of 0.9 and no losses due to parasitic resistances. Although these are idealized, the model does enable one to make a somewhat realistic estimate of the required bandgaps.

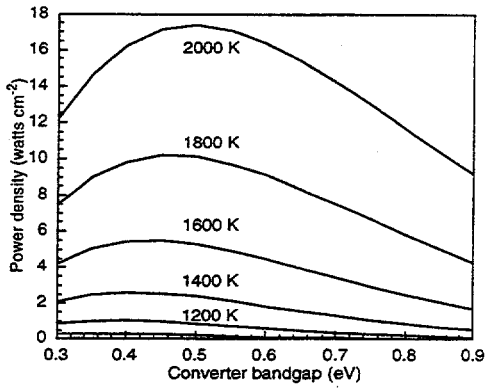

Figure 1: Power density as a function of converter bandgap with emitter temperature treated parametrically

Both broad-band and selective emitter-based TPV systems are presently under development in the United States and components of both types of system have been discussed at the National Renewable Energy Laboratory's (NREL) conferences on the subject [3, 4]. The conference proceedings represent the state-of-the-art of the subject. In this paper, we shall discuss a cross-section of the papers reported at these meetings.

COMPONENTS OF A TPV SYSTEM

All TPV systems must include (1) a fuel and a burner, (2) a radiator, (3) a means of recovering unuseable long-wave photons, (4) a photovoltaic converter, and (5) a system for waste-heat recuperation. We shall briefly review progress in these areas.

Burners

In the United States, the burner industry consists of a very diverse and fragmented collection of manufacturers that are mainly small businesses. Radiant burners have been developed primarily to operate in the 1500 K range and are near-ideal for TPV systems. In the majority of applications (such as drying of paper, crops, inks, and paints), the long-wave radiation is useful because it penetrates further into the material and assists uniform drying. For TPV systems, the long-wave radiation is problematic. In the United States, the burners are mainly of the porous ceramic type (such as silicon carbide), although some are based on metal-mesh

approaches. There is no incentive to operate above 1500 K because problems with NO_x emissions increase exponentially with temperature. In surveys we have conducted, manufacturers of burners are generally unaware of the existence of TPV and several appear interested in becoming involved. We have not been able to identify any insurmountable barriers in burner technology and this component of a TPV system appears to be the most readily adaptable to needs. Burners are durable, can accomodate a wide variety of fuels, have both high and low thermal masses (as desired), and are a small part of the total cost of prospective systems.

Selective Emitters

In rare-earth oxides, the 5s and 5p electron shells begin to fill before the 4f shell, which contains the valence electrons, is filled. The valence electrons are, therefore, screened, and rare-earth ions behave like gaseous ions and emit line-spectra, rather than continuous spectra. This causes the selectivity of rare-earth oxides for which they are exploited in some TPV systems. The emissivity is high within the emission band and low outside it. The 5s and 5p electrons ensure that the environment around the atoms has little effect on them. Hence, their optical and electrical properties are relatively invariant, whether as oxides or as dopants in other materials.

The emission band of Yb_2O_3 corresponds to the bandgap of silicon; Er_2O_3 corresponds to Ge (or GaSb); and Ho_2O_3 corresponds to III-V alloys, such as $Ga_xIn_{1-x}As$ and $Ga_xIn_{1-x}As_ySb_{1-y}$, bandgaps of approximately 0.5 eV [7]. Chubb et al. [8] analysed both thin-film and small-particle selective emitters [8, 9] and showed that (1) the emission characteristics are governed by the diameter of the particles or the thickness of the films, and (2) the optimum characteristic dimension is approximately 8-20 μm, for an emitter temperature of 1500-2000 K. The approach divided the radiation into three bands, corresponding to the in-band, high-energy, and low-energy, components. The efficiency was defined as the ratio of the in-band component of radiated energy to the total radiated energy. This was expressed as a function of particle size, particle concentration, emitter thickness, and various other material parameters. The emissivity increases to near unity at some upper wavelength limit, due to lattice vibrations. The long-wave radiation must be reflected back to the radiator to maximize system efficiency, a requirement that is common to both selective and broad-band radiators. Chubb et al. [8] showed that the efficiency of the in-band process could exceed 0.6, with radiated power densities exceeding 10 watts cm^{-2}.

Nelson [7] was one of the pioneers of this technology and was originally responsible for producting the first practical selective emitter system. This used a "rug" of fibers of Yb_2O_3, produced by a replication process. Rayon fibers were impregnated with ytterbium nitrate and dried. They were then tufted into a porous ceramic support structure and subjected to a controlled heat-treatment. This converted the nitrate into oxide and, with further heat-treatment, the organic fiber was burned off, leaving behind a ceramic skeletal structure. The diameter of the ceramic fibers was about 10 μm, and they were strong and resistant to mechanical vibration, but their production is labor-intensive. A schematic of the structure is shown in Figure 2. The fuel passes through the body of the plenum and then through the porous ceramic substrate. It is burned above the substrate surface, but below the tips of the fiber loops. Only the fibers are heated, and there is insignificant broad-band radiation from the substrate.

The silicon-convertible radiation was measured as a function of the fuel/air mixture, the pre-heating temperature of the fuel, and the fuel load. Figure 3 shows the silicon-convertible exitance (or emittance), without pre-heating, as a function of the fuel load. This shows that at least 4 watts cm^{-2} are available for conversion. In a private communication, Nelson reported a radiator yielding approximately 6 watts cm^{-2} of silicon-convertible energy which, if converted by the high-quality silicon solar cells, would give greater than 2 watts cm^{-2}. It was claimed that NO_x emissions were low, although the fuel-to-photon conversion efficiency appears to be poor

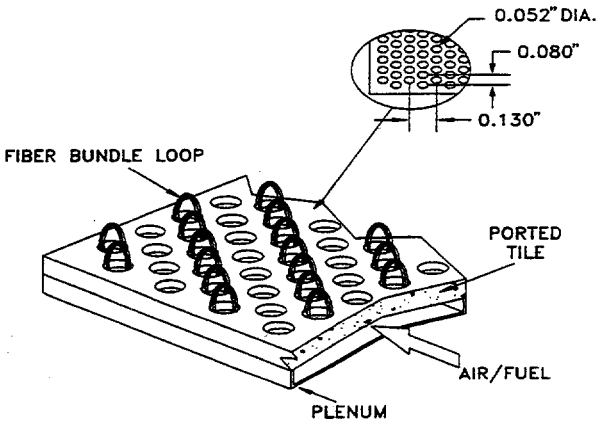

Figure 2: Selective emitter based on fibers of Yb_2O_3 (Courtesy of the Tecogen Division of the Thermo Power Corporation)

at present. The design has been used in conjunction with self-powered gas furnaces, which eliminates safety concerns caused by electric power supply failure.

Holmquist [10] discussed a selective emitter based on Yb_2O_3, fabricated using a replication process. A rayon-felt mat of fibers was first coated with ytterbium nitrate. This was reacted with ammonia to form the hydroxide, which coated the rayon fibers. Finally, the mat was heated in oxygen to form the oxide. The heating schedule was crucial,

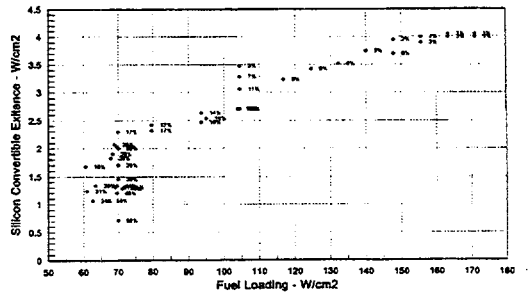

Figure 3: Silicon-convertible exitance vs. fuel loading (Courtesy of the Tecogen Division of the Thermo Power Corporation.)

because there was substantial shrinkage. At this stage, the oxide was amorphous but was made crystalline (and stronger) by heating to a much higher temperature in an inert atmosphere. The diameter of the fibers was about 10 μm, consistent with the theoretical considerations discussed above. It was claimed that a temperature of 2000 K was achieved with an oxygen/methane mixture, although there was apparently some localized melting of the emitter. It was also claimed that high-efficiency silicon converter cells gave an output of 2.4 kilo watts, although the efficiency of the system is uncertain.

Lowe et al. [11] developed selective emitters based on erbium and holmium-doped yttrium aluminum garnet (YAG). The erbium emission matches an $In_{0.53}Ga_{0.47}As$ converter grown lattice-matched on an InP substrate, whereas holmium matches $In_{0.8}Ga_{0.2}As$, grown lattice-mismatched on an InP substrate. The YAG substrates were cut from Czochralski-grown crystals, polished on both sides; measurements were made of the spectral emittance and the emitter efficiency of samples placed at the window of a furnace. Their temperature was approximately 1472 K. At the time of publication, no attempt had been made to optimize the doping or the thickness of the samples; they were commercially available and typically used for solid-state lasers. It was mentioned that two dopants may be used for use in tandem TPV devices and to increase the overall efficiency of emission. The measured efficiencies were approximately 60% within the emission band, for YAG doped with 40% Er/1.5% Ho. It was stressed that there was a significant temperature gradient across the films, and this must have modified the emission characteristics. The spectral emittance of an Er-25%/Ho-40% doped YAG is shown in Figure 4, from which it is seen that the emittance reaches almost 60%. However, the off-band emission was between 20-30%, which is too large. There may be additional problems of fragility, manufacturability, and excessive vapor pressures with fibrous emitter systems, although their proponents do not regard these as insurmountable. There are also very few estimates of the conversion efficiency of fuel to photons. Doped YAG emitters appear to have significant potential although they may be economically unacceptable.

Broad-Band Emitters

Black and grey-bodies emit across a wide range of wavelengths according to Planck's equation. Many photons have energies less than the bandgap of typical converters and must be returned to the radiator to conserve energy. Many absorbed photons have more energy than needed to excite band-to-band transitions of electrons, implying that thermalization of excited charge causes the cells to heat and necessitate cooling. Modelling of converter peformance shows the optimum bandgap does not depend very sensitively on the radiator temperature in the range 1300-1700 K, but must be aproximately 0.4-0.7 eV [6], as illustrated in Figure 1.

Pernisz et al. [12] developed a novel silicon carbide (SiC) radiator using a precursor chemistry that provided considerable flexibility in manufacture. The precursors were organic siloxanes based on methyl, phenyl, and vinyl groups. Prior to pyrolization, the precursor was formed into the desired shape using pressing or extruding techniques, and then machined to achieve the desired dimensions and surface finish. After this, the "green body" was pyrolized at 1600-2200°C to form SiC. The density and porosity of the finished radiator could be controlled with additives and by the temperature of pyrolysis. The spectral emissivity was measured and found to be at least 0.84 over most of the wavelength range from 1.2-3 μm. The ability to control the poros

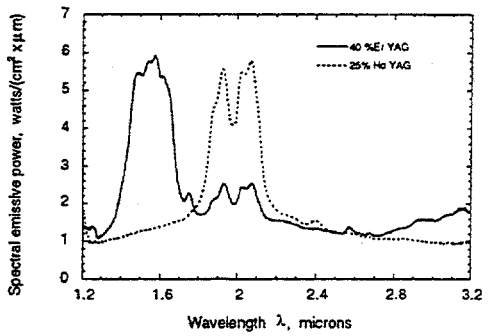

Figure 4: Spectral emittance of Er-40%:Ho-25% doped YAG

ity implies that the SiC could be used as the burner element. This may be, for example, in the form of a tube with fuel burning in the center and the outer surface radiating to the converter cells.

A variant of this was used by Fraas et al. [13] in a configuration known as a "spine disc burner/emitter". A schematic of the system is shown in Figure 5. Fuel is passed through holes machined in a set of SiC discs to an ignitor chamber, where it is burned. After combustion in the ignitor chamber, the hot exhaust gases pass through central holes in a second set of discs; the spine discs. Successive spine-discs are rotated with respect to each other, resulting in turbulence of the hot gas and efficient heating of the discs. The infrared radiation is incident on the TPV cells, which are positioned a small distance from the outer surface of the spine discs. After passing through the spine discs, the hot exhaust gases are passed back to the first set of discs and pre-heat the incoming fuel. All components of a full system are shown here, including the TPV cells and a silica heat shield. This absorbs all radiation of wavelength greater than 4 μm, causing it to heat and re-emit half the radiation back to the radiator.

The broad-band approach is simpler than using a selective emitter, it is easier to manufacture, may be more durable, and is less labor-intensive.

PHOTOVOLTAIC CONVERTERS

It was originally envisaged that selective emitters would be used at as high a temperature as practicable (2000 K being the objective), in conjunction with silicon photovoltaic converter cells. If systems using Yb_2O_3 in conjunction with silicon cells can be reduced to practicality, they should give high power densities at low cost per watt. This is still the basis of the work being done by Nelson et al. [7] and by Holmquist [10]. There are, however, significant engineering problems in working at such a high temperature, and other

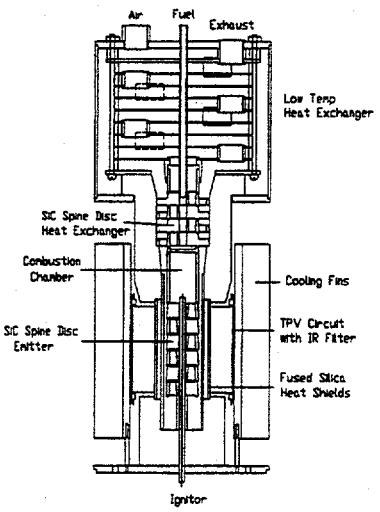

Figure 5: Vertical cross-section through spine-disc burner (Courtesy of JX Crystals, Inc.)

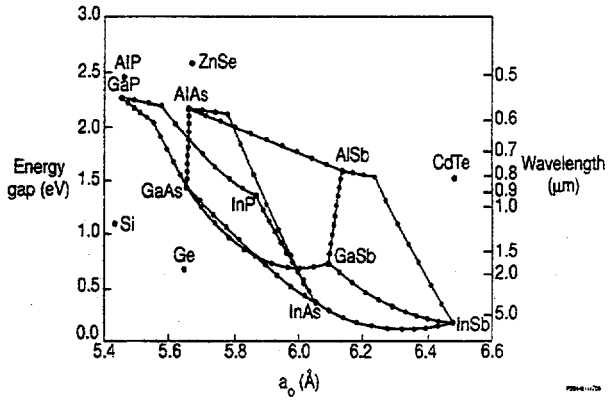

Figure 6: Bandgap and lattice constant data for some III-V compounds and alloys

interesting approaches are being investigated.

Lower radiator temperatures may increase system durability, lessen heat-loss problems, and would cause less NO_x emission. They also necessitate lower bandgap converters, used with broad-band, erbia or holmia radiators. The issue then becomes the fabrication of the optimum converter, which has not been fully resolved at this point. In this section, we shall review ongoing research into the development of low-bandgap converters, based on the III-V family of semiconductors.

Figure 6 shows the variation of bandgap with lattice constant for the some compounds and alloys from the III-V family of semiconductors. By drawing an abscissa at approximately 0.5 eV, we can establish the materials of relevance for TPV converters. Fraas et al. [13] successfully used GaSb (with Eg = 0.73 eV), using a simple diffusion process. They argued that this approach offers significant economic advantages, compared with fabrication of devices using epitaxial processes. Nevertheless, the cost of GaSb substrates is high and this, rather than the specific device fabrication process, may dominate the cost.

Modelling studies [6] showed that, in principle, the bandgap of GaSb is slightly too large; the ideal being approximately 0.5 eV. This, however, remains to be resolved practically because there may be additional issues (for example, elevated operating temperature, additional recombination processes, parasitic series-resistance losses, and others) that complicate the choice. There is, at present, no recognizably near-ideal semiconductor converter and several options are being investigated.

Wojtczuk [14] performed an empirical investigation to determine the ideal bandgap. Cells were grown using atmospheric pressure organometallic vapor phase epitaxy (APOMVPE) using InP substrates. $Ga_{0.47}In_{0.53}As$ has the same lattice-constant as InP, but its bandgap of 0.73 eV is larger than ideal. By increasing the atomic proportion of indium, the bandgap may be reduced but the epitaxial layers are then in biaxial compression. The device performance is impaired by dislocations that form to relieve the strain. The devices made by Wojtczuk [14] had bandgaps in the range 0.73-0.5 eV; compressive stresses increased with decreasing bandgap, and the concentration of defects increased accordingly. It was established that the optimum bandgap was 0.64 eV, because the increasing concentration of defects at lower bandgaps caused performance to deteriorate much quicker than the simple modelling predicted.

In an effort to reduce the concentration of dislocations in the epitaxial layers, Wanlass et al. [6] and Wilt et al. [15] used both continuous- and step-grading, whereby the composition of the $Ga_{1-x}In_xAs$ was gradually made increasingly indium-rich from the InP substrate upwards to the final device layers. In both cases, growth was performed using APOMVPE, and grading reduced the strain in the active layers of the converter, enabled the $Ga_{1-x}In_xAs$ bandgap to be reduced to 0.5 eV (for x~0.75) and allowed good device performance to be obtained. Figure 7 illustrates deterioration in carrier collection with increasing indium and decreasing bandgap, indicating that recombination at dislocations was probably dominating over the near-to-optimum bandgap. At a bandgap of 0.49 eV, the performance was no longer adequate, presumably because there was a severe increase in the concentration of defects. In addition, even if dislocation-free material could be grown, it is possible that Auger recombination may become important at lower bandgaps, as reported by Kurtz et al. [16]. Figure 8 shows the J/V characteristic for a mismatched device with a bandgap of 0.55 eV and with excellent performance.

Referring again to Figure 5, we see that it is possible to grow materials in the family $Ga_xIn_{1-x}As_ySb_{1-y}$ that are lattice-matched to either InAs or GaSb, and with bandgaps of 0.36-0.73 eV. These are being developed for long-wavelength and intermediate wavelength lasers. Efforts are being made to use it to eliminate the dislocation problems in GaInAs described above to grow epitaxial layers with bandgaps of 0.5-0.55 eV.

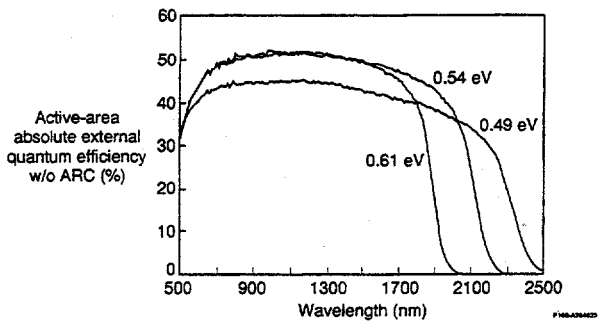

Figure 7: Quantum efficiencies of three $Ga_xIn_{1-x}As$ devices grown lattice-mismatched on InP substrates. Active area was used to calculate QE, and no anti-reflection coatings were applied.

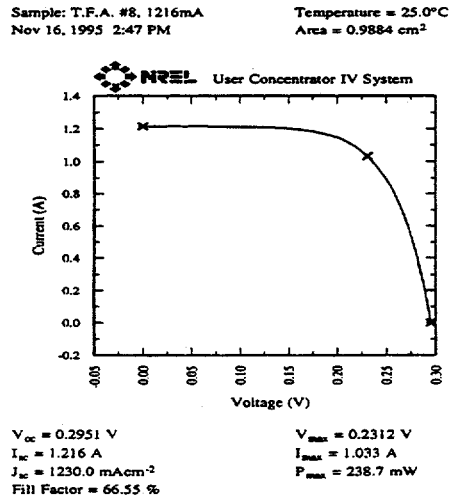

Figure 8: J/V characteristic for a 0.55 eV TPV converter grown lattice-mismatched on an InP substrate. A double-layer anti-reflection coating of ZnS/MgF_2 was used.

Wong et al. [17], for example, grew layers of $Ga_{0.82}In_{0.18}As_{0.16}Sb_{0.84}$, which is lattice-matched to GaSb and has a bandgap of 0.6 eV, using molecular-beam epitaxy (MBE). The aim was to fabricate a tandem cell with the junctions responding to the selective emissions from Er_2O_3 and Ho_2O_3, respectively. The bottom cell of the tandem was formed from the quaternary alloy, and the top cell was made of GaSb. Measurable output was obtained from both sub-cells, and this must stand as the first tandem TPV device. It should also be noted that this approach could also be used with a broad-band spectrum. Calculations indicate that the above bandgaps are too large: values of 0.55 eV and 0.4 eV are more suitable. This is based on modelling of tandem cells by Horner et al. [18], who suggested an advanced concept using the alloy Ga_2AsSb.

OPTICAL CONTROL

In the modelling mentioned above, it was assumed that the sub-bandgap photons are returned to the radiating surface and re-absorbed with high efficiency. Several approaches are being investigated to achieve this, as briefly reviewed below.

Plasma/Interference Filters

A thin-film with a carrier concentration of about 10^{20} cm^{-3} exhibits a transition from high transmittance to high reflectance at a wavelength of around 3 μm, the plasma wavelength. This approach has been used by various workers, including: Ehsani et al. [19], who attempted to used degenerately doped silicon; Wu et al. [20], who developed filters based on cadmium stannate; and by Murthy et al. [21], who used indium tin oxide. In each case, free-carrier absorption was excessive. A plasma filter may be combined with a multi-layer dielectric edge-filter. The edge filter (on one side of a transmissive substrate) may be used to reflect photons in the range between the plasma wavelength and the bandgap of the converter, and also to transmit shorter wavelengths. Edge filters always exhibit side-bands, and the plasma filter (on the opposite side of the transmissive substrate) reflects the radiation before reaching the dielectric filter. Nevertheless, absorption is still problematic.

Back-Surface Reflector

If a transmissive substrate is used, sub-bandgap radiation is transmitted to the back surface and is reflected back to the radiator. Charache et al. [22] suggested that this could be achieved by growing a quaternary alloy grown on GaSb. The substrate must be conductive (i.e., relatively heavily doped) to minimize contact resistance, but free carriers absorb some of the sub-bandgap radiation, which heats the substrate. A low contact resistance is required, but not at the expense of optical absorption. The back contact must be highly reflective, and various approaches were tried. These included the use of a non-alloyed contact to an InAs substrate, a heavily doped back-surface layer on a GaSb or InP substrate, and an alloyed grid contact used in conjunction with a planar metal reflector. Modelling work showed that a specific contact resistance less than $5x10^{-5}$ Ω cm^{-2} and as high a reflectance as possible were required. Each of the approaches investigated was promising and gave a specific contact less than the target value, with sub-bandgap reflectances of greater than 80%. Hence, the use of a back-surface reflector appears more promising than the plasma/interference filter approach.

Resonant Filter Array

Horne et al. [23] discussed the use of a high-density array of antenna elements. Two concepts were investigated, and both required high-resolution lithography using electrons or ions. Slots etched into a metal film cause inductive resonance, and the film acts as a band-pass filter. Metal ele-

ments deposited onto a dielectric substrate, produce a capacitive resonance (a rejection filter). In both cases, the dimensions must be of the same order as the wavelength of the radiation. The band-pass filter had reflectances near 100% for wavelengths greater than about 2 μm. Although the performance was excellent, production costs may be excessively high.

CONCLUSIONS

Intensive research is being conducted on all aspects of TPV components and systems. In this short review, we have attempted to describe a representative cross-section. Well-developed systems are being assembled for space application, and systems are being developed for use with solar heating and storage. Many options are open for burners/emitters, converters, photon recirculation, and heat recovery. An embryonic industry is beginning to form, although most funding at present is military in origin. There are potentially, however, many non-military applications that could command a very large market. At present, the main economic issue is the cost of the converters, which mainly use expensive substrates. If cells on low-cost substrates could be made, then business prospects would be excellent.

REFERENCES

1. C. W. Kim and R. J. Schwartz, "A p-i-n Thermo-Photovoltaic Diode," IEEE Trans. Elec. Dev., **ED-16**, 1969, pp. 657-663.
2. R. M. Swanson, "Recent Developments in Thermophotovoltaic Conversion," *Proc. Int. Elec. Dev. Meeting*, 1980, pp. 186-189.
3. *AIP Conference Proceedings 321*, American Institute of Physics, New York (First NREL Conference on Thermophotovoltaic Generation of Electricity, Copper Mountain, Colorado, 1994)
4. *AIP Conference Proceedings 358*, American Institute of Physics, New York (Second NREL Conference on Thermophotovoltaic Generation of Electricity, Colorado Springs, Colorado, 1995)
5. M. W. Wanlass, J. S. Ward, K. A. Emery, A. Duda, and T. J. Coutts, "Improved Large-Area, Two-Terminal InP/$Ga_{0.47}In_{0.53}As$ Tandem Solar Cells," *Conference Record of the Twenty-Fourth IEEE Photovoltaic Specialists Conference*, IEEE, New York, 1994, pp. 1717-1720.
6. M. W. Wanlass, J. S. Ward, K. A. Emery, and T. J. Coutts, "$Ga_xIn_{1-x}As$ Thermophotovoltaic Converters," *Conference Record of the Twenty-Fourth IEEE Photovoltaic Specialists Conference*, 1994, IEEE, New York, pp. 1685-1691.
7. R. E. Nelson, "Thermophotovoltaic Emitter Development," 1st NREL/TPV Conference, pp. 80-98.
8. D. L. Chubb, R. A. Lowe, and B. S. Good, "Emittance Theory for Thin Film Selective Emitter," 1st NREL/TPV Conference, pp. 221-228.
9. D. L. Chubb, and R. A. Lowe, "A Small Particle Selective Emitter for Thermophotovoltaic Energy Conversion," 2nd NREL/TPV Conference, pp. 263-277.
10. G. A. Holmquist, "TPV Power Source Development for an Unmanned Undersea Vehicle," 1st NREL/TPV Conference, pp. 308-314.
11. R. A. Lowe, D. L. Chubb, and B. S. Good, "Radiative Performance of Rare Earth Garnet Thin Film Selective Emitters," 1st NREL/TPV Conference, pp. 291-300.
12. U. C. Pernisz and C. K. Saha, "Silicon Carbide Emitter and Burner Elements for a TPV Converter," 1st NREL/TPV Conference, pp. 99-105.
13. L. Fraas, R. Ballantyne, J. Samaras, and M. Seal, "Electric Power Production Using New GaSb Photovoltaic Cells with Extended Infrared Response," 1st NREL/TPV Conference, pp. 44-53.
14. S. Wojtczuk, "$In_xGa_{1-x}As$ TPV Experiment-based Performance Models," 2nd NREL/TPV Conference, pp. 387-393.
15. D. M. Wilt, N. S. Fatemi. R. W. Hoffman, Jr., P. P. Jenkins, D. Scheiman, R. Lowe, and G. A. Landis, "InGaAS PV Device Development for TPV Power Systems," 1st NREL/TPV Conference, pp. 210-220.
16. S. R. Kurtz, R. M. Biefeld, and L. R. Dawson, "Modification of Valence-Band Symmetry and Auger Threshold Energy in Biaxially Compressed $InAs_{1-x}Sb_x$," Phy. Rev. B, pp., **51**, 1995, pp. 7310-7313.
17. E. M. Wong, P. N. Uppal, J. P. Hickey, C. H. Waldman, and G. A. Holmquist, "Multiband Spectral Emitters Matched to MBE Grown Photovoltaic Cells," 2nd NREL/TPV Conference, pp. 278-289.
18. G. S. Horner, T. J. Coutts, and M. W. Wanlass, "Proposal for a Second-Generation, Lattice Matched, Multiple Junction Ga_2AsSb TPV Converter," 1st NREL/TPV Conference, pp. 390-403.
19. H. Ehsani, I. Bhat, J. Borrego, R. Gutmann, E. Brown, R. Dzeindziel, M. Freeman, and N. Choudhury, "Characteristics of Degenerately Doped Silicon for Spectral Control in Thermophotovoltaic Systems," 2nd NREL/TPV Conference, pp. 312-328.
20. X. Wu, W. P. Mulligan, J. D. Webb, and T. J. Coutts, "TPV Plasma Filters Based on Cadmium Stannate," 2nd NREL/TPV Conference, pp. 329-338.
21. S. D. Murthy, E. Langlois, I. Bhat, R. Gutmann, E. Brown, R. Dzeindziel, M. Freeman, and N. Choudhury, "Characteristicsof Indium Oxide Plasma Filters Deposited by Atmospheric Pressure CVD," 2nd NREL/TPV Conference, pp. 290-311.
22. G. W. Charache, D. M DePoy, P. F. Baldasaro, and B. C. Campbell, " Characteristics of Thermophotovoltaic Devices Utilizing a Back Surface Reflector for Spectral Control," 2nd NREL/TPV Conference, pp. 339-350.
23. W. E., Horne, M. D. Morgan, and V. S. Sundaram, "IR Filters for TPV Converter Modules," 2nd NREL/TPV Conference, pp. 35-51.

DENSITY OF STATES MEASUREMENTS IN A P-I-N SOLAR CELL

Richard S. Crandall and Qi Wang
National Renewable Energy Laboratory,
1617 Cole Blvd., Golden, CO 80401

ABSTRACT

We describe results of density of states (DOS) profiling in p-i-n solar-cell devices using drive-level capacitance (DLC) techniques. Near the p-i interface the defect density is high, decreasing rapidly into the interior, reaching low values in the central region of the cell, and rising rapidly again at the n-i interface. We show that the states in the central region are neutral dangling-bond defects, whereas those near the interfaces with the doped layers are charged dangling bonds.

INTRODUCTION

Knowledge of the defects and their distribution in space and energy is a fundamental ingredient in solar-cell modeling. To date this information is lacking, as the information about defects is obtained from measurements on homogeneous films. In a device, the structure is far from homogeneous. Charged dangling bonds, distributed from the interfaces with the doped layers into the bulk, are produced by defect thermodynamics [1] . However, their spatial and energy distributions are postulated theoretically, but yet unmeasured in actual cells. Defects at interfaces are not necessarily present in the bulk.

Therefore, it is important to develop new techniques to determine the defects in a cell. Among the most useful techniques developed to profile defects in crystalline semiconductors is capacitance-voltage (C-V) profiling. Unfortunately, this technique is difficult to interpret in amorphous silicon because the depletion charge is not fixed, but depends on applied bias. In addition, the large spread in deep-state emission energies makes results dependent on measurement time scales. To overcome this difficulty, Michelson et al. [2] developed the drive-level capacitance (DLC) technique and applied it to n-type Schottky barrier structures. They obtained a picture of the density of states (DOS) throughout the doped layer. In this paper we describe how this technique is used to measure the spatial profile of defects in the i layer of solar cells. We combine the analytic form of DLC with simulations of the solar-cell devices using the AMPS solar cell modeling program [2] .

EXPERIMENTAL DETAILS

The a-Si:H solar cells are fabricated using radio-frequency glow discharge of silane and doping gases. Details of the deposition conditions are published elsewhere [3] . Trimethylboron (TMB) and phosphine, respectively, are used for the p- and n-type doping. The H content of the samples is about 10%. The films are grown on 1 in. x 1 in. 7059 glass substrates coated with SnO_2, which serves as a back contact to the p layer. The i layer thickness varies between 500 and 4000 nm.

The capacitance is measured by a standard lock-in technique using frequencies between 100 and 10 kHz. The devices are mounted in an evacuated liquid nitrogen Dewar capable of maintaining a stable temperature. Measurements are performed at different temperatures between 299 K and 470 K. The DLC theory gives the defect density (N_{DL}) in terms of an expansion of the measured capacitance (C). The theory was developed for an n-type junction, device and the quantities defined below apply to the n layer.

$$C = Co + C1dV + C2(dV)2 \qquad (1)$$

The terms in the expansion of C are obtained by measuring C at a variety of ac drive voltages (dV). The defect density is obtained from

$$N_{DL} = - \frac{C_o^3}{2q\varepsilon A^2 C_1} \qquad (2)$$

where q is the magnitude of the elemental charge, ε, the dielectric constant, and A the sample area. To obtain the defect profile, measurements are made as a function of bias, and N_{DL} is plotted versus the depletion width (W). The depletion width is measured from the junction.

$$W = eA/Co \qquad (3)$$

The defect density corresponds most closely to the density at the edge of the depletion width.

EXPERIMENTAL RESULTS

Figure 1 shows typical C-V data for a thick p-i-n device. Measurements at lower frequency or higher temperature would show correspondingly higher values of capacitance as more states would be able to respond to the ac voltage. To obtain the DOS, we typically measure at seven peak-to-peak ac voltages between 0.02 and 0.14

V. The data are then fit to obtain C_o and C_1 at each dc bias value.

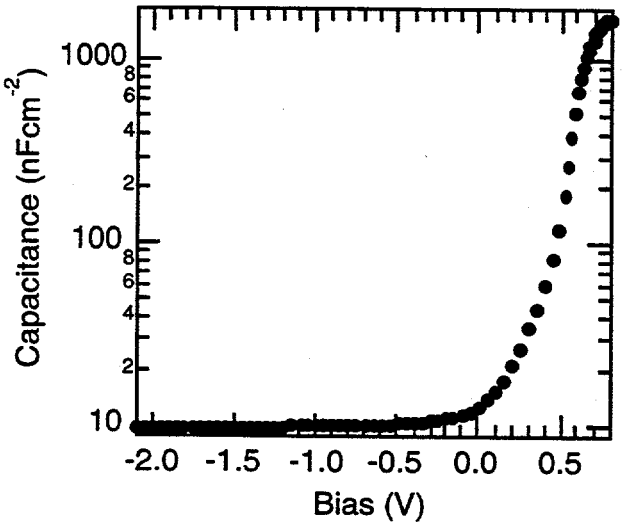

Fig. 1. Capacitance vs. dc bias for a plasma-enhanced chemical vapor deposited p-i-n solar cell. The i layer is 1.3 μm thick. The measuring frequency is 10 kHz and the temperature is 297 K. The peak-to-peak ac voltage is 0.03 V.

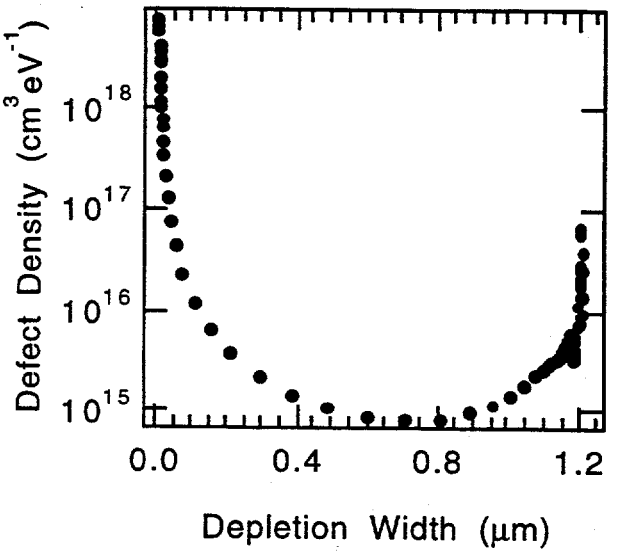

Fig. 2. DOS vs. depletion width in the solar cell depicted in Fig. 1. The attempt-to-escape frequency is taken to be 1 x 10^{12} s^{-1}.

In general, we find the DOS is of the form shown in Fig. 2. The distance from the p layer is taken equal to W as derived in Eq. 3. Near the p-i interface there is a gradual fall off in the DOS, reaching low values in the central region of the cell, and rising rapidly at the n-i interface. The DOS in Fig. 2 contains only those states lying within 0.7 eV of the conduction band edge. Deeper states would not be able to respond to the 10-kHz measuring frequency at this temperature. To determine the nature of the defects that are in the different regions of the i layer requires the use of solar-cell simulation. To do this we use the AMPS solar-cell model [2] .

SOLAR CELL SIMULATION

The AMPS solar cell model has been under development at Pennsylvania State University to model single- and multi-junction amorphous silicon cells. Here, we use it to gain insight into what we measure by DLC. This model calculates the field profiles, energy bands, and defect occupancies throughout the cell. We use it to find W as a function of bias and the nature of the defects at the point in the i layer corresponding to W. Unfortunately, AMPS does not treat the dangling bond as an amphoteric defect, but rather, uses neutral acceptor or donor states to denote the possible transitions. Furthermore, AMPS is a steady-state, rather than a transient simulation. To calculate the ac capacitance, one must use a transient simulation. However, we can still use AMP to obtain qualitative insight rather than quantitative agreement with experiment.

Figure 3 depicts such a simulation for a 1.3-μm-thick i layer at 0.5 V bias. In the figure, W_e and W_h represent the electron and hole depletion widths, respectively. These widths are determined by the condition that the charge involved in the transition can respond at the ac measuring frequency. For electrons this condition is that

$$E_{ed} = E_c - E_f = k_B T \ln(\nu_e/f) \qquad (4a)$$

and for holes,

$$E_{hd} = E_f - E_v = k_B T \ln(\nu_h/f) \qquad (4b)$$

T is the absolute temperature, f the measuring frequency, ν the attempt-to-escape frequency, and k_B is the Boltzmann constant. The subscripts e and h refer to holes and electrons, respectively. E_f is the Fermi level and E_{ed} and E_{hd} are electron and hole demarcation levels respectively. Because $E_f - E_v > 0.5$ eV throughout the i layer, we do not expect the holes to be able to respond at the temperature and frequency used for measurements. If the frequency were much lower and/or the temperature

higher, the holes might be able to respond. However, $E_c - E_f > 0.15$ eV throughout the i layer so that electrons can respond. This approximation greatly simplifies the analysis and permits an unambiguous determination of the DOS. In what follows then, we take $W=W_e$ in all the analysis.

In the DLC measurement, W_e denotes the point at which the DOS is measured. With increasing negative bias, W_e moves further toward the n-i interface; with increasing positive bias, W_e moves toward the p-i interface. To see what states are occupied and can take part in transitions, we again use AMPS to find the defect occupancy. The occupied states are shown in Fig. 4.

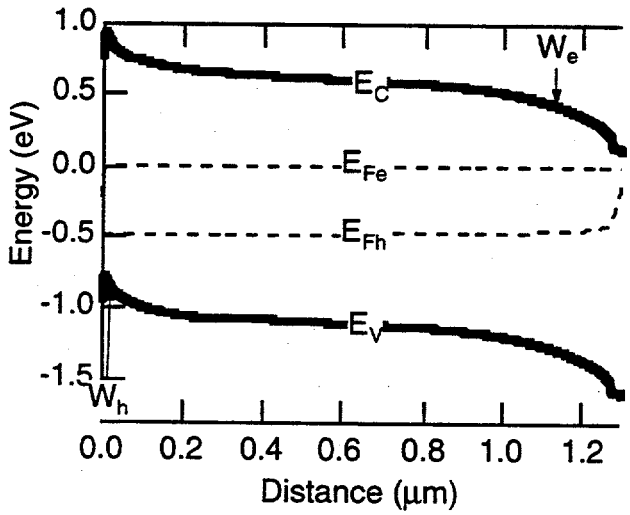

Fig. 3 Potential energy vs. distance in a 1.3 μm thick p-i-n solar cell at 0.5 V bias. The p layer is 10 nm thick and begins at 0. The n layer is 25 nm thick. The i layer contains 5×10^{15} $cm^{-3}eV^{-1}$ dangling bonds. The electron and hole quasi-Fermi levels are shown by dashed lines, and the electron and hole depletion widths are marked by arrows.

Figure 4 shows the both the occupied bandtail states and the dangling bonds. Bandtail states near the p-i interface are occupied with holes; those near the n-i interface are occupied with electrons. The dangling bonds (D) can be neutral or charged. The charge state is denoted by the superscript on D. Because AMPS does not treat the dangling bond as amphoteric, but AMPS rather uses neutral acceptor or donor states to denote the possible transitions, we determine the charge state by the Fermi-level position. Figure 4 shows that a significant fraction of the of the i layer contains neutral dangling bonds, with only a small fraction containing charged dangling bonds. The latter are situated near the doped layers where the quasi-Fermi levels are close to the band edges.

If we compare Figs. 3 and 4, we see that W_e is located in a region where there is a high density of D^-. From Fig. 3 we conclude that $W=W_e$ = 1.1 μm. Fig. 4 indicates that at W_e=1.1 μm, the occupied bandtail states are insignificant compared to the D^-. However, for larger W_e, the bandtail states dominate the W_e.

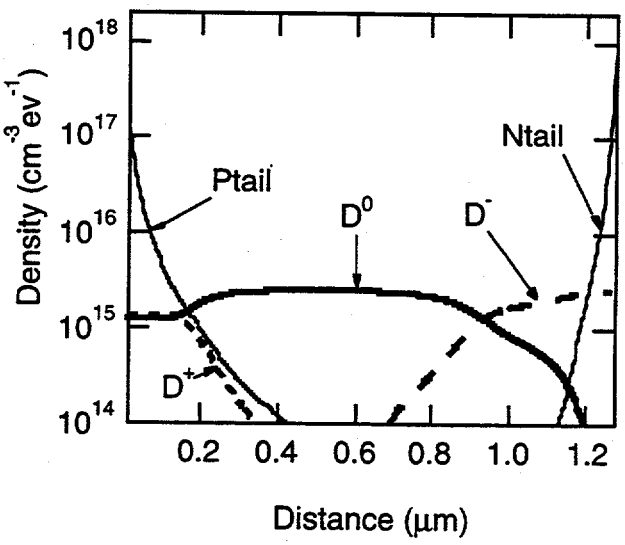

Fig. 4. DOS derived from AMPS simulation, using conditions as in Fig. 3 , showing the occupied tail states and dangling bonds. The superscript on the D represents the charge state of the dangling bond.

At larger forward bias, W_e moves rapidly to smaller values and probes the D^0 and D^+. For example, at W_e = 0.2 μm the D^+ and bandtail states occupied with holes are about equal. For smaller W_e, the density of D^0 and D^+ remain constant and the bandtail states occupied with holes increases. However, holes in bandtail states are not observed in DLC because they are too deep (>1.3 eV) in the gap to respond at the conditions of measurement. One might argue that we are observing a transitions between the valence band and an occupied bandtail state. However, two facts exclude this possibility. The first is that if the holes could respond, the W_h would lie near the n-i interface rather than the p-i interface. In this region, any states occupied by holes are too few in number to account the data. The second reason is that the measured DOS observed for small W are independent of temperature and frequency. This indicates that they are transitions involving shallow states. The only shallow states that can respond are D^+. The 0/+ transition of these defects is

located within about 0.5 eV from the conduction band [4]. However, Fig. 4 indicates that the density of D^+ is too low to account for the measured DOS in Fig. 2 close to the p-i interface.

To reconcile the DOS measured by DLC profiling with those from a standard AMPS simulation, it is necessary to include charged dangling bonds produced by thermodynamic equilibrium during growth [1] . Our previous calculation [1] indicates that there are high densities of negatively charged dangling-bond defects near the n-i interface and somewhat lower densities of positively charged dangling bonds near the p-i interface. Near the n-i interface these defects would be much larger than those produced by tail state occupancy. However, near the p-i interface they would be on the order of the occupied tail state density.

Figure 5 shows the result of including these charged dangling-bonds in an AMP simulation. The shape of the DOS for these charged dangling bonds mirrors that of the bandtails [1] . By including the D^+ and D^- near the p-i and n-i interfaces, one is better able to reconcile modeling an experiment.

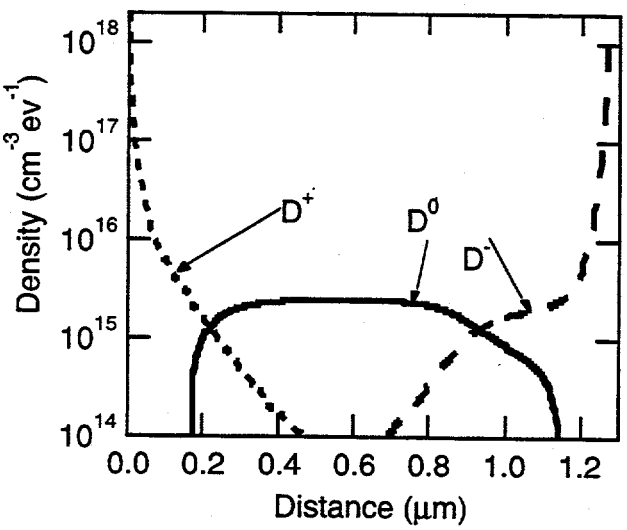

Fig. 5. DOS derived from AMPS simulation, using conditions as in Fig. 3, showing the charged dangling bonds determined from defect thermodynamics[1].

DISCUSSION AND SUMMARY

Although Figs. 2 and 5 are similar, it remains to argue that the defects shown in Fig. 5 are the ones detected in the DLC measurements. Figure 6 shows the transitions of the D defect in its three configurations [4]. Because the 0/+ transition of the D^+ is located at $E_c - E <$ 0.6 eV, this state is responsible for transitions that determine W_e in this part of the layer. The transitions that are measured when W_e is in the central portion of the i layer, are 0/- transitions of the D^0; when W_e is in near the n-i interface, transitions are the 0/- of the D^-. Comparing Figs. 2 and 5 shows that DLC measures two orders of magnitude fewer D^- than indicated by the simulation. the reasons for this are not yet clear.

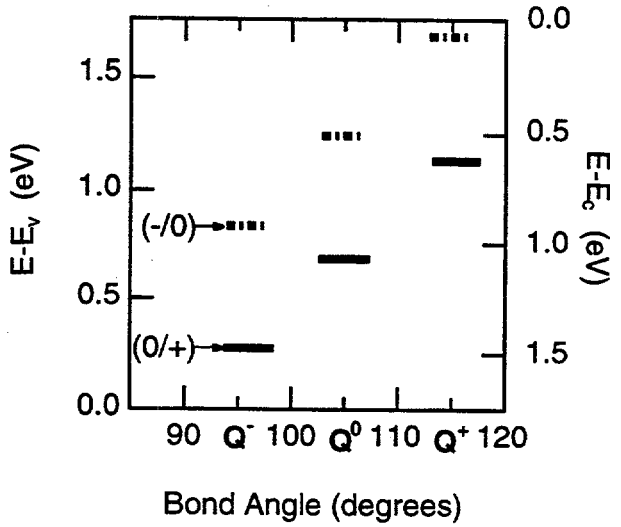

Fig. 6 Dangling bonds transitions in amorphous silicon as function of bond angle corresponding to the three charge states [4].

ACKNOWLEDGMENTS

The authors thank Yueqin Xu for the sample preparation. This work is supported by the U. S. Department of Energy under contract No. DE-AC36-83CH10093.

1. R. S. Crandall and H. M. Branz in *Proceedings of the Proc 21st IEEE Photovoltaics Specialist Conf.*, Kissimmee, FL, (1990), 1630.
2. J. K. Arch, F. A. Rubinelli, and S. J. Fonash, *J. App. Phys. 69,* 7057 (1991).
3. Y. S. Tsuo, Y. Xu, R. S. Crandall, H. S. Ullal, and K. Emery in *Amorphous Silicon Technology-1989*, edited by A. Madan, M. J. Thompson, P. C. Taylor, Y. Hamakawa, and P. G. LeComber (Materials Research Society, Pittsburgh, 1989), 471.
4. H. M. Branz and E. A. Schiff, *Phys. Rev. B* 48, 8667 (1993).

CONTROL OF BACK SURFACE REFLECTANCE FROM ALUMINUM ALLOYED CONTACTS ON SILICON SOLAR CELLS

Michael Cudzinovic and Bhushan Sopori
National Renewable Energy Laboratory
1617 Cole Boulevard
Golden, CO 80401

ABSTRACT

A process for forming highly reflective aluminum back contacts with low contact resistance to silicon solar cells is described. By controlling the process conditions, it is possible to vary the silicon/aluminum interface from a specular to a diffuse reflector while maintaining a high interface reflectance. The specular interface is found to be a uniform silicon/aluminum alloy layer a few angstroms thick that has epitaxially regrown on the silicon. The diffuse interface consists of randomly distributed (111) pyramids produced by crystallographic out-diffusion of the bulk silicon. The light trapping ability of the diffuse contact is found to be close to the theoretical limit. Both types of contacts are found to have specific contact resistivities of 10^{-5} Ω-cm^2. The process for forming the contacts involves illuminating the devices with tungsten halogen lamps. The process is rapid (under 100 s) and low temperature (peak temperature < 580°C), making it favorable for commercial solar cell fabrication.

INTRODUCTION

The ability to control the back surface reflectance to facilitate light trapping in silicon solar cells becomes increasingly important as cell thickness is decreased. To achieve the full benefits of light trapping and avoid parasitic losses, the back surface must have a high reflectance [1]. In most cell designs, a full backside aluminum metallization is used for the back contact. This serves as an electrical contact, so it must be sufficiently sintered to reduce the contact resistance. Because sintering roughens and spreads out the silicon/aluminum interface, lowering the interface reflectance, one is faced with balancing the optical and electrical properties of the contact. Several studies [2-4] discuss the decrease in total reflectance from aluminum back contacts on silicon as the processing temperature and/or time are increased. However, they do not differentiate between decreases in reflectance caused by light trapping (due to increased roughness of the silicon/aluminum interface) and interfacial absorption (due to silicon/aluminum alloying).

In this paper we show that good reflecting properties and ohmic characteristics can be attained simultaneously by producing a thin alloyed region at the interface. We describe a process that can be controlled to vary the silicon/aluminum interface from a specular to a diffuse reflector, while maintaining a high interface reflectance and low contact resistance. The optical and electrical properties of such contacts are given.

Single crystal, (100) silicon wafers were used to evaluate the effects of processing on reflectance. The wafers were polished on both sides, and a 3800 Å aluminum film was evaporated onto one side of each wafer, completely covering that side. The wafers were then processed in an Optical Processing Furnace [5]. The furnace consists of a bank of tungsten-halogen lamps that illuminate the sample from the top. The lamp power density is controlled during the process, and the sample temperature is monitored by placing the samples on another silicon wafer that has a thermocouple attached. An additional 2000 Å aluminum film was deposited on the samples after processing. The total integrated reflectance of the processed samples was measured using a Cary 2300 spectrophotometer.

FORMATION OF A SPECULAR BACK CONTACT

An unprocessed silicon/aluminum interface gives the highest possible total reflectance; however, it makes a poor electrical contact. Some heat treatment is required to reduce the contact resistance. To maintain a specular contact, the silicon/aluminum interface must remain abrupt and smooth. This requires a fast, low temperature process to limit the diffusion of silicon into the aluminum. Figure 1 shows the lamp power and sample temperature as a function of time for a specular back contact process. The maximum sample temperature is only 372°C and the lamp process takes less than 100 seconds.

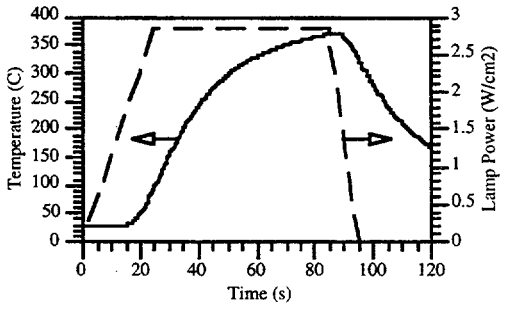

Fig. 1: Lamp power density and sample temperature profiles for formation of a specular back contact. Note the lamp process is under 100 seconds and the sample only reaches 372°C.

This process results in an atomically smooth interface, where the silicon/aluminum alloy has epitaxially regrown on the silicon. This is shown in the cross-sectional transmission electron microscope (TEM) picture in Figure 2.

Figure 3 compares the total integrated reflectance from a sample with this contact to an unprocessed sample. Note that for wavelengths greater than 1.2 μm (where the silicon absorption is low and the reflectance is dominated by the back surface), the reflectance of the specular back contact remains close to the unprocessed silicon/aluminum interface value. By assuming specular reflections from the silicon/aluminum interface, low absorption in the silicon, and accounting for multiple reflections, one can calculate the reflectance of the interface for the unprocessed and processed samples. Using the measured total reflectance at 1.3 μm and a reflectance of 0.32 from the front silicon surface, one finds there is only a 5% drop in interface reflectance for the sample processed for specular reflectance as compared to that of the unprocessed sample.

Fig. 2: Cross-sectional TEM picture of silicon/aluminum interface on a specular back contact. The alloyed layer is only a few hundred angstroms thick and has epitaxially regrown on the silicon.

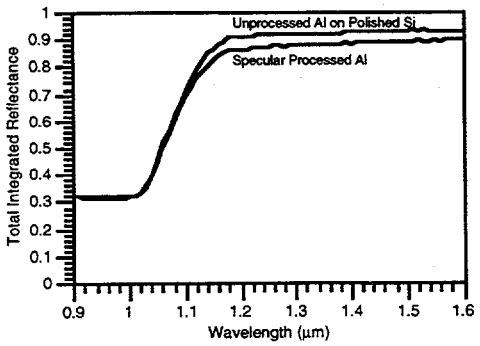

Fig. 3: Comparison of total integrated reflectance from unprocessed aluminum on polished silicon and specular processed aluminum. The specular processed contact reflectance has only decreased by 5% from the unprocessed case.

FORMATION OF A DIFFUSE BACK CONTACT

Increasing the process time and/or temperature will increase the diffusion of silicon into the aluminum. The diffusion rate across the interface will be non-uniform because of variations in the thickness of the native silicon oxide, resulting in a roughening of the interface. The roughness increases the light trapping ability of the contact, but the diffusion spreads out the interface, increasing the parasitic absorption. To obtain a diffuse reflector with a high reflectance, one needs an abrupt rough interface. An unprocessed interface of aluminum on rough silicon would be the limiting case.

Figure 4 compares the total integrated reflectance from two unprocessed samples: one sample was polished on both sides with aluminum on one side; the second was polished on only one side and had aluminum on the unpolished (rough) side. The unprocessed aluminum on rough silicon sample is a completely diffuse reflector because the only specular component of the total reflectance is from the front surface (this is easily determined by comparing the total measured reflectance and the reflectance measured with the specular component excluded). The silicon aluminum interface for this sample has a high reflectance of 92%. The much lower total reflectance for wavelengths greater than 1.2 μm for this sample is a result of light trapping.

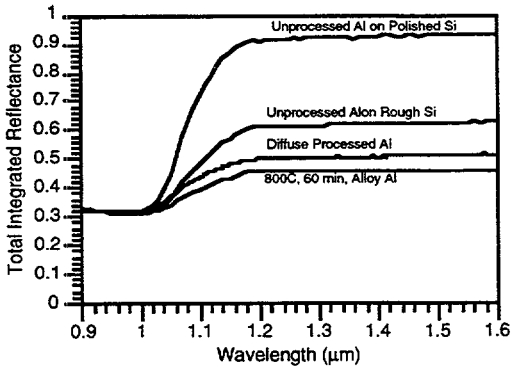

Fig. 4: Comparison of total integrated reflectance from unprocessed aluminum on polished silicon, unprocessed aluminum on rough silicon, diffuse processed aluminum, and alloyed aluminum (800°C, 60 minutes).

While the unprocessed aluminum on rough silicon sample has good optical properties - it is a diffuse reflector with high reflectance - it does not have good electrical properties. It will behave as a diode. The aluminum must be heat treated in order to achieve an ohmic contact with reasonable contact resistance.

Figure 5 shows the lamp power and sample temperature as a function of time for a diffuse back contact process. The maximum sample temperature is 580°C and the sample is above 500°C for only 30 seconds. This process results in randomly distributed (111) pyramids at the interface, produced by crystallographic out-diffusion of the silicon. These pyramids can be seen after removing the silicon/aluminum alloy, as shown in Figure 6.

The total integrated reflectance from a sample with this contact is shown in Figure 4. For wavelengths greater than 1.2 μm, the reflectance is below that for an unprocessed rough interface, indicating that there is some parasitic absorption occurring at the interface.

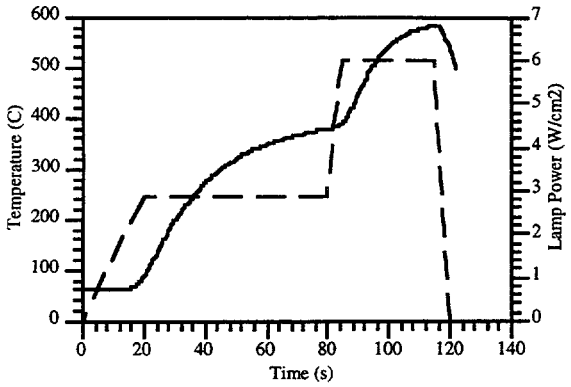

Fig. 5: Lamp power density and sample temperature profiles for formation of a diffuse back contact. Note the sample reaches 580°C and is above 500°C for only 30 seconds.

Assuming the interface is a perfectly diffuse reflector (which is easily checked by comparing the total reflectance and the reflectance measured with the specular component excluded), one can calculate the interface reflectance [1]. Using the measured total reflectance at 1.3 μm and a value of 0.32 for the reflectance from the front silicon surface, one finds there is only a 7% decrease in the interface reflectance for the diffuse processed sample as compared to that of the unprocessed sample.

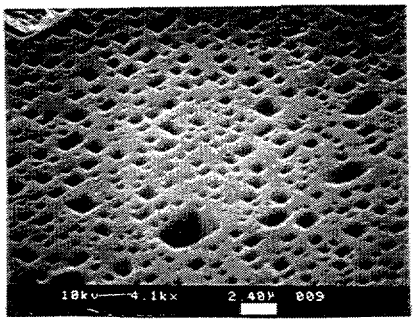

Fig. 6: SEM picture of silicon surface of diffuse processed sample after aluminum has been removed. The pits are randomly distributed (111) pyramids produced by crystallographic out-diffusion of the silicon.

If one continues to increase the temperature and time of the process, the interface absorption increases. This is also illustrated in Figure 4, in which the reflectance of a sample processed at 800°C for 60 minutes is shown to be even lower than the diffuse contact, and far below the limit for aluminum on rough silicon. The calculated interface reflectance for this contact drops by 12% from the unprocessed interface limit.

DETERMINATION OF THE SPECIFIC CONTACT RESISTIVITY

The specific contact resistivity was measured using the transmission line method [6]. The contacts were fabricated on boron diffused channels with a sheet resistivity of 45 Ω/square and a surface concentration greater than 10^{19} cm^{-3}. The contacts were processed using the procedures described above. Both the specular back contact process and the diffuse back contact process achieved ohmic contacts with specific contact resistivities of 10^{-5} Ω-cm^2. These values are sufficiently low to reduce the resistive power losses at the contacts in a solar cell to a negligible level [6].

CONCLUSION

We have described processes for forming specular and diffuse aluminum back contacts on silicon that maintain a high interface reflectance and low contact resistance. These processes result in only a 7% decrease in the reflectance from the silicon/aluminum interface, limiting the parasitic losses of light. The optical properties of these contacts make them ideally suited for light trapping schemes. The processes for forming these contacts are rapid and low temperature, making them favorable for commercial solar cell manufacturing. We are currently applying these processes to our solar cell fabrication.

ACKNOWLEDGMENTS

The authors would like to thank K. Jones for Figure 1, R. Matson for Figure 2, and L. Roybal for fabricating the structures for contact resistivity determination. This work was supported under U.S. Department of Energy contract No. DE-AC36-83CH10093.

REFERENCES

[1] J. M. Gee, "The Effects of Parasitic Absorption Losses on Light Trapping in Thin Silicon Solar Cells," *20th IEEE PVSC* (1988), p. 549.

[2] K. D. Rasch, K. Roy, R. Schilling, H. Fischer, "Compatibility of BSR and BSF Solar Cell Technology," *14th IEEE PVSC* (1980), p. 141.

[3] K. D. Rasch, K. Roy, K. H. Tentscher, "Advanced Thin Silicon Solar Cell With Controlled Optical Absorptance," *E.C. PVSEC* (1980), p. 205.

[4] P. A. Iles and C. L. Chu, "TPV Cells With High BSR," *2nd NREL Conference on Thermophotovoltaic Generation of Electricity* (1995), p. 361.

[5] B. Sopori et al., "Optical Processing: A Novel Technology for Fabricating Solar Cell Contacts," *23rd IEEE PVSC* (1993), p. 97.

[6] D. K. Schroder and D. L. Meier, "Contact Resistance: Its Measurement and Relative Importance to Power Loss in a Solar Cell," *IEEE Trans. Elec. Dev.*, **ED-31**, No. 5, May 1984.

ESTIMATING SERVICE LIFETIMES OF A POLYMER ENCAPSULANT FOR PHOTOVOLTAIC MODULES FROM ACCELERATED TESTING

A. W. Czanderna and F. J. Pern
National Renewable Energy Laboratory, Golden, CO 80401-3393

ABSTRACT

In this paper, most of the emphasis is on A9918 ethylene vinyl acetate (EVA) used commercially as the pottant for encapsulating photovoltaic (PV) modules, in which the efficiencies in field-deployed modules have been reduced by 10-70% in 4-12 years. Yet, projections were made by several different research groups in the 1980s that the EVA lifetime could range from 2-100 years. We (1) elucidate the complexity of the encapsulation problem, (2) indicate the performance losses reported for PV systems deployed since 1981, (3) critically assess the service lifetime predictions for EVA as a PV pottant based on studies by others for which we review the inherent errors in their assumptions about the Arrhenius relation, (4) show how degradation of minimodules in laboratory experiments that simulate reality can produce efficiency losses comparable to those in field-degraded PV modules reported in the literature, and (5) outline an acceptable methodology for making a service lifetime prediction of the polymer encapsulant, including the essential need for relating accelerated lifetime testing to real-time testing with a sufficient number of samples.

INTRODUCTION

The major purposes of this paper are given by (1) through (5) in the Abstract, which are all related to a goal for a 30-year service lifetime for PV systems [1]. The major literature resources have been reported by us in a recent critical review chapter [1]. Man-made solar-energy conversion systems such as PV modules are subjected to a unique set of stresses that may alter their stability and, hence, their performance and **life-cycle costs**, in addition to the initial costs of the systems. We focus on the stresses relevant to EVA. The stability of EVA is (or potentially is) affected by the following: ultraviolet (UV) insolation including wavelengths and intensity; temperature and its cycling (T and delta T); stabilizing additives and their concentrations [A]; gases present (e.g., humidity and oxygen) and their concentrations [G]; impurity ions present and their sources [M^+]; degradation products and concentrations [D]; contact with interfaces including adhesives and primers (I); electric fields (**E**); electron transport (e); processing during manufacture, extrusion, lamination, and curing, including the influence on the resultant structure and bulk properties [P]; interphase thickness; and the synergism of all of these variables [2]. The photo-oxidation of Elvax 150™ (Du Pont)in either A9918 or 15295 EVA may result in changes in the optical, mechanical, dielectric, permeability, and chemical properties, all of which may compromise the designed function of the encapsulant. The stability of the polymer depends on chemical kinetic reactions, and each of the many possible reaction paths is governed by an activation energy, which may range from zero kJ/mol (non-activated) to more than100 kJ/mol. Although one reaction usually dominates at a particular temperature, the rate-controlling reactions may be different, even over relatively narrow temperature ranges [2]. A critical component of a PV module is the polymeric pottant that provides structural support, optical coupling, electrical isolation, physical isolation/protection, and thermal conduction for the solar-cell assembly [3]. A list of specifications and requirements for pottants is available [3]. To be economically and practically useful, the pottant has to meet the requirements of low cost, good processability, high optical transmission, high dielectric constant, low water absorptivity and permeability, high resistance to UV degradation and thermal oxidation, good adhesion, mechanical strength, and chemical inertness.

PV CELL AND MODULE ENCAPSULATION AND LOCATION OF POTENTIAL DEGRADATION

The four basic functions of the materials in a PV module encapsulation system have been summarized [1,3], in which the encapsulation provides all necessary functions except for the cell materials and the balance of system (BOS) for conducting the generated electricity from the module outlet terminals. A cross-section of a contemporary multilayered configuration of an EVA-encapsulated PV cell is shown in Fig. 1. Materials degradation and/or performance losses can occur by weathering and/or soiling of the cover glass; photothermal, oxidative, or other degradation of the pottant (more below); interdiffusion of ions into the pottant;

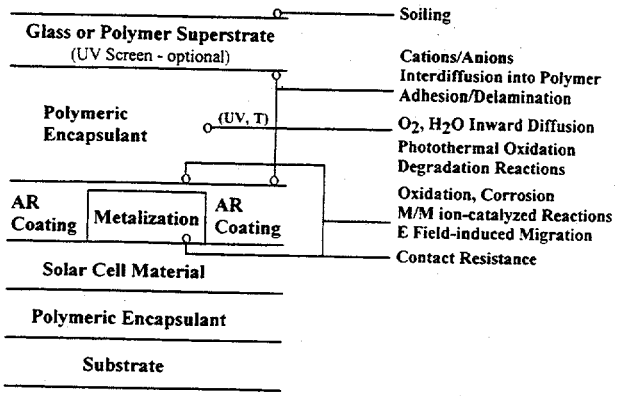

Fig. 1. Cross-section of a typical encapsulated Si PV cell and potential or actual causes of loss in performance.

metalization corrosion; electric-field-induced ion migration or degradation and polymer/metal-oxide surface reactions or delaminations. Many of these processes may depend on initial impurity concentrations and trapped gases (vapors), concentration changes during use, and the introduction of reaction products during use [1]. **Module durability of 30 years is obviously much more complex than a pottant stability issue.** We emphasize the complexity of the entire module because most of this article is concerned with the yellowing or discoloration of EVA. Thus, for the desired service lifetime to be reached, we must not only use a suitable polymer, but we also must establish that other degradative reactions are too slow to impact the performance adversely over 30 years. After the requisite stability of the "bulk" materials is achieved, interface reactions are known to be thermodynamically driven because of the higher free-energy state of atoms at interfaces [4]. A further need may then be to choose the different materials carefully to permit achieving a 30-year "stability" or to modify the interfaces for attaining the same goal.

PERFORMANCE LOSSES OF PV SYSTEMS

The effects of the discoloring EVA reactions on its properties, color changes in field-deployed modules, simulated degradation in the laboratory, and characterization methods have been summarized previously [5,6]. The known degradation mechanisms (e.g., photothermal, thermochemical, and Cyasorb photodecomposition) were also summarized along with those not studied [1,5]. In our initial evaluation of observed degradation in deployed PV systems, we reported that EVA discoloration had only been reported for modules in hot-and-dry or hot-and-humid climates (i.e., site locations and maximum operating temperatures are important) [5]. The discoloration ranged from light yellow (least) to dark brown (greatest), in which the greatest percentage performance losses are qualitatively correlated with the greatest discoloration (dark brown). A recent survey and site visits confirmed our qualitative observations [7], but detailed analysis shows the variances are large, i.e., the same class of modules with the same visual discoloration can have widely varying power outputs [1]. The qualitative and quantitative performance losses in large-scale PV systems have been summarized [1,8].

EVA STABILITY AS AN ENCAPSULANT

From a technological perspective, knowing the **rate** of degradative reactions is crucial to predicting the service lifetime of a device. The reactivity of some polymeric materials in an environment of solar irradiation, thermal and humidity cycles, and mechanical stresses are clear limitations. For considering the established degradation mechanisms of EVA, which is a random copolymer of ethylene and vinyl acetate, the copolymer is 33% (by weight) vinyl acetate and has an average molecular composition of $—(CH_2—CH_2)_{6.14}—(CH_2\text{-}CHAc)—$ in which Ac is the acetate pendant group, $—OCOCH_3$. The major sequences of the photothermal degradation of EVA have been summarized [1] and are a composite of several published reports on the thermal and photothermal stability of polyvinyl acetate and EVA [1]. The principal reactions are Norrish Type II to produce acetic acid and polyenes (the discoloring chromophore) or Norrish Type I to produce acetaldehyde followed by other gases, e.g., CO, CO_2, CH_4. Pern and Czanderna [5,6] investigated the general degradation mechanisms of stabilized, cured EVA through a series of simulated degradation experiments. Their results indicate that the EVA discoloration results primarily from the formation of polyconjugated C=C bonds (polyenes) by multistep deacetylations and α,β-unsaturated carbonyl groups [6]. Furthermore, acetic acid that is produced by thermal and photothermal decomposition exhibits an autocatalytic effect on the EVA yellowing [5]. Detailed absorption spectra [6] illustrate the effects of structural changes of the absorbing (and fluorescent) chromophores in EVA on various thermal and photothermal treatments. During the EVA discoloration, a competing photobleaching reaction also plays an important role in the presence of air (O_2) [1]. Degradation mechanisms are induced from photo-, thermal-, photothermal, HAc-catalyzed, and metal and metal-ion catalyzed effects. We reviewed all of these in detail [1], as well as aspects of photobleaching of discolored EVA and photothermal degradation of additives in EVA, especially Cyasorb UV 531™ and Lupersol 101.™

ACCELERATED LIFETIME TESTING AND SERVICE LIFETIME ESTIMATES

No studies have been carried out to date that can be used to predict a service lifetime of the EVAs or any other potential replacement as an encapsulant in a PV module. During our literature reviews [1,8] and through our interactions with the PV industry since 1990, we have encountered **serious** oversimplifications and misconceptions about correctly interpreting the meaning of accelerated lifetime testing and predicting the service lifetime for PV cells, modules, arrays, and systems. The most discouraging assumption is that "reaction rates double for each 10°C increase in temperature." This "rule of thumb" is based on **generalizations** about **all** chemical reactions collectively and does not consider the **specifics** of applying $k=A \exp(-E_A/RT)$, the Arrhenius equation, to the **dominating** degradative reaction. In applying this equation, it is essential to know, at least, that (a) the value of E_A is for **the dominant** reaction, (b) the mechanism involved in the dominant reaction does not change with temperature, and (c) E_A is independent of temperature over the range of any extrapolation. It is also implicit that the reactions occurring under accelerated conditions are the same as the reactions under the reality of normal operating conditions; e.g., the reactions of a free-standing polymer exposed in air cannot simulate those of a polymer in an encapsulated PV device (Fig.1).

Specific examples of projected lifetimes have been reviewed [8] for the variables actually used in the prior studies, and the lifetime projections are typically in error because variables have been selected incompletely in the test matrix, reality has not been properly simulated, or the Arrhenius relationship has been improperly applied. None of the investigators we cite [8] could claim (a), (b), **and** (c) for their projections. The examples ranged from using a highly accelerating thermal oxidative environment in the absence of UV to incorrect statements about the concentration of degradation products.

The greatest error made by those using the "rule of thumb" is in prescribing a value for E_A for **an unknown reaction mechanism.** For example, the plot in Fig. 2 shows the rate of reaction k for a series of activation energies in which k has been arbitrarily assigned a value

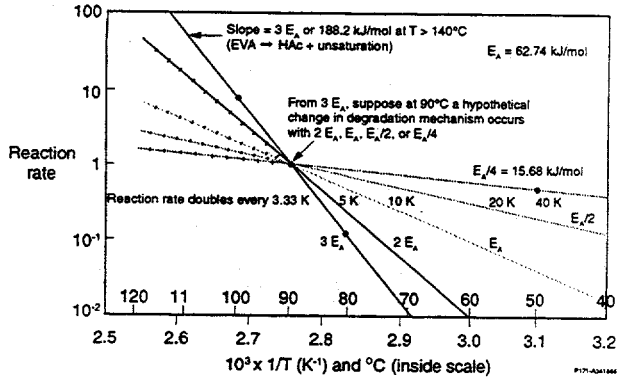

Fig. 2. Influence of hypothetical change(s) in degradation mechanism to several lower values of E_A at a reaction rate k = 1 (arbitrary units) at 90°C. Note the ΔT to double changes from 3.33 K at 3 E_A to 40 K at $E_A/4$.

of 1 at 363 K (90°C). The slope for $3E_A$ (188 kJ/mol) corresponds closely to the measured rate of (only) thermally induced deacetylation for EVA (E_A = 186 kJ/mol). The slopes branching from k = 1 at 363 K (90°C) are at an arbitrarily chosen temperature and reaction rate for discussion only. They show how the value of k (relative to extrapolating k values from $3E_A$) is dramatically increased for $2E_A$, E_A, $E_A/2$, and $E_A/4$, in which the ΔTs to double the rate are 5, 10, 20, and 40 K, respectively, compared with a ΔT of only 3.33 K for $3E_A$. The lowering of E_A might result from any one or a combination of the 10 catalytic factors cited in the section on thermally induced degradation in our review [1], but again it shows that serious errors from accelerated testing will be made unless rate projections are based on **known values for E_A rather than on assumed values.** Finally, other errors result from the "rule of thumb" because E_A must have a precise value at a particular temperature to yield the doubling factor; so those using the generalization are assigning a value to E_A without determining it experimentally [1,8]. Finally, reaction rates may also depend on synergistic influences; in the case of polymers, photothermal degradation is typically 5 to 10 times that for thermal degradation alone. This is the **most** serious error made in the work in the 1980s. Their accelerated test conditions did not simulate the reality of UV, T, RH, confinement of EVA in a multilayer stack in which the degradation products are restricted from outward diffusion, and where the device is actually operating to produce a current.

The complexity of making a service lifetime prediction is easily illustrated from two known and competing reactions, i.e., the formation of polyenes (that result in chromophores) that cause the discoloration and photobleaching reactions that will eventually eliminate the discoloration. The criteria necessary for making successful service lifetime predictions from accelerated testing include that (a) the accelerated test must not alter the degradation mechanism(s); (b) the mechanisms and activation energies of the dominant reaction(s) at normal operating conditions and accelerated test conditions must be the same; (c) both the specimens (including materials and components only) and accelerating parameters (UV, T, RH, product entrapment, etc.) must simulate reality; (d) full-sized cells and/or modules must be used in both the accelerated and real-time tests; (e) the time-dependent performance loss (e.g., power loss for PV modules) must be correlated with the degradative reactions; and (f) a sufficient number of samples must be used so the distribution of degraded devices can be accurately modeled. Obviously, predicting a service lifetime requires a definition of "failure," i.e., what loss in efficiency is acceptable after how many years; failure has not been defined for PV modules, even though power losses of 1% to 2.5% per year are typically being observed and reached 10% per year at Carrisa Plains.

PV CELL EFFICIENCY LOSSES

Only two crucial matters are ultimately of concern when considering the EVA discoloration phenomenon, i.e., do the degradative reactions limit the lifetime of the PV module, and does the discoloration cause direct efficiency losses. Incredibly, measurements of the latter for individual cells and/or modules have received almost no attention. Performance (efficiency) measurements on individual modules have only been reported on individual modules on a post-mortem basis for Carrisa Plains modules and on 189 modules in Israel that were retrofitted for I-V measurements after 5 years [1].

For individual cells, we reported on one post-mortem attempt on a retrofitted cell from Carrisa Plains [5]. Pern has carried out one detailed study on single-cell minimodules as a precursor to future studies in which we plan to correlate performance changes with encapsulant and other degradation in the cells [9]. Although degradation processes in cells are complex (Fig. 1), a number of complications from individual modules are eliminated, e.g., interconnect degradation, cell/module mismatch, and differences in degradation in each cell that are averaged for the entire module.

In his study comparing the effects of thermal, photothermal, **accelerated,** and simulated, degradation on the EVA-encapsulated solar cells, Pern [9] showed that the losses in short-circuited current (I_{sc}) and efficiency because of net reduction in light transmission by EVA browning are more than 13% and 19%, respectively. Figures 3a and 3b give an example showing the continuously decreasing spectral response (absolute quantum efficiency) as the EVA film discolored increasingly to a light yellow color in the solar cell heated in an 85°C oven for 198 days (Fig. 3a) or to a brown color when exposed to an RS4 UV light source at 85°C for 198 days. All solar cells showed little change in open-circuit voltage (V_{oc}) or fill factor (an important quantitative relationship for describing the performance of PV cells and modules), except for the noticeable decreases in I_{sc} caused by EVA discoloration. Electrically, except for one solar cell, no significant change in the series resistance was measured (by dark I-V) for the solar cells studied over the 198-day period [9].

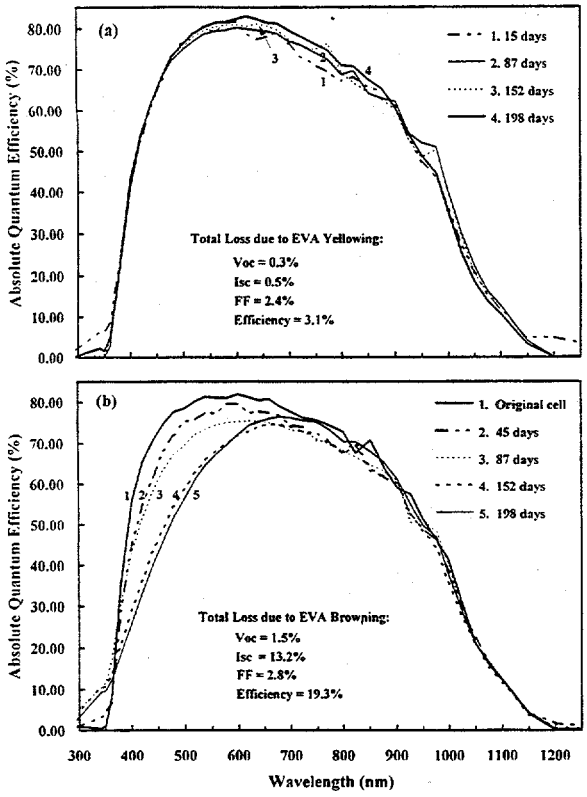

Fig. 3. Wavelength dependence of the absolute quantum efficiency of 2" x 4" polycrystalline-Si cells encapsulated in glass/EVA/Si/EVA/back foil and exposed for 198 days to (a) an oven at 85°C±2°C or (b) RS4 UV and 85°C±2°C.

TEST PROTOCOL FOR FUTURE WORK

Our protocol for future work will be based on preparing minimodules as active devices consisting of the multilayer stack: glass or polymer superstrate with or without a UV screen/pottant polymer/active PV device with an antireflective coating and base contact/polymer/substrate.

The active devices will be of the same construction as those in contemporary modules and be a minimum of 5 cm x 5 cm (2" x 2") and a maximum of 12.5 cm x 12.5 cm (5" x 5"), with output leads suitable for obtaining I-V and efficiency measurements. Identical test specimens will be subjected to accelerated testing in controlled T and RH chambers and (a) a xenon light source of 1, 2, or 3 suns, (b) a condensed xenon light source (solar simulator) of 3 to 12 suns from 290 nm to 400 nm in which the test variables simulate reality. We also would like to be able to subject specimens to UV accelerated testing in an outdoor environment in which the minimodule T will be maintained at normal operating temperatures, but natural sunlight will be concentrated from 5 to 10 times. Finally, we would also like to deploy minimodules to at least six sites in the United States with representative and carefully recorded natural environmental exposure conditions. Specimens at these "real-time testing" sites would be periodically monitored for their efficiency. Degradation mechanisms will be deduced from specimen "failures" from accelerated lifetime testing (ALT) and real-time testing (RTT). When they are the same, models will be developed to relate the complexity or simplicity of the multiplying factor from ALT to those for RTT, and the service lifetime will be estimated based on the interpretation of all the data acquired.

REFERENCES

[1] A. W. Czanderna and F. J. Pern, "Encapsulation of PV Modules Using Ethylene Vinyl Acetate Copolymer as a Pottant: A Critical Review," *Solar Energy Materials and Solar Cells*, **43**, 1996, In Press.

[2] A. W. Czanderna, in L. Mrig, Ed., *Photovoltaic Performance and Reliability Workshop,* "Possible Causes of EVA Degradation in PV Modules," SERI/CP-4079, October 1990, pp. 159-215 and "EVA Degradation Mechanisms: Review of What is and is Not Known," NREL/CP-410-6033, September 8-10, 1993, pp. 311-357, National Renewable Energy Laboratory, Golden, CO.

[3] E. Cuddihy, C.Coulbert, A. Gupta, and R. Liang, *Flat-Plate Solar Array Project, Final Report, Volume VII: Module Encapsulation,* JPL Publication 86-31, Oct. 1986, Jet Propulsion Laboratory, Pasadena, CA.

[4] A. W. Czanderna, "Surface and Interface Studies and the Stability of Solid Energy Materials," *Solar Materials Science*, L.E. Murr, Ed., Academic, New York, 1980, pp. 93-143.

[5] F. J. Pern and A. W. Czanderna, *Solar Energy Materials and Solar Cells*, **25**,1992, p. 3; F. J. Pern and A. W. Czanderna, in R. Noufi, Ed., *AIP Conference Proceedings*, **268**, PVARD Project, Am. Inst. Physics, NY, 1992, pp. 445-451.

[6] F. J. Pern, "Luminescence and Absorption Characterization of the Structural Effects of Thermal Processing and Weathering Degradation on Ethylene Vinyl Acetate (EVA) Encapsulant for PV Modules," *Polymer Degradation and Stability*, **41**, 1993, pp. 125-139.

[7] W. H. Holley, *"Advanced Development of PV Encapsulants,"* NREL/TP-411-5800, Dec. 1993, National Renewable Energy Laboratory, Golden, CO.

[8] A. W. Czanderna and F. J. Pern, "Estimating Lifetimes of a Polymer Encapsulant for Photovoltaic Modules from Accelerated Testing," *Durability Testing of Non-Metallic Materials,* **ASTM STP 1294,** Robert J. Herling, Ed., American Society for Testing and Materials, Philadelphia, PA, 1996, In Press.

[9] F. J. Pern, in L. Mrig, Ed., "A Comparative Study of Solar Cell Performance Under Thermal and Photothermal Tests," *Proc. PV Performance and Reliability Workshop*, NREL/CP-411-5148, Sept. 1992, pp. 327-344, National Renewable Energy Laboratory, Golden, CO.

ACKNOWLEDGMENTS

The authors are pleased to acknowledge support by the U.S. Department of Energy under contract No. DE-AC36-83CH10093 and our project manager, R. DeBlasio, for his suport of our task entitled "Reliability Science of Encapsulated PV Cells."

DOE/OER-SPONSORED BASIC RESEARCH IN HIGH-EFFICIENCY PHOTOVOLTAICS

S. K. Deb and J. P. Benner
National Renewable Energy Laboratory
1617 Cole Boulevard, Golden, CO 80401-3393

ABSTRACT

A high-efficiency photovoltaic project involving many of the national laboratories and several universities has been initiated under the umbrella of the U.S. Department of Energy (DOE) Center of Excellence for the Synthesis and Processing of Advanced Materials. The objectives of this project are to generate advances in fundamental scientific understanding that will impact the efficiency, cost, and reliability of thin-film photovoltaic cells. The project is focused on two areas: (1) Silicon-Based Thin Films, in which key scientific and technological problems involving amorphous and polycrystalline silicon thin films will be addressed, and (2) Next-Generation Thin-Film Photovoltaics, which will be concerned with the possibilities of new advances and breakthroughs in the materials and physics of photovoltaics using non-silicon-based materials.

INTRODUCTION

Continued advances in the technology of solar photovoltaic (PV) energy conversion are critically dependent on the fundamental understanding of the synthesis and properties of the materials that compose solar cells. Reduced cost, improved conversion efficiency, and long-term reliability are the major objectives of the DOE PV Five-Year Program Plan [1]. Thin-film semiconductor materials and device technologies are key to achieving these objectives. Currently, there are several important classes of thin-film PV materials at various stages of research and development; but, in all cases, there is a lack of understanding of the fundamental scientific issues associated with each of these technologies. Therefore, this program is motivated by the scientific exploration of new solid-state physics as it relates to photon absorption and carrier transport, novel materials synthesis techniques, the characterization and control of defect structures, and, ultimately, designs of new material architectures.

The project is sponsored by the Division of Materials Science (DMS) of the DOE Office of Energy Research (OER) and Office of Basic Energy Sciences (BES) in fiscal year 1996 through its Center of Excellence for Synthesis and Processing of Advanced Materials (CSP).

CSP—A NEW KIND OF PARTNERSHIP

Recognizing the importance of materials synthesis and processing (S&P) and responding to a national need to strengthen this area of materials science and engineering, the Division of Materials Sciences (DMS) of DOE's Office of Basic Energy Sciences in the Office of Energy Research established the *DOE Center of Excellence for the Synthesis and Processing of Advanced Materials (CSP).* The Center, which is a distributed center concept, is a coordinated, cooperative partnership among twelve DOE laboratories and includes appropriate university grant research funded by DMS, as well as collaborations with both small and large companies. Its overall objective is:

"To enhance the science and engineering of materials synthesis and processing in order to meet the programmatic needs of the Department of Energy and to facilitate the technological exploitation of materials."

Synthesis and processing are those essential elements of materials science and engineering (MS&E) that deal with (1) the assembly of atoms or molecules to form materials, (2) the manipulation and control of structure at all levels from the atomic to the macroscopic scale, and (3) the development of processes to produce materials for specific applications. Clearly, S&P represents a large area of MS&E that spans the range from fundamental research to technology. The goal of basic research in this area (which is the primary focus of the Center) ranges from the creation of new materials and the improvement of the properties of known materials, to the understanding of such phenomena as diffusion, crystal growth, sintering, and phase transitions in relation to S&P. On the applied side, the goal of S&P is to translate scientific results into useful materials by developing processes capable of producing high-quality, cost-effective products in an environmentally conscious manner.

The Center's emphasis is on elucidating and applying fundamental S&P principles directed toward the rapid improvement or development and ultimate use of advanced materials. By bringing together synergistic activities and capabilities at the participating institutions in selected focus areas, the Center's goal is to provide added value and impact beyond what can be achieved by the participants working separately. A technology Steering Group—with members from industry and DOE technology program offices—provides the Center with an energy technology and industrial perspective.

The current emphasis of the Center is on seven focused multilaboratory projects that draw on the complementary strengths of the participants in their ongoing research programs. These projects include: (1) Metals

Forming, (2) Materials Joining, (3) Tailored Microstructures in Hard Magnets, (4) Microstructural Engineering with Polymers, (5) Processing for Surface Hardness, (6) Mechanically Reliable Surface Oxides for High-Temperature Corrosion Resistance, and (7) High-Efficiency Photovoltaics. These projects, which represent a relatively small fraction of DMS' programs, were selected from among many potential choices on the basis of the following criteria:

- Scientific excellence
- Clear relationship to energy technologies
- Involvement of several laboratories
- Strong existing or potential partnerships with programs funded by DOE Technologies Offices.

The projects address the scientific underpinnings of critical technological issues with a near- to intermediate-term perspective. Each project is coordinated by an appropriate representative from one of the participating laboratories.

The overall coordination of the Center's projects is done by Dr. George A. Samara of Sandia National Laboratories in Albuquerque, NM.

HIGH-EFFICIENCY PHOTOVOLTAICS PROJECT AT CSP

The high-efficiency photovoltaics project, which is the latest addition to the Center projects, was structured as a result of two planning workshops held in San Jose, CA, and Golden, CO, in fiscal year 1995.

Objectives

The objectives of this project are to generate advances in scientific understanding that will impact the efficiency, cost and reliability of their film photovoltaic cells by addressing the short- and long-term basic research issues. The overall approach of the project is to effectively couple existing programs in photovoltaics technology to relevant scientific research efforts in the DOE Basic Energy Science mission.

Project Scope

Initially, the project includes 20 collaborative research projects involving the national laboratories and a number of universities currently funded by OER/BES/DMS, the DOE Office of Energy Efficiency and Renewable Energy (EERE), and the Electric Power Research Institute (EPRI). The project focuses on two areas: (1) Silicon-Based Thin Films, which will address key scientific and technological problems involving amorphous and polycrystalline silicon thin films, and (2) the Next-Generation Thin-Film Photovoltaics, which will be concerned with the possibilities of new advances and breakthroughs in the materials and physics of PV using non-silicon-based materials. It is intended to complement the more extensive applied PV research program funded by EERE. A strong participation in the project by the National Renewable Energy Laboratory (NREL) serves as the natural point of contact between OER/BES and EERE photovoltaic research efforts and the PV industry.

Silicon-Based Thin Films

The major emphasis in this area will involve amorphous and polycrystalline silicon thin-film materials and devices. The key scientific and technological problem that hydrogenated amorphous-silicon materials have faced during the last 20 years is a light-induced metastability (the Staebler-Wronski effect) that leads to a degradation in cell efficiency during operation. This problem can be traced directly to a lack of detailed understanding of the physical and electronic structure and homogeneity of hydrogenated amorphous silicon and how that structure evolves under solar irradiation. New characterization techniques are needed to study atomic coordination, hydrogen content, and microvoid structure. Also, new synthesis techniques based on hot-filament-assisted growth of hydrogenated amorphous silicon appear to be promising alternatives to glow-discharge deposition for growing materials with a high degree of stability; but the reasons for this improved stability are not known at present.

Polycrystalline-silicon thin films have strong potential as future PV materials because of the low cost and wide availability of silicon. Importantly, *thin films* of polycrystalline silicon have very different synthesis, microstructure, and defect characterization issues than do thick films or polycrystalline substrates. Indeed, new solar-cell device designs that have been developed in the last 3 years are motivating fundamentally different approaches to synthesis and processing of polycrystalline silicon on low-cost substrates. These new cell designs, which use much thinner active absorber regions, also motivate fundamentally different optical design and defect characterization problems, as the ratio of physical thickness to absorption length is much smaller than for conventional silicon PV cells. The individual project title and the participating organizations are given in Table 1.

Next-Generation Thin-Film Photovoltaics

The projects in this area concern the possibilities of new advances and breakthroughs in the materials and physics development of PV using non-silicon-based materials. The tasks in this area are broken into several categories, starting with novel PV device and physics concepts, and new materials systems, with the concurrent requirement of substrates. After defining the new concepts, the second theme is thus concerned with synthesis, materials growth, and material properties issues that may arise from the first phase. An integral part of the research program for *Next-Generation Thin-Film Photovoltaics* are interface, defects, and impurity issues, which constitute the third part of this program. Finally, advanced characterization techniques will be required to substantiate the material and physics concepts being proposed for *Next-Generation Thin-Film Photovoltaics*. The specific projects in this area are identified in Table 2.

Project Implementation

Because no new funding was available, the individual

projects identified in Table 1 and 2 will be implemented by restructuring closely related projects that currently are funded mainly by DOE/OER/BES DMS and the PV division of DOE/EERE and, to a limited extent, by other sources of funding like EPRI. The Division of Materials Sciences of OER/BES provides some "glue funding" that is used to encourage collaboration through the exchange visits and workshops. A teaming structure is being developed to ensure closer interaction between closely related projects and to organize team meetings and workshops at some regular intervals.

ACKNOWLEDGEMENTS

The authors acknowledge the strong support of this project from Drs. Bob Gottschall, Jerry Smith, and Iran Thomas of the DOE Division of Materials Sciences of OER/BES, Mr. James Rannels and Dr. Jeff Mazer of DOE/EERE and Dr. George Samara of Sandia National Laboratories.

REFERENCES

[1] U.S. Department of Energy, "The National Photovoltaics Program Plan for 1996-2000," DOE/GO-10096-017 (January 1996).

Table 1. Silicon-Based Thin Films
Project Coordinators: Harry Atwater (Cal Tech) and Bhushan Sopori (NREL)

Project Title	Participating Labs
1. Defect relaxation and metastable defect formation in a-Si:H	NREL & Ames
2. Hydrogen diffusion in a-Si:H and related alloys	Iowa State Univ., Ames, NREL, & CSM
3. Measurement of void structure in a-Si:H with positron annihilation	BNL & NREL
4. Atomic-scale understanding and control of H-incorporation in thin-film PV materials	Univ. Illinois, Ames, & NREL
5. Grain-boundary effects in polysilicon PV devices	U. of Calif. (Santa Barbara), Ames, NREL, & Iowa State Univ.
6. Low-temperature epitaxial approaches to large-grained polycrystalline silicon	Cal. Tech. & ORNL
7. Control of microstructure evolution in polycrystalline-silicon thin film	Cal. Tech. & LLNL
8. Structure and properties of amorphous and polycrystalline-Si films by molecular dynamic simulation	ANL
9. Defect characterization in Si-based PV semiconductors	LBL
10. Silicon-based thin-film point defects and impurities	MIT

Ames = Ames Laboratory (Iowa State Univ.), ANL = Argonne National Laboratory, BNL = Brookhaven National Laboratory, LBL = Lawrence Berkeley Laboratory, LLNL = Lawrence Livermore National Laboratory, ORNL = Oak Ridge National Laboratory, NREL = National Renewable Energy Laboratory, CSM = Colorado School of Mines, Cal. Tech. = California Institute of Technology), MIT = (Massachusetts Institute of Technology).

Table 2. Next-Generation of Thin-Film Photovoltaics
Coordinators: Eric Jones (SNL) and Richard Ahrenkiel (NREL)

Project Title	Participating Labs
1. Hot-carrier solar cells	NREL, SNL, & LBL
2. Chalcopyrite semiconductors for PV	NREL
3. Theory of crystal-lattice defects and electrical properties of transparent conducting oxides	BNL & NREL
4. Optimal I-II-VI materials for solar-energy conversion	ONRL & NREL
5. Microstructure of defects in PV materials	BNL, NREL, LBL, & Univ. of Ill.
6. Identification of ordered/disordered phases of I-III-VI chalcopyrites	SNL & Univ. of Florida
7. Synthesis and use of low-toxicity precursors for growth of II-VI and III-VI compounds by MOCVD	LBL
8. Study of CIS surface layer and CDS/CIS interface	PNL & Wash. St. Univ.

* Projects 9 and 10 at the University of Utah and SUNY Buffalo currently under design.
SNL = Sandia National Laboratories, PNL = Pacific Northwest Laboratory.

TEMPERATURE DEPENDENCE OF PHOTOVOLTAIC CELLS, MODULES, AND SYSTEMS

K. Emery, J. Burdick, Y. Caiyem, D. Dunlavy, H. Field, B. Kroposki, T. Moriarty,
L. Ottoson, S. Rummel, T. Strand, and M.W. Wanlass
National Renewable Energy Laboratory
1617 Cole Blvd., Golden, CO, 80401-3393 USA

ABSTRACT

Photovoltaic (PV) cells and modules are often rated in terms of a set of standard reporting conditions defined by a temperature, spectral irradiance, and total irradiance. Because PV devices operates over a wide range of temperatures and irradiances, the temperature and irradiance related behavior must be known. This paper surveys the temperature dependence of crystalline and thin-film, state-of-the-art, research-size cells, modules, and systems measured by a variety of methods. The various error sources and measurement methods that contribute to cause differences in the temperature coefficient for a given cell or module measured with various methods are discussed.

INTRODUCTION

This paper investigates temperature-dependent current *versus* voltage (I-V) measurements performed on several continuous light sources and the SPIRE 240A pulsed solar simulator. Simulator-based temperature coefficients (*TC*) are also compared with temperature coefficients for a wide variety of PV technologies derived from regression analysis of data taken under natural sunlight at the module and system level.

The temperature coefficient *TC* for a given parameter *Z* can be written as:

$$TC(part/°C) = \frac{1}{Z}\frac{\delta Z}{\delta T}\bigg|_{T_n=25°C}, \quad (1)$$

where the normalization temperature T_n was chosen to be 25°C because it corresponds to the standard reference temperature for terrestrial and most space PV. It is important for comparison purposes that the normalization temperature be standardized or at least explicitly stated. Once *TC* is measured for a parameter *Z*, it can be translated from a given temperature *T* to another temperature *T'* using:

$$Z' = Z + \frac{TC \cdot Z \cdot (T' - T)}{1 - TC \cdot (T_n - T)}. \quad (2)$$

For multijunction devices and any device where different current conduction mechanisms occur at different temperatures, *Z* is nonlinear. The value of *TC* can also change with the spectral content of the light source that *Z* is measured under because the quantum efficiency *TC* varies with wavelength. The value of *TC* also varies with irradiance because in Eq. 1 the value of *P* changes with irradiance. Equation 2 assumes that *Z* is a linear function of temperature. Commercial data-acquisition systems often require the temperature coefficient to be expressed in units of amps/°C and volts/°C at a given irradiance. Expressing the temperature coefficient in absolute units allows the entire current *versus* voltage (I-V) curve to be translated for temperature. Corrections for temperature using absolute temperature coefficients also require the number of cells in series and the number of parallel strings.

MEASUREMENT METHODS

The temperature coefficient can be measured under simulated or natural light. Determining system temperature dependence requires measurement under actual operating conditions. Typically, the irradiance level is restricted to minimize variations in the temperature dependence with total or spectral irradiance.

Temperature-dependent I-V measurements can be grouped into the categories of pulsed-light or continuous-light solar simulators. In pulsed light solar simulators, the light-induced temperature gradient across the PV sample is negligible except at very high concentrations. This results in a very low error in the temperature of the PV device. The uncertainty in temperature coefficient determined by pulsed-light measurements can be affected by bias-rate-related artifacts and noise in the measured data.

Continuous-light sources allow for a very low random error in the measured I-V characteristics when long-integration-time, high-accuracy voltmeters are used to simultaneously measure the voltage, current, and irradiance. Bias-rate-related errors that occur in many thin-film material systems, high-lifetime silicon, and any high-capacitance PV design can be minimized or eliminated with a data-acquisition system using a continuous-light source [1]. Under continuous illumination, a temperature gradient will exist between the PV junction and the measured front- or back-surface temperature. A procedure employed at the National Renewable Energy Laboratory and elsewhere is to place the sample at the desired temperature in the dark at open-circuit conditions after "light soaking," if any has been performed. The open-circuit voltage (V_{oc}) is then monitored as the shutter is opened. The highest V_{oc} observed is the V_{oc} at the desired temperature. The sample is then cooled, if possible, until this maximum V_{oc} is reached. The uncertainty associated with this method is limited by the shutter speed, voltage sampling rate, response time of the V_{oc} to the shutter being opened, and the amplitude stability of the light source.

A variety of methods have been employed to vary the temperature for simulator based temperature dependent measurements including:

- Control the cell temperature with a temperature-controlled vacuum plate. This method minimizes temperature gradients.
- Heat a module in an environmental chamber and then place the heated module in an insulated box and measure the sample's I-V characteristics as it slowly cools down. This method results in the back of the module being warmer than the front because heat is radiated off the front surface, while the back surface is insulated.
- Heat the cell or module in a temperature controlled chamber with a window. This method minimizes temperature variations.
- Heat the module with a blanket from below and measure the I-V characteristics after the temperature has reached equilibrium. This procedure also has a typical temperature gradient between the back and front surface of 2°C.
- Adjust the room temperature to obtain the I-V characteristics at different temperatures. This method has a minimal temperature gradient and temperature range. The *TC* of the equipment may add to the error.

Ideally the temperature, spatial uniformity, and contacting should not be changed as the I-V characteristics are measured at different temperatures. This is because differences in spatial uniformity, irradiance level, or contacting can exceed the variation with temperature. Hysteresis in the I-V characteristics as a function of temperature can also occur because of different temperature gradients between the sample and sensor in the heating and cooling modes, sample degradation, or transient behavior. Hysteresis loops are especially evident in CdS/CdTe cells and modules because of light-soaking effects [1].

Careful placement of the temperature sensor on the back surface or front surface is essential to minimize errors introduced because the measured temperature is different than the junction temperature.

EXPERIMENTAL RESULTS

The measured temperature coefficients for a variety of cell and module PV technologies under "1-sun" illumination are summarized in Fig. 1. Table 1 illustrates the range of temperature coefficients for silicon cells and modules that have been measured.

Fig. 3 illustrates how the temperature coefficient changes with irradiance for a multicrystalline silicon module. The temperature coefficient for the CdS/$CuInSe_2$ module shown in Fig.2 was representative of the modules in the Siemens Solar array deployed at the NREL Outdoor Test Facility. This module was also measured outdoors over the restricted irradiance range of 950–1050 W/m^2, giving a normalized maximum-power temperature coefficient of -6720 ppm/°C [8]. The maximum-power temperature coefficient for the CIS system, determined by measuring the array performance with a portable I-V tracer over the restricted irradiance range of 900–1100 W/m^2 is -7690 ppm/°C with a correlation coefficient of 0.87.

For many outdoor temperature coefficient measurements, the random error in the maximum power (P_{max}) and efficiency is correlated with the random error in I_{sc}. By looking at the P_{max} or efficiency temperature coefficient as P_{max}/I_{sc} instead of P_{max}/E_{tot}, the random error can be substantially reduced. This method assumes that I_{sc} is linear with irradiance over the irradiance range being corrected and that I_{sc} is corrected for temperature. An additional negligible source of error in this normalization procedure for P_{max} is the assumption that the *TC* of I_{sc} is constant over the irradiance range being corrected for. For the portable I-V tracer data above the P_{max} *TC* was -7410 ppm/°C with a correlation coefficient of 0.94.

The temperature coefficient *versus* current density (Fig.4) is most appropriate for characterizing thermophotovoltaic devices because the spectral and total irradiance of the thermal emitter is application specific and not standardized. The temperature coefficients were measured with a continuous light source and the V_{oc} method to obtain the I-V at a known temperature.

The nonlinear temperature dependence of a multijunction a-Si/a-Si:Ge module is illustrated in Figure 5. The nonlinear behavior occurs because the voltage temperature coefficient for each junction is different. The temperature dependence will vary greatly, depending on the spectrum of the light source that the temperature dependence was measured under [9, 10].

The hysteresis in Fig. 6 is not temperature-related because there was no measurable hysteresis in *Voc versus* temperature. This module is typical of the modules in the CdTe system described elsewhere [11]. The P_{max} *TC* for the system was 1100 ppm/°C for the positive subarray and 1600 ppm/°C for the negative subarray [10]. One of the modules of the same type as the system was evaluated outdoors and a P_{max} *TC* of -800 ppm/°C was obtained. This P_{max} *TC* for this module measured under a pulsed solar simulator was -3600 ppm/°C.

The measured I_{sc} temperature coefficient varies, depending on the light source, because the quantum efficiency does not vary with temperature in a multiplicative manner (Figs. 7,8). This changing quantum efficiency with temperature gives rise to a changing spectral mismatch error with temperature, the magnitude of which depends on how well the light source and reference spectrum are matched. An unexpectedly large variation (>50%) in the I_{sc} temperature coefficients for the same samples with temperature sensors attached circulated between various laboratories have been observed [11,12]. Table 2 shows temperature coefficients measured for a monocrystalline Si reference cell with an attached temperature sensor under the spectra shown in Fig. 9.

SUMMARY

The temperature coefficients for a variety of PV technologies have been presented. The various strategies and precautions for measuring the temperature coefficients under simulated and natural sunlight have been presented. The temperature coefficient varies within given technologies with irradiance level and spectrum.

ACKNOWLEDGMENTS

The authors wish to thank everyone who allowed us to evaluate their samples. This work is performed under contract No. DE-AC36-83CH10093 to the U.S. Department of Energy.

REFERENCES

[1] K. Emery and H. Field, "Artificial Enhancements and Reductions in the PV Efficiency," *24th IEEE PVSC*, 1994, pp. 1833-1838.

[2] K. Emery, J. Caiyem, D. Dunlavy, H. Field, S. Rummel, and L. Ottoson, "Temperature and Irradiance Behavior of Photovoltaic Devices," Photovoltaics Performance and Reliability Workshop, September 1995, NREL tech. rep. TP-411-20379.

[3] B.E. Anspaugh, T.A. Casad, D.M. Beckert, R.G. Downing, T.F. Miyahira, and R.S. Weiss (Eds.):Characterization of Solar Cell for Space Applications," *Jet Propulsion Laboratory Publication* 78-15, 1978.

[4] M.A. Green, K. Emery, and A.W. Blakers, "Silicon Solar cells With Reduced Temperature Sensitivity," *Electronics Letters*, **18**, 1982, pp. 97-98.

[5] S. Yoon and V. Garboushian, "Reduced Temperature Dependence of High-Concentration Photovoltaic Solar Cell Open-Circuit Voltage (Voc) at High Concentration Levels," *24th IEEE PVSC*, 1994, pp. 1500-1504.

[6] S. Nann and K. Emery, "Spectral Effects on PV-Device Rating," *Solar Energy Materials and Solar Cells*, **27**, 1992, pp.189-216.

[7] C.R. Osterwald, T. Glatfelter, and J. Burdick, "Comparison of the Temperature Coefficients of the Basic I-V Parameters for Various Types of Solar Cells," *19th IEEE PVSC*, 1987, pp. 188-193.

[8] T. Strand, B. Kroposki, R. Hansen, and D. Willet, "Siemens Solar CIS Photovoltaic Module and System Performance at NREL," this conference.

[9] G.F. Virshup, B-C Chung, M.L. Ristow, M.S. Kuryla, and D. Brinker, "Temperature Coefficients of Multijunction Solar Cells," *21st IEEE PVSC*, 1990, pp. 336-338.

[10] D.J. Friedman, "Modeling of Tandem Cell Temperature Coefficients," this conference.

[11] B. Kroposki, T. Strand, R. Hansen, R. Powell, and R. Sasala, "Technical Evaluation of Solar Cells, Inc. CdTe Module and Array at NREL," this conference.

[12] J. Metzdorf, T. Wittchen, K. Heidler, K. Dehne, R. Shimokawa, F. Nagamine, H. Ossenbrink, L. Fornarini, C. Goodbody, M. Davies, K. Emery, and R. DeBlasio, "The Results of the PEP '87 Round-Robin Calibration of Reference Cells and Modules, Final Report," PTB Tech. Rep. PTB-Opt-31, Braunschweig, Germany, November 1990, ISBN 3-89429-067-6.

[13] K.A. Emery, D. Waddington, S. Rummel, D.R. Myers, T.L. Stoffel, and C.R. Osterwald, "SERI Results from the PEP 1987 Summit Round Robin and a Comparison of Photovoltaic Calibration Methods," SERI Tech. Rep. TR-213-3472, March 1989.

Table 1. Single-crystal and multicrystalline silicon temperature coefficients in units of ppm/°C [2-5].

Type	V_{oc}	I_{sc}	FF	P_{max}
Space Si cell [3]	-3490- -4510	380- 710	-1000- -1600	-4070- -1600
PESC Si cell [4]	-2690	650	-940	-3200
c-Si module	-2817	411	-1265	-3619
c-Si module	-3413	130	-1642	-5035
p-Si module	-2632	435	-1172	-3318
p-Si module	-3675	675	-1732	-4690
p-Si module	-2925	407	-1556	-3996
p-Si cell production	-4330- -679	738- 1230	-84- -2159	-3067- -5569
Thin film Si	-2429	493	-993	-2929
Si Conc.1/ 250 suns [5]	-2584/ 1724	488/ 168	-1079/ -680	-2916/ -2282

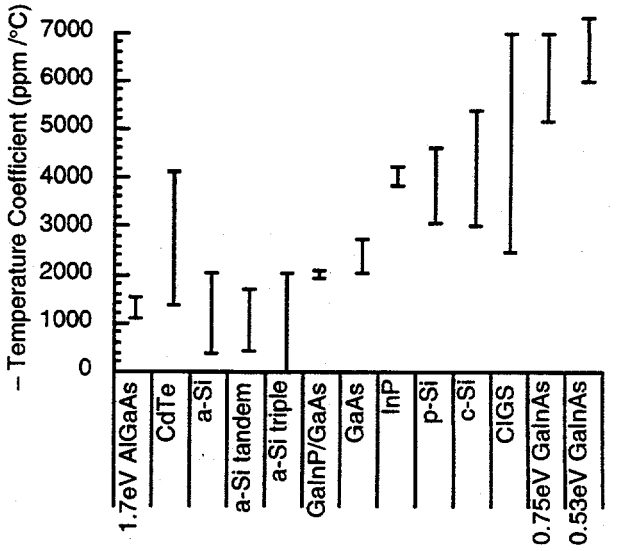

Figure 1. Range of P_{max} TC of cells and modules evaluated at NREL [2,6,7].

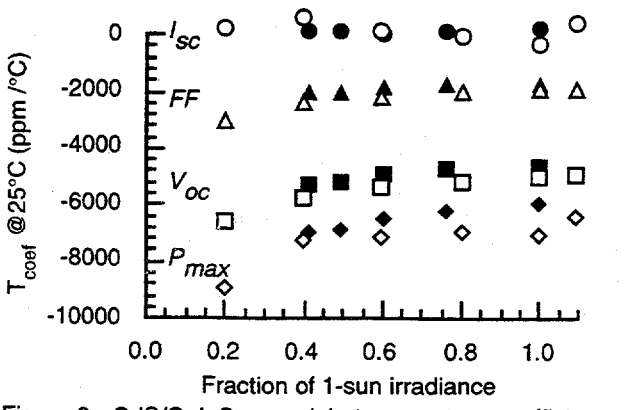

Figure 2. $CdS/CuInSe_2$ module temperature coefficient as a function of light level measured under the SPIRE 240A pulsed solar simulator (closed symbols) and Atlas Climatic SC1600 environmental chamber with metal halide lamps (open symbols).

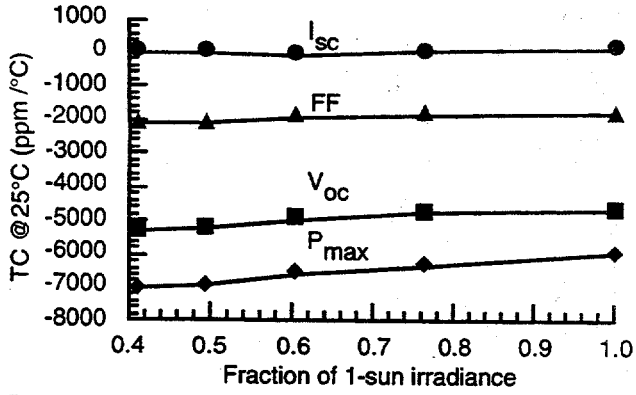

Figure 3. Multicrystalline Si module temperature coefficient as a function of light level.

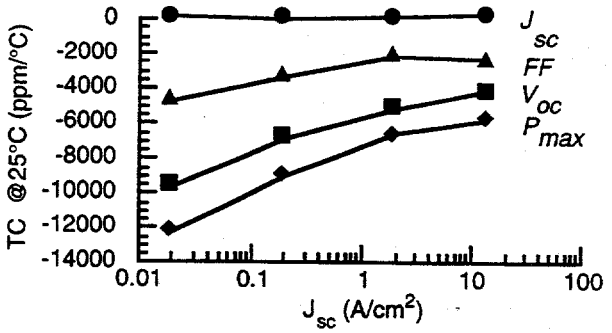

Figure 4. Variation in the temperature coefficient for a thermophotovoltaic cell with an energy gap of 0.626 eV.

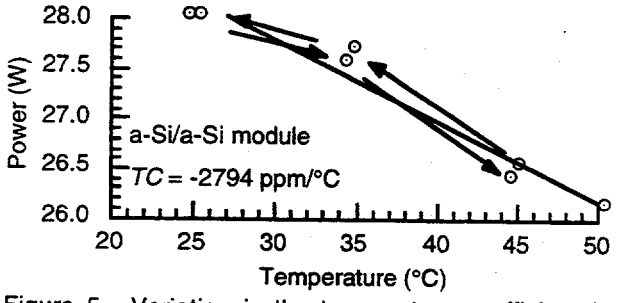

Figure 5. Variation in the temperature coefficient for a multijunction amorphous silicon module.

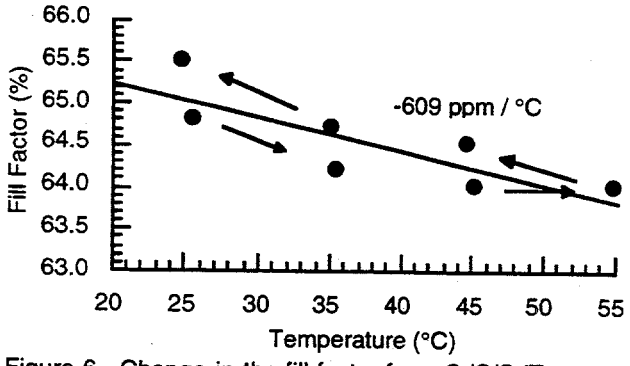

Figure 6. Change in the fill factor for a CdS/CdTe module showing significant hysteresis. This same module showed no significant hysteresis in V_{oc} or I_{sc}.

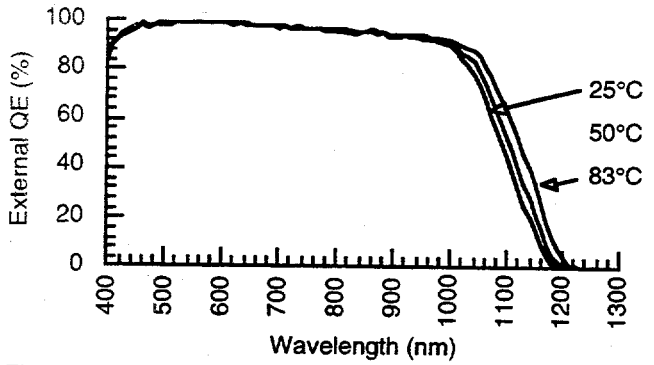

Figure 7. Variation in the absolute external quantum efficiency with temperature for a silicon cell showing the temperature dependence of the energy gap.

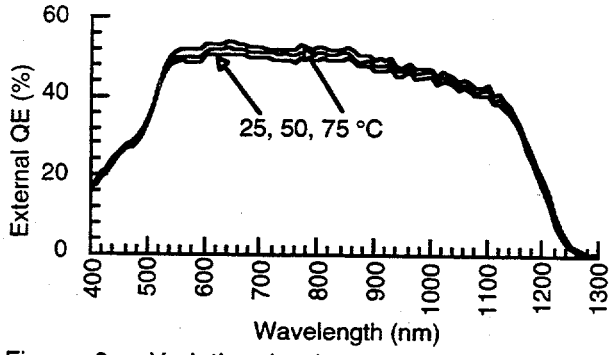

Figure 8. Variation in the quantum efficiency with temperature for a state-of-the-art CdS/Cu(Ga,In)(S,Se) cell showing minimal wavelength shift.

Table 2. The *TC* (ppm/°C) for a monocrystalline solar cell depends on the spectral nature of the light source used. The first three sources were set to generate the current equivalent to 1/7-sun illumination.

Source	I_{sc}	V_{oc}	FF
X25	736	-2968	-1106
EKE Lamp	990	-3018	-1138
X25 w/ 950 LWP	5608	-2467	-1172
X25 (1 sun)	829	-3335	-

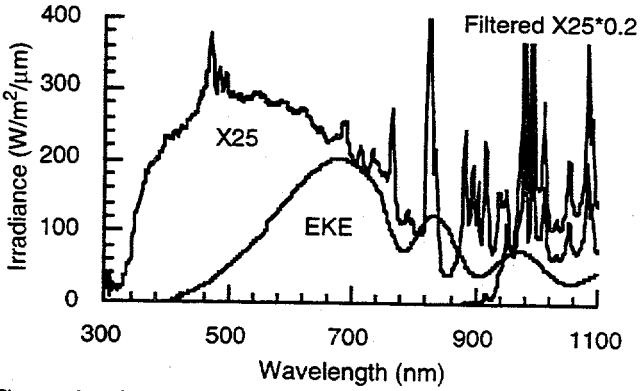

Figure 9. Spectra for the sources used to measure the temperature coefficients reported in Table 2. X25 indicates the Spectrolab X25 solar simulator. The EKE projector bulb (21V, 150W with dichroic reflector) operated at 11V.

MODELLING OF TANDEM CELL TEMPERATURE COEFFICIENTS

D. J. Friedman
National Renewable Energy Laboratory, 1617 Cole Blvd., Golden, CO 80401

ABSTRACT

This paper discusses the temperature dependence of the basic solar-cell operating parameters for a GaInP/GaAs series-connected two-terminal tandem cell. The effects of series resistance and of different incident solar spectra are also discussed.

INTRODUCTION

For both terrestrial and space applications, a detailed understanding of device temperature coefficients is vital if the results of simulator testing are to be used for quantitative prediction of performance in the field. This paper analyzes the temperature dependence of open-circuit voltage (V_{OC}), short-circuit current (J_{SC}), and fill factor (FF) for a two-terminal series connected tandem cell, extending the work of Fan on single-junction cells [1]. For the purpose of quantitative discussion, the GaInP/GaAs system is considered for detailed examination. This particular system is of specific practical interest due to its demonstrated high efficiencies in one-sun, concentrator, and space applications [2-4].

MODEL

The model used for the current-voltage (J–V) calculations has been described elsewhere [5]. For convenience, the essentials are reproduced very briefly here.

An idealized spectral response determined only by the cell absorption coefficients is assumed. All photons absorbed by the top cell, as determined by the top-cell thickness t and absorption coefficient $\alpha_t(\lambda)$, are assumed to contribute to the top-cell short-circuit current J_{SCt}:

$$J_{SCt} = \int_0^\infty e\, I_0(\lambda)(1-\exp[-\alpha_t(\lambda)t])\, d\lambda, \qquad (1)$$

where I_0 is the incident spectral intensity. The bottom cell is idealized to be infinitely thick, so that all photons transmitted through the top cell and above the band gap E_{gb} of the bottom cell are assumed to contribute to the bottom-cell short-circuit current J_{SCb}:

$$J_{SCb} = \int_0^{hc/E_{gb}} e\, I_0(\lambda) \exp[-\alpha_t(\lambda)t]\, d\lambda. \qquad (2)$$

The absorption coefficient $\alpha_t(\lambda)$ depends on the bandgap E_{gt} of the top cell; the form of Kurtz et al. [5] is used:

$$\alpha_t(E) = 4.55\,(E-E_{gt})^{1/2} + 2.05\,(E-E_{gt}-0.1)^{1/2}. \qquad (3)$$

In the present work, the temperature dependence of the short-circuit currents is accounted for by assuming a linear temperature dependence of E_{gt} and E_{gb} in the above equations; any other temperature effects on the spectral response are neglected. For the GaInP top cell, we take $dE_g/dT = -0.46$ meV/K, valid around 300 K [6]. For the GaAs bottom cell, we take $dE_g/dT = -0.45$ meV/K, valid around 300 K [7]. The general conclusions drawn later do not depend on these precise numbers.

The voltage V_{tandem} for the tandem device is the sum of the top and bottom cell voltages:

$$V_{tandem} = V_t + V_b\,. \qquad (4)$$

For the top and bottom cells, an ideal resistanceless solar cell has been assumed (except in the section discussing series resistance effects), with the top (bottom) cell voltage depending on the top-cell short-circuit current $J_{SCt(b)}$ and dark current $J_{0t(b)}$ by the relationship

$$V_{t(b)} = kT/e \ln[(J + J_{SCt(b)})/J_{0t(b)} + 1] \qquad (5)$$

where w have set the junction ideality factor n=1. J_0 depends strongly on the temperature T through its proportionality to the square of the intrinsic carrier concentration n_i:

$$J_0 = e\,(L_e/\tau_e)(n_i^2/N_A)\tanh(x_p/L_e) + e\,(L_h/\tau_h)(n_i^2/N_A)\tanh(x_p/L_h)\,, \text{ with} \qquad (6)$$

$$n_i^2 = 4M_cM_v(2\pi kT/h^2)^3\,(m_e^*m_h^*)^{3/2}\exp(-E_g/kT), \qquad (7)$$

and more weakly through temperature dependencies of materials parameters such as mobilities and minority-carrier lifetimes. Here L is the minority-carrier diffusion length

$$L_{e(h)} = (\tau_{e(h)}\,D_{e(h)})^{1/2}, \qquad (8)$$

and D is the diffusion constant

$$D_{e(h)} = kT\mu_{e(h)}/e. \qquad (9)$$

Any temperature dependence of mobilities μ, minority-carrier lifetimes τ, effective masses m^*, is ignored.

However, the temperature dependence of the bandgap E_g is taken into account as described above.

V_{OC} TEMPERATURE COEFFICIENT

Because the tandem voltage is the sum of the top- and bottom-cell voltages, the tandem V_{OC} temperature coefficient dV_{OC}/dT is simply the sum of the top- and bottom-cell temperature coefficients. Numerically calculating the GaInP top- and GaAs bottom-cell temperature coefficients dV_{OCt}/dT and dV_{OCb}/dT at 300 K, including the temperature dependence of minority-carrier diffusion constants and lifetimes as described above, gives dV_{OCt}/dT = –2.20 mV/°C, dV_{OCb}/dT = –1.99 mV/°C. The resulting tandem dV_{OC}/dT = –4.2 mV/°C. Neither top- nor bottom-cell temperature coefficient varies significantly with temperature. A simple analytic expression for a single-junction (e.g., either a top or bottom subcell) dV_{OC}/dT may be obtained from $V_{OC} \approx kT/e \ln[(J_{SC})/J_0]$ by neglecting the temperature dependence of J_0 on materials parameters such as diffusion lengths and minority-carrier lifetimes, so that $J_0(T) \approx \text{const} \times T^3 \exp(-E_g/kT)$. Setting n=1, we get

$$\frac{dV_{OC}}{dT} \approx \frac{1}{T}\left[V_{OC} - \frac{3kT}{e} + \frac{T}{e}\frac{dE_g}{dT} - \frac{E_g}{e}\right] + \frac{kT}{e}\frac{1}{J_{SC}}\frac{dJ_{SC}}{dT} \quad (10)$$

which is Fan's eq. 6 [1]. This last term must be computed numerically; Fig. 1 shows that for GaInP/GaAs it is on the order of $(10^{-3}kT/e)/K$. This is roughly 0.02 mV/K at 300 K, which is negligible. It should be noted that the spectrum affects only this last term. With this last term neglected, Eq. (10) gives dV_{OCt}/dT = –2.25 mV/°C, dV_{OCb}/dT = –2.02 mV/°C, very close to the more precise calculation.

For real devices, the single-junction ideality factor n is generally somewhat greater than 1, resulting in an greater magnitude of dV_{OC}/dT compared to its magnitude for n=1.

For comparison with the calculated –4.2 mV/°C value, a recent on-sun measurement [8] of dV_{OC}/dT for a GaInP/GaAs tandem under an approximately AM1.5 direct spectrum gave –3.9 mV/°C, close to the calculated value, implying that n≈1 for both subcells of this specific device.

J_{SC} TEMPERATURE COEFFICIENT

The dependence of the tandem J_{SC} temperature coefficient on the top and bottom cells and on temperature is more complex than the V_{OC} dependence. Figure 1 shows the top and bottom subcell currents J_{SCt} and J_{SCb} as a function of temperature for a tandem cell with a 1.15-μm-thick top cell, calculated for the standard AM1.5 direct spectrum. (The effect of varying the spectrum will be discussed later.) For this spectrum and top-cell thickness, J_{SCt} is slightly less than J_{SCb} at 300 K. Because the top and bottom cells are in series, the tandem J_{SC} is limited to be the lesser of J_{SCt} and J_{SCb}. For the tandem illustrated in the figure, at 300 K the tandem is slightly top-cell current-limited. This is illustrated in the figure, which shows the tandem J_{SC} resulting from J_{SCt} and J_{SCb}.

Also shown is J_{SC} for a cell equivalent to a bottom cell but without a top cell filtering the incident light. The temperature variation dJ_{SCb}/dT of J_{SC} for the bottom cell as filtered by the top cell in the tandem structure is much smaller than for the unfiltered bottom cell. This difference

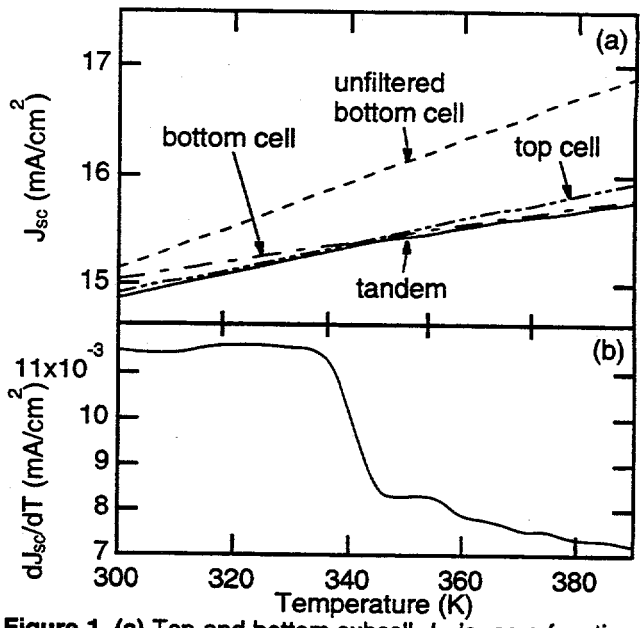

Figure 1. (a) Top and bottom subcell J_{SC}'s as a function of temperature for a tandem cell with a 1.15-μm-thick top cell, calculated for the standard AM1.5 direct spectrum. Also shown is J_{SC} for an bottom cell unfiltered by a top cell. This unfiltered J_{SC} has been shifted down on the graph for easy comparison with the standard bottom-cell J_{SC}. **(b)** The resulting temperature coefficient dJ_{SC}/dT for the tandem cell.

is because the lowering of the tandem cell's bottom-cell bandgap with increasing temperature, which increases the amount of light the bottom cell absorbs, is partially compensated by the simultaneous lowering of the top-cell bandgap, which decreases the amount of light that is transmitted to the bottom cell. The temperature dependence of the top cell, in contrast, is determined only by the temperature dependence of the top-cell band gap. As illustrated in Fig. 1, a tandem cell that is slightly top-cell current-limited at some starting temperature T_0 will eventually become bottom-cell-limited at a crossover temperature $T_x > T_0$. As a result, as the temperature is raised through T_x, the tandem J_{SC} temperature coefficient dJ_{SC}/dT will abruptly change from $dJ_{SC}/dT = dJ_{SCt}/dT$ to $dJ_{SC}/dT = dJ_{SCb}/dT$. This crossover occurs at $T_x \approx$ 350 K for the tandem cell illustrated in the figure.

FF TEMPERATURE COEFFICIENT

The temperature coefficient dFF/dT of the tandem fill factor *FF* depends strongly on how close the top and bottom subcells are to current matching. Figure 2(a) shows FF calculated for GaInP/GaAs tandem cells with top-cell thicknesses of 1.05 μm, 1.15 μm, and 1.25 μm. The tandem with the 1.05-μm top cell is current-limited by the top cell in the temperature region shown in the figure, while the tandem with the 1.25-μm top cell is current-limited by the bottom cell in this temperature region. However, as discussed in the preceding section, the tandem cell with the intermediate top-cell thickness of 1.15 μm is top-cell-limited below the crossover temperature $T_x \approx$ 350 K, and becomes bottom-cell-limited above T_x.

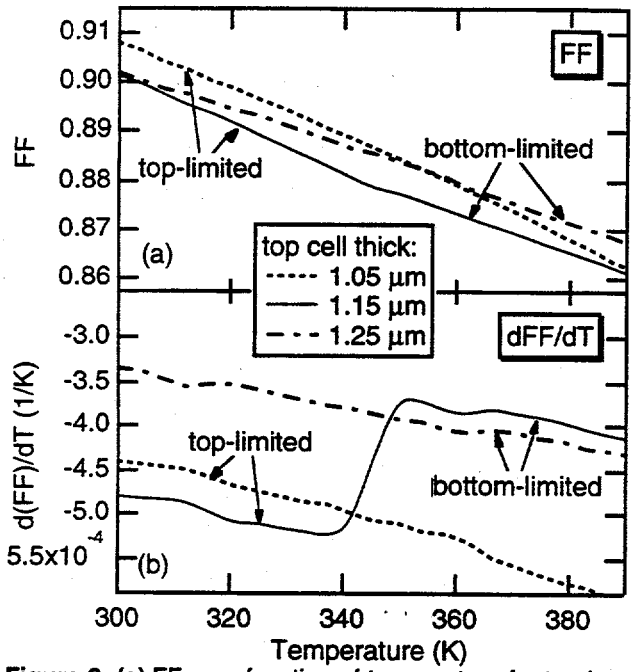

Figure 2. (a) FF as a function of temperature for tandem cells with top cells of various thicknesses, calculated for the standard AM1.5 direct spectrum. **(b)** *d(FF)/dT* for the FF's of panel (a).

For the tandems that are current-mismatched (either top-cell-limited or bottom-cell-limited), FF depends smoothly on temperature. However, for a device which passes through current-matching at a crossover temperature T_x (350 K for the tandem with the 1.15-μm top cell in Fig. 2). *dFF/dT* changes in the region of T_x. This is because, for top and bottom cells with given fill factors, the tandem FF will be determined by the current-limiting subcell. Therefore, as the temperature is raised through the current-matching temperature T_x, the device transitions from top-cell-limited to bottom-cell-limited, and *dFF/dT* changes accordingly. Therefore, *dFF/dT* becomes less negative as the temperature is raised through T_x. This behavior is illustrated in Fig. 2(b), which shows the derivatives *dFF/dT* of the FF's of Fig 2(a).

EFFICIENCY

The efficiency is proportional to $V_{OC}J_{SC}FF$. Figure 3 shows FF, V_{OC}, J_{SC}, and the resulting efficiency (solid lines, left axis) and their temperature derivatives (dashed lines, right axis) for a tandem with a 1.15-μm-thick top cell. The increase in J_{SC} with increasing temperature is less than the decrease of $V_{OC}FF$ with temperature, so the efficiency decreases with temperature. Both J_{SC} and *FF* show a small but perceptible change in their temperature dependencies as the temperature is raised through the point at which top and bottom cells are current-matched, as illustrated in Figs. 1 and 2 above. These changes are in opposite directions: dJ_{SC}/dT decreases, while *dFF/dT* increases, as the temperature is raised through the current-matching temperature. As a result the $J_{SC}FF$ product, and hence the efficiency, do not show a significant change at the current-matching temperature.

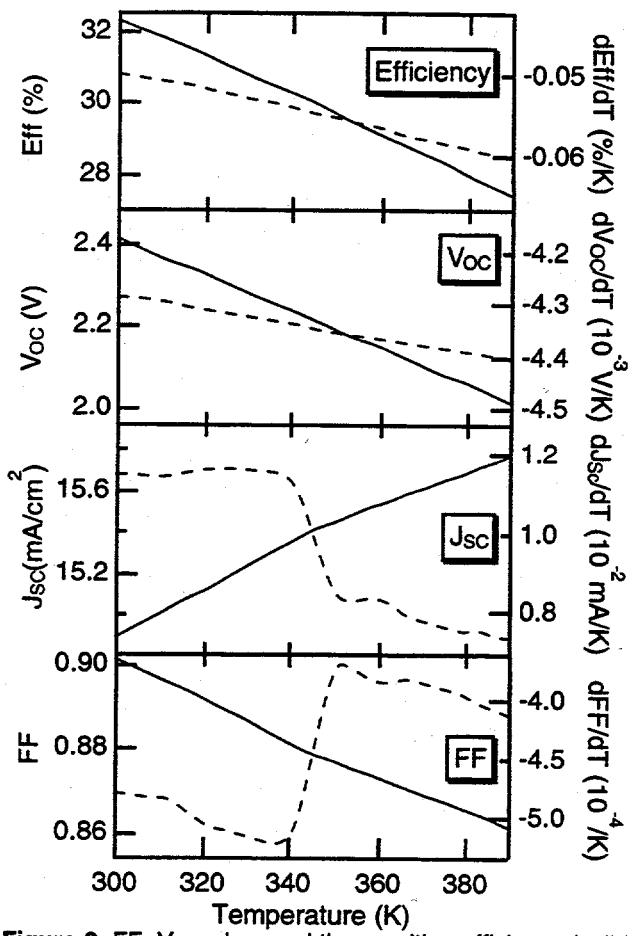

Figure 3. FF, V_{OC}, J_{SC}, and the resulting efficiency (solid lines, left axis) and their temperature derivatives (dashed lines, right axis) for a tandem with a 1.15-μm-thick top cell, calculated for the standard AM1.5 direct spectrum.

EFFECT OF SERIES RESISTANCE

In this section we consider the effect of a finite series resistance R_S, which in all the other sections is neglected. This effect is modelled by adding a JR_S term to the ideal V(J) relation: $V(J) = V_{R=0}(J) + JR$. This R_S has no effect on V_{OC}. Furthermore, for high-fill-factor devices such as the

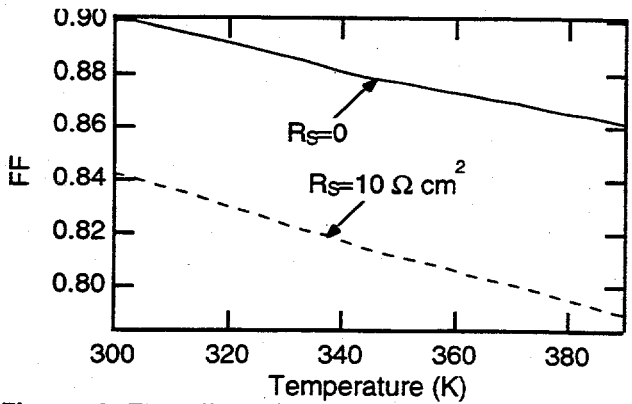

Figure 4. The effect of series resistance R_S on the temperature-dependent fill factor FF.

GaAs and GaInP cells, series resistance has a very small effect on J_{SC} as long as the series resistance does not dominate the J-V curve. Thus, the main effect of series resistance is on the fill factor FF. Figure 4 compares the temperature dependence of FF for R_S=0 (as shown in Fig. 2) with FF calculated for R_S=10 Ω cm^2. The behavior of FF(T) is not qualitatively changed by the series resistance. The main difference is that the magnitude of the relative temperature coefficient (1/FF) d(FF)/dT is increased by the introduction of R_S.

EFFECT OF SPECTRUM

As has been discussed above, the temperature dependence of J_{SC}, $J_{SC}(T)$ depends on the incident solar spectrum. This dependence in turn affects FF(T). Figure 5 shows $J_{SC}(T)$ and FF(T) calculated for the AM1.5 direct spectrum compared with a calculation for the AM0 spectrum; $V_{OC}(T)$ has been omitted because, as discussed above, its J_{SC} dependence and hence spectrum dependence is very weak. To make the spectrum comparison meaningful, the thicknesses of the top cells have been chosen so that in both cases, the devices are current-matched at approximately the same temperature of around 330 K. These thicknesses are 1.15 μm for AM1.5 direct (as elsewhere in this paper) and 0.5 μm for AM0. The figure shows that the qualitative behavior of the temperature coefficients is the same for the different solar spectra.

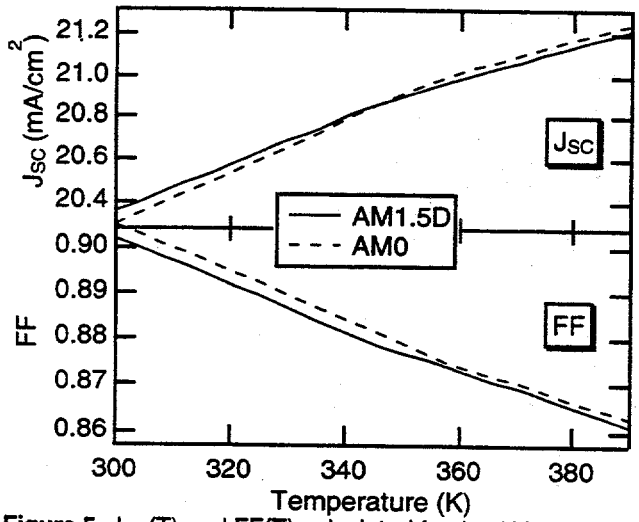

Figure 5. $J_{SC}(T)$ and FF(T) calculated for the AM1.5 direct and AM0 spectra. Top cell thicknesses are 1.15 μm for AM1.5 direct and 0.5 μm for AM0. To facilitate comparison of the J_{SC} curves, the AM1.5-direct J_{SC} has been shifted upwards by 5.45 mA/cm^2 to overlay it with the AM0 J_{SC}.

CONCLUSIONS

The bottom-cell J_{SC} of the GaInP/GaAs series-connected tandem has a much smaller temperature variation than does an unfiltered GaAs cell. For this reason, the rate of increase of the full tandem J_{SC} with temperature becomes smaller as the temperature is raised through the crossover temperature at which the top and bottom cells are current-matched. The transition from top-cell to bottom-cell-limited operation as the temperature is raised through the crossover temperature also results in a change in dFF/dT at the crossover temperature. V_{OC}, in contrast, remains essentially linear through the crossover temperature. The variations in dFF/dT and dJ_{SC}/dT at the crossover temperature cancel each other out when multiplied together, so that dEfficiency/dT is a smooth, fairly linear function of T, even through the crossover temperature.

ACKNOWLEDGMENTS

This work was supported by U.S. Department of Energy contract No. DE-AC36-83CH10093.

REFERENCES

[1] J.C. Fan, "Theoretical temperature dependence of solar cell parameters", *Solar Cells* **17**, 1986, pp. 309-315.

[2] K.A. Bertness, S.R. Kurtz, D.J. Friedman, A.E. Kibbler, C. Kramer, and J.M. Olson, "29.5%-efficient GaInP/GaAs tandem solar cells", *Appl. Phys. Lett.* **65**, 1994, pp. 989-991.

[3] D.J. Friedman, S.R. Kurtz, K.A. Bertness, A.E. Kibbler, C. Kramer, and J.M. Olson, "30.2% efficient GaInP/GaAs monolithic two-terminal tandem concentrator cell", *Progr. Photovolt.* **3**, 1995, pp. 47-50.

[4] S.R. Kurtz, K.A. Bertness, D.J. Friedman, A.E. Kibbler, C. Kramer, and J.M. Olson, "19.6% electron-irradiated GaInP/GaAs cells", *1st World Conference on Photovoltaic Energy Conversion*, 1994, pp. 2108-2111.

[5] S.R. Kurtz, P. Faine, and J.M. Olson, "Modeling of two-junction, series-connected tandem solar cells using top-cell thickness as an adjustable parameter", *J. Appl. Phys.* **68**, 1990, pp. 1890-1895.

[6] S.C. Lu, M.C. Wu, C.Y. Lee, and Y.C. Yang, "Temperature dependence of photoluminescence from Mg-doped $In_{0.5}Ga_{0.5}P$ grown by liquid-phase epitaxy", *J. Appl. Phys.* **70**, 1991, pp. 2309-2312.

[7] J.S. Blakemore, "Semiconducting and other major properties of GaAs", *J. Appl. Phys.* **53**, 1982, pp. R123-R181.

[8] D.J. Friedman, S.R. Kurtz, K. Sinha, W.E. McMahon, J.M. Olson, J.B. Lasich, A.X. Cleeve, and I. Connaughton, "On-sun concentrator performance of GaInP/GaAs tandem cells", (this conference).

ON-SUN CONCENTRATOR PERFORMANCE OF GaInP/GaAs TANDEM CELLS

D. J. Friedman S. R. Kurtz, K. Sinha, W. E. McMahon, and J. M. Olson
National Renewable Energy Laboratory, 1617 Cole Blvd., Golden, CO 80401

J. B. Lasich, A. X. Cleeve, and I. Connaughton
Solar Research Corporation Pty. Ltd, 6 Luton Lane, Hawthorn, Victoria 3122, Australia

ABSTRACT

The GaInP/GaAs concentrator device has been adapted for and tested in a prototype "real-world" concentrator power system. The device achieved an on-sun efficiency of 28% ± 1% in the range of approximately 200-260 suns with device operating temperatures of 38°C to 42°C. We discuss ways of further improving this performance for future devices.

INTRODUCTION

The monolithic two-terminal GaInP/GaAs solar cell [1] is a promising candidate for application in terrestrial concentrator power systems, due to its demonstrated efficiency in excess of 30% for concentrations in the range of 100–300 suns [2]. This device has been adapted for evaluation on-sun in a parabolic-reflector concentrator system [3], the first measurement of this device under real-world concentrator conditions. This paper describes the necessary adaptations, presents the on-sun measurement results, and compares these results with the modeled behavior to aid in predicting the performance of future generations of the device.

DEVICE REQUIREMENTS AND GRID DESIGN

The requirements for a device usable in the concentrator system are more stringent than for devices measured on a simulator. To obtain acceptable signal to noise in the concentrator system, a device with an effective size of 1.0 cm^2 is used. This device, a top view of which is pictured in Fig. 1, consists of four 0.25-cm^2 "subdevices" on a single wafer, processed and mesa-etched for electrical isolation so that the subdevices can be tested individually if desired. Each subdevice has a bus bar on only one side of the device. For the on-sun testing, the bus bars of the four subdevices are connected electrically to give a device that is thus actually a 1.0-cm^2-illuminated-area device with bus bars on opposite sides of the device. In contrast, the original GaInP/GaAs concentrator device [2] was 0.1 cm^2. For ease of soldering contacts to the bus bars, the bus bars are 0.75 mm wide.

The ultimate concentration goal for this application is 500 suns. However, the requirement of the large device size as described above puts heavy demands on the grid fingers of the front metallization. A highly conductive, narrow, thick (and thus, high-aspect-ratio) finger with good contact resistivity is called for. For the first iteration of the device, a Au-plated front-contact metallization is used for convenience. This metallization is limited in the conductivity, narrowness, and height of the grid fingers it can provide — a significant limitation for high-concentration devices, especially for the grid-finger lengths of the device shown in Fig. 1. Typical resistivity for the Au-plated metallization is 5×10^{-6} Ω-cm, more than twice the tabulated bulk Au resistivity of 2.2×10^{-6} Ω-cm. The difference is due to the relatively grainy character of the metal deposited in the electroplating process. In principle, limitations in the grid finger resistivity can be compensated for by increasing the thickness of the finger. However, for the plated metallization, the thickness is limited by the photoresist thickness to about 2.5 μm. Increasing the finger conductance by increasing the finger width must be balanced against the grid-coverage shadow loss; for this reason, narrow high-aspect-ratio grid fingers are preferred. The plated-metallization process, however, cannot reliably produce grid finger widths significantly below 10 μm, and the limitations of the finger thickness and conductivity for this metallization diminish the importance of narrower grids. Finally, I^2R losses due to the emitter sheet resistance (about 200 Ω/sq for the top cell of the device

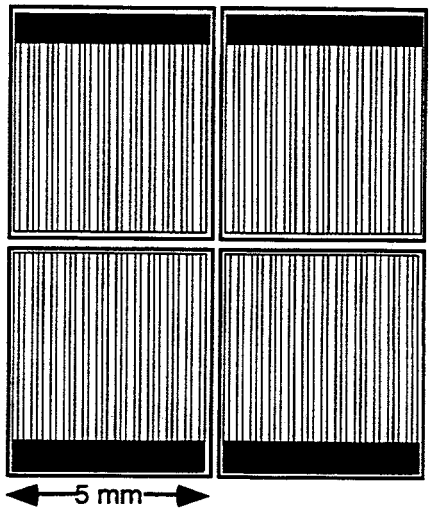

Fig. 1. Schematic top view of the device. The subdevices are electrically isolated with a mesa etch, so the area between them is not photoactive. All four bus bars were connected electrically for testing, resulting in an effectively 1-cm^2 device. Grid fingers are 10 μm wide and are spaced 150 μm apart.

described here) demand that grid fingers be spaced close together. This emitter sheet resistance loss combined with the grid-finger resistivity loss (plus several other loss terms [2] of less importance for the device described here) must be balanced against the grid-coverage shadow loss to arrive at a final grid design.

The initial iteration of the device has grids optimized for a lower concentration of 200 suns; the optimal grid spacing at this concentration for the plated metallization is 150 μm. Even at this lower concentration, the deficiency of the plated metallization limits the device efficiency. Future iterations of the device will use an evaporated metallization that should overcome the grid-finger limitations of the plated grids, permitting fingers 3 μm wide and 5 μm thick, or better. The evaporated metallization also provides grid-finger resistivities much closer to the book values (i.e., much lower than the plated metallization provides), due to the superior density and grain structure provided by the evaporation process.

DESIGN OF TOP CELL

The on-sun spectrum is, of course, not precisely the ASTM E891 standard AM1.5 direct spectrum, and indeed it varies during the day. For the series-connected tandem device described here, the ideal top-cell thickness depends on the spectrum. This dependence arises because the top-cell thickness determines the relative photocurrents of the top and bottom cells; the tandem cell photocurrent is maximized when the top and bottom cell photocurrents are matched, because the tandem current is limited by the series connection to the lesser of the two subcell photocurrents [4].

For the first iteration of the device, we have chosen to design for the standard AM1.5 direct spectrum, with a top-cell thickness of 1.0 μm. Future iterations of the device may be tuned to some time-average of the actual incident spectrum. A detailed discussion of the performance of multijunction devices as a function of variations in the incident spectrum is given elsewhere [5,6]. The overall conclusion of these works is that spectrum fluctuations affect the performance of series-connected tandems more than the performance of 1-junction devices, but that the overall performance advantage of the tandem is not changed by this efficiency fluctuation.

DEVICE MEASUREMENT AND PERFORMANCE

The wafer was mounted on a receiver substrate with good thermal contact to cooling water. The light flux onto the receiver region was apertured so that only a well-defined area on the wafer is illuminated. The flow and temperature of the receiver cooling water were precisely measured, permitting a direct calorimetric measurement of the incident flux given the reflectance of the device. Thus no assumptions about the linearity of the short-circuit current (J_{sc}) with concentration need be made, in contrast to typical simulator measurements. This is not a trivial issue, because nonlinear response has been reported for GaAs solar cells [7]. Nor are spectral corrections needed, because the actual solar spectrum is being used.

The temperature of the device was not held at 25°C, the conventional simulator-measurement reporting temperature, but rather was allowed to reach the temperature it would operate at if the concentrator system were being used to generate power. Therefore, no temperature correction need be applied to the device performance parameters to predict the device performance under actual operating conditions. However, the device temperature must be taken into account in the modeling of the device behavior.

Figure 2 shows the measured concentration-dependent open-circuit voltage (V_{oc}), fill factor, and efficiency. For V_{oc}, the open symbols show what V_{oc} would be at 25°C, using a temperature coefficient of -3.9 mV/°C as measured for this device. For comparison with the data, the dashed lines show the modeled behavior. V_{oc} is modeled by assuming an effective ideality factor of n=2, appropriate for a series-connected tandem with ideal (n=1) top and bottom cells. The calculated V_{oc} describes the temperature-corrected measurements very well. The fill factor (FF) is modeled by calculating I-V curves [8], with the addition of an effective series resistance [2,9]. The measured fill-factor data points appear to be consistent with the modeled curve, to the degree to which the two can be compared given the scatter in the measurements.

The linearity of J_{sc} at concentration C is given by the ratio of the one-sun-normalized J_{sc} to the concentration, $(1/C)\ J_{sc}(C)/J_{sc}(1)$. The concentration C is given by the ratio of the calorimetrically-measured photon energy flux $\Phi(C)$ to its one-sun value: $C=\Phi(C)/\Phi(1)$. The measured J_{sc} linearity is shown in Fig. 3. The difference between the measurements and the ideal-linearity case is presumably due almost entirely to noise in the measurement of Φ, because the linearity would not be expected to vary as nonmonotonically with C as the data of Fig. 3 does. Thus a

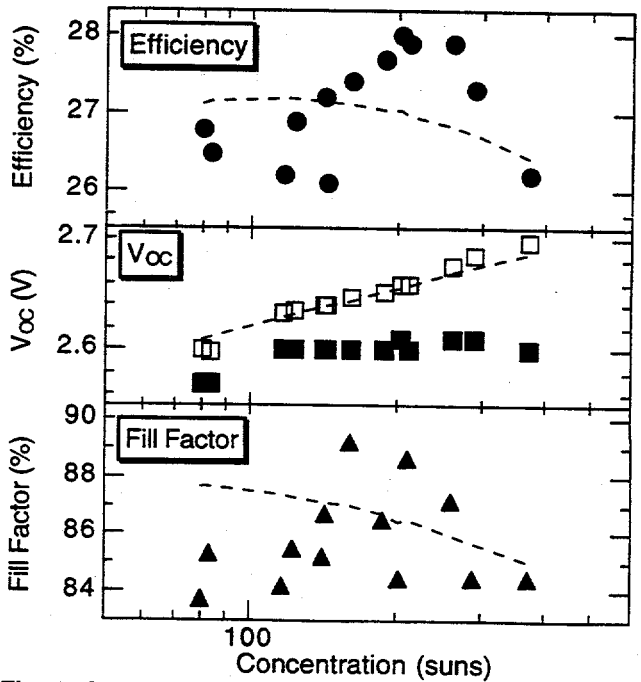

Fig. 2. On-sun performance of the device, "MA215". The data are shown as the filled symbols. The open squares show V_{oc} corrected to 25°C operating temperature. The dashed lines show the modeled behavior, including temperature correction for V_{OC} (but not for FF).

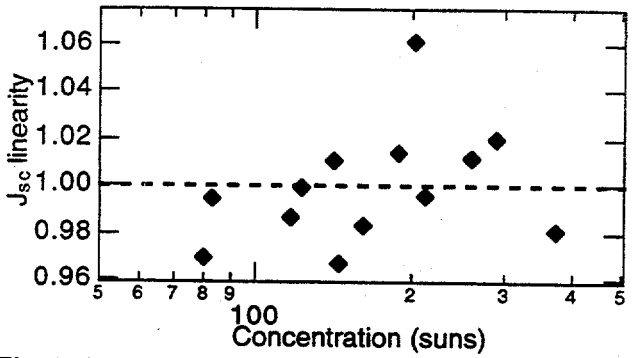

Fig. 3. J_{sc} linearity. The dashed line represents the case of perfect linearity.

determination of the device nonlinearity awaits data with better signal to noise in Φ. Working with larger device areas should help with this measurement.

Finally, the measured efficiency shown in Fig. 2 is given by $J_{sc}V_{oc}FF/\Phi$. The modeled efficiency, which uses the temperature-corrected V_{oc}, is shown for comparison. The efficiency data appear to have a maximum with concentration that is much sharper than the modeled curve. However, this is most likely an artifact of the noise in the FF and Φ data. From the scatter in the data, we estimate a relative uncertainty of about 2% in the FF and Φ measurements, giving a relative uncertainty (not including systematic errors, which are hard to quantify) of about 3% (i.e., about 1% absolute) in the efficiency numbers. With these error bars, we can summarize the peak performance of the device as 27% ± 1% in the range of approximately 80-400 suns. The modeling suggests that the efficiencies are in the lower end of this range. It should be emphasized that the efficiencies in this concentration range are achieved with device operating temperatures of as high as 50°C.

FUTURE WORK

The most important direction for improving the performance of future devices will be the adoption of an evaporated-metal/liftoff front grid metallization. Modeling a device with this improved metallization, at 500 suns a gain on the order of 6% in the relative cell performance (about 2% in absolute efficiency) can be expected. Better current-matching of the top and bottom cells to the solar spectrum being used may also lead to a further improvement in the device efficiency. Fabricating 1-cm^2 devices without the mesa-etch division into four subdevices will reduce perimeter recombination by a factor of two.

To optimize total module efficiency, a single bus bar running down the center of the cell would reduce the total cell area compared to the two side bus bars used in the device shown in Fig. 1. The single-central-bus-bar configuration does not change the effective lengths of the grid fingers, and so the performance of such a device should not suffer compared to that of the present two-bus-bar design. Future work will include the examination of this bus bar design.

ACKNOWLEDGMENTS

This work was supported by the U.S. Department of Energy contract No. DE-AC36-83CH10093.

REFERENCES

[1] K.A. Bertness, S.R. Kurtz, D.J. Friedman, A.E. Kibbler, C. Kramer, and J.M. Olson, "29.5%-efficient GaInP/GaAs tandem solar cells", *Appl. Phys. Lett.* **65**, 1994, pp. 989-991.

[2] D.J. Friedman, S.R. Kurtz, K.A. Bertness, A.E. Kibbler, C. Kramer, J.M. Olson, D.L. King, B.R. Hansen, and J.K. Snyder, "GaInP/GaAs monolithic tandem concentrator cells", *1st World Conference on Photovoltaic Energy Conversion*, 1994, pp. 1829-1832.

[3] J.B. Lasich, A. Cleeve, N. Kaila, G. Ganakas, M. Timmons, R. Venkatasubramanian, T. Colpitts, and J. Hills, "Close-packed cell arrays for dish concentrators", *1st WCPEC*, 1994, pp. 1938-1941.

[4] J.M. Olson, S.R. Kurtz, A.E. Kibbler, and P. Faine, "A 27.3% efficient Ga0.5In0.5P/GaAs tandem solar cell", *Appl. Phys. Lett.* **56**, 1990, pp. 623-625.

[5] S.R. Kurtz, J.M. Olson, and P. Faine, "The difference between standard and average efficiencies of multijunction compared with single-junction concentrator cells", *Solar Cells* **30**, 1991, pp. 501-513.

[6] P. Faine, S.R. Kurtz, C. Riordan, and J.M. Olson, "The influence of spectral solar irradiance variations on the performance of selected single-junction and multijunction solar cells", *Solar Cells* **31**, 1991, pp. 259-278.

[7] G. Stryi-Hipp, A. Schoenecker, K. Schitterer, K. Bücher, and K. Heidler, "Precision spectral response and I-V characterization of concentrator cells", *Proceedings of the 23rd IEEE Photovoltaic Specialists Conference*, 1993, pp. 303-308.

[8] S.R. Kurtz, P. Faine, and J.M. Olson, "Modeling of two-junction, series-connected tandem solar cells using top-cell thickness as an adjustable parameter", *J. Appl. Phys.* **68**, 1990, pp. 1890-1895.

[9] T.A. Gessert and T.J. Coutts, "Grid metallization and antireflection coating optimization for concentrator and one-sun photovoltaic solar cells", *J. Vac. Sci. Technol. A* **10**, 1992, pp. 2013-2024.

THE VALUE OF CUSTOMER PREFERENCE

Christy Herig and Ashley Houston
National Renewable Energy Laboratory
1617 Cole Blvd., Golden, CO 80401, USA

ABSTRACT

Customer preference (CP), or green pricing, may be the financial hedge for electric supply industry integration of photovoltaics. CP is currently defined as a voluntary contribution for energy generated with renewable resources. Several utilities have examined the CP financing of renewables through experimental or implemented programs and market research. This paper first expands the concept of customer preference to include both voluntary and involuntary customer contributions. It then categorizes the features of existing and proposed CP programs. The connections between these features and market research and marketing strategies for new product development from a competitive industry are analyzed.

INTRODUCTION

As utilities transition into the competitive arena, many are examining customer preferences to define mechanisms and attributes to differentiate products. As with most competitive businesses, it will be the customer who will decide which attributes define good, better, or best. The obvious areas to differentiate are price and reliability. However, the market has proven that customers are willing to pay for service attributes beyond these basics. Progressive technology and environmental compatibility top the preferences as demonstrated by high-technology stock activity, the electronics industry, and consumer goods plugging or environmental friendliness. Environmental stewardship is a popular public relations mechanism for all businesses running the gambit of retail to chemical processing. With this awareness, the electric industry is exploring renewables as a customer preference. Would customers prefer to buy clean, green, environmentally friendly power? More importantly, are they willing to pay more? Americans have become increasingly aware of environmental impacts and increasingly supportive of environmental mitigation [1]. Even putting aside any association with nuclear generation, electric utilities have not been viewed as good environmental stewards [2].

Though customer preference seems to advocate green-product differentiation, most utilities that have either researched and/or implemented green marketing programs have realized minimal success. On average, only 10% of funds predicted by the market research have been obtained when a program was implemented [3]. Many reasons have been given for this minimal success, such as faulty market research, time lags, and poor response to customer requests. However, these are small pieces of the larger puzzle. To define the larger puzzle, we must examine the product development process in the competitive marketing arena.

THE PRODUCT DEVELOPMENT PROCESS

Preliminary results from the recently completed annual Product Development Practices Survey [4] indicate that the best (based on market share, sales, and qualitative success criteria) product development teams were twice as likely to know that they were working with well-defined products, and they understood:

- Total organizational support
- Strategic alignment
- User needs
- Product positioning
- Competitive analysis.

Examining the green marketing efforts to date, and applying the above-noted product development process elements, indicates the need to look at the broader picture. The more successful programs have taken a strategic approach to renewable product deployment. The success of product deployment requires a utility to identify the deployment of the (in this case, renewables) as an element of the company's overall strategic plan; this is especially true as the utility transitions from a monopolistic to a competitive marketing arena. With continual down-sizing and re-alignment, accountabilities within the utility are confusing. A top-down approach to product development is required to achieve total organizational support.

The best teams also identified supplier partnering and consistent management planning tools as product development success factors. The management planning tools "often" or "always" used include:

- Market share estimate
- Technology forecast
- Product portfolio analysis
- Line or division strategy.

These are all new management planning areas for electric utilities. The protected monopolistic environment required conservative, low-risk decisions based on established, proven technologies. As technical, regulatory, and economic pressures force utilities into a

more competitive market, the approach to decision criteria will change. However, the changes required for successful product development are not unique to the utility industry. The five challenge-to-change areas identified for the 1995 American Product Excellence (APEX) award winners were: technical; cultural; partnering with customers, distributors, and other stakeholders; process; and product. All the APEX winners underwent change in more than one of the areas, but none took on all five. Other attributes noted among the APEX winners were that all were risk takers, mistakes were made, and none were slaves to perfection. The message noted by the chairperson's summary was to move forward boldly, but don't try to change everything at once: be strategic. Bold approaches, changes, and risk may be alien to utilities initially [4]. The opportunity for strategic product development during the transition to a more competitive market is enormous. While the customer base is still captive, the utility can economically identify customer preferences, analyze product portfolios, and implement strategic alignment; the partnering opportunities in the renewables industry are boundless.

MARKET RESEARCH

Market research, either through surveys or focus groups, is the basis for identifying user needs, product positioning, and competitive or market share analysis. Market research mechanisms also identify partnering opportunities for successful new-product development. Though many survey instruments have been implemented and focus groups conducted, only the utilities that have incorporated the customer preference into their product development strategic plan have achieved and even surpassed the results predicted by the market research.

Thus far, 24 utilities have conducted or are planning to conduct market research related to customer preference for renewable-energy electric generation. These utilities include Sacramento Municipal Utility District (SMUD), Southern California Edison, Public Service of Colorado, Platte River Power Authority, Florida Power Corporation (FPC), Gainesville Regional Utilities, Hawaii Electric Light Company, New England Electric System (NEES), New England Power Corporation (NEPC), Niagara Mohawk, New York State Electric and Gas, Portland General Electric, Green Mountain Power, Puget Power and Light, Wisconsin Public Service, Central and Southwest, Northern States Power, Arizona Public Service, City of Tallahassee, City of Austin Electric Utility, Detroit Edison, City of Anaheim, Ontario Hydro, and Florida Power and Light.

The market research performed to date shows that there is strong interest in contributing to the development of renewable electric generation. The majority of those surveyed express a preference for renewables, and a significant portion would be willing to pay more for it.

Market Surveys

Due to the statistical nature of survey instruments, the results are often the numerical basis for market share analysis. However, unless the survey is crafted to address existing perception and cognizance, the results may be misleading. Prior to implementing a measurement survey, the consumer level of understanding related to the product attributes must be known, which typically requires another survey or focus group.

Twenty-two utilities have conducted surveys, most of which were targeted at measurement. Figure 1 represents a sample of comparable willingness-to-pay survey results.

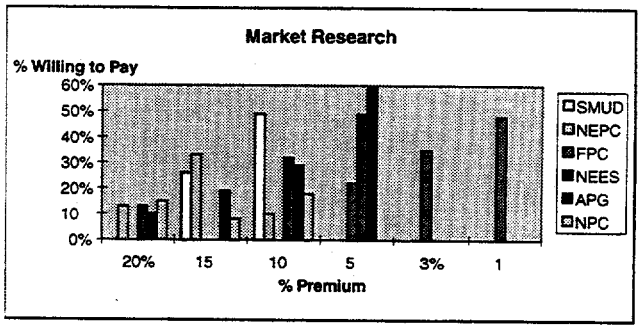

Fig. 1 Utility Willingness-to-Pay Customer Survey Results.

Applied Energy Group (AEG) conducted market surveys for several utilities and represents the largest survey sample. Preference for renewables is evidenced by the survey results, but the product reference was different between surveys, and most utilities implemented only one survey. Therefore, without product descriptions targeted at consumer awareness, the results of the measurements questions may be erroneous. The SMUD results noted above have been proven valid. SMUD has implemented market research in several areas, such that the measurement is targeted to the awareness level.

Focus Groups

Focus groups are another very useful tool that can be used to gauge interest and also receive important customer feedback on barriers, needs, and attributes preferred in a product. Focus groups allow customers to voice concerns and shed light on issues related to the product, often identifying innovative applications and partnering opportunities. Focus groups have been conducted or are planned by Public Service of Colorado, Hawaiian Electric Light Corporation, New England Electric Service, Niagara Mohawk, Portland General Electric, and Ontario Hydro.

Many of the focus groups were segmented by customer class and energy consumption. Additionally, some of the residential focus groups were segmented by

income level. All the focus groups revealed that customers want a diversified resource mix and are willing to pay a premium to ensure that renewables are part of the mix. The groups further revealed that there is confusion about higher rates for customers interested in funding the acquisition of renewables. This suggests that education and communication would need to be an integral part of any green pricing program. Niagra Mohawk customers preferred solar energy because it was perceived to be low maintenance and abundant. Residential customers were more receptive to the idea of green-pricing than commercial customers, but both groups agreed that the higher rates for green resources should apply to all customers, not just the group that is willing to pay. All focus groups identified the need for broad public education as well as specific information on the utilities planned projects, position on environmental issues, and strategies for offering the product. Most utilities have concluded from the focus groups that the specific projects must be identified, and community-based projects or systems supplying direct benefits to the green payer are preferred. The benefits do not have to be energy related. SMUD customers pay a premium for rooftop systems that do not supply energy to the building. The customers' benefit is identification of environmental stewardship by allowing SMUD to use the roof area.

EXISTING PROGRAM OVERVIEW

Customer preference programs can be implemented in two forms: (1) voluntary programs where only customers that choose to participate fund the development of renewables and (2) programs where all customers pay equally through a legislative mechanism like an infrastructure reserve account.. Infrastructure reserves are commonly used for water, sewer, transportation, parks/recreation, and even environmental protection. Energy-related infrastructure reserves have not been implemented in the United States, but are gaining strong public support in Germany and Switzerland. However, of all the customer preference programs currently in place, all but one are voluntary programs, even though market research indicates the need for direct relational benefits.

Reserve Account

Arizona Public Service Company is the only utility thus far that has implemented a program where customers are funding renewables deployment through a millage rate based on energy use. The Energy Efficiency and Solar Energy (EEASE) fund is described as a demand-side management cost-recovery mechanism, as well as a development and implementation cost-recovery fund for renewables projects. However, it is a surcharge that accumulates and is then administered through approval of the Arizona Commerce Commission staff.

In Germany and Switzerland, the reserve accounts are administered by the utilities through a one mill per kWh surcharge. Renewable-energy generation is then paid for at a kWh rate for a specified period of time, which allows for the developer's reasonable economic benefit, but only if the project generates. The utilities are only administrators of the reserve and are not allowed to participate in renewable generation development.

A similar program in the United States would have incredible results. According to the Energy Information Agency (EIA), the residential sector uses 998 tera-Wh per year, the commercial uses 886 tera-Wh, and the industrial sector uses 940 tera-Wh. A one mill surcharge would result in a $2.8 billion dollar per year.

Voluntary

The vast majority of customer preference programs are voluntary programs where only those customers that choose to participate fund the development of renewables. There are several types of customer preference programs within the voluntary realm. These types include programs where there is direct customer consumption either on- or off-grid, programs where the monetary contributions are pooled in a general fund for the development of renewables, community-based programs, and programs that involve customer aggregation and targeting.

Direct customer consumption programs are those in which the customer realizes direct benefit from the system. The renewable generating unit is located at the residence or place of business. The unit can either be off-grid or grid-connected, in which case the benefit may not be energy-related.

SMUD's PV Pioneers program is probably the most widely known and successful direct customer consumption program. SMUD's customers, both residential and commercial, pay a 15% premium on their monthly utility bill for 10 years for a 4-kW, grid-connected, rooftop PV panel that does not supply energy to the building. There are currently 300 participants, with 100 new customers being added to the program each year and a growing waiting list.

Utilities involved in the Utility Photovoltaic Group (UPVG) Technology Experience to Accelerate Markets in Utility Photovoltaics (TEAM-UP), PV-friendly pricing effort include the City of Anaheim, the City of Austin, Arizona Public Service, Central and Southwest, Detroit Edison, New York State Electric and Gas, Northern States Power, and Wisconsin Public Service. Detroit Edison is the farthest along in developing its program. The 2-year SolarCurrents program will enable customers to pay a $6.95 monthly premium for each 100 watts of power consumed from a 28.4-kW grid-connected PV installation.

General fund programs have been implemented by several utilities, but are the least successful green-pricing program. Under this type of program, customer contributions are collected in a fund that is used to

develop renewable-energy projects. The program does not specify the development of any particular technologies or projects at the outset, but ensures that there will be an increase in the amount of renewable energy in general. Utilities involved with this type of program are Public Service of Colorado, Niagara Mohawk, Portland General Electric, New England Electric Service, and initially, Ontario Hydro. Information from the focus groups predict this result due to a lack of specific project information and directly related benefits. Due to focus group results, Ontario Hydro is examining ways to address these problems or is considering an alternative pricing mechanism.

Community-based programs are those in which customers contribute funds for the utility to develop a project that has community benefits. Traverse City Power and Light's green-pricing program is the best example. Under this program, both residential and commercial customers pay a 1.58 cent/kWh premium to subsidize the development and operation of a 600-kW wind turbine in the community. Residential customers are asked to make a 3-year commitment, where as commercial customers are asked to make a 10-year commitment (and an incentive of no fuel-related rate increases is guaranteed). The program is oversubscribed. and has a waiting list.

The Solar for Schools program, being implemented by Gulf Power, is another example of a community-based program. The program seeks not only to offset conventionally generated electricity, but also to increase the community's awareness of renewables energy and energy-efficiency technologies through the educational system.

Customer aggregation and targeting programs allow environmental stewardship benefits to be shared and municipalities to implement policy related to constituency choice. Portland General is marketing to large and wholesale customers a blend of conventional power and renewable power from two wind projects. PGE has signed one contract thus far with the City of Portland to purchase (over a 5-year period) 11.2 million kWh, or 5% of its total power consumption, from the wind projects.

Bonneville Power Administration is marketing a green power product to the public utility districts it serves. The program was set up to fund two wind and two geothermal projects that would have been abandoned otherwise. Salem Electric Cooperative has implemented a 20-year fixed contract that allows the choice of the resource mix from the four BPA renewable projects. The board of directors of Salem Electric Cooperative set a goal to have 17% of the utility's load served by renewable-energy projects, prompting the deal with BPA.

Ontario Hydro is considering similar programs such as the two mentioned above.

CONCLUSIONS

It is evident through market research and successfully implemented programs that customer preference exists for clean renewable power. The willingness to pay depends on the product, direct relation of the benefits, and understanding the utility strategy.

The successful programs are based on an overall strategy to deploy renewables, with a green-pricing mechanism as an element of the new product development. SMUD was directed by its customers to replace the decommissioned nuclear power generation with renewables and energy efficiency. New products, such as the PV Pioneer, were developed to implement this strategy. They are currently experiencing participation from customers definitively not green. Traverse City also developed a green-pricing mechanism from the original strategy of renewables deployment. Additionally, the market research reinforces this, by revealing the customer's need to understand the overall utility strategy as related to a green marketing mechanism.

REFERENCES

[1] B. C. Farhar, "Trends in US Public Perceptions and Preferences on Energy and Environmental Policy," *Annu. Rev. Energy Environ*, 1994, pp. 214,217, & 229

[2] Cambridge Reports, Cambridge Energy Research Associates, "US Public Opinion and the Electric Power Industry: Challenges of Competition," 1995

[3] Brian Nyrnes et al., "Talk is Cheap: Electric Customer Willingness to Pay for Environemntal Externalities," Colorado Renewable Energy Forum, 1995

[4] "Product Development Best Practices Report," March 1996, pp.1-2

PHOTOVOLTAIC MODULE ENERGY RATING METHODOLOGY DEVELOPMENT

B. Kroposki, D. Myers, K. Emery, and L. Mrig
National Renewable Energy Laboratory
Golden, CO

C. Whitaker and J. Newmiller
Endecon Engineering
San Ramon, CA

ABSTRACT

A consensus-based methodology to calculate the energy output of a PV module will be described in this paper. The methodology develops a simple measure of PV module performance that provides for a realistic estimate of how a module will perform in specific applications. The approach makes use of the weather data profiles that describe conditions throughout the United States and emphasizes performance differences between various module types. An industry-representative Technical Review Committee has been assembled to provide feedback and guidance on the strawman and final approach used in developing the methodology.

INTRODUCTION

Based on the results of previous energy ratings research [1], the National Renewable Energy Laboratory (NREL) has initiated an effort to develop a consensus-based approach to rating photovoltaic modules. This new approach was intended to address the limitations of the de facto standard module power rating at Standard Test Conditions (STC[1]). Using technical input from a number of sources and under the guidance of an industry-based Technical Review Committee, the approach described in this paper was developed.

This paper describes testing and computation procedures required to generate a Module Energy Rating (MER) for a particular module type and presents results from some initial validation. The MER consists of 10 estimates of how much energy a single typical module of a particular type will produce in one day, one for each of five different weather/location combinations and two load-types. Because reproduction of these exact testing conditions in the field or laboratory is not feasible, testing was limited and modeling procedures were based on a predefined data set.

The five weather/location combinations provide the basic range of environmental conditions anticipated for typical uses of PV modules in the United States.

Two load types are assumed, corresponding to the two most common loads connected to PV modules: maximum power tracking for grid-tied applications and fixed voltage for battery charging. For purposes of rating comparison, a 14.4-volt operating voltage per battery is assumed. The 14.4 V value may be divided by the recommended number of modules and multiplied by the recommended number of batteries to obtain a fixed voltage for purposes of rating. If the manufacturer does not recommend this module for battery application, then the modules need not be rated for fixed voltage. It is assumed that no charge regulation occurs; that is, the module operates at 14.4 volts whenever there is sufficient sun, and that there is no voltage drop between the PV module and battery.

MODULE ENERGY RATING COMPUTATION

The Module Energy Rating Methodology consists of measuring module characteristics, defining sets of weather and load conditions, and estimating module performance under those conditions using a combination of models. A detailed description of the ratings methodology and module characteristics is given in [2].

Figure 1 shows conceptually the flow of data and the relationships between the various models. The description will start at the right side of the diagram and work our way to the left. First, the algorithms used in each of the computational process (the circles in Figure 1) are described. Next, the input variables (the rectangles in the figure) required for each process are presented.

Model Algorithms

Energy Model: Energy is computed from the daily power production curves by numerical integration of dc power over time.

DC Power Model: The power output of the module (P) is computed from the plane-of-array irradiance (adjusted for spectral and incidence-angle effects), the module temperature, and appropriate coefficients. Ultimately this methodology will specify only one power model. For validation purposes, five models were investigated: linear interpolation, Anderson [3], Blaesser [4], and the lumped four-parameter (L4P) [5] model. Each model is required to estimate power output for maximum power and fixed-voltage conditions. The linear model depends only on irradiance. The interpolation model uses raw data from a module characterization process. The Anderson and Blaesser models use translation methods. The L4P model is an analytical model that describes a module in terms of an equivalent circuit.

---

[1] STC: 1000 W/m^2 irradiance with an Air Mass 1.5 spectrum and 25°C cell temperature.

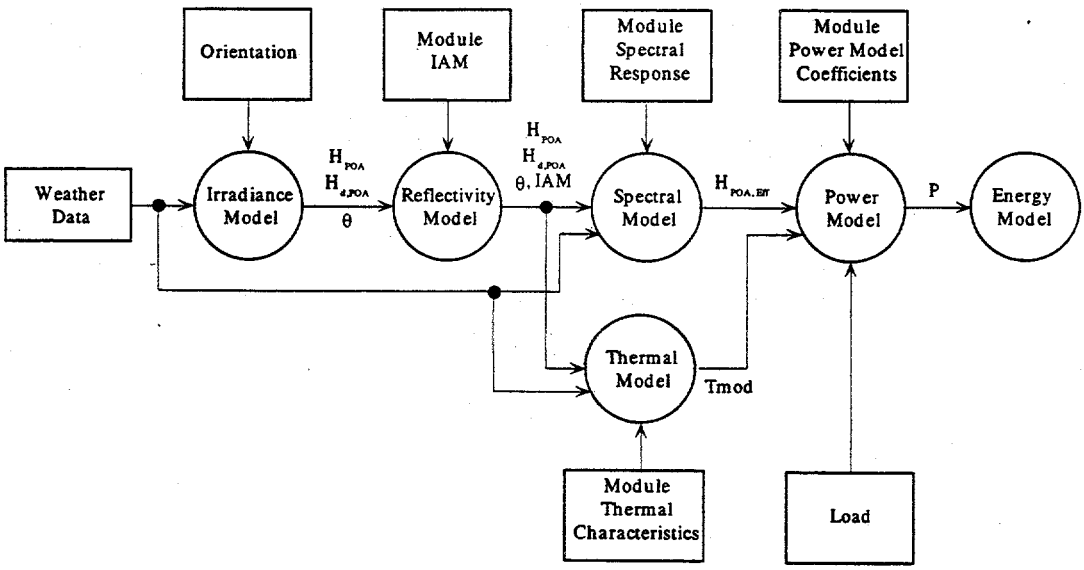

Figure 1. Model flow diagram.

Spectral Model: The spectral model adjusts both the diffuse and beam irradiance incident on the plane-of-array surface as necessary to account for variations in the incident spectrum under the assumed weather conditions. The resulting adjusted irradiances must be referenced to the flash testing spectrum and must account for the module spectral response. The general approach used is to compute the ratio of the actual effective irradiance to the reference effective irradiance, where an effective irradiance is the combined effect of a spectrum and a spectral response. This approach has been discussed Emery [6]. In order to make adjustments based on field and test spectra, these spectra need to be available. Since these data are very rare, a model is used to estimate the spectrum corresponding to the weather data set. To accomplish this, the model uses the perceptible water vapor, solar geometry, diffuse horizontal and plane-of-array (broadband) irradiances, and the beam (broadband) irradiance. In addition, two fixed data sets are required: one representing the exoatmospheric spectrum and clear-sky spectral characteristics, and the other representing a set of empirically derived spectral cloud-cover model coefficients. This model was developed by Nann and Riordan [7].

Module Thermal Model: Another explicit input to several of the PV performance models is module temperature (T_{mod}). Module output varies by roughly 0.5%/°C change in temperature. This module temperature coefficient is less for most thin-film devices and for higher-efficiency devices. The temperature of a PV module depends on module construction, module mounting, ambient conditions and conversion efficiency.

Reflectivity Model: The reflectivity model uses the plane-of-array incident irradiance angle(θ) to obtain an incidence angle modifier (IAM) that accounts for reflection effects. This IAM can be multiplied by the total plane-of-array irradiance (H_{POA}) to estimate the total absorbed plane-of-array irradiance for the thermal model, or included in the spectral model normalization computation.

Irradiance Model: The irradiance model transforms commonly available time-correlated global horizontal and direct irradiance and other weather measurements and plane-of-array orientation into incidence angle and full-spectrum incident beam and diffuse irradiance estimates using astronomical solar-position equations and the Perez diffuse radiation model [8]. The steps in these computations are: determine the true local solar time, compute the local solar position, compute the plane-of-array beam irradiance and incidence angle, and the evaluate the Perez diffuse radiation model.

Model Inputs

Module Load Type: The power output of any module depends on the voltage or current at which it is operated. Two load types representative of typical installations are specified, maximum power tracking (i.e. grid-connected) and ideal voltage source (fixed voltage).

Location: The location is specified using the latitude, longitude, and time zone.

Environmental Data: The environmental conditions include time, date, global horizontal irradiance, direct normal irradiance, ambient

temperature, dew point, relative humidity, barometric pressure, wind speed, cloud cover modifiers, and atmospheric absorption coefficients.

Module Characteristics: The module characteristic input parameters include tilt angle, azimuth angle, incident angle modifier coefficients, spectral response function, nominal operating cell temperature (NOCT), efficiency at NOCT, and temperature and irradiance power coefficients.

REFERENCE DAY DEVELOPMENT

Five reference days were selected from the National Solar Radiation Database as being representative of extreme conditions within the United States. The five reference days were selected based on the criteria listed in Table 1. The table describes four extreme days and one average day, with the set of conditions representing the various types of weather extremes found in the United States.

Table 1. Reference Day Criteria

Profile	Irrad. Peak Watts	Daytime Temp °C	Wind Speed	Relative Humidity	Cloud Cover
Sunny-Hot	>1000	>35	Low	Low	0%
Sunny-Cold	>900	<0	Avg.	High	<30%
Cloudy-Hot	<400	>30	Avg.	High	>50%
Cloudy-Cold	200 to 400	<0	High	High	>90%
Avg-Nice	800 to 900	20	Avg.	Avg.	30%

PRELIMINARY VALIDATION

This paper presents preliminary results of module energy output for five typical modules representing single-crystal silicon, polycrystalline silicon, amorphous silicon, copper indium diselenide (CIS), and cadmium telluride (CdTe). The paper compares actual energy output measured on various days at NREL with projected energy output from the same modules using the methodology described in this paper. Energy ratings based on five selected reference days will also be compared.

Figure 2 shows the % from measured energy that each module produced for a maximum-power tracking load as predicted by each of the four tested models and for five different module types. This data is based on a sunny, hot day in July in Colorado. This graph shows that although no single model was ideal in predicting energy, most predictions were within 10%. The linear model did considerably better than the rest in this specific case because it was developed from the same data that it was predicting. This linear model would not have worked as well if it was predicting energy for different types of days.

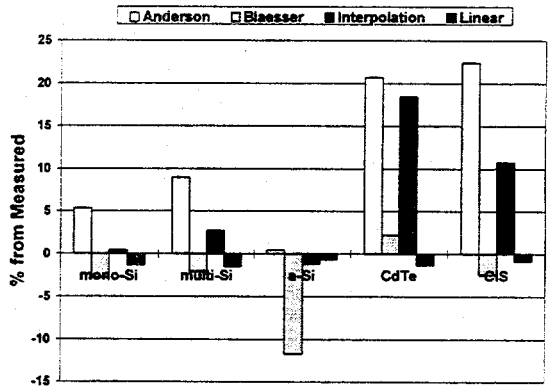

Figure 2. % from measured value of 4 power models for 5 types of modules using max-power module energy output.

Figure 3 shows the % from the measured current that each module produced for a fixed-voltage load on a clear sunny day as predicted by each of the three tested for five different types of modules. The linear model was not used because it does not apply to the fixed voltage condition.

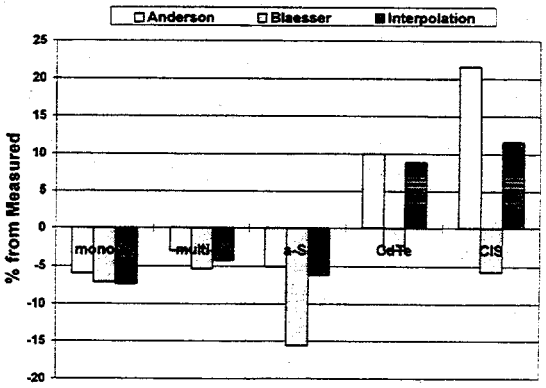

Figure 3. % from measured value of 4 power models for 5 types of modules using fixed-voltage current output.

For the most part, the models predicted energy and total current within 10%. There are some modeling problems with modules CdTe and CIS because they are research-prototype polycrystalline thin-film modules which were difficult to characterize accurately.

With appropriate models, this approach will provide a set of numbers that an end-user or a system designer can use to compare modules from different manufacturers under conditions that are similar to what the installed array will experience.

MODULE ENERGY RATING

Using the procedure outlined in Figure 1, for the reference days defined in Table 1, a module energy rating can be determined. The module energy rating will be a set of 10 numbers based on five different weather conditions and two different load conditions. An example of how this may be displayed on the back of a module is shown in Figure 4. This layout gives fictitious numbers that shows how much energy and current a module produces under the different reference conditions. The peak power energy will be given in watt-hours (Wh), while the fixed voltage current will be described in amp-hours (Ah). This terminology should be useful to the system designer. The MER approach as well as the selected reference days were approved by the TRC.

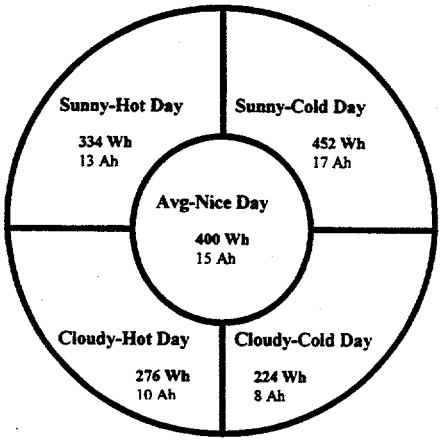

Figure 4. Sample layout for module energy rating [9].

FUTURE WORK

Continuing work is needed in several areas: model development, input data standardization, and validation of the rating methodology. Work is currently being conducted in all of these areas. Since the power models do not sufficiently address high and low irradiance conditions, power model development is necessary. Input parameters concerning fixed voltages and changing voltages as related to battery charging are still being discussed. A better thermal model needs to be defined. Also standard procedures for developing module performance characteristics (i.e. temperature and irradiance coefficients) are being developed. Selection of the standard extreme and average days is being researched. The validation of this rating methodology will take place once all parameters have been defined.

ACKNOWLEDGMENTS

The authors would like to thank Jerry Anderson from Sunset Technologies, who developed the idea of using the four extreme and one average reference day for energy comparison. He has also continued to develop new translation equations for module parameters. Thanks to Steve Rummel, Yehoshua Caiyem, and Larry Ottoson for module measurement and characterization. Finally, thanks to Richard DeBlasio and Roland Hulstrom for their continued support of module energy ratings.

REFERENCES

1. Kroposki, B. et al., "A Comparison of Photovoltaic Module Performance Evaluation Methodologies for Energy Ratings," *24th IEEE*, Dec. 1994, pp. 858-862.

2. Kroposki, B. et al., "Development of a Photovoltaic Module Energy Ratings Methodology," *13th NREL PV Program Review, AIP Conference Proceedings 353*, May 1995

3. Anderson, A. J., "Photovoltaic Translation Equations: A New Approach," Final Report for Task 1.0 of NREL Subcontract No. TAD-4-14166-01, November 1994.

4. Blaesser G. and W. Zaaiman, "On-Site Power Measurements on Large PV Arrays," *10th E.C. PVSEC*, April 1991, pp. 1240-1243.

5. Townsend T., "A Method for Estimating the Long-Term Performance of Direct-Coupled Photovoltaic Systems," MS Thesis, University of Wisconsin, 1989.

6. Emery, K. A. et al. "Methods for Measuring Solar Cell Efficiency Independent of Reference Cell of Light Source," *18th IEEE PVSC*, Oct. 1985 pp. 623-628.

7. Nann, S. ,Riordan, C. "Solar Spectral Irradiance under Clear and Cloudy Skies: Measurements and a Semiempirical Model," *Journal of Applied Meteorology*, Vol. 30, April 1991, pp.447-462.

8. Perez, R., R. Stewart, R. Seals, and T. Guertin, "The Development and Verification of the Perez Diffuse Radiation Model," Contractor Report SAND88-7030, Sandia National Laboratories, Albuquerque, NM, 1988.

9. Anderson, A. J., "An Energy Rating Concept for Photovoltaic Modules," Final Report for Task 2.0 of NREL Subcontract No. TAD-4-14166-01, March 1995.

TECHNICAL EVALUATION OF SOLAR CELLS, INC. CdTe MODULE AND ARRAY AT NREL

B. Kroposki, T. Strand, and R. Hansen
National Renewable Energy Laboratory
Golden, CO

R. Powell and R. Sasala
Solar Cells, Inc.
Toledo, OH

ABSTRACT

The Engineering and Technology Validation Team at the National Renewable Energy Laboratory (NREL) conducts in-situ technical evaluations of polycrystalline thin-film photovoltaic (PV) modules and arrays. This paper focuses on the technical evaluation of Solar Cells, Inc., (SCI) cadmium telluride (CdTe) module and array performance by attempting to correlate individual module and array performance. This is done by examining the performance and stability of the modules and array over a period of more than one year. Temperature coefficients for module and array parameters (P_{max}, V_{oc}, V_{max}, I_{sc}, I_{max}) are also calculated.

INTRODUCTION

The Engineering and Technology Validation Team at NREL conducts in-situ technical evaluations of polycrystalline thin-film PV modules and arrays. The focus of this research is on the performance of CdTe PV modules from SCI. The research team is attempting a "first effort" attempt to correlate individual module performance with array performance for this polycrystalline thin-film technology. This is done by looking at module and array performance over time. Also, temperature coefficients for different PV parameters (P_{max}, V_{oc}, V_{max}, I_{sc}, I_{max}) are determined on the module and array level. These evaluations on module/array performance and stability are conducted at the NREL Photovoltaic Outdoor Test Facility (OTF) in Golden, CO. The modules and arrays are located at 39.7 °N latitude, 105.2° W longitude and at 1782 meters elevation.

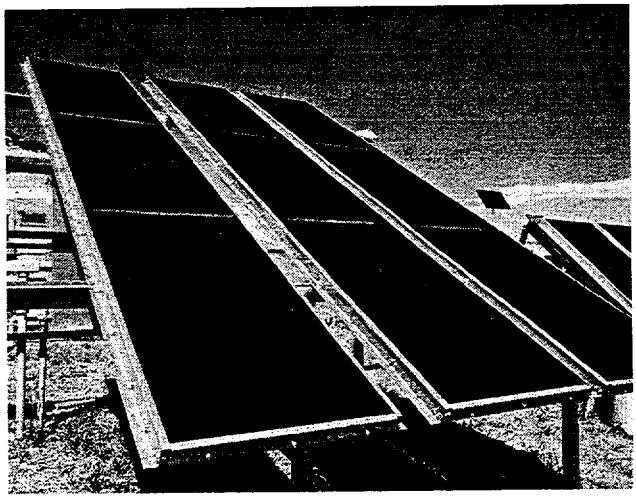

Figure 1. SCI 400-W_{dc} photovoltaic array

EXPERIMENTAL PROCEDURE

Module and Array Description

The SCI CdTe module is a glass-on-glass construction with CdS/CdTe as the active semiconductor. The modules used in this experiment were early production modules. These modules incorporate the old junction box and framing structure, which has been converted to a pigtail lead and frameless mount in new SCI designs. The modules used in this experiment had an aperture area of 0.68 m^2 (57.7 cm by 117.7 cm). Figure 1 shows a picture of the SCI array.

The individual module was installed at a 40° tilt and is loaded at maximum power during the day, except when I-V curves are taken. Data collection for this module started April 1994 and ended December 1995. The module had the following electrical characteristics prior to deployment: P_{max} = 49.3 W, V_{oc} = 89 V, I_{sc} = 0.89 A, V_{max} = 64 V, and I_{max} = 0.77 A.

The array consists of eight modules mounted at a 30° tilt and comprises two monopoles; each monopole uses four series-connected modules. The summation of module max-powers (as measured by NREL) was approximately 400 W_{dc}. The array is operated at its max-power point by an Omnion series 2200 inverter. The output of the Omnion inverter was fed to the local utility's power distribution grid. The modules in the array were deployed at intervals beginning February 1994 and ending May 1994. Data collection on the array began on July 1994 and ended July 1995. The average module from this group had the following electrical characteristics prior to deployment: P_{max} = 51 W, V_{oc} = 89 V, I_{sc} = 0.93 A, V_{max} = 65 V, and I_{max} = 0.79 A.

Individual Module Data Acquisition

Individual module performance is monitored with a multiple I-V curve-tracing unit. The unit is capable of testing up to 15 individual modules. For this experiment, the module is loaded at its maximum power point except when I-V curves are taken. These data are acquired every half hour between irradiances of 975-1025 W/m^2.

Array/System Data Acquisition

In monitoring and evaluating system performance, two sets of data are collected: instantaneous and long-term data measurements. The instantaneous array performance is monitored via a portable I-V curve tracer. These I-V traces are acquired once a month (weather permitting) at plane-of-array (POA) irradiances between 900 and 1100 W/m^2. Long-term array/system performance is monitored via a datalogger. Data collected include current, voltage, back-of-module and ambient temperatures, and POA

irradiance. Data are sampled every 5 s and are stored as 15-min averages.

RESULTS AND DISCUSSION

Solar Cells, Inc., CdTe Module Performance

Figure 2 shows the normalized P_{max} (to 1000 W/m^2) and back-of-module temperature versus time for the module. This graph shows that the CdTe module has a weak inverse correlation between P_{max} and the back-of-module temperature. This effect can be attributed to the wider bandgap of the CdTe material as compared to other polycrystalline thin-film modules. Gaps in the data occur where the data acquisition system was down, but the module remained exposed.

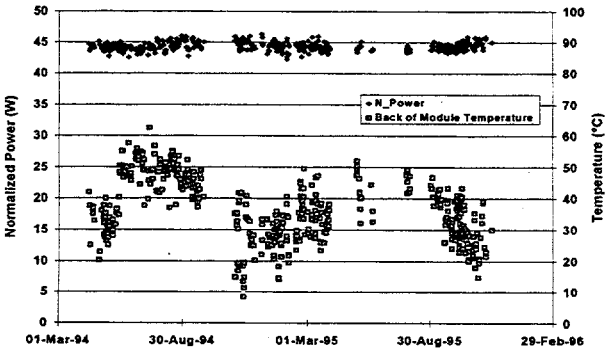

Figure 2. Normalized power and module temperature vs. time

To correct the performance data to 25°C, a temperature coefficient for the module was calculated. Using a linear regression of power (normalized to 1000 W/m^2) vs. back-of-module temperature, a temperature coefficient was calculated (Figure 3). The coefficient was obtained through a first-order regression analysis and was calculated to be -0.08 %/°C. This temperature coefficient had an R^2 of 0.2. The R^2 values are provided as a means by which to evaluate the quality or fit of the model. Given the R^2 value obtained for the P_{max} coefficient above, the coefficient will only describe 20% the variation in P_{max} due to temperature. For this module, the P_{max} and back-of-module temperature data are noisy, but the trend of the data appears valid. This module was calculated to have a P_{max} rating of 44.4 W at 25°C.

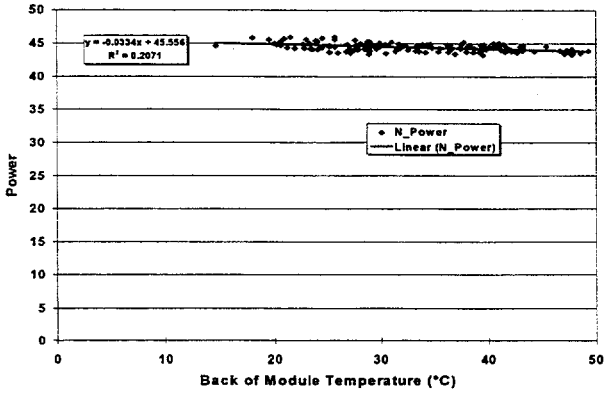

Figure 3. Normalized power vs. module temperature

Figure 4 shows the P_{max} data corrected to 25°C using the P_{max} temperature coefficient of -0.08%/C°. Because the temperature coefficient is very small, there is little change from figure 2. The figure shows that this module had good stability over the test period and that temperature has little effect on the module output.

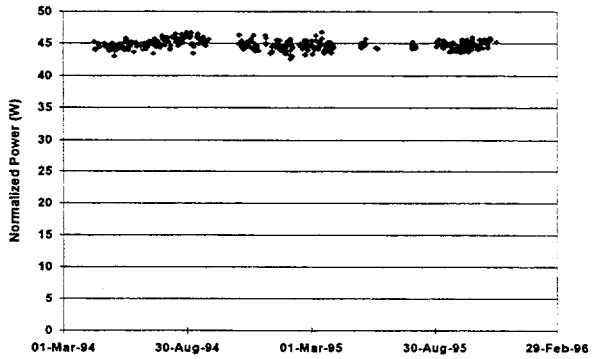

Figure 4. Normalized and temperature corrected power vs. time

To examine why the P_{max} temperature coefficient was so low, the same procedure was used to obtain temperature coefficients for current and voltage. Figure 5 shows normalized currents I_{sc} and I_{max} versus temperature. The low R^2 values and low line slope indicate that there is little correlation between temperature and current, although the I_{max} values show a slight increase with increasing temperatures. The temperature coefficients for I_{sc} and I_{max} were 0.06%/°C and 0.07%/°C respectively.

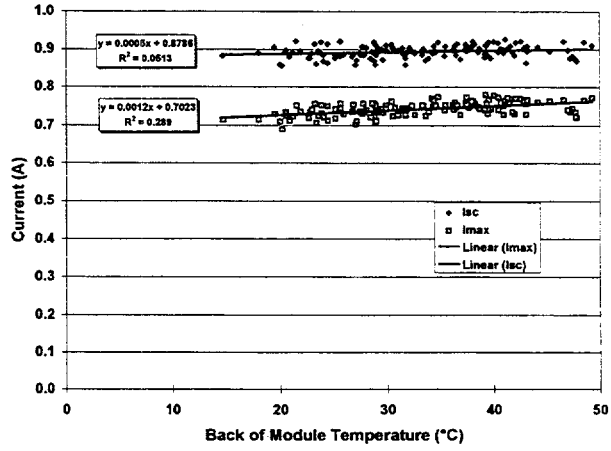

Figure 5. Normalized I_{sc} and I_{max} vs. temperature

Figure 6 shows that the voltage decreases as temperature increases for the module. This figure shows less scatter in the data compared with current and a relatively good correlation between voltage and temperature.

The temperature coefficients for V_{oc} and V_{max} were -0.24%/°C and -0.25%/°C respectively. The R^2 values were reasonably high with the data showing good correlation. Because there is a slightly negative temperature coefficient for V_{max} and a slightly positive temperature coefficient for I_{max}, this causes the temperature coefficient for P_{max} to become close to zero for this module.

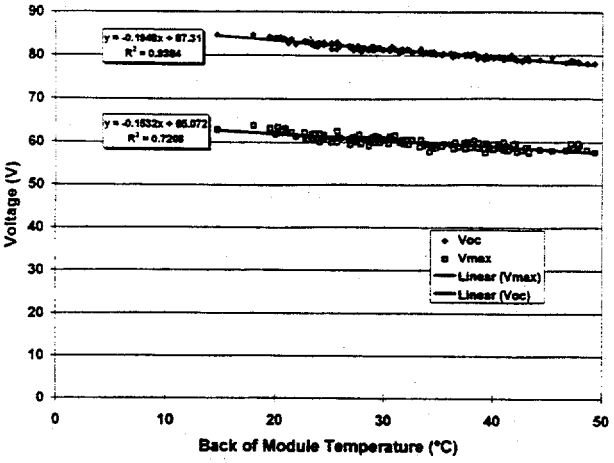

Figure 6. Normalized V_{oc} and V_{max} vs. temperature

Solar Cells, Inc., CdTe System/Array Performance

Figure 7 shows dc power, ac power, back-of-module temperature, and ambient temperature versus time for the 400 W_{dc} array. The data are fit with moving-average trend lines to aid visually in establishing any trends. The dc power before October 1994 is not shown because of problems with the data acquisition system. The data used in the figure were restricted to POA irradiance between 900 W/m^2 and 1000 W/m^2. Dc and ac power were normalized to 1000 W/m^2 for the figure. The back-of-module temperature ran at an average of 26°C above the ambient. This figure shows that temperature had little effect on ac power output at or near one-sun. However, dc power shows a weak inverse correlation with temperature. This discrepancy is possibly due to the low input level at which the 400 W_{dc} array operated the 2- kW_{ac} Omnion inverter. The figure further shows that array/system performance was relatively stable over this test period.

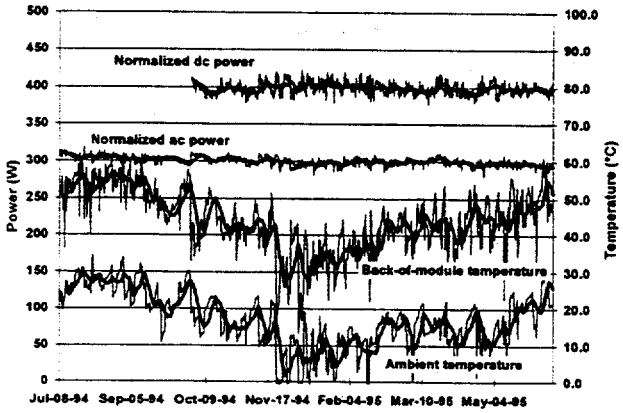

Figure 7. Normalized ac and dc power vs time

Figure 8 shows the performance of the positive and negative monopoles of the system. The temperature coefficient data are based on the performance of the two monopoles of the system.

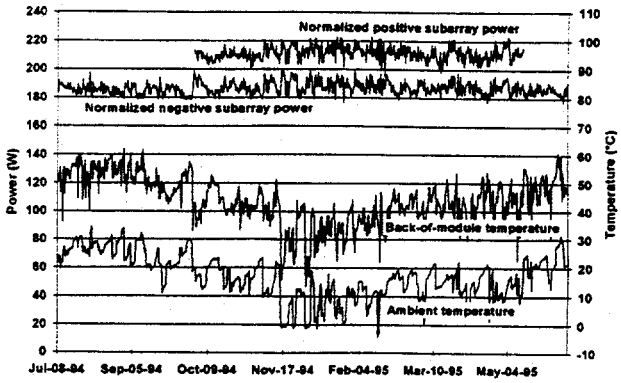

Figure 8. Normalized dc power for both monopoles

Figure 9 shows normalized power versus back of module temperature for the two monopoles. . Based on these data a preliminary temperature coefficient for P_{max} was calculated. The coefficient obtained was calculated to be -0.11%/°C and -0.16 %/°C for the positive and negative monopoles, respectively. The corresponding R^2 values for these coefficients are 0.14 and 0.33. Even though the P_{max} temperature coefficient has a low R^2, the trend appears valid.

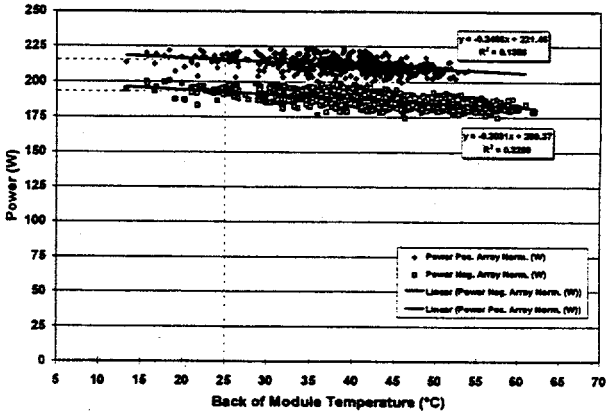

Figure 9. Normalized dc power vs. temperature

Figure 10 shows the two monopoles' dc power corrected for temperature and normalized to 1000 W/m^2 versus time. Note that the temperature coefficient used slightly reduces the variation in P_{max} due to temperature. Even though the P_{max} temperature coefficient has a low R^2, the trend appears valid.

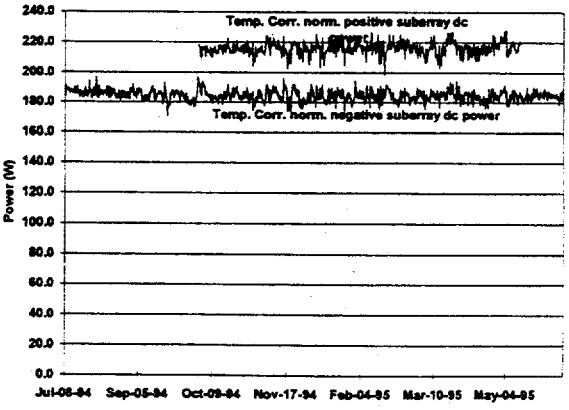

Figure 10. Normalized and temperature-corrected dc power for both sub-arrays

Again a similar approach was taken to obtain the temperature coefficients for I_{max} and V_{max}. For I_{max} the temperature coefficients were calculated to be 0.011%/°C and -0.06%/°C for the positive and negative monopoles respectively. For V_{max}, the temperature coefficients were calculated to be -0.1%/°C and -0.1%/°C for both the positive and negative monopoles. A summary of the array temperature coefficients is given in Table 1. The same type of module was examined under a pulsed-simulator indoors and was found to have a temperature coefficient for Pmax of -0.36%/°C[1]. The difference in these results show there are some artifacts when measuring CdTe under different light sources.

Table 1. Temperature Coefficients

	Module	R^2	Pos. mono-pole	R^2	Neg. mono -pole	R^2
P_{max}	-0.08	0.21	-0.11	0.14	-0.16	0.33
I_{sc}	0.06	0.05	*	*	*	*
I_{max}	0.07	0.29	0.01	0.0	-0.06	0.05
V_{oc}	-0.24	0.94	*	*	*	*
V_{max}	-0.25	0.72	-0.10	0.06	-0.10	0.06

* - no data taken

CONCLUSIONS

Temperature coefficients for P_{max}, I_{sc}, I_{max}, V_{oc}, and V_{max} for CdTe at the module and array level were calculated. Opposite signs in I_{max} and V_{max} with temperature results in a weak negative temperature dependence of -0.08%/°C for the modules power. Table 1 summarizes these results. The data were not corrected for spectrum. Therefore, these preliminary temperature coefficients could change due to spectral influences.

Temperature was shown to have little effect on P_{max}, I_{sc}, and I_{max} at both the module and array level. Temperature did show a slight effect on voltage. Both module and array/system performance were relatively stable over the test period. One note is that because these modules were made in early production runs, these coefficients may not be applicable to SCI's current CdTe module technology.

The values for temperature coefficients for P_{max} show good correlation between the module and array data. Given the low R^2 values obtained for the P_{max} temperature coefficient, these values should be examined more closely, but may be considered to be marginally acceptable because their basic trends appear valid.

The current coefficients for the module and array data are extremely small. This shows that the current is not affected very much by temperature.

The voltage coefficients for both the module and array are slightly negative. Even though the coefficients for voltage are negative, they are relatively small and this keeps the power temperature coefficient small.

There are two facts about CdTe module and array performance that show excellent promise for commercialization. Our observations show that the Solar Cells, Inc. CdTe modules have a very small temperature coefficient as compared to crystalline silicon. The CdTe modules also appear to be very stable over the time period tested. These facts show that CdTe module and array output stays very constant over periods of time. This can be very helpful when designing a system because the array output appears to be constant throughout the year.

ACKNOWLEDGMENTS

The authors would like to thank Dick DeBlasio and Roland Hulstrom for their support in module and system testing at NREL. We thank Keith Emery, Steve Rummel, and Larry Ottoson for their support in module measurement and characterization. We also thank Ken Zweibel and Harin Ullal for their work in the Thin-Film PV Partnerships. Finally, this work was supported by the U.S. Department of Energy under contract No. DE-AC36-83CH10093.

REFERENCES

[1] K. Emery, J. Burdick, Y. Caiyem, D. Dunlavy, H. Field, B. Kroposki, T. Moriarty, L. Ottoson, S. Rummel, T. Strand, and M. Wanlass, "Temperature Dependence of Photovoltaic Cells, Modules, and Systems", this conference.

ESTIMATING AND CONTROLLING CHROMATIC ABERRATION LOSSES FOR TWO-JUNCTION, TWO-TERMINAL DEVICES IN REFRACTIVE CONCENTRATOR SYSTEMS

Sarah R. Kurtz
National Renewable Energy Laboratory, Golden, CO 80401

Mark J. O'Neill
ENTECH, Inc., Keller, TX 75261

ABSTRACT

Although previous studies have measured and calculated chromatic aberration losses and proposed methods for reducing these by modifying the optics, significant work remains to be done toward understanding how to quantify the losses and how various parameters affect this loss. This paper presents an analytical definition and calculation method for chromatic aberration losses. The effects of sheet resistance of the midlayers of the cell, total irradiance, incident spectrum, cell width, and diode quality factor are studied. A method for measuring the midlayer resistance in finished cells is described.

INTRODUCTION

Although commercial concentrator systems based on two-junction $Ga_{0.5}In_{0.5}P$/GaAs cells are not yet a reality, several companies are interested in their development. Both Applied Solar Energy Corporation (ASEC) and Spectrolab have developed production capabilities of these cells for space applications and could quickly produce adequate supplies for concentrator systems. The New Millennium space flight is planned to use a photovoltaic system [1] based on $Ga_{0.5}In_{0.5}P$/GaAs cells made by ASEC and linear Fresnel lenses developed by ENTECH [2]. The success of this system could lead to widespread use of this concentrator technology in space. For terrestrial applications the cells are still quite expensive, implying the need for very high concentration ratios (1000X). Companies such as Solar Research Corporation [3], ENTECH, and EDTEK could incorporate the two-junction cells into their concentrator systems. Outdoor efficiencies of 27% have been measured [3]. However, two-junction, two-terminal devices present a special problem in that they must be current-matched to attain their best efficiencies. This implies that variations in the spectrum caused by the focusing optics are a potential problem. Development of concentrator systems using the two-junction technology depends on an ability to mitigate the chromatic aberration (CA) losses. Previously, we showed [4] that the CA losses in the ENTECH terrestrial system were significant, but could be controlled to 4% if the alignment of the system was optimal. We suggested that small amounts of CA could be controlled by lateral current flow in the layers connecting the two junctions. James proposed [5] that the CA losses could be minimized by Fresnel elements that alternately focus red and blue light or that use an optical secondary. Concentrator systems based solely on reflective optics are immune to CA losses. If any refractive element is used there will be some small CA loss that should be quantified and controlled. The purpose of this paper is to provide tools and a working knowledge of how to quantify the losses both analytically during the design phase and experimentally. Although the calculations are 1-dimensional, simulating a linear focusing element, the methods and conclusions should help to understand CA losses in point-focus systems as well.

CALCULATION METHODS

Accurate calculation of the CA loss must include the effects of various cell parameters. Fig. 1 shows a schematic of the diodes and resistors in the simplest situation, assuming a linear concentrating element. This simple model can be solved for each tandem cell voltage by adjusting the voltage at point 1. Starting with an estimate of the voltage at point 1, currents T1 and B1 are calculated and their difference defines both the current and the voltage drop for R1. Working across the network, the solution is obtained when the adjusted voltage at point 1 results in equal currents through T20 and B20.

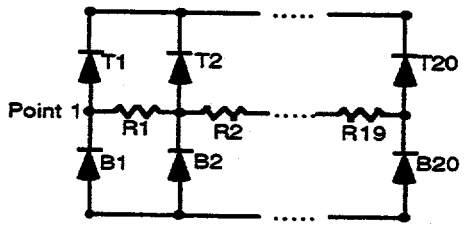

Fig. 1. Schematic indicating network of top- and bottom-cell diodes and connecting resistors. The resistors represent the combined sheet resistances of the bottom-cell emitter, the tunnel junction, and the top-cell base and are referred to in the text as the midlayer resistances or simply as sheet resistance.

Difficulties arise with this calculation in two cases: First, for tandem-cell voltages causing one or both cells to go strongly into forward bias, the voltage at point 1 must be adjusted to a very high precision, sometimes a higher precision than double-precision data storage allows. In the present study, for high sheet resistances, this problem sometimes prevented convergence at the maximum power point. Convergence is much easier in reverse bias, since

relatively large changes in voltage may cause only small changes in current. The second limitation of this method of calculation occurs when the complexity of the network is increased, i.e., when a 2-dimensional network is used. In either case an alternative calculation method involves adjusting lateral currents. This approach is much more challenging since the number of variables to be adjusted is greatly increased and the step sizes needed to adjust each current element may differ and vary exponentially as the tandem I-V curve is scanned.

Using the solution of the circuit shown in Fig. 1 for enough voltages to define the maximum power point, we propose to define the CA loss as the difference in the maximum power output from a network with all of the lateral resistances set to zero compared with the maximum power from the network of interest. It is also possible to define the loss relative to uniform flux profiles with the same average irradiance, but then losses associated with the non-uniform flux profile will also be lumped into the CA loss. A more complicated definition could be used that has the average shape of the top- and bottom-cell flux profiles, but gives equal currents to both the top and bottom cells at all locations. We choose to use the zero resistance definition both because it is convenient and because it is the one method that quantifies the CA loss and no other loss factors. This definition is very precise and convenient when calculating CA losses, but is impractical for experimental measurements. Direct measurement of the CA loss by itself is very difficult. Experimental measurement methods are discussed below.

The lateral resistances represent the combined sheet resistances of the bottom-cell emitter, the tunnel junction layers, and the top-cell base. For GaInP/GaAs cells the combined sheet resistance is usually in the range 50 - 1000 Ω/sq. Lower values should be achievable. The shapes of the bottom- and top-cell I-V curves were calculated assuming one-sun J_{sc} values of 15 mA/cm^2 and V_{oc} values of 0.95 and 1.35 V for the bottom and top cells, respectively. These values are suitable for GaInP/GaAs tandem cells. Similar results may be obtained for other materials systems, but the losses are expected to be lower for lower-band-gap materials because these have higher dark currents (lower fill factors). For the same reason, the diode quality factor has a significant effect on the CA loss. Unless otherwise noted, its value was set to unity. The effects of shunt and series resistances are discussed briefly.

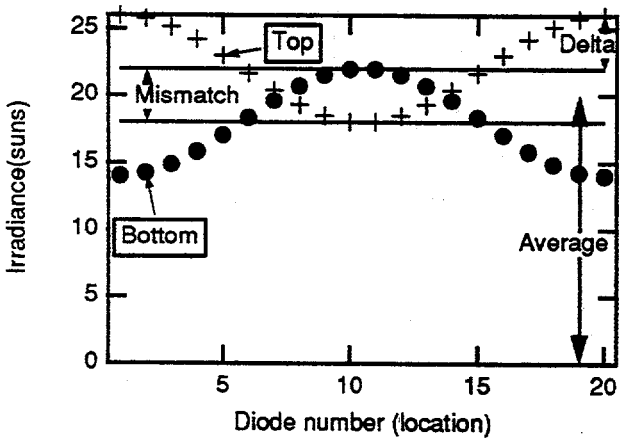

Fig. 2. Cosine-shaped flux profiles for irradiance relevant to top and bottom cells. The parameters Average, Delta, and Mismatch were varied for the calculations.

We previously [4] defined the CA loss as the difference between the powers expected for a device connected in a 2-terminal configuration compared with the 4-terminal configuration. In practice, this definition will also incorporate losses from not only CA current mismatch, but also any current mismatch that exists on average. Thus, if a cell has been optimized for operation under the AM1.5 direct spectrum and the test spectrum deviates from this standard spectrum, the cell will become current mismatched even under uniform irradiance, causing a difference between the 2- and 4-terminal powers. Thus, it is convenient to quantify the CA loss by comparison with the zero sheet resistance case, as described above.

CALCULATED RESULTS

As shown in Fig. 2, flux profiles for the 20 diodes were defined by

Flux = Average ± Mismatch/2 ± Delta cos[2π(*x*-1)/19],

where *x* is the diode number (location) and values for Average, Delta, and Mismatch are in units of suns and are shown schematically in Fig. 2.

The shape of the I-V curve was found to depend on the midlayer's sheet resistance as shown in Fig. 3. The voltage at the maximum power point first decreased since small CA losses result in I-V curves similar to what is expected for any small series resistance loss. For higher sheet resistances, the CA loss increases and the shape of the I-V curve shows an apparent shunt (see Fig. 3), causing the maximum power point to move to greater voltages. This dramatic change is caused when the subcell with the (locally) larger photocurrent is forced locally into forward bias. Bringing the tandem cell into reverse bias far enough will eventually move the forward-biased regions closer to their maximum power points, allowing for greater current collection.

For curves similar to those shown in Fig. 3, the power loss was calculated and is plotted in Fig. 4 along with data for other average irradiance values. Delta was always chosen to be 20% of average for this set of curves. In general, under close examination, a slow increase in power loss is observed for small sheet resistances. This is

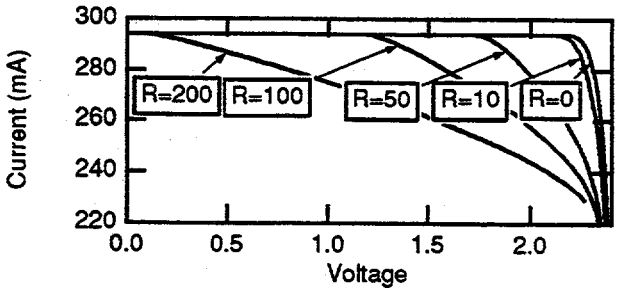

Fig. 3. Change in I-V curve shape as a function of sheet resistance, R, in units of Ω/sq for Average = 20 suns, Delta = 8 suns, Mismatch = 0 suns, and Cell width = 1 cm.

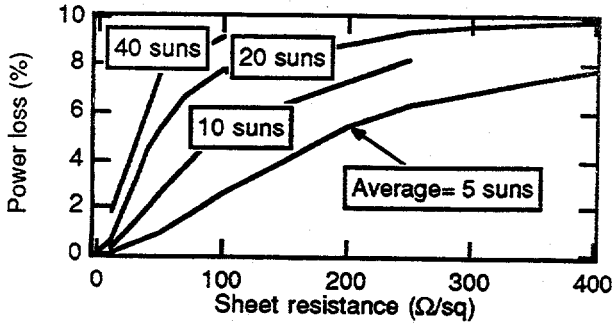

Fig. 4. Power loss from CA for various irradiance levels. Values for other parameters were Delta = 20% of Average, Mismatch = 0, and Cell width = 1 cm.

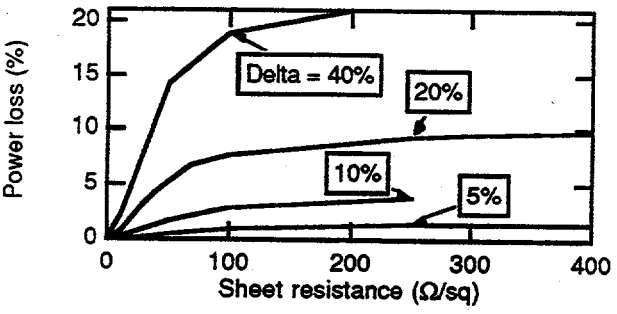

Fig. 5. Effect of size of CA on the power loss. Average = 20 suns, Mismatch = 0 suns, and Cell width = 1 cm.

the region for which the I-V curve shows an apparent small series resistance loss and a decreased voltage at the maximum power point. As local regions begin to be driven into forward bias the loss increases more steeply, eventually leveling off toward the maximum loss, about half of Delta in this case. In general, the maximum loss is obtained for infinite sheet resistance and can be estimated by adding the lower of the top- and bottom-cell currents for the 20 diodes and comparing this with the sum of all of the bottom-cell currents (or with the sum of all of the top-cell currents if that number is lower). This simple method of estimating the maximum loss from the current loss will overestimate the loss since the voltage at the maximum power point will increase slightly. The midlayer conductance needed to mitigate the power loss strongly depends on the size of the CA (see Figs. 4 and 5).

Using a mismatched spectrum, i.e., one that produces different photocurrents in the top and bottom cells on average, reduces the CA power loss, as shown in Fig. 6. Whether extra light was generated in the top or bottom cell created negligible difference when the two cells had the same diode quality factor. The smaller CA loss is a direct result of the mismatch loss, as shown in Fig. 7. The highest mismatch case has the lowest power even though it shows the smallest CA loss. When a system is limited by top-cell current everywhere, the extra bottom-cell flux distribution is unimportant.

The cell width has a large effect on the sheet resistance needed to mitigate losses (see Fig. 8). The farther the current needs to travel, the lower the sheet resistance needed to avoid significant voltage variations and forward biasing.

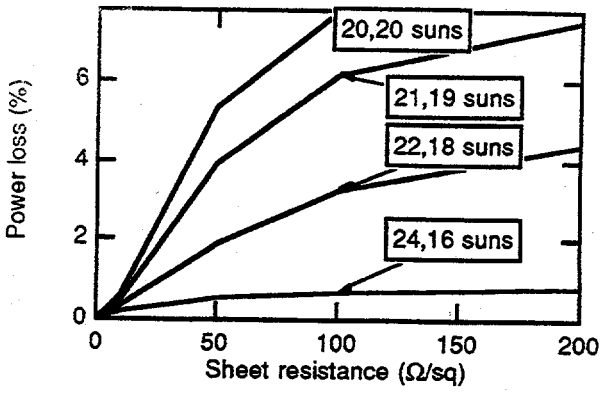

Fig. 6. Effect of current mismatch on the CA power loss; Average = 20 suns, Delta = 4 suns, and Cell width = 1 cm.

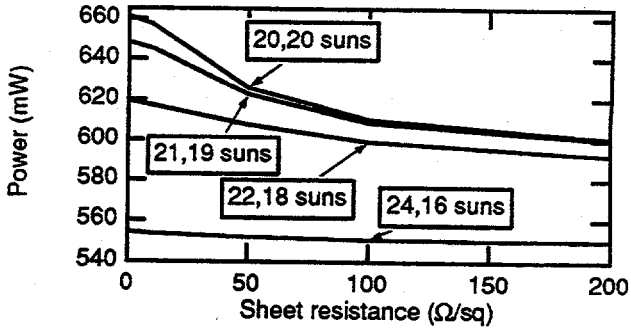

Fig. 7. Power output for mismatch values between 0 and 8 suns. Data are the same as plotted in Fig. 6.

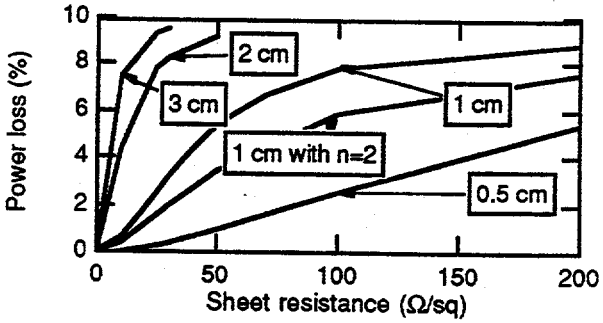

Fig. 8. Effect of cell width; Average = 20 suns, Delta = 4 suns, and Mismatch = 0. The curve labeled 1 cm with n=2 used a diode quality factor of 2.

The shape of the top- and bottom-cell I-V curves can affect the CA losses. The most important parameter is the diode quality factor. Also shown in Fig. 8 is a curve showing that the power loss is less when the diode quality factor is 2 rather than 1. This is because current changes less with voltage drops when the dark current is less steep (n=2 is less steep than n=1). Similarly, changes in temperature will affect the slope of the dark current, although less than the diode quality factor. Shunt and series resistances were included in the calculation for completeness (these are not shown in Fig. 1). However, resistors introducing power losses on the order of 1% typically changed the CA losses by 0.1% or less. Thus, it was practical to omit them in the rest of the calculations.

EXPERIMENTAL DETAILS

Measurement of the midlayer sheet resistance is demonstrated for a 1-cm-wide tandem cell. Two filters were used, one passing primarily top-cell light while the other passed primarily bottom-cell light. The fill factor and J_{sc} of the cell were measured as the filters were moved from one side to the other. Fig. 9 shows how the cell J_{sc} went through a maximum when the filter location was such that the photocurrents from the top and bottom junctions were equal. At this point, the photocurrent flowed laterally across the cell, causing the fill factor to drop by 30%. Fig. 10 shows I-V curves measured for three filter positions, including placement of only one filter over the entire cell.

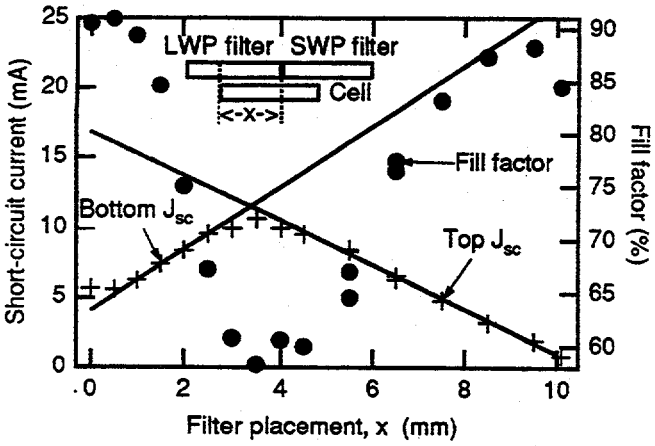

Fig. 9. Short-circuit current and fill factor as a function of the position of two filters (a long-wave pass, LWP, and a short-wave pass, SWP).

The first step in fitting the data in Fig. 10, was to determine the tandem-cell I-V curve parameters (diode quality factor, shunt resistances, etc.) by fitting dark I-V and uniform-light I-V measurements. The second step was to obtain the illumination levels of both the top and bottom cells for each of the filters. The measured J_{sc} reflects the smaller of the two photocurrents. The larger of the two currents can be obtained graphically from Fig. 9 by using the linear fits for the top- and bottom-cell J_{sc} values. The top-cell current generated under the short-wave pass filter is about 17 mA, since the 0 location corresponds to placement of the short-wave pass filter across the entire cell. In practice, the squareness of the edges of the filters (and whether the dielectric coating reaches the edge of the filter) limits the accuracy with which the currents can be measured. The parallel sheet resistance of the bottom-cell emitter and tunnel junction was measured to be 235 - 260 Ω/sq using a transmission line plated on a sister sample from which the top cell had been removed. This measurement did not include any contribution from the base of the top cell, but this contribution is believed to be fairly small for this n-on-p device. Fitting the dashed I-V curve (the curve with the lowest fill factor) and selecting the value of midlayer resistance which best fit the measured fill factor, the two-filter method gives a midlayer sheet resistance of 260 Ω/sq. This is consistent with the measured values, demonstrating the validity of the model.

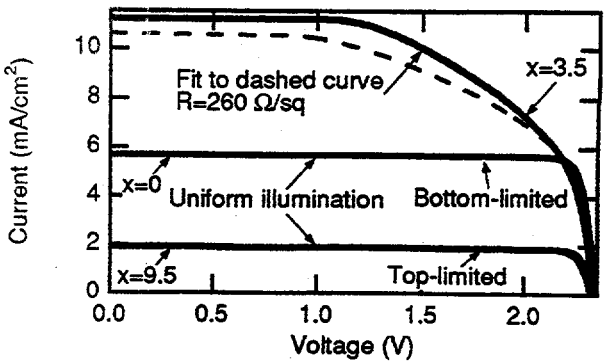

Fig. 10. I-V curves measured and calculated for the x=0, 3.5, and 9.5 data of Fig. 9. The thick lines were calculated and the thinner lines were measured. The fit for the dashed curve gives better prediction of fill factor than of current.

SUMMARY

Careful design of the focusing optics is essential to keep the size of the CA small. However, residual power loss from CA can be mitigated by lateral conduction when the sheet resistance of the midlayers is low, the size of the cell is small, and the amount of current that needs to be moved because of the aberration is small. The midlayer sheet resistance can be measured on a finished cell by shining top-cell light on one half and bottom-cell light on the other half, then modeling the resulting I-V data.

ACKNOWLEDGMENTS

We thank D. Friedman for useful discussions and C. Kramer for the sample preparation. This work was completed under DOE contract No. DE-AC36-83CH10093.

REFERENCES

[1] Jones, P.A., D.M. Murphy, D.M. Allen, and M. Piszczor, "The SCARLET Light Concentrating Solar Array," *25th IEEE Photovoltaic Specialists Conference*, 1996, this proceedings.

[2] O'Neill, M.J., "Line-Focus Optics for Multijunction Cells in Space Power Arrays," *25th IEEE Photovoltaic Specialists Conference*, 1996, this proceedings.

[3] Friedman, D.J., S.R. Kurtz, K. Sinha, B. McMahon, J.M. Olson, J.B. Lasich, A.X. Cleeve, and I. Connaughton, "On-Sun Concentrator Performance of GaInP/GaAs Tandem Cells," *25th IEEE Photovoltaic Specialists Conference*, 1996, this proceedings.

[4] Kurtz, S.R., D.J. Friedman, and J.M. Olson, "The Effect of Chromatic Aberrations on Two-junction, Two-terminal Devices in a Concentrator System", *1st World Conference on Photovoltaic Energy Conversion*, 1994, pp. 1791-1794.

[5] James, L.W., "Effects of Concentrator Chromatic Aberration on Multi-junction Cells", *First World Conference on Photovoltaic Energy Conversion*, 1994, p. 1799-1802.

HIDDEN BUT IMPORTANT PARAMETERS IN $Ga_{0.5}In_{0.5}P$ CELL GROWTH

Sarah R. Kurtz, J. M. Olson, K. A. Bertness, K. Sinha, B. McMahon, and S. Asher
National Renewable Energy Laboratory, Golden, CO 80401

ABSTRACT

Despite their best intentions, authors often omit from publications many important technical details. These omissions can lead to contradictions in the literature and inhibit researchers' abilities to duplicate published results. Here, we explore "hidden" parameters that are usually not reported, either because they are unknown (e.g., impurity levels) or because they are considered to be of little importance. Specifically we focus on the effects – and how to reduce the effects – of growth parameters in nearby layers (diffusion), impurities (oxygen), and the cool-down atmosphere (hydrogen passivation).

INTRODUCTION

$Ga_{0.5}In_{0.5}P$/GaAs two-terminal, two-junction solar cells have achieved world-record efficiencies and have been put into production at both Tecstar (Applied Solar Energy Corporation) and Spectrolab. The immediate market for these devices is in space, but terrestrial concentrator companies also have interest. Although these devices have achieved near-theoretical efficiencies, and have been studied by a significant number of groups [1-7] much remains to be understood about the $Ga_{0.5}In_{0.5}P$ top cell. In general, uniform results have been obtained, but some reports are contradictory. For example, growth of p-on-n cells with $Al_{0.5}In_{0.5}P$ windows has yielded a range of results. Wojtczuk et al. [7] reported that the $Al_{0.5}In_{0.5}P$ caused a poor contact, resulting in a low (34%) fill factor for the device, whereas Sharps et al. [2] and van Geelen et al. [6] reported fill factors of 87% and 85%, respectively. van Geelen found that thick $Al_{0.5}In_{0.5}P$ windows were necessary [6] for passivation, but most groups [2, 7] report successfully using very thin (30-nm) layers. Careful reading of these studies fails to clarify why sometimes the problem is with fill factor and sometimes with blue response (poor passivation of the front surface.) Our early studies of Al-containing back-surface-fields in n-on-p cells were unsuccessful, but later studies [4] showed that Al-containing back-surface fields *can* improve the cell. This study attempts to explain some of these contradictions and gives examples of how device results depend on factors that are unknown, uncontrolled, or unreported. Specifically, we focus on effects related to diffusion, oxygen contamination, and hydrogen passivation.

EXPERIMENTAL METHOD

The samples were grown by atmospheric-pressure (620-torr) organometallic chemical vapor deposition in a vertical-flow, quartz reactor using trimethylgallium, trimethylindium, trimethylaluminum, arsine, and phosphine in 6 slm palladium-purified hydrogen carrier gas. In-line arsine and phosphine purifiers were used. Diethylzinc in a bubbler at -33°C, 700 ppm hydrogen selenide in H_2, 100 ppm disilane in N_2, and carbon tetrachloride at -13°C were used as dopants. The cell growth conditions are described in Tables 1 and 2. We used GaAs substrates

Table 1. Growth steps used for n-on-p cells. The first 4 steps simulate steps used in the tandem cell. The Set Temp. is the requested growth temperature; the time to equilibrate within a couple of degrees of a new temperature is < 1 min.

Layer Description	Growth	Thickness(μm)	Growth Rate (μm/h)	Group V Flow (sccm)	Doping (sccm)	Set Temp. (°C)
set-up	GaAs	0.2	2.3	22 As	20 Zn	700
set-up	As	0.5 min.		22 As	10 Zn	620
set-up	GaAs	0.011	2.3	0.6 As	10 Zn	620
set-up	As	0.25 min.		4.4 As		600
tunnel junction	GaAs	0.011	2.3	4.4 As	20 C	600
back-surface field	$Ga_{0.5}In_{0.5}P$	0.05	4.4	15 P	20 Zn	600
base	$Ga_{0.5}In_{0.5}P$	0.84	4.4	44 P	6 Zn	700
i-layer	$Ga_{0.5}In_{0.5}P$	0.007	4.4	44 P		700
emitter	$Ga_{0.5}In_{0.5}P$	0.1	4.4	90 P	0.8 Se	700
window	$Al_{0.5}In_{0.5}P$	0.025	4.4	90 P	3 Se	700
cap	GaAs	0.48	6.3	4.5 As	60 Se	700
cap	GaAs	0.016	6.3	4.5 As	60 Se + 10 Si	700
delta-doped layer	As	0.5 min.		4.5 As	10 Si	700
cap	GaAs	0.01	6.3	4.5 As	60 Se + 10 Si	700
cool down	As			4.5 As		to 450

Table 2. Growth steps used for p-on-n cells. The first steps provide a way to make a back contact and were used only for samples shown in the cool-down experiment. The dopant is turned off during growth of the base because the Se flow could not be controlled in the desired range, resulting in base electron concentrations of 3-6 X 10^{15} cm^{-3}.

Layer Description	Growth	Thickness (μm)	Growth Rate (μm/h)	Group V Flow (sccm)	Doping (sccm)	Set Temp. (°C)
back contact	GaAs	0.15	1.1	3 As	8 Se	700
back contact	GaAs	0.017	6.6	4.5 As	60 Se	700
delta-doped layer	As	0.5 min.		4.5 As	10 Si	700
back contact	GaAs	0.01	6.6	4.5 As	60 Se + 10 Si	650
set-up	As	0.5 min.		4.5 As	0.8 Se	650
back-surface field	$Al_{0.25}Ga_{0.25}In_{0.5}P$	0.044	4.4	91 P	0.8 Se	650
set-up	P	0.1 min.		44 P		650
base	$Ga_{0.5}In_{0.5}P$	0.85	4.4	44 P		650
emitter	$Ga_{0.5}In_{0.5}P$	0.17,0.1*	4.4	91 P	80+,40** Zn	650
window	$Al_{0.5}In_{0.5}P$	0.025	4.4	91 P	220+,55,0 Zn	650
cap	GaAs	0.5	6.6	9 As	220+,80** Zn	650
cool down				0,100 As		

* Thickness for high-Zn data; ** Flow for low- and no-Zn data; + Flow for high-Zn and cool-down data.

misoriented by 2° to the (110) from (100), doped with Si or Zn, and prepared by etching in 2:1:10 aqueous ammonia: hydrogen peroxide: water. The contact resistances through the $Al_{0.5}In_{0.5}P$ window and the emitter sheet resistances were measured using a transmission line and a current-crowding model. The quantum-efficiency (QE) curves were measured at 0 V bias using a monochromator-based system. The samples had no anti-reflection coatings. The grids and back contacts were electroplated gold.

EFFECTS OF NEARBY LAYERS (DIFFUSION)

Diffusion during growth and cool down can have significant effects on a device. Here, we show (see Table 3) how the *emitter* sheet resistance (and, sometimes, the blue response) may depend on the doping or group V flows used for the *window* and *cap* layers for $Ga_{0.5}In_{0.5}P$ cells. If no diffusion occurs, the emitter sheet resistance should be independent of the window and cap growth; but Table 3 shows that the emitter sheet resistance does vary. When Si doping or no doping was used in the window, the emitter sheet resistance was 230-270 Ω/sq. However, when the window was doped with Se, the emitter sheet resistance was reduced. It is unclear from the data presented here why the emitter sheet resistance first decreased, then increased as the window doping (Se flow) was increased. Reduced arsine flow during cap growth reduced the emitter sheet resistance even more, implying increased diffusion, consistent with secondary-ion mass spectrometry (SIMS) data for other samples indicating that the group V flow had a significant effect on diffusion. The SIMS data have shown that the Se diffuses from the cap down into the emitter and base of the cell, piling up in the same region as zinc that diffuses in from the back [8]. Fig. 1 shows a case where the Zn and Se diffusion is obvious even though the pile-up is not seen.

Table 3. Emitter sheet resistance measured for a 0.1-μm-thick $Ga_{0.5}In_{0.5}P$ emitter doped using 0.8 sccm 700 ppm hydrogen selenide and 1.5% phosphine at 700°C. The last line gives the electron con. for a thick calibration layer.

Window/Cap Doping Flow (sccm)	Cap Arsine Flow (sccm)	Electron concen. (cm^{-3})	Emitter Sheet Resistance (Ω/sq)
10 Si/60 Se	4.5		271
0.5 Si/60 Se	4.5		264
none/60 Se	4.5	1.7e18	260
0.5 Se/60 Se	4.5		146
3 Se/60 Se	4.5		206
3 Se/20 Se	1.3	3.5e18	122
3 Se/6 Se	4.7	1.8e18	231
calibration layer		1.75e18	

Dopant diffusion in GaAs and InP is enhanced by the presence of point-defects [9-13]. (We assume that $Ga_{0.5}In_{0.5}P$ and $Al_{0.5}In_{0.5}P$ behave similarly.) The most mobile of the point defects are group III and group V interstitials and vacancies. The *equilibrium* concentrations [14] of point defects depend on the charge states of the point defects and increase with the local dopant concentration or Fermi level. Diffusion of a single carrier type in a semi-infinite material, e.g. Zn in InP, is

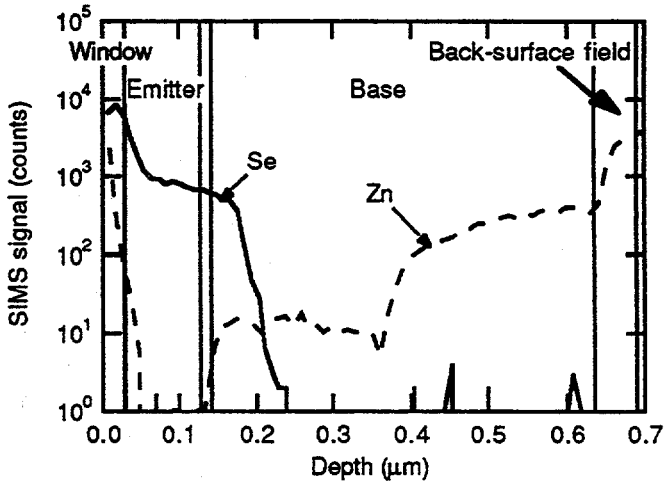

Fig. 1. SIMS scans of Zn (dashed line) and Se (solid line) for a top cell. The relative conconcentrations of Zn and Se cannot be deduced from this graph.

reasonably well understood [9,11]. Positively charged point defects like Ga interstitials form more readily in p-type material, and negatively charged group III vacancies dominate in n-type material. Diffusion of Ga interstitials causes movement of Zn atoms by the kick-out mechanism: a Ga interstitial near a Zn atom moves onto the group III lattice site, "kicking out" the Zn into an interstitial position. The Zn can then move quickly through the lattice.

In contrast, our understanding of the diffusion of multiple dopant types and point defects in multi-layered heterostructures is not complete. Several recent studies [12,13] shed some light on the problem, but do not necessarily explain all of the diffusion anomalies that we and others have observed. In general, studies of diffusion in complex systems strongly suggest that internal electric fields have a significant effect on the rate and direction of dopant diffusion. There is growing evidence that Fermi-level pinning during growth causes non-equilibrium point defect concentrations [10,12,13] when subsequent growth covers the surface layer. Specifically, during growth of the n-type cap, bulk data show that the dominate point defects are Ga vacancies. However, when the Fermi level is pinned at the surface during growth, more Ga is incorporated, giving the lower Ga vacancy concentration appropriate for the pinned Fermi level. When this surface layer is covered, the Fermi level relaxes back to its n-type position, causing a deficiency of Ga vacancies and excess of Ga interstitials. The excess interstitials move out of the n-type region and are trapped in near-by p-type regions where they are stable in their positively charged state. The excess interstitials in the p-type layer cause Zn diffusion. The Se diffusion is more directly related to group V point defect movement. Both of these are dependent on group V overpressure and we observe that increasing the group V flow in the n-type layers reduces the diffusion of both Zn and Se.

Thus, dopant diffusion can be reduced by increasing the group V flows during the cap growth or by reducing the doping levels. Other more obvious ways to reduce dopant diffusion include shorter growth times (faster growth rates), lower growth temperature, replacing group II (Zn) and VI (Se) dopants with slower-moving group IV (C or Si) dopants, and using diffusion barriers.

EFFECTS OF IMPURITIES

Oxygen-containing impurities degrade any Al-containing layers. The structures studied here contained an $Al_{0.5}In_{0.5}P$ window, causing the blue response and contact resistance through the $Al_{0.5}In_{0.5}P$ window to be sensitive to oxygen contamination. We have observed that the purity of the trimethylindium is most likely to be problematic, but that oxygen can come from anywhere. We recently found a phosphine cylinder that was so dirty it saturated the phosphine purifier. Fig. 2 shows how the unpurified, dirty phosphine (#1) cylinder degraded the blue response of a $Ga_{0.5}In_{0.5}P$ cell with a Si-doped $Al_{0.5}In_{0.5}P$ window. An unpurified, "clean" (<0.5 ppm H_2O) cylinder of phosphine (#2) caused no or very little degradation. We believe that phosphine #1 was contaminated with water. High-purity phosphine usually contains about 100X more water than O_2. To check the effect of water directly, a bubbler containing water was

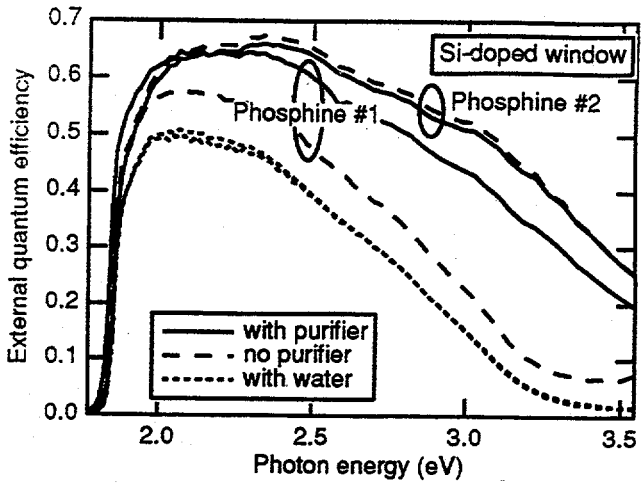

Fig. 2. QE of $Ga_{0.5}In_{0.5}P$ cells with and without a phosphine purifier for two different phosphine sources and when water was added (two different runs) intentionally by passing 0.1 sccm of hydrogen through a bubbler containing water at 3°C. The with-purifier performances differ for the two phosphine sources because the device structures were different. The top four curves were measured on two-junction ($Ga_{0.5}In_{0.5}P$/GaAs) devices.

added to the system and maintained at 3°C. A flow of 0.1 sccm through this bubbler would be expected to add the same amount of water as 10 ppm water in the phosphine. (Other experiments indicated that the transport of the water was not well controlled, and the 10 ppm number is approximate.) Fig. 2 shows the large degradation in blue response, similar to, but greater than, what was observed when the dirty phosphine was used.

If adequate Si or Se dopant was added to the window and phosphine #2 was used, the purifier had negligible effect; but if the doping was lowered, degradation was observed (see Fig. 3). Samples grown with no dopant flow for the window layer still have doped windows since the dopant diffuses in from the cap, as shown above. Previously, we had reported [8] that the blue response was improved by the use of a purifier if Se doping was used, but that a cell with a Si-doped window was unaffected by

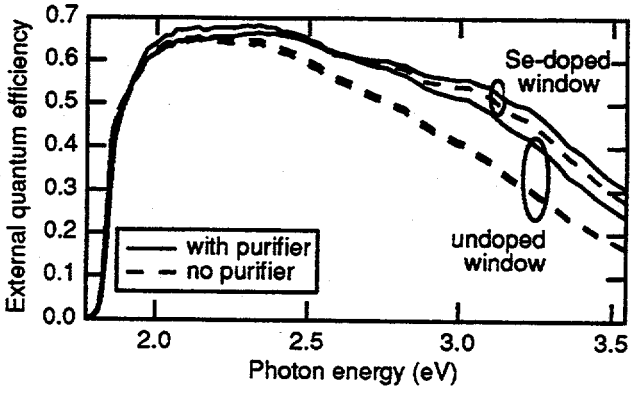

Fig. 3. QE of the $Ga_{0.5}In_{0.5}P$ cells with and without the purifier for Se-doped and undoped (two duplicate samples) $Al_{0.5}In_{0.5}P$ windows, using phosphine #2.

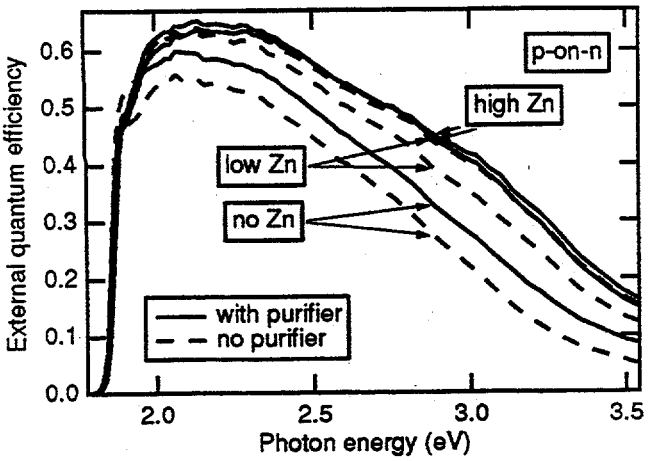

Fig. 4. QE of p-on-n $Ga_{0.5}In_{0.5}P$ cells with Zn-doped windows using phosphine #2. The Zn flows used for the window layers were varied by a factor of 4 for the high- and low-doping conditions. The high-Zn samples had 0.1-μm-thick emitters; the rest were 0.17 μm thick.

use of the purifier. From Figs. 2 and 3, we see that the identity of the dopant in the window is less important than the net free-carrier concentration.

Figure 4 shows that the blue responses of p-on-n cells with highly doped windows are also insensitive to use of the purifier. However, when the doping was reduced, some degradation was observed. When no dopant flow was used, the blue response was seriously degraded (more so than for the n-on-p case), even when high-purity phosphine was used. The blue response of p-on-n devices with undoped windows is clearly the most sensitive to oxygen, reducing the QE even near the band edge. Thus, although the blue responses of the p-on-n and n-on-p cells are affected in qualitatively similar ways by impurities, the effect of the window doping is stronger for the p-on-n case. The sensitivity of the p-on-n blue response is further complicated by the difficulty of obtaining high hole concentrations in Zn-doped $Ga_{0.5}In_{0.5}P$ and $Al_{0.5}In_{0.5}P$.

Impurities also degrade the contact resistance through the $Al_{0.5}In_{0.5}P$ window, as summarized in Table 4. The resistances for the p-on-n structures are about 1000 times greater than those for the n-on-p structures. The effect of the impurities on the contact resistance is comparable to the reproducibility of measurement for the n-on-p cells, whereas for p-on-n cells, the increase is large and potentially problematic, especially for concentrator cells. The high contact resistance is more likely to reduce the efficiency of a device than the reduced blue response, consistent with the results of Wojtczuk et al. [7].

Al-containing back-surface fields (BSFs) in n-on-p devices are also especially susceptible to oxygen. Our earlier report that AlGaInP was not a good BSF [15] became suspect when we discovered that the phosphine purifier on that system had contaminated the phosphine line, causing degradation of the blue response, and apparently the back passivation as well.

We find that a Zn-doped $Al_{0.5}In_{0.5}P$ benchmark is the best way to monitor the oxygen level. The comparable n-type benchmark is not sensitive enough. The Zn-doping is chosen to be somewhat less than what is used in the device, and the material is checked with an aqueous-semiconductor junction. Samples with semiconductor-like behavior (diode-like, light current-voltage (I-V) curves) are considered good, whereas samples that appear resistive in the light are bad (see Fig. 5).

EFFECTS OF COOL-DOWN ATMOSPHERE

We observed that p-on-n $Ga_{0.5}In_{0.5}P$ cells exhibited lower emitter doping than we would have predicted from calibration runs. The literature contains numerous reports [16-20] of hydrogen passivation of zinc-doped III-V materials. Hydrogen can be incorporated either during

Table 4. Contact resistances and emitter sheet resistances measured for the samples described in Figs. 2-6.

Description	Purifier	Contact Resistance ($m\Omega cm^2$)	Emitter Sheet Resistance (Ω/sq)	Figure
n-on-p; phosphine #1; Si-doped window	ON	0.02	240	2
n-on-p; phosphine #1; Si-doped window	OFF	0.15	253	2
n-on-p; phosphine #2; Si-doped window	ON	0.04	262	2
n-on-p; phosphine #2; Si-doped window	OFF	0.04	214	2
n-on-p; Se-doped window	water added	>100,000	?	2
n-on-p; Si-doped window	water added	27	337	2
n-on-p; Se-doped window	ON	0.01	206	3
n-on-p; Se-doped window	OFF	0.03	243	3
n-on-p; undoped window	ON	0.11	257	3
n-on-p; undoped window	OFF	0.05, 0.12	305,288	3
p-on-n; high zinc-doped (220 sccm) window	ON	20	2380	4
p-on-n; high zinc-doped (220 sccm) window	OFF	43	2820	4
p-on-n; low zinc-doped (55 sccm) window	ON	76	2850	4
p-on-n; low zinc-doped (55 sccm) window	OFF	230	2960	4
p-on-n; undoped (0 sccm) window	ON	14,000	?	4
p-on-n; undoped (0 sccm) window	OFF	>1,000,000	?	4
p-on-n; hydrogen cool down (220 sccm wind.)	ON	160	1750	6,7
p-on-n; arsine cool down (220 sccm window)	ON	1400	6350	6,7

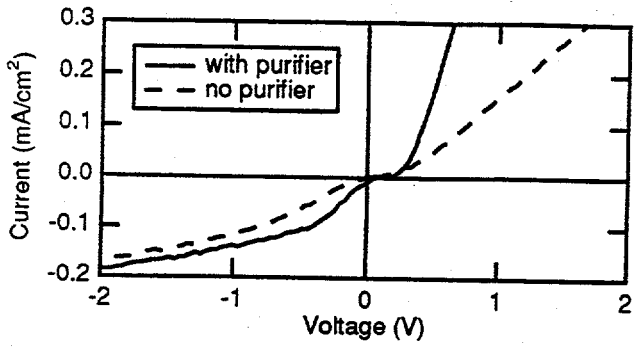

Fig. 5. Light I-V curve for a Zn-doped $Al_{0.5}In_{0.5}P$-aqueous junction. The layers were grown using 80 sccm Zn, 23 sccm of phosphine #2, and a growth rate of 4 μm/hr at 650°C.

growth or during the cool down. During cool down, arsine decomposes, providing an atomic hydrogen source. Phosphine also releases some hydrogen, but a much smaller amount. The hydrogen diffuses rapidly through a p-type GaAs cap, but is blocked by n-type GaAs. The hydrogen attaches by breaking the Zn-P bond, passivating the zinc, and reducing the hole concentration.

To test the sensitivity of the p-n $Ga_{0.5}In_{0.5}P$ cell to the cool-down atmosphere, we compared two devices grown and processed identically, except that one was cooled in hydrogen and the other was cooled in 0.9 torr of arsine in hydrogen. The arsine was switched off at 170°C for the second sample, whereas the first had no group V overpressure from the time the growth was terminated and the heat was switched off at 650°C. The cool-down atmosphere had a dramatic effect on the contact resistance through the $Al_{0.5}In_{0.5}P$ window. Fig. 6 shows the I-V curves for the two devices. The conditions for the arsine cool down were taken from a private communication with Wojtczuk, describing the arsine flow and switch-off temperature used in their report of non-ohmic conduction through the $Al_{0.5}In_{0.5}P$ [7]. They used a growth temperature of 725°C, 75° higher than used here. The fill factor they observed was 34%, lower than the 70% reported here. Wojtczuk et al. did not vary the cool-down atmosphere, so we cannot determine whether hydrogen passivation was the sole cause or only a part of their low fill factor. Their $Al_{0.5}In_{0.5}P$ was nominally doped to $10^{17}/cm^3$. The $Al_{0.5}In_{0.5}P$ used in Fig. 6, but grown as a 1-μm-thick layer, had a hole concentration of 5 X $10^{16}/cm^3$. The cool down for the 1-μm-thick layer is much less important because of the larger volume of the layer and because the calibration layer was grown on a p-type substrate that allows the hydrogen to move on into the substrate rather than being trapped in the emitter by the n-type base. The loss in fill factor is primarily a result of the increased contact resistance through the $Al_{0.5}In_{0.5}P$ window; but the emitter sheet resistance was also increased by a factor of 3 for the sample cooled in arsine, contributing to the decrease in fill factor. The contact resistance measured with the transmission line overestimates the fill-factor reduction, because the transmission line measures the average resistance for forward and reverse conduction (which, in this case, is

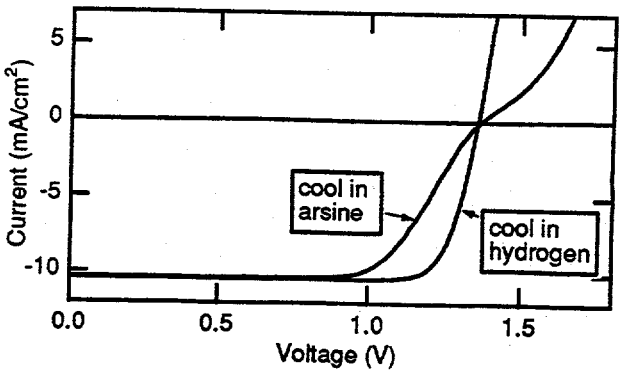

Fig. 6. I-V curves showing nonohmic behavior for the contact through the $Al_{0.5}In_{0.5}P$ for p-on-n $Ga_{0.5}In_{0.5}P$ cells cooled in different atmospheres. The grid coverage was 2%. The arsine cool down was designed after that used by Wojtczuk et al. [7].

larger than the resistance observed in Fig. 6.)

The QEs of the devices described in Fig. 6 are shown in Fig. 7. Although the short-circuit currents for these devices were identical, the QE curves show that the sample cooled in hydrogen has a better blue response (consistent with the doping dependence of the blue response shown in Fig. 4), but a lower red response. This result was reproduced on another similar set of samples. We do not have enough data to explain the change in red response.

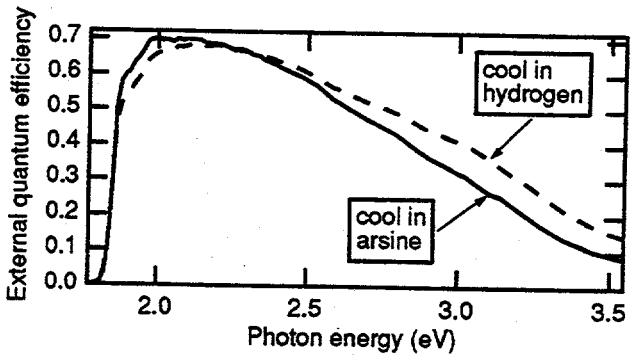

Fig. 7. QEs of devices from Fig. 6. The short-circuit currents are identical, but the loss in blue response and gain in red response for the sample cooled in arsine is reproducible.

GENERAL DISCUSSION

In addition to the three hidden parameters explored here, there are a large number of other subtle effects that are often unknown or unreported. Examples of these include the geometry of the reactor, memory effects, growth interrupts or lack of growth interrupts, and substrate/susceptor preparation. We once found that water cooling of the reactor walls increased the dopant memory effects to the point where we couldn't grow a tunnel junction. Growth interrupts have the potential for changing the surface depending on the gases flowing and the material exposed; yet omission of growth interrupts

can cause even worse effects if flows for the layer have not yet stabilized, causing growth of a mismatched or inappropriately doped layer. Cleaning or lack of cleaning of the susceptor can cause contamination from the cleaning solutions or from particulate generated by a used susceptor. Particulate from anywhere in the system tends to cause problems with $Ga_{0.5}In_{0.5}P$ growth, frequently causing shorted devices.

CONCLUSIONS

We have shown that dopant diffusion, oxygen incorporation, and hydrogen passivation can all affect $Ga_{0.5}In_{0.5}P$ devices. Dopant diffusion can be reduced by lowering the doping levels, increasing the group V flows in the n-type layers, using group IV dopants, decreasing the growth time or temperature, and using diffusion barriers. The sensitivity of $Al_{0.5}In_{0.5}P$ windows to oxygen can be reduced by increasing the doping level of the $Al_{0.5}In_{0.5}P$ window. P-type $Al_{0.5}In_{0.5}P$ is especially sensitive to oxygen, implying that it is the best benchmark and that the p-on-n cell is more sensitive to oxygen than the n-on-p cell. The failure of a p-on-n cell with oxygen contamination may be as much or more from an increased resistance through the window as from a poor blue response. Hydrogen passivation during cool down under arsine can cause similar problems even when oxygen levels are very low, but can be avoided by cooling in hydrogen. Because of all of the changes that can occur during device growth and cool down, we conclude that it is useful to characterize the layers grown in the device rather than or in addition to using separate calibration runs. Furthermore, efforts should be made to report more details of the device growth and processing.

ACKNOWLEDGMENTS

We thank C. Kramer for her tireless work on device growth and fabrication, J. Geisz for help with the growth system, and L. Roybal for his assistance. This work was completed under U.S. Department of Energy contract No. DE-AC36-83CH10093.

REFERENCES

[1] K.A. Bertness et al., "29.5%-Efficient GaInP/GaAs Tandem Solar Cells", *Appl. Phys. Lett.* **65**, 1994, p. 989.

[2] P.R. Sharps et al., "Development of p-on-n $GaInP_2$/GaAs Tandem Cells", *First World Conference on Photovoltaic Energy Conversion*, 1994, pp. 1725-1728.

[3] T. Takamoto et al., "High Efficiency InGaP Solar Cells for InGaP/GaAs Tandem Cell Application", *First World Conference on Photovoltaic Energy Conversion*, 1994, pp. 1729-1732.

[4] P.K. Chiang et al., "Large Area $GaInP_2$/GaAs/Ge Multijunction Solar Cells for Space Applications", *First World Conference on Photovoltaic Energy Conversion*, 1994, pp. 2120-2123.

[5] Y.C.M. Yeh and C.L. Chu, "Status of Multijunction Solar Cells", *SPRAT XIV*, 1995, pp. 57-64.

[6] A. van Geelen et al., "AlGaInP Windows for p on n GaInP Solar Cells", *12th EC PVSEC*, 1994, p. 1382.

[7] S.J. Wojtczuk, S.M. Vernon, and M. Sanfacon, "Comparison of Windows for p-on-n InGaP Solar Cells", *23rd IEEE Photovoltaic Specialists Conference*, 1993, p. 655.

[8] K.A. Bertness et al., "High-efficiency GaInP/GaAs Tandem Solar Cells for Space and Terrestrial Applications", *First World Conference on Photovoltaic Energy Conversion*, 1994, pp. 1671-1678.

[9] R.M. Cohen, "Application of the Charged Point-Defect Model to Diffusion and Interdiffusion in GaAs", *J. Appl. Phys.* **67**, 1990, p. 7268.

[10] D.G. Deppe, "Thermodynamic Explanation to the Enhanced Diffusion of Base dopant in AlGaAs-GaAs npn Bipolar Transistors", *Appl. Phys. Lett.* **56**, 1990, p. 370.

[11] S.N.G. Chu et al., "Concentration Dependent Zn Diffusion in InP during Metalorganic Vapor Phase Epitaxy", *J. Appl. Phys.* **78**, 1995, pp. 3001-3007.

[12] C.Y. Chen et al., "Enhanced Zn Diffusion in GaAs pnpn Structures: Growth Versus Annealing", *Appl. Phys. Lett.* **67**, 1995, pp. 1402-1404.

[13] N. Fujii et al., "Zn Diffusion Mechanism in n-GaAs/Zn-AlGaAs/Se-AlGaAs Structures", *J. Cryst. Growth*, **145**, 1994, pp. 808-812.

[14] S.B. Zhang and J.E. Northrup, "Chemical Potential Dependence of Defect Formation Energies in GaAs - Application to Ga Self-Diffusion", *Phys. Rev. Lett.* **67**, 1991, pp. 2339-2342.

[15] D.J. Friedman et al., "Back Surface Fields for $GaInP_2$ Solar Cells", *22nd IEEE Photovoltaic Specialists Conference*, 1991, pp. 358-360.

[16] G.R. Antell et al., "Passivation of Zinc Acceptors in InP by Atomic Hydrogen Coming from Arsine During MOVPE", *Appl. Phys. Lett.* **53**, 1988, pp. 758-760.

[17] Y. Nishikawa et al., "Effects of Residual Impurities on Zn Electrical Activity in Zn-Doped InGaAlP Grown by MOCVD", *J. Cryst. Growth* **123**, 1992, pp. 181-187.

[18] A. Ishibashi et al., "Suppression of Zn Diffusion Due to Hydrogen Passivation in p-AlGaInP", *Appl. Phys. Lett.* **65**, 1994, pp. 1275-1277.

[19] A. Ishibashi, M. Mannoh, and K. Ohnaka, "Annealing Effects on Hydrogen Passivation of Zn Accepters in AlGaInP with p-GaAs Cap Layer Grown by Metalorganic Vapor Phase Epitaxy", *J. Cryst. Growth* **145**, 1994, p. 414.

[20] K. Kadoiwa et al., "Mechanism of Zn Passivation in AlGaInP Layer Grown by Metalorganic Chemical Vapor Deposition", *J. Cryst. Growth* **145**, 1994, pp. 147-152.

DYNAMICS OF PHOTOEXCITED CARRIER RELAXATION AND RECOMBINATION IN CdTe/CdS THIN FILMS

D.H. Levi, B.D. Fluegel, and R.K. Ahrenkiel
National Renewable Energy Laboratory, 1617 Cole Blvd., Golden, Colorado 80401 USA

A.D. Compaan
Department of Physics and Astronomy, The University of Toledo, Toledo, OH 43606 USA

L.M. Woods
Golden Photon Inc., Golden, Colorado 80401 USA

ABSTRACT

Efficiency-limiting defects in photovoltaic devices are readily probed by time-resolved spectroscopy. This paper presents the first direct optical measurements of the relaxation and recombination pathways of photoexcited carriers in the CdS window layer of CdTe/CdS polycrystalline thin films. Femtosecond time-resolved pump/probe measurements indicate the possible existence of a two-phase CdS/CdSTe layer, rather than a continuously graded alloy layer at the CdTe/CdS interface. Complementary time-resolved photoluminescence (PL) measurements show that the photoexcited carriers are rapidly captured by deep-level defects. The temporal and density-dependent properties of the photoluminescence prove that the large Stokes shift of the PL relative to the band edge is due to strong phonon coupling to deep-level defects in CdS. We suggest that modifications in the CdS processing may enhance carrier collection efficiency in the blue spectral region.

ENHANCED PERFORMANCE OF CdS/CdTe THIN-FILM DEVICES THROUGH TEMPERATURE PROFILING TECHNIQUES APPLIED TO CLOSE-SPACED SUBLIMATION DEPOSITION

Xiaonan Li, Peter Sheldon, Helio Moutinho, and Richard Matson
National Renewable Energy Laboratory, 1617 Cole Boulevard, Golden, CO 80401

ABSTRACT

We describe a methodology developed and applied to the close-spaced sublimation technique for thin-film CdTe deposition. The developed temperature profiles consisted of three discrete temperature segments, which we called the nucleation, plugging, and annealing temperatures. We have demonstrated that these temperature profiles can be used to grow large-grain material, plug pinholes, and improve CdS/CdTe photovoltaic device performance by about 15%. The improved material and device properties have been obtained while maintaining deposition temperatures compatible with commercially available substrates. This temperature profiling technique can be easily applied to a manufacturing environment by adjusting the temperature as a function of substrate position instead of time.

INTRODUCTION

Thin-film CdS/CdTe solar cells are strong contenders for large-scale terrestrial photovoltaics, with devices and modules realizing improved efficiencies during recent years. One of the most promising techniques used to deposit thin-film CdTe is close-spaced sublimation (CSS). The CSS technique has demonstrated success in both the laboratory and manufacturing environments [1,2].

In this study, we describe a methodology that we have developed and applied to the CSS technique for thin-film CdTe deposition. By modifying and optimizing the source and substrate temperature profiles during deposition, we have significantly improved both the material properties of CdTe thin films and the performance of CdS/CdTe photovoltaic devices fabricated from these films. The influences of deposition temperature profiles on grain growth, film quality, and device performance are assessed using scanning electron microscopy (SEM), atomic force microscopy (AFM), current-voltage (I-V) measurements, and spectral response (QE) analysis.

EXPERIMENTAL

The CSS technique has been used by many groups to grow single-crystal materials as well as polycrystalline thin films [3-6]. In our CSS apparatus, the source and substrate susceptors were independently heated by quartz lamps whose output was controlled by programmable temperature controllers. The space between the source and substrate susceptors was 2 mm and was maintained using quartz spacers. The entire assembly was enclosed in a quartz tube with gas inlet and exhaust.

Temperature profiles are defined by separately controlling the source and substrate temperatures as a function of deposition time. This process can be translated to a manufacturing environment by adjusting the temperature as a function of substrate position. In this study, the source and substrate temperatures were controlled within the range of 650°-680°C and 500°-645°C, respectively. Total system pressure ranged from 10-30 Torr and was measured with a capacitance manometer pressure transducer.

The CdS/CdTe photovoltaic device configuration used in this research work consisted of Glass/SnO_2/CdS/CdTe/HgTe:Graphite and silver paste structure [7]. About 4 to 6-μm-thick CdTe films were deposited onto the Glass/SnO_2/CdS substrates by the CSS technique with a deposition rate of about 1 μm/min.

RESULTS AND DISCUSSION

Earlier work indicated that the substrate temperature (T_{sub}) during CSS deposition played an important role in determining the properties of CdTe films and devices [7]. We have observed that both the grain size and the inner grain quality are strongly enhanced by increasing T_{sub}. In addition, higher substrate temperatures led to improved device performance with increased open-circuit voltages (V_{oc}). However, we found that as T_{sub} increased to temperatures above 610°C, material properties continued to improve, but the device V_{oc} decreased sharply. Similarly, the device QE improved as T_{sub} increased up to 620°C, beyond which degradation was evident. Using a constant substrate temperature throughout the deposition (referred to as the "conventional" profile), the highest efficiency achieved for this sample set was 10.4 % [7].

Although "conventional" profiles have produced efficient devices, several critical questions remain unanswered: (i) Can improved material properties, associated with the higher deposition temperatures, be obtained without incurring the detrimental device performance effects? and (ii) Can these results be achieved while maintaining processing temperatures compatible with commercially available low-cost soda-lime

glass (where processing temperatures cannot exceed 600°C for extended periods of time). To meet these criteria, we have developed a novel temperature profiling technique that reduces the total time the substrate remains at high processing temperatures, yet retains many of the benefits associated with the higher processing temperatures (including increased grain growth and improved device performance).

"Conventional" CSS temperature profiles consist of a constant source and substrate temperature throughout the deposition. We find that by adjusting the temperature during the initial stages of deposition, we can strongly influence the film nucleation. Figure 1 shows a modified temperature profile which uses a high-temperature "nucleation" segment (T_n) in the initial stages of deposition. Figure 2 is SEM micrographs of CdTe films grown for about 1 minute and nucleated at temperatures of T_n = 620°C and T_n = 645°C (Fig. 2a and 2b, respectively). These micrographs clearly show that as the nucleation temperature is increased from 620° to 645°C, the initial grain size increases and the films become much more faceted (indicating improved crystalline quality). Unfortunately, commercial-grade glass substrates cannot withstand these high processing temperatures for extended periods of time. Therefore, the temperature must be reduced shortly after the peak nucleating temperature is obtained.

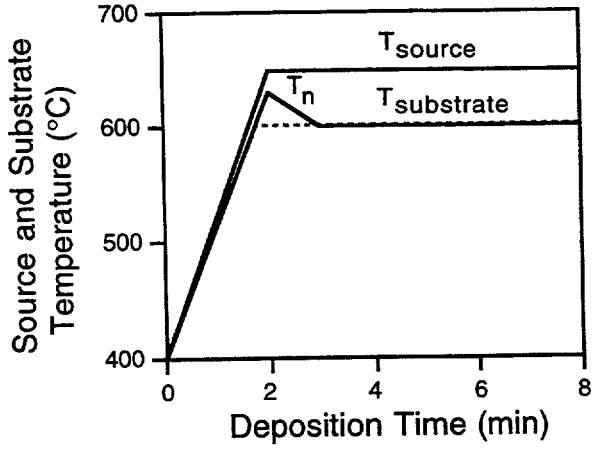

Fig. 1. Modified temperature profile used for CdTe films deposition. A high-temperature "nucleation" segment is added to the conventional profile in the initial stages of deposition.

To determine if the benefits of a high T_n could be realized if the bulk of the film is grown at a lower conventional deposition temperature, films were deposited using a variety of nucleating temperatures with profiles similar to the one shown in Fig. 1. Figure 3 shows AFM images of films deposited at a substrate temperature of 600°C, but nucleated at temperatures of T_n = 625°C and T_n = 645°C (Fig 3a and 3b, respectively). From these micrographs it is clear that, although the bulk of the film was grown at the same temperature, the T_n had a significant effect on the final grain size. For about 6-μm-thick films nucleated at 625°C, the average grain size is about 3 μm in diameter. If the nucleating temperature is increased to 645°C, the average grain size increases by a factor of 2, to about 6 μm in diameter.

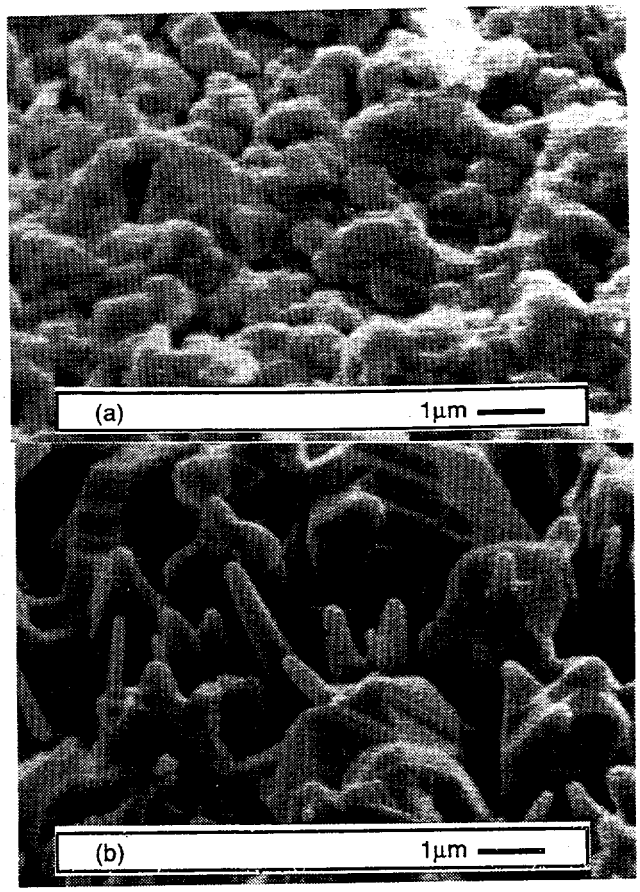

Fig. 2. SEM micrographs of CdTe on Glass/SnO_2/CdS substrate nucleated at temperatures of (a) T_n = 620°C, and (b) T_n = 645°C.

Device V_{oc} values are also strongly affected by the deposition temperature, as shown in Fig. 4. We find that using "conventional" temperature profiles (see dashed line in Fig. 4), the device V_{oc} increases steadily until a substrate temperature of 610°C is obtained. At temperatures in excess of 610°C, the device V_{oc} decreases rapidly. However, by using a modified temperature profile, similar to that shown in Fig. 1, we can extend the range and increase the maximum V_{oc}. This is shown by the solid line in Fig. 4, where the x axis now indicates the nucleating temperature T_n; the bulk of the film was deposited at T_{sub} = 600°C. Nucleating temperatures up to about 630°C can now be used before the degradation in V_{oc} is observed. From these results, it is clear that although the duration of the nucleation segment is short, it has a significant impact on device performance.

On the other hand, we find that when the ratio of the grain size to the film thickness is ≥1, pinholes are often observed. The ratios greater than one are generally

realized at the higher nucleation temperatures for the film thickness around 4 to 6 μm. The increase in the pinhole or "void" density is coupled with a decrease in the device's V_{oc}, which substantially reduces device performance. We believe that the voids are introducing shunt paths between the back contact layer and the SnO_2/CdS front contact. This would explain the rapid degradation in V_{oc}, shown by the solid line in Fig. 4.

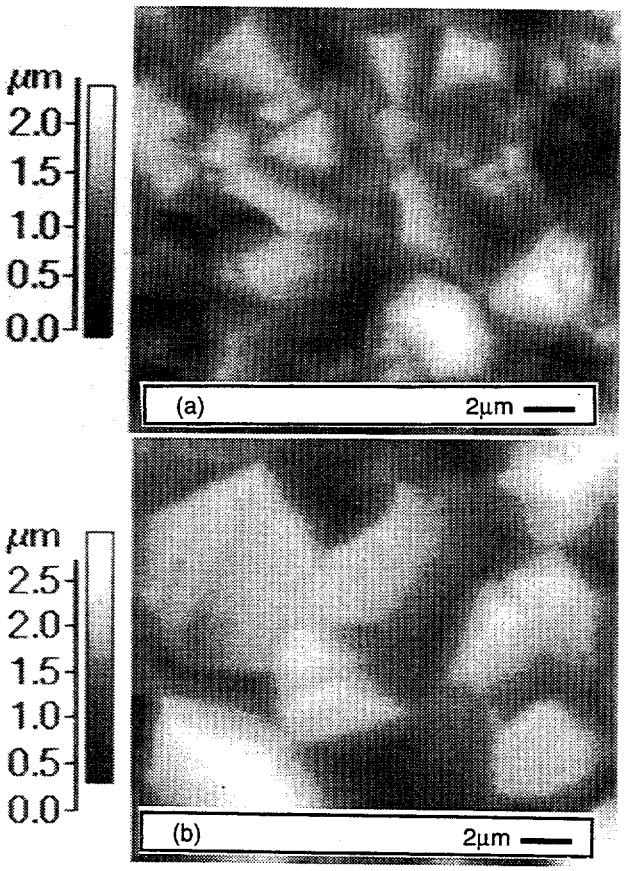

Fig. 3. AFM image of CdTe thin films deposited at a substrate temperature of 600°C and nucleated at temperatures of (a) T_n = 625°C, and (b) T_n = 645°C.

To overcome these shunting problems and maintain the benefits associated with the higher nucleation temperature, a low-temperature segment was incorporated into the profile. This low- temperature segment, called the "plugging" temperature (T_p), effectively increases the nucleation site density, forming a high density of small grains. Fig. 5 shows a pair of SEM images taken from films nucleated at 645°C and deposited at 600°C, both with and without a 525°C plugging segment. The SEM images reveal that by using a plugging temperature of 500°-550°C immediately after the higher-temperature T_n segment, secondary nucleation sites form and the void density is significantly reduced.

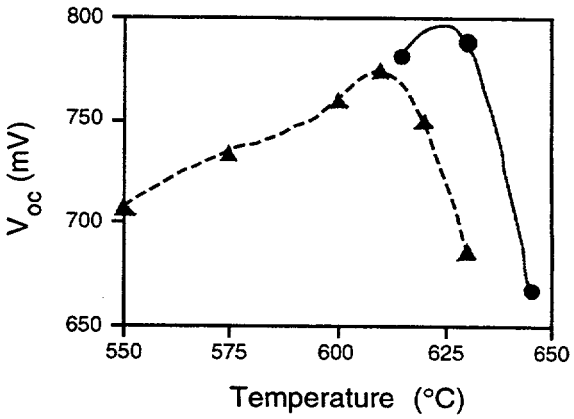

Fig. 4. The device's V_{oc} as a function of nucleation temperature with the bulk of the film deposited at T_{sub} = 600°C (solid line). Dashed line shows the V_{oc}'s as a function of constant substrate temperature profile.

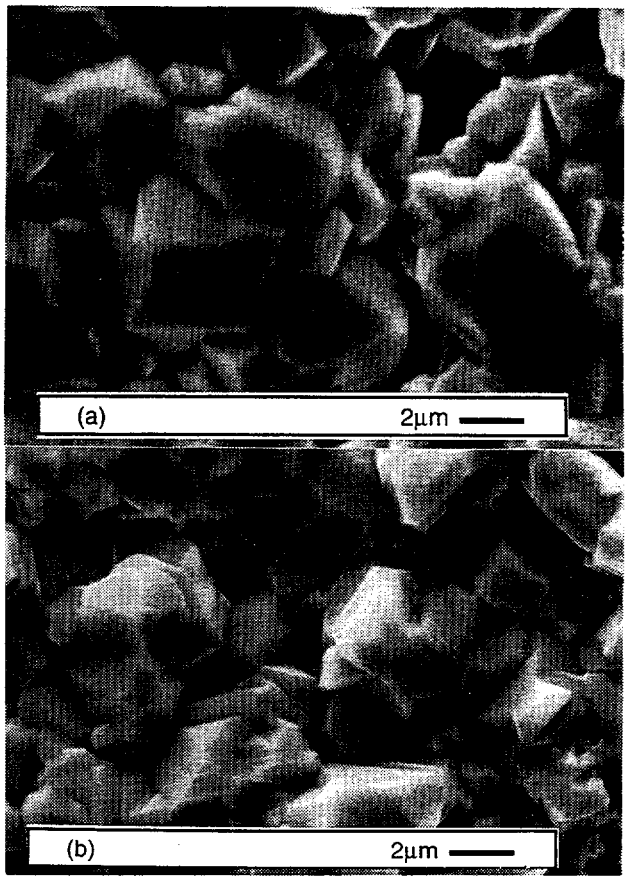

Fig. 5. SEM plane views of CdTe films taken from samples deposited with and without plugging temperature. (a) CdTe film deposited with T_n = 645°C. (b) CdTe film deposited with T_n = 645°C and T_p = 525°C.

To maintain the bulk CdTe film quality after depositing the low-temperature "plugging" segment, a third segment was added to the profile. An "annealing" segment (T_a) was introduced, resulting in the "two-wave" temperature profile shown in Fig. 6. Using the "two-wave" profile, we realized a significant improvement in device performance as compared to devices produced using the "conventional" constant temperature profile. Fig. 7 shows I-V data from two devices: one where the CdTe layer was deposited using a "conventional" temperature profile and the other deposited using the "two-wave" temperature profile. The V_{oc} and device conversion efficiency increased from 0.774 V and 10.4 % to 0.827 V and 12.0 %, respectively.

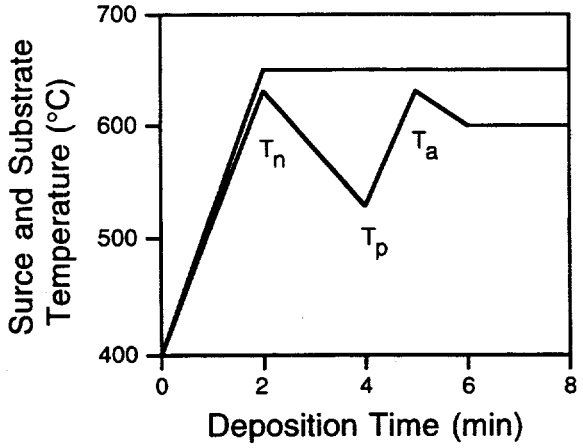

Fig. 6. The "two-wave" temperature profile used for CSS deposition, where T_n is nucleation temperature, T_p is plugging temperature, and T_a is annealing temperature.

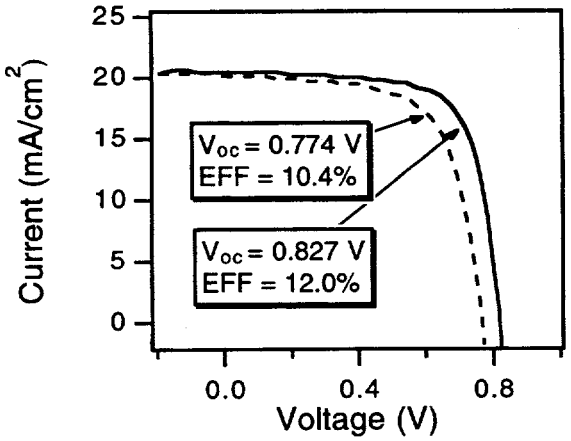

Fig. 7. Improved CdS/CdTe device performance obtained by using the "two-wave" temperature profile (solid line), compare with device performance obtained by using the conventional temperature profile (dashed line).

CONCLUSION

We have demonstrated that by modifying the source and substrate temperature profiles used during deposition, we can maintain the advantages associated with higher substrate temperatures, without suffering the detrimental effects on device performance. Our temperature profiling techniques can be used to grow large-grain material, plug pinholes, and improve device V_{oc} and efficiency. Improved material properties and device performance have been obtained while maintaining deposition temperatures compatible with commercially available substrates. Furthermore, the temperature profiling technique can be easily applied to a manufacturing environment in a technology that is nearing commercialization. Finally, modified temperature profiles have resulted in a 15% increase in device efficiency over devices produced using more conventional temperature profiles.

ACKNOWLEDGMENTS

This work was supported by the U.S. Department of Energy under contract No. DE-AC36-83CH10093.

REFERENCES

1. C. Ferekides, J. Britt, Y. Ma, and L. Killian, *Proc. 23rd IEEE Photovolt. Spec. Conf.*, (New York: IEEE, 1993), 389.

2. T. X. Zhou, R. A. Sasala and R. C. Powell, *Proc. of 13th NREL Photovoltaics Program Review Meeting,* (1996), 31.

3. F. H. Nicoll, *J. Electrochem. Soc.*, **110**, (1963), 1165.

4. J. Saraie, M. Akiyama, and T. Tanaka, *J. J. Appl. Phys.*, **11**, (1972), 1758.

5. T. C. Anthony, A. L. Fahrenbruch, and R. H. Bube, *J. Vac. Sci. Technol.*, **2(3)**, (1984), 1296.

6. T. L. Chu, S. S. Chu, S. Tang, and M. K. Mantravadi, *Solar Cells,* **21**, (1987), 73.

7. X. Li, D. Albin, S. Asher, H. Moutinho, B. Keyes, R. Matson, F. Hasoon, and P. Sheldon, *Proc. of 13th NREL Photovoltaics Program Review Meeting,* (1996), 376.

HOT WIRE DEPOSITED HYDROGENATED AMORPHOUS SILICON SOLAR CELLS

A. H. Mahan, E. Iwaniczko, B. P. Nelson, R. C. Reedy Jr., and R. S. Crandall,
National Renewable Energy Laboratory, Golden, CO 80401

S. Guha and J. Yang, United Solar, Troy, MI 48084

ABSTRACT

This paper details the results of a study in which low H content, high deposition rate hot wire (HW) deposited amorphous silicon (a-Si:H) has been incorporated into a substrate solar cell. We find that the treatment of the top surface of the HW i layer while it is being cooled from its high deposition temperature is crucial to device performance. We present data concerning these surface treatments, and we correlate these treatments with Schottky device performance. We also present first generation HW n-i-p solar cell efficiency data, where a glow discharge (GD) μc-Si(p) layer was added to complete the partial devices. No light trapping layer was used to increase the device Jsc. Our preliminary investigations have yielded efficiencies of up to 6.8% for a cell with a 4000 Å thick HW i-layer, which degrade less than 10% after a 900 hour light soak. We suggest avenues for further improvement of our devices.

INTRODUCTION

This paper describes recent device results obtained using the hot wire (HW) deposition technique. Using this technique we previously found, by raising the substrate temperature (T_S) to values higher than that used to deposit GD a-Si:H films commonly used in cells and modules, that device quality a-Si:H could be deposited for the first time with bonded H contents as little as 1 at. % [1,2]. We also observed that the saturated defect densities of these high T_S, low H content films, as measured by the constant photocurrent (CPM) technique, were significantly lower than has been previously reported [3,4]. These HW a-Si:H films were deposited at deposition rates between 4-8Å/sec. Thus, we have undertaken to incorporate this HW a-Si:H material into a solar cell. We originally attempted to incorporate a HW i-layer into a superstrate p-i-n solar cell [5], but we were unable to reach the high T_S needed to deposit the low H content a-Si:H material which has exhibited a reduced Staebler-Wronski effect. This paper details preliminary results obtained using the SS/n-i-p/ITO substrate cell approach. To explore incorporation of a high T_S HW i-layer into a substrate solar cell, we first examine the Schottky barrier structure, because this structure must be optimized in any case to optimize an n-i-p solar cell [6]. Then, results on our first generation n-i-p HW "hybrid" cells, deposited with HW n- and i-layers and GD μc-Si(p) layers, will be described. This "hybrid" device structure was chosen because we have not yet optimized deposition of a-Si(p) layers by the HW technique.

EXPERIMENTAL

The HW films were deposited in a non-load-locked, single chamber apparatus using deposition conditions described elsewhere [1,2,7]. The polished SS substrates were supplied to us by United Solar. No texturing (light trapping) layers were used in this feasibility study. The n-layers were either deposited by GD or HW. In the former case, the GD n-layers were cooled and then transferred at room temperature in air to the HW chamber, where they were heated to the T_S (360°-400°C) of the HW i-layer. Nominally, these GD n-layers sat at the elevated temperatures for 1 h before the HW i-layer deposition to insure substrate temperature uniformity and adequate chamber outgassing. When the n- and i-layers were deposited by HW in the same chamber, a purging procedure was used to attempt to minimize dopant contamination of the i-layer. After the HW i-layer deposition, the partial device was cooled, and was finished by either a Pd top contact, or in the case of the completed devices, a μc-Si(p)/ITO combination. In the latter case, the partial devices were sent to United Solar for completion. All i-layer thicknesses were typically 4000-4500 Å, with the deposition rates for all HW films ~ 8 Å/s. For the completed devices, the light soaking was done under 100 mW/cm^2 ELH light at ~40°C, and I-V measurements were done using an XT-10 simulator and a 4 probe geometry.

RESULTS

In our initial Schottky barrier study, we used GD n-layers for all devices, with an n-layer T_S of ~375°C. This elevated temperature was used to roughly match the HW i-layer T_S that we commonly used. To illustrate our expertise in the Schottky device area using a well established technology, we first made a 4000 Å thick, all-GD Schottky device, using 100% silane and a substrate temperature of 250°C for the i-layer, and demonstrated that we could obtain device parameters similar to those reported elsewhere

SAMPLE	I-LAYER CONFIGURATION	FILL FACTOR
TH ni#7	GD (4000 Å)	FF = .63
TH ni#10	GD (2000 Å) / GD (2000 Å)	FF = .61
TH ni#14	GD (2500 Å) / HW (1600 Å)	FF = .52
TH ni#11	GD (250 Å) / HW (4000 Å)	FF = .52
TH ni#9	HW (4000 Å)	FF = .51

Table 1. Schottky barrier FF under white light illumination as a HW deposited i-layer is progressively substituted for the GD i-layer. Everything else in the device (type of n-layer, air break at n/i interface, total i-layer thickness) is kept the same.

[8]. These results are shown in Table 1. Next, we deliberately introduced a room temperature air break in the middle of the GD i-layer deposition and found (FF=0.61) that this air break was not crucial to device performance, suggesting that the GD i-layer, when exposed to air at room temperature for short times, is not very reactive. We deposited this device structure to test the feasibility of transferring i-layers in a device between different deposition systems which are not connected with a load lock. In this device, the T_S of the GD i-layer deposited after the air break was raised to 350°C to roughly mimic the T_S that would be needed for the HW Schottky devices. Then, on successive depositions, we progressively substituted the (high T_S) HW i-layer for the GD i-layer, while keeping the total device thickness the same. As can be seen, when either a thin or thick HW i-layer is substituted for the GD i-layer, the device FF under white light illumination drops from >0.60 to ~0.52 and is independent of the thickness of the HW i-layer [9].

The constancy of the FF when HW i-layers of different thicknesses were progressively substituted for GD i-layers suggested that the Schottky device performance was not limited by the transport properties of the (different) i-layers, but rather by some inferior interface layer. Therefore, we decided first to vary the surface treatment of the HW i-layer as we cooled it from its high T_S and to correlate these surface treatments with device performance. In other words, we wanted to investigate the deposition procedure used to fabricate the i/Pd interface. In this investigation, HW n-layers were used for all the devices. A partial summary of these results is shown in Table 2. As can be seen, stopping the HW i-layer growth completely and cooling the SS/n-i structure in vacuum produces a device with a very low FF, while various surface treatments during cooling yield a significant FF improvement. Fig. 1 shows SIMS H profile measurements on two selected devices with widely varying surface treatments. As can be seen, without any special procedures (i.e., stopping the HW growth and cooling in vacuum), a significant amount of H diffuses out of the sample during cooling, particularly near the surface, producing a device with a very poor (white light) FF (0.27), while a surface treatment designed to address this problem adds H to the surface and produces a device with a significantly higher FF (0.60). Our best HW results to date for our low H content, high T_S, high deposition rate HW material yield a FF of 0.65 and a V_{OC} of 0.54. These device parameters compare quite favorably to those for our best GD devices deposited in the same deposition reactor, which have a white light FF of 0.63 and a V_{OC} of 0.51.

We now report on the device performance, including the results of light soaking measurements, of our first generation n-i-p HW "hybrid" devices, which were made in collaboration with United Solar. In these devices, the n- and i-layers were both deposited by HW in the same chamber, since in our initial study no significant difference was found in devices fabricated with either GD or HW n-layers [10]. Based on published results, a state-of-the-art GD SS/n-i-p/ITO device with a 4000Å i-layer and no light trapping would have an initial efficiency of ~

SAMPLE	SURFACE TREATMENT PROCEDURE	WHITE FILL FACTOR
TH ni#12	COOL IN VACUUM	FF = .27
TH ni#31	COOL IN LOW PRESSURE OF SILANE	FF = .46
TH ni#54	DEPOSIT THIN LOWER T CAP W/O BREAKING VACUUM	FF = .50
TH ni#21	VERY SLOW DEPOSITION WHILE COOLING	FF = .52
TH ni#46	COOL DURING ENTIRE I-LAYER DEPOSITION	FF = .57
TH ni#126	PRESENT SURFACE TREATMENT	FF = .65

Table 2. Typical FF values of HW deposited devices as a function of i-layer surface treatment while the complete device is cooled from its high T_S. The i-layer thickness of all devices is ~4000 Å.

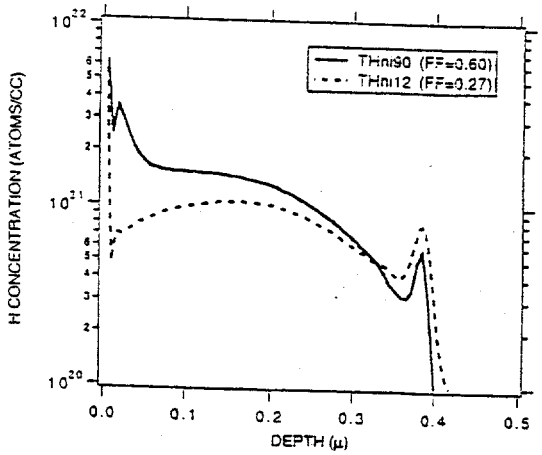

Figure 1. SIMS H depth profiles for two HW Schottky barrier devices subjected to different surface treatments during cooling.

7.8 % and would degrade after 600 h light soaking under one sun by ~16%, to an efficiency of ~6.5% [11]. Note that changes (reduction) in all three I-V parameters were reported when this GD test device was light soaked. These results have been corroborated at NREL, using our XT-10 Simulator, on a standard United Solar device kindly sent to NREL for ananysis. Table 3 shows the I-V results for a typical HW device, both in its initial state, and after having been light soaked for 887 h. The range in Jsc is representative of the spread in the 11 (out of 12) active devices which were measured. The primary change in the I-V parameters, measured after the light soaking, is seen to be in the FF. The Voc changed minimally over the course of the light soaking, and we observed no measurable decrease in the device Jsc. As a consequence, the overall device efficiency degraded by ~10%. Other HW "hybrid" devices fabricated by the same procedure degraded by a similar amount. This degradation compares quite favorably to changes reported in GD n-i-p devices containing i-layers of similar thickness [11].

The major differences in the initial state between the GD and HW "hybrid" devices are in the values of the Voc (0.94 vs. 0.88 V) and the white light FF (0.66 vs. 0.605). Addressing first the issue of the differences in Voc, we suggest that the lower Voc for the HW "hybrid" device is due primarily to the lower Tauc's bandgap of the high T_S HW i-layers (1.65-1.70 eV), compared with those of GD i-layers deposited with hydrogen dilution (> 1.70 eV) . Indeed, the Voc of a second HW "hybrid" device, with the HW i-layer deposited at a lower T_S (280°C) and thus exhibiting a higher bandgap, exhibits a similarly high Voc (0.93 V). Therefore, we suggest that the feasibility of depositing a μc-Si(p) layer on a high T_S HW a-Si:H i-layer has been successfully demonstrated, as seen by the high Voc of our "hybrid" device.

We now address possible reasons for the low white light FF of the HW "hybrid" device compared to its GD counterpart, when both are measured in their initial states. Several indicators point to the need to reexamine the fabrication of the device n/i interface, rather than being concerned about and probing the quality of the HW i-layer in the device itself. First, if the low FF's in our devices are due to high HW i-layer defect densities, then thinner Schottky devices should have higher FF's, and we do not observe this within the i-layer thickness range 2000-8000 Å. Further, we fabricated a HW Schottky device with an i-layer thickness of 1.5 μ. Using a cutoff filter (> 610 nm), we measured the red light FF in this device under high illumination intensity (>5 mA/cm2). The FF we observed (0.54) is much higher than that predicted (<0.50) using AMPS modeling and standard AMPS parameters; the only way to explain this high value for such a thick device is to assume a low bulk defect density (< 1 x 10^{16} cm^{-3}) and a narrower valence bandtail (39 mV). Note that this modeling prediction is consistent with the enhanced hole mobilities recently reported in our low H content HW material by time of flight measurements [12].

Second, SIMS P depth profiles of representative devices, in which the HW n- and i-layers were (again) deposited consecutively in the same chamber, show consistent tailing of the dopant into the i-layer. A representative profile is shown in Fig. 2. We observed that wide variations in our gas purging procedure, ranging from a weekend pump to a 5 min purge between deposition of the HW n- and HW i-layers, made little difference in either the SIMS P profiles or the device FF's. We now believe that we had inadequate "burial" of the P on the chamber walls before we deposited the i-layer, due primarily to the geometry of the shutter used for device fabrication. We are now redesigning our next generation HW reactor to address this problem.

Finally, we acknowledge the use of H

THDni113	as grown	887 hr light soak
white FF	.605	.545
Voc (V)	0.88	0.86
Jsc (mA/cm2)	11.0 to 12.8	no change
efficiency (%)	6.81 (best)	6.13 (best)
% change		- 10%

Table 3. Light soaking data for a typical SS/n(HW)-i(HW)-μc-Si(p)(GD)/ITO device. No measuring mask was used to define the area, and thus determine the samplke Jsc.

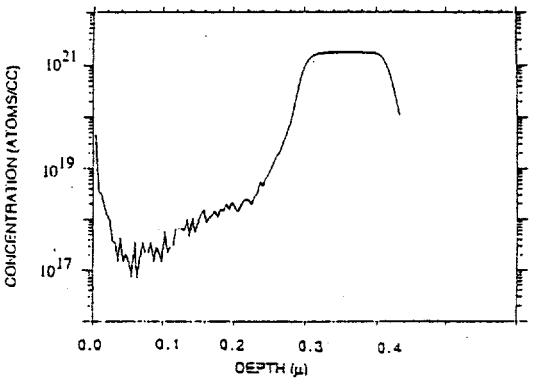

Figure 2. SIMS P depth profile for a typical HW Schottky device, where the HW n- and i-layers were deposited consequtively in the same deposition reactor.

dilution to deposit the i-layer in GD SS/n-i-p device fabrication [11], and note that such dilution seems necessary only to fabricate the n/i interface, and need not be used throughout the GD i-layer [13]. In particular, an increase in the low light intensity red FF from 0.63 to ~0.70 has been achieved in a 4000 Å thick GD Schottky device by depositing 200 Å of H diluted a-Si:H at the n/i interface, with the rest of the i-layer deposited using 100% silane. We are currently exploring the possibilities of using H dilution with the HW deposition, and also of using a GD n/i structure, with the thin, initial GD i-layer deposited using H dilution and the rest of the i-layer deposited by HW using our standard conditions.

CONCLUSIONS

We present device performance data, including the results of light soaking, on our first generation HW "hybrid" SS/n-i-p/ITO solar cells, where the n- and the i-layers were deposited by HW and the μc-Si(p) layer by GD. No light trapping layers were used in this initial feasibility study. We show that we can fabricate high efficiency substrate solar cells, where the n- and i-layers are deposited by HW at high substrate temperatures and at high deposition rates. A major consideration in obtaining the reported solar cell efficiencies is the procedure used to treat the top surface of the HW i-layer while it is cooling from its high deposition temperature. When this is taken into account, initial solar cell efficiencies as high as 6.8% can be achieved, and the amount of device degradation compares quite favorably with published reports of GD cells with similar i-layer thicknesses. Finally, we discuss research avenues in device fabrication which, in our opinion, will result in further improvements in HW "hybrid" devices.

ACKNOWLEDGMENTS

We thank S. E. Asher for SIMS measurements, Y. Xu for GD device fabrication, V. Dalal and S. Hugedus for QE measurements, and A. C. Gallagher for valuable support and many stimulating discussions during the entire course of this work. The work at NREL was supported by the U. S. Department of Energy under Contract No. DE-AC36-83CH10093, and the work at United Solar was supported in part by NREL under subcontract No. ZAN-4-13318-02.

REFERENCES

[1]. A. H. Mahan, J. Carapella, B. P. Nelson, R. S. Crandall, and I. Balberg, *J. Appl. Phys.* **69**, 6728 (1991).

[2]. A. H. Mahan, B. P. Nelson, S. Salamon, and R. S. Crandall, *MRS Symp. Proc.* **219**, 673 (1991).

[3]. A. H. Mahan and M. Vanecek, *AIP Conference Proc.* **234**, 195 (1991).

[4]. R. S. Crandall, A. H. Mahan, B. P. Nelson, M. Vanecek and I. Balberg, *AIP Conf. Proc.* **268**, 81 (1992).

[5]. B. P. Nelson, E. Iwaniczko, R. E. I. Schropp, A. H. Mahan, E. C. Molenbroek, S. Salamon, and R. S. Crandall, *Proc. 12th European PV Solar Energy Conference*, 679 (1994).

[6]. A. H. Mahan, B. P. Nelson, E.I waniczko, Q. Wang, E. C. Molenbroek, S. E. Ashewr, R.C. Reedy Jr., and R. S.Crandall, *AIP Conf. Proc.* **353**, 67 (1995).

[7]. E. C. Molenbroek, E. J. Johnson, and A. C. Gallagher, *Proc. 13th European PV Solar Energy Conference*, 1995, in press.

[8]. X. Deng, S. J. Jones, J. Evans and M. Izu, *MRS Symp. Proc.* **377**, 803 (1995).

[9].When these initial HW Schottky barrier structures were made, we were in fact, due to our initial shutter design, continuing to grow very slowly during the i-layer cooling, so the FF's of these HW devices mirror that of device TH ni#21 in Table 3.

[10]. We believed at the time that an air break at the n/i interface, necessitated by the fabrication of the n- and the i-layers in different deposition systems, was more detrimental to device performance than possible trace P contamination in the HW i-layer when both layers were deposited in the same deposition system.

[11]. S. Guha, J. Yang, S. J. Jones, Y. Chen and D. L. Williamson, *Appl. Phys. Lett.* **61**, 1444 (1992).

[12]. Q. Gu, E. A. Schiff, R. S. Crandall, E. Iwaniczko, A. H. Mahan and B. P. Nelson, *Proc. 1996 MRS Spring Meeting*, in press.

[13]. Q. Wang and Y. Xu, private communication.

CELL SHUNT RESISTANCE AND PHOTOVOLTAIC MODULE PERFORMANCE

T.J. McMahon, T.S. Basso, and S.R. Rummel
National Renewable Energy Laboratory, Golden, Colorado 80401

ABSTRACT

Shunt resistance of cells in photovoltaic modules can affect module power output and could indicate flawed manufacturing processes and reliability problems. We describe a two-terminal diagnostic method to directly measure the shunt resistance of individual cells in a series-connected module non-intrusively, without de-encapsulation. Peak power efficiency vs. light intensity was measured on a 12-cell, series-connected, single crystalline module having relatively high cell shunt resistances. The module was remeasured with 0.5-, 1-, and 2-ohm resistors attached across each cell to simulate shunt resistances of several emerging technologies. Peak power efficiencies decreased dramatically at lower light levels. Using the PSpice circuit simulator, we verified that cell shunt and series resistances can indeed be responsible for the observed peak power efficiency vs. intensity behavior. We discuss the effect of basic cell diode parameters, i.e., shunt resistance, series resistance, and recombination losses, on PV module performance as a function of light intensity.

BACKGROUND

The continuing search for new materials and change in manufacturing processes to reduce cost and improve photovoltaic module performance requires a complete set of techniques for measuring and forecasting the performance of such devices. Energy rating methods now being considered to rate module output take into account module performance at low light levels [1-5]. Such a rating is far more useful for predicting module performance throughout the day than the commonly used maximum power efficiency or peak power for a module under standard test conditions (1 kW/m^2, 25 C, AM1.5 global spectrum) alone. Low shunt resistance, R_{sh}, reduces peak power efficiency when illumination levels fall below 1 kW/m^2. When intensity levels fall, as on cloudy days or when the sun is lower in the sky, low cell R_{sh} becomes an increasing concern.

Acquiring absolute R_{sh} values for individual cells is important for: (i) Qualification testing – cell-by-cell values for R_{sh}, rather than the gross module output, lets us know which cell(s) is degrading module performance after fabrication or qualification or other accelerated stress tests; (ii) Module performance testing – R_{sh} allows us to define the light intensity at which each cell will stop contributing to the module output; (iii) Failure analysis – R_{sh} of each cell measured non-intrusively in a failed module. De-encapsulation will alter cell properties, making it impossible to determine the location of the failure. Other cell-by-cell evaluation techniques are also available [6-8] and have been discussed elsewhere [9].

If a cell has very low shunt conductance, i.e., high shunt resistance, the slope of the light current-voltage (I-V) curve through zero-bias, $\sigma_{I\text{-}V}$, will be determined by the voltage-dependent carrier collection efficiency, i.e., recombination. Electrical shunts caused by manufacturing flaws such as scribe line errors, material deposition problems, or mechanical handling contribute to an increased shunt conductance in the dark, σ_{sh}. If a cell has high shunt current, $\sigma_{I\text{-}V}$ will be dominated by the effect of these shunt currents. It is important to know whether $\sigma_{I\text{-}V}$ is controlled by recombination or by electrical shunts, because these are entirely different physical mechanisms. If $\sigma_{I\text{-}V}$ is controlled by recombination, cell peak-power efficiency will increase with a reduction in light intensity. If $\sigma_{I\text{-}V}$ is controlled by electrical shunts, cell peak-power efficiency will fall with a reduction in light intensity[10].

The R_{sh} of a series-connected module can easily be measured between manufacturing steps by contacting individual cells. However, after a module is encapsulated, we can measure R_{sh} of individual cells only by methods such as our new two-terminal technique [9]. This two-terminal diagnostic method allows one to directly measure R_{sh} of the individual cells within a series-connected module non-intrusively, without de-encapsulation. Being a phase-sensitive, lock-in technique, individual-cell R_{sh} values are measured over a wide range, from a fraction of an ohm to thousands of ohms. This method has been used on amorphous Si, crystalline Si, CdTe, and $CuInSe_2$-based modules, some with as few as 8 cells in series, but usually with 28 to 118 cells. "Two-terminal values" are more accurate for cells that have lower shunt resistance, i.e., the "problem" cells. Cells with visual defects may be a significant problem if they provide a substantial shunt path.

We also show that knowing R_{sh} allows us to accurately predict the performance of a series-connected module as a function of light intensity. We study the peak power performance of a 12-cell, series-connected, monocrystalline Si module before and after connecting shunt resistors (0.5-2 ohms) across each cell. These low R_{sh} values can be the result of new emerging technologies, processing flaws, or the result of a module undergoing stress testing. These modules, as well as the 12-cell test module, show losses in the experimentally observed peak-power module efficiencies vs. light intensity, which can be explained by low R_{sh} values. Due to manufacturer sensitivity to public release of such data, we can only present data for our 12-cell test module.

TWO-TERMINAL TECHNIQUE

We now describe our method to measure the individual-cell shunt resistances in finished two-terminal, series-connected modules [10]. Figure 1 shows the two-terminal measurement equipment configured with a series-connected module having N cells. The procedure is as follows: (1) Set up a circuit consisting of a 1-10-Hz low-frequency AC voltage source (signal generator), a DC voltage source, and an operational amplifier connected to a phase-sensitive lock-in amplifier. (2) Calibrate the system by connecting a 1000-ohm resistor in place of the module and adjusting the AC voltage (approx. 2-5 mV) to get a reading of 1 mV on the lock-in amplifier output. (3) Reconnect the module and adjust the DC voltage so that the module is biased to the open-circuit voltage, V_{OC}, for the light conditions under which the module will be tested (sunlight through a window–about 30 mW/cm^2– is adequate). (4) With the module exposed to constant, uniform light, simultaneously apply both DC and AC voltages to the terminals of the module. The lock-in amplifier measures the AC current passing through the module at V_{OC}. This current is proportional to the conductance of the module in the light where the I-V curve passes through the voltage axis. The inverse of this conductance is the resistance of all cells in series at V_{OC} in the light, R_A, in ohms if the lock-in amplifier output in mV is divided into 1000. (5) Sequentially darken the i^{th} cell in the module with an opaque tape or rubber mat. Adjust the DC voltage to the new open-circuit condition and again divide the lock-in amplifier output in mV into 1000 to obtain $R_B{}^i$. Finally (6), the difference $R_C{}^i = R_B{}^i - R_A$ is exactly the difference of the resistance of the i^{th} cell in the dark minus the resistance of the i^{th} cell in the light.

The equations in the upper right summarize steps 4-6 for obtaining cell shunt resistances. If $R_B{}^i \gg R_A$, then $R_C{}^i$ is the shunt resistance of the i^{th} cell. If $R_B{}^i$ is nearly the same as R_A, then from experience we have found that $R_C{}^i$ is still the shunt resistance of the i^{th} cell even though it cannot be proven so mathematically.

Step 4: $R_A = \sum_{1}^{n} R_i^{light}$

Step 5: $R_B = \sum_{1}^{n-ith} R_i^{light} + R_i^{dark}$

Step 6: $R_C \equiv R_B - R_A = R_i^{dark} - R_i^{light}$

If $R_B \gg R_A$, then $R_C = R_i^{dark} - R_i^{light} \approx R_i^{shunt}$

If $R_B \sim R_A$, then cell i is shunted;
by experience, $R_C \approx R_i^{shunt}$

We verified this shunt measurement method on a 40-cell Si test module where individual-cell contact could be made. The individual-cell shunt resistances measured by the "two-terminal method" are shown in Fig. 2 and can be compared to the individually contacted cell values shown in Fig. 3. Cell 29 intermittently shorted and, when shorted, measured 0.33 ohms and 0.42 ohms as shown in Figs. 2 and 3, respectively. Comparing Figs. 2 and 3 shows that the two-terminal method works well for most cells; however, for cells with higher resistance values, we find systematically lower values. We believe incomplete darkening of covered cells more greatly affects and reduces the apparent resistance of the higher resistance cells shown in Figs. 2 and 3. Even though we make the opaque covering larger than the cell, some light can still find its way into the junction region of the masked cell.

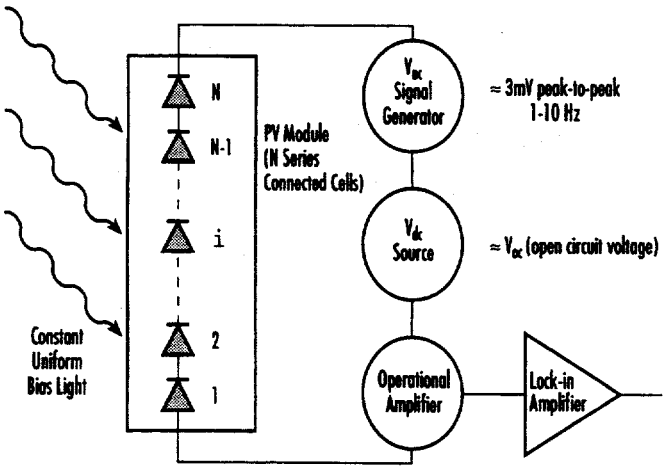

FIGURE 1. Two-terminal measurement equipment connected to a PV module. The system is calibrated by inserting a 1000-ohm resistor in place of the module and adjusting the AC signal generator so that a 1-mV output is achieved from the lock-in amplifier.

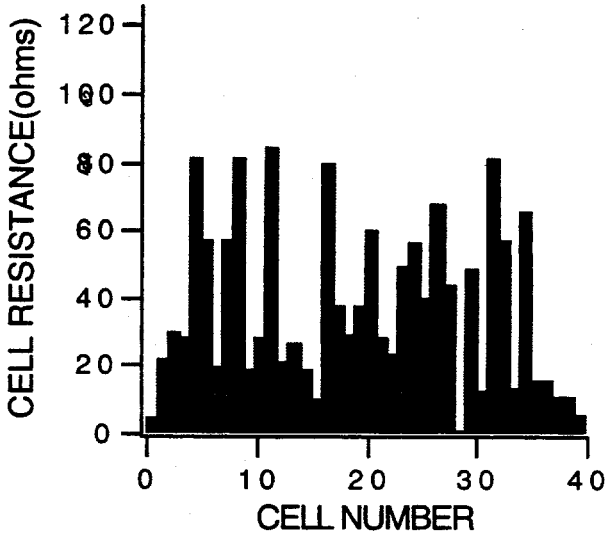

FIGURE 2. Individual-cell shunt resistances of a 40-cell test module by the two-terminal technique. Cell # 29 has a shunt resistance of 0.33 ohms.

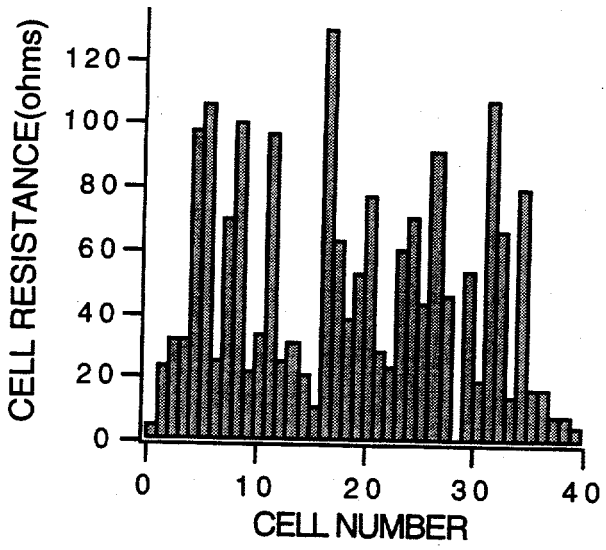

FIGURE 3. Individual-cell shunt resistances of a 40-cell test module by individual cell contact. Cell # 29 has a shunt resistance of 0.42 ohms.

MODULE PERFORMANCE

Many module peak-power efficiencies have been characterized as a function of light intensity to see what efficiencies would be expected at reduced light intensity as a result of shunt losses. Because of the proprietary nature of these kind of data, only the data measured on the single-crystal silicon module can be discussed. This module had three parallel strings with 12 cells in each string. One string was then isolated to perform the tests. The module was configured to have access to each of the 100 cm^2 cells.

Figure 4 shows how the 12-cell module was tested with a xenon pulse solar simulator (SPIRE 240A). Performance (I-V) curves were taken with 1000 W/m^2 (1-sun) illumination and no shunt resistance added. Intrinsic R_{sh} values are between 38 and 272 ohms/cell. A filter was

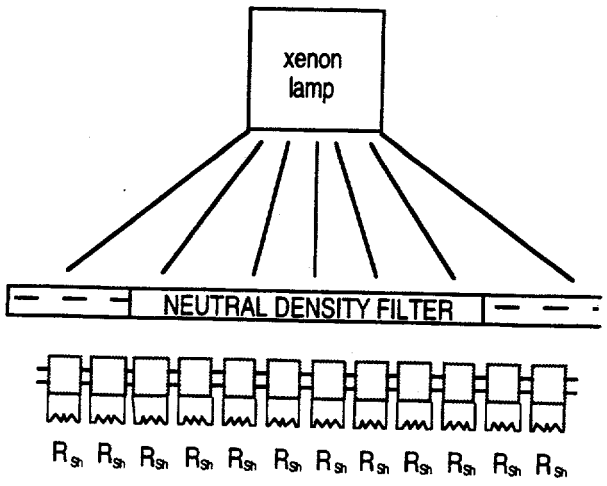

FIGURE 4. Measurement setup for peak-power efficiency

constructed using sheets of drafting film (Herculene), which was placed over the sample to provide different illumination levels. Changing the number of sheets from 18 down to none, allows us to measure performance at 9%, 15%, 25%, 35%, 50%, 75%, and 100 % of 1-sun (1% error).

We chose to connect shunt resistors having values of 0.5, 1, and 2 ohms across each cell in this study because we have observed these values on cells in modules under development. These values of resistance were placed across each cell to demonstrate the values of cell shunt resistance that might be found for real cells made with emerging technologies. Half-ohm shunt resistors were placed across each cell in the string, and the modified module was remeasured as before. The above procedure was then repeated with 1- and 2-ohm shunt resistors. These cell shunt resistance values are typical of the range of values found for the 100- to 150-cm^2 cells in series-connected modules from emerging technologies.

Figure 5 shows peak-power efficiencies vs. light intensity for this module compared to the unshunted module. The 1-ohm shunts reduced the measured peak power by 22% at the 100% of 1-sun condition and by 82% at the 9% of 1-sun condition. The 2-ohm shunted cells caused decreases of 9% and 66%, respectively, of the peak-power efficiency as compared to the intrinsic shunted condition. The situation is worst when the 0.5-ohm resistors were used under 100% and 9% illumination: efficiency decreased by 32% and 91%, respectively.

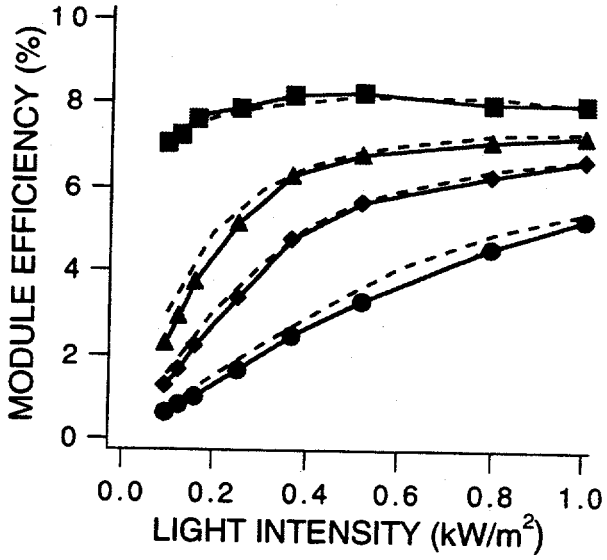

FIGURE 5. Measured (points) and calculated (dashed line) peak-power efficiencies v. light intensity for the intrinsic module(top curve), and for the 2-, 1-, and 0.5-ohm cell shunt conditions(lower curves).

MODELING

Calculations were performed using the PSpice Electrical Circuit Simulator to see if R_{sh} losses alone can explain the experimentally observed peak module efficiencies vs. light intensity. The 12-cell module had intrinsic individual-cell shunt resistances of 141, 154, 217,

272, 242, 210, 250, 224, 215, 260, 38.8, and 150 ohms. The series resistance of the module is approximately 0.5 ohm. We arbitrarily chose to distribute the 0.5-ohm series resistance by assigning a value of 0.040 ohms/cell. The forward dark current of a cell was measured and approximated by a single exponential with a saturation current of 3×10^{-5} A and a diode quality factor, n = 1.7, despite the fact that there was a low-voltage range where n = 2.08 and a high-voltage range where n = 1.2. The intrinsic 12-cell Si module data shown by the top data points and solid lines in Fig. 5 are to be compared to the calculated dashed line that approximately follows the same points. The fit was obtained with only *one* adjustable parameter--the short-circuit current, I_{sc}, is set to 2.3 A. Using the actual I_{sc} of 2.05 A produced poorer fits.

Next, using PSpice, we calculated the artificially shunted module peak-power efficiencies using the same fixed parameters as determined above, except that R_{sh} values were set to 2, 1, and 0.5 ohms/cell to match the three shunt situations seen in Fig. 5. The excellent agreement allows us to make firm conclusions about the effect of R_{sh} on the energy output, and allows us to confirm or predict the impact that cell shunt resistance will have on module performance using PSpice calculations.

The effect that shunts have on module performance when illumination levels fall below 1 kW/m^2 is striking. A shunt path in a cell only carries so much current. A cell with a shunt path may work at very high light levels, but as light intensity is reduced, such as on cloudy days or during daylight hours when the sun is lower in the sky, the shunt path will carry some or all of the cell's photocurrent away from the intended load. Hence, the energy rating of a module with high cell shunt current will be lower than expected from the standard efficiency usually reported under AM1.5 global illumination conditions. If no shunts were present, there would be no losses in efficiency as light intensity drops. If only recombination losses or series-resistance losses were present, module efficiency would *increase* as the light intensity decreases.

In general, both types of losses occur, and $\sigma_{I\text{-}V}$ is determined by shunt and recombination losses; the mixed case will yield losses in both high- and low-intensity regimes. The impact of these losses on module energy ratings is clear. Modules having identical AM1.5 global I-V curves can have very different energy ratings. In the first case, where $\sigma_{I\text{-}V}$ is determined by shunt losses, the energy rating will be substantially lower (due to the poorer performance at lower light levels) than in the second case, where $\sigma_{I\text{-}V}$ is determined by recombination losses. Hence, cell shunt resistances within a module are important parameters to measure.

CONCLUSIONS

We have demonstrated an accurate method to measure individual shunt resistances while the series-connected module is still intact. This non-intrusive technique is useful for qualification testing, failure analysis, and module performance characterization.

Measurement and calculation show how a cell's shunt resistance diminishes the module power output capacity under operational conditions where light levels are reduced, as they are in real-world conditions. Shunt losses are contrasted with recombination losses with regard to the impact on a module's energy rating. Cell shunt resistances within a module are important parameters that need attention.

ACKNOWLEDGMENTS

We would like to thank R. DeBlasio, K. Emery, and J. Burdick for their involvement and encouragement. This work was conducted within the PV Module and System Performance and Engineering Project under U.S. Department of Energy contract No. DE-AC36-83CH10093.

REFERENCES

[1] Gay, C.F., Rumburg, J.E., and Wilson, J.H., "'AMPM'--All-day Module Performance Measurements," *Proc. 16th IEEE Photovoltaic Spec. Conf.*, 1982.

[2] Gonzalez, C.C. and Ross, R.G., "Energy Prediction Using NOCT-Based Photovoltaic Reference Conditions," *Proc. Ann. Am. Sol. Energy Soc. Conf.*, 1983.

[3] Heidler K., Raicu, A., and Wilson, H., "A New Approach for the Performance Evaluation of Solar Cells Under Realistic Reporting Conditions," *Proc. 21st IEEE Photovoltaic Spec. Conf.*, 1990.

[4] Raicu, A., Heidler, K., Kleiss, G., and Bucher, K., "Annual and Seasonal Energy Rating of Mono-Si, a-Si, and GaAs Test Cells for the USA by the RRC Method," *Proc. 22nd IEEE Photovoltaic Spec. Conf.*, 1991.

[5] Kroposki, B., Emery, K., Meyers, D., and Mrig, L., "A Comparison of PV Module Performance Evaluation Methodologies for Energy Ratings," *Proc. 24th IEEE Photovoltaic Spec. Conf.*, 1994.

[6] Abete, A., F. Cane, C. Rizzitano, M. Tarantino, and R. Tomnasini, 1991, "Performance Testing Procedures for Photovoltaic Modules in Mismatching Conditions," *Proc. IEEE PV Specialists Conf.*, p. 807.

[7] Maire, J., B. Theys, and P. Baruch, 1981, "Detection of a Defective Cell in a Solar Module through Photoresponse Modulation," Proc. *IEEE PV Specialists Conf.*, p. 1134.

[8] Baruch, P., B. Benghanem, B. Leroy, C. Picard, and J.A. Roger, 1984, "Analysis of Photovoltaic Generators by Modulated Light Excitation of Individual Cells: Application to Testing and Detection of Faulty Cells," *Proc. IEEE PV Specialists Conf.*, p. 621.

[9] McMahon, T. J., and Basso, T. S., "Two-Terminal Diagnostics for Cells in Series-Connected Photovoltaic Modules," presented at the ASME International Solar Energy Conference, Lahaina, HI, Mar 19-24, 1995.

[10] McMahon, T. J., and Bennett, M. S., "Film Morphology, Excess Shunt Current and Stability in Triple-Junction Cells," presented at the MRS Meeting, San Francisco, Spring 1992.

BENEFITS FROM THE U.S. PHOTOVOLTAIC MANUFACTURING TECHNOLOGY PROJECT

Richard L. Mitchell,[1] C. Edwin Witt,[1] Holly P. Thomas,[1] Lloyd O. Herwig,[2] Douglas S. Ruby,[3] Clay C. Aldrich[4]
1 National Renewable Energy Laboratory, Golden, CO; 2 U.S. Department of Energy, Washington, D.C.;
3 Sandia National Laboratories, Albuquerque, NM; and 4 Solar Energy Industries Association, Washington, D.C.

ABSTRACT

This paper examines the goals of the Photovoltaic Manufacturing Technology (PVMaT) project and its achievements in recapturing the investment by the photovoltaic (PV) industry and the public in this research. The PVMaT project was initiated in 1990 with the goal of enhancing the world-wide competitiveness of the U.S. PV industry. Based on our analysis, PVMaT has contributed to PV module manufacturing process improvements, increased product value, and reductions in the price of today's PV products. An evaluation of success in this project was conducted using data collected from 10 of the PVMaT industrial participants in late fiscal year (FY) 1995. These data indicate a reduction of 56% in the weighted average module manufacturing costs from 1992 to 1996. During this same period, U.S. module manufacturing capacity has increased by more than a factor of 6. Finally, the analysis indicates that both the public and the manufacturers will recapture the funds expended in R&D manufacturing improvements well before the year 2000.

BACKGROUND

The Photovoltaic Manufacturing (PVMaT) project was started in 1990 to help U.S. industry extend its world leadership role in manufacturing and commercially developing PV modules and systems. It is a U.S. Department of Energy/U.S. industry cost-shared program that focuses on identifying and improving manufacturing processes that affect the cost and production of PV modules and systems. Each candidate project is evaluated on its own technical merit and its promise for contributing to the PVMaT goals, independent of the technology being proposed or of other projects that might be selected for funding. Furthermore, organizations interested in the various photovoltaic technologies have been equally eligible to respond to the procurements and to make their case for participation in this manufacturing technology project.

PVMaT was designed to help the U.S. PV industry improve manufacturing processes, accelerate manufacturing cost reductions for PV modules, improve commercial product performance, and lay the groundwork for a substantial scale-up of U.S.-based PV manufacturing plant capacities. Four separate phases comprise the PVMaT project to date. Each phase was designed to address selected R&D activities required to achieve PVMaT goals and support the specific needs of the PV industry.

Phase 1 was a problem-identification phase of about 3 months duration. It consisted of 22 small (less than $50,000 of DOE funding each) subcontracts resulting from 38 offers. During Phase 1, the status and needs of the U.S. PV manufacturing industry were identified, and a Phase 2 procurement responsive to industry's needs was developed. The Phase 1 subcontracts were completed in 1991.

Phase 2 addressed process-specific module manufacturing problems of individual manufacturers. The first solicitation under this phase (Phase 2A) was open only to organizations that received awards under the Phase 1 solicitation. Seven 3-year subcontracts were initiated in early 1992 and have been completed. The next PVMaT Phase 2 effort (Phase 2B) was a solicitation open to all U.S. PV industrial firms. This allowed organizations not ready for the earlier Phase 2A procurement cycle, or which were not participants in Phase 1, to have a chance to "ramp on" and participate in this process-specific solution phase of the PVMaT project. Four 3-year subcontracts, selected from 13 proposers, were awarded under this solicitation in late 1993.

Phase 3A addressed generic module manufacturing needs using a team approach. Seven proposals were submitted in response to the solicitation. Two subcontracts were awarded in January of 1993.

Phase 4A, Product-Driven Manufacturing, is the next step in the phased PVMaT project. It is a broader approach to addressing the overall goal of improved U.S. market share by meeting the market challenges. The solicitation requested proposals from individual or teamed U.S. PV and related industries to address the manufacturing of PV end-products, as well as the sub-elements of these products. Proposers could be firms or teams that may not be typically associated with PV systems, components, or products, but may have applicable expertise. The objectives of this phase were to stimulate broader interest in the production of PV products. They were also to encourage and support risk-taking by industry to explore new manufacturing options and ideas for improved PV products or components, influence system and product integration, and stimulate advances in balance-of-systems or developments in design that will lead to the overall reduced system life-cycle costs of the PV end-product. The thrust is to emphasize the importance of cost reduction, improved efficiency, and manufacturing flexibility and broader market applications for PV systems as a whole.

To accomplish the Phase 4A goals, the solicitation was divided into two parts: (1) Product-Driven System and Component Technology–4A1, with goals of improving integration efficiency, advancing design elegance, and improving component integration and manufacturing, and (2) Product-Driven PV Module Manufacturing Technology–4A2, addressing manufacturing flexibility and module manufacturing cost reduction for a wider range of PV products. Thirteen awards, selected from 31 proposals, have been made in Phase 4A: eight in Phase 4A1 and five in 4A2.

Total funding for PVMaT, including both federal and industry cost-share, and including projected funding to the end of PVMaT 4A, is $118 million. Cost-sharing by industry will total about 43%. Figure 1 shows a breakdown of the anticipated total funding by technology for both the DOE contribution and the subcontractor cost-shares. The technology areas are crystalline silicon (c-Si), concentrators (Conc), amorphous silicon (a-Si), cadmium-telluride-based systems (CdTe), copper-indium-diselenide-based systems (CIS), and general (Gen). The general area includes generic efforts in areas such as encapsulation, system integration, and balance-of-systems.

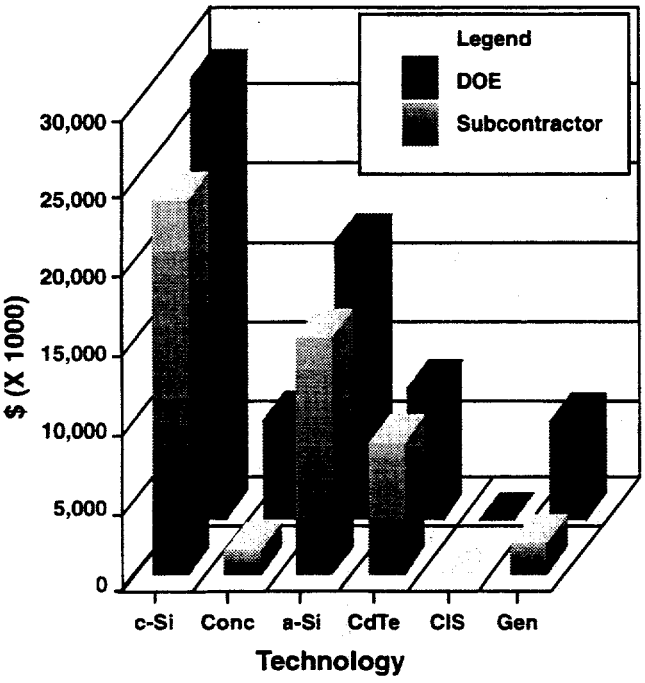

Figure 1. Cost-sharing by technology.

GOALS

The goals of PVMaT are to work jointly with the U.S. PV industry to improve manufacturing processes, accelerate manufacturing cost reductions for PV modules, improve commercial product performance, and lay the groundwork for a substantial scale-up of U.S.-based PV manufacturing plant capacities. Obvious elements for measurement are the cost reductions and the manufacturing capacities and volumes. But to actually evaluate the benefits to manufacturers and users, one must look at how these advances can be translated into savings. The following sections in this paper present the expected recapture of funds spent on the manufacturing R&D performed under PVMaT Phases 2A and 2B. Other participants (e.g., 4A2 participants) were not included because we felt they had not been involved long enough to have made cost impacts under PVMaT. The baseline from which these benefits are measured is based on 1992 data, which corresponds roughly to the initiation of Phase 2 efforts.

DISCUSSION

Progress of the individual industrial PVMaT participants has been described in published subcontractor reports and conference papers. Although this information on improvements in manufacturing processes was very encouraging, it was difficult to relate this progress to the progress of the PVMaT project as a whole. To get a better idea of progress toward accomplishing its goals of accelerating manufacturing cost reductions and stimulating a scale-up in capacity, the PVMaT manufacturing participants involved in Phases 2A and 2B were asked to provide specific data regarding their module manufacturing costs and capacity. For each year from 1992-2000, the industrial participants were asked to include costs directly associated with their module production, including manufacturing overhead costs. They were asked to exclude categories such as marketing, sales, administration, or the overhead associated with these areas. Capacity data were to represent the levels at which a manufacturer was capable of producing, based on equipment in place at the time, required maintenance, individual company policies, and unlimited product orders. These data, representing plant capabilities and company business plans, are considered highly sensitive by the individual companies. Therefore, Fig. 2 presents aggregate data in the form of a weighted average of module manufacturing costs and a summation of the manufacturing capacity (in place in each year through 1995 and projected for later years) for the 10 industrial participants that currently have active production lines. The weighted average represents the average cost per watt of modules (weighted by each participant's capacity) produced by these 10 PVMaT industrial participants. Figure 2 indicates that PV manufacturing capacity has increased by more than a factor of 6 in the last 4 years, from 11.6 MW to 88.7 MW. Additionally, the weighted-average cost for manufacturing PV modules has been reduced by about 56%. Although we saw these as important results regarding the progress the U.S. PV industry was making toward regaining its international competitiveness, it was still not clear how much of this progress should be attributed to the PVMaT project.

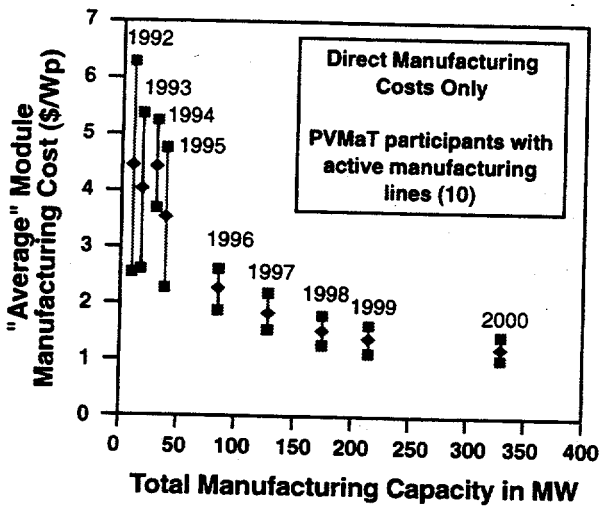

Figure 2. PVMaT Manufacturing cost/capacity.

To further address the impact of the PVMaT project, information was requested from the PVMaT participants on the payback from their R&D progress. Each of the 10 PVMaT manufacturers was asked to identify, by year, the specific technical improvements that have resulted in cost reductions for their product. They also established the value in $/watt for each of their improvements. Finally, manufacturers were asked to identify what portion of each improvement cost reduction they would pass on to the public as price reductions and how much would be used by the companies as internal reductions in their manufacturing costs. The data provided by the PVMaT manufacturers represented improvements in module fabrication such as improved junction boxes and improvements in module performance. The module performance improvements were, however, only taken as a cost reduction when the power output increase and the concomitant module cost reflected an actual reduction in $/watt.

The annual and cumulative data on the recapturing of funds spent on this research by the individual companies and the public were analyzed from the initiation of each subcontract to identify the magnitude of the benefit to each participant. Because benefit to either the public or the manufacturer would not be realized if the products were not actually manufactured, actual and projected production levels (as opposed to manufacturing capacities) provided by the individual manufacturers were used in calculating the annual dollars saved. Additionally, the value of these benefits would not be realized unless they represented competitive products; therefore, the analysis used only the cost reductions that reduced the cost of manufacturing below the $4.50/watt weighted average that the PVMaT participants reported for 1992. No benefit was accrued to either the individual companies or to the public until this level of cost had been achieved, and only the portion that represented a value below this level was used in subsequent years. Improvements that are to be used in all future product manufacturing, such as improved encapsulation configurations, will be of benefit in all subsequent-year products and were included in those years. Finally, the public benefit results of this analysis were normalized to the funding provided by the DOE. Data for the industrial participants were normalized to their cost-shared portion of the PVMaT subcontract.

As can be seen in Fig. 3, both the public and industry have benefited in this research. The public will recapture its portion of the funds spent on this research in 4.1 years through a direct reduction in the price of PV products. If only the U.S. sale of these PV products is used, at approximately 30% [1] of the production volume, the public savings due to price reductions will result in the U.S. public recapturing its portion of the funds spent in about 5.2 years. However, this approach does not take into account the value recaptured by the U.S. public through an increase in world market share and jobs, and an improved trade deficit.

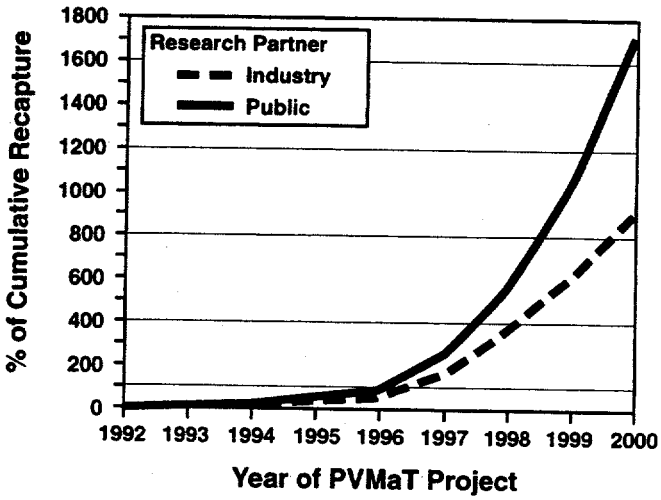

Figure 3. Recapture of PVMaT Research Funding. (U.S. and international sales)

The 10 PVMaT manufacturers with active production lines will recapture the funds they have individually cost-shared in an average of 2.8 years from the start of their subcontracts. The aggregate funds cost-shared by PVMaT industrial partners will have been recaptured in 4.4 years. This benefit may take any of several forms, such as decreased losses, increased profits, investment in increased production capacity, or performance of additional R&D.

The results shown in Fig. 3 represent the benefits achieved by the 10 industrial participants that currently have active production lines. The industry benefits are only for these 10. However, the public investment in other PVMaT industrial partners (those who are not currently active in the manufacturing of PV products) was included in the public costs requiring recapture. If current production projections by the 10 PVMaT participants are accurate, the public will have recouped over 17 times its original investment in the

PVMaT Phase 2A and Phase 2B research efforts by the year 2000. If, as above, only the U.S. sale of these PV products at the 30% level is used, the recoupment is still 5 times the original investment. The industrial participants will have also shared in benefits from their cost-shared participation in this research, with recovery of almost 9 times their investment by the year 2000. Even if these are optimistic predictions (and predictions often are), it seems very likely that the investment in PVMaT through Phase 2B will more than have been recovered before the end of the decade.

Finally, what has happened to the U.S. PV market share? Figure 4 shows the U.S. market share fell to about 31% in 1992, the first year of the PVMaT 2B efforts. Since that time, it has increased to about 43% [1].

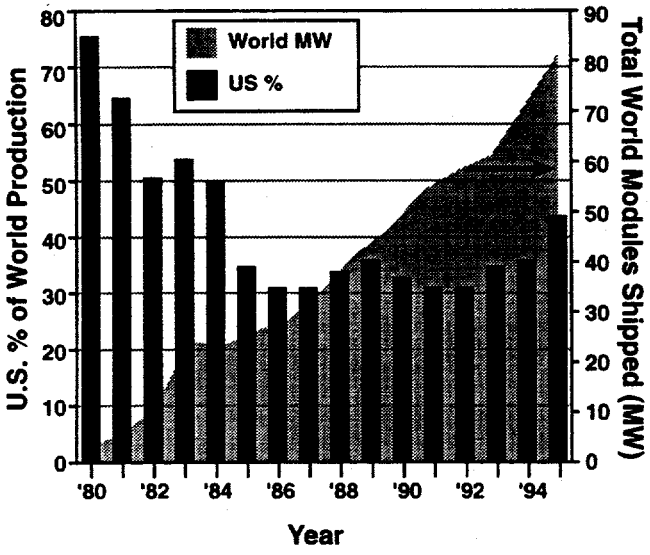

Figure 4. U.S. market share of world production.

We believe elements of this strengthening position include a new generation of PV modules with improved performance and durability, as well as advanced and refined module manufacturing processes. These modules have been developed with the help of government/industry partnerships that are the cornerstone of the PVMaT project. The efforts of industry and the government/industry partnerships have all contributed to PV technology and market status improvements, and PVMaT has been a significant contributor to those benefits.

We intend to continue to update both cost and capacity data for the manufacturers in real time. Additional improvements to be gained as Phase 2B subcontracts reach their end and new research results from the current Phase 4A2 subcontracts are obtained will also be included in future evaluations on the PVMaT benefits to industry and the U.S. public.

CONCLUSIONS

PVMaT Phases 2A, 2B, and 3A are near completion. An evaluation of the information now available indicates PVMaT is a success in achieving increased production and lower cost. Data collected in late FY 1995 from 10 PV manufacturing lines participating in the PVMaT project have allowed an evaluation of the success of this project. Increased production capacity, reduced module-manufacturing direct costs, and the recapturing of funds spent in PV manufacturing R&D have been reported by the PVMaT Phase 2 participants. The weighted average module manufacturing cost has declined an estimated 56% and production capacity has increased by more than a factor of 6 in the last 4 years. Recapture of the funds spent for manufacturing improvements is achieved in about 5 years, and by the year 2000, it will significantly exceed the investment by the U.S. public and the U.S. manufacturers. Finally, the late-1980s/ early-1990s decline in U.S. PV manufacturing market share of world production has reversed. U.S. market share has risen to 43% in 1995, after falling to a low of about 30% in 1992. The U.S. PV industry is getting stronger, and the PVMaT government/industry collaboration is contributing to a growing U.S. PV technology with a positive recapture of investments in manufacturing R&D.

ACKNOWLEDGEMENTS

This work is supported under DOE contract No. DE-AC36-83CH10093 with NREL. Many people have contributed to the development and implementation of the Photovoltaic Manufacturing Technology project and to the R&D efforts carried out in this program. The authors recognize this paper represents their work, and it is those people who are the real authors of the accomplishments presented. We thank them, each and every one.

REFERENCES

[1] Data for figure developed from the following sources:
PV Insiders Report, Vol. XIII, No. 2, 1994, p. 1.
PV News, Vol. 3, No. 2, 1984, p. 2.
PV News, Vol. 15, No. 2, 1996, p. 3.
Solar Energy Intelligence Report, Set. 9, 1986, p. 81.
The World PV Market, July 1985, p. 50.
Solar Collector Manufacturing Activity, 1993, DOE/E1A/0174 (93), Aug 1993, p. 19.

GROWTH ANALYSIS OF CADMIUM SULFIDE THIN FILMS BY ATOMIC FORCE MICROSCOPY

H.R. Moutinho, R.G. Dhere, K. Ramanathan, P. Sheldon and L.L. Kazmerski
National Renewable Energy Laboratory, 1617 Cole Blvd., Golden CO 80401

ABSTRACT

CdS films have been deposited by solution growth on SnO_2 and glass substrates. Nucleation on SnO_2 occurs at early deposition times, and complete conformal coverage is observed at low thickness values. The average grain size of the CdS films is established at these early times. In films deposited on glass substrates, nucleation is slower and occurs through 3-dimensional islands that increase in size and number as deposition proceeds. Optical measurements show that the bandgap values of CdS films deposited on SnO_2 depend mainly on substrate structure. Hydrogen heat treatment does not affect the surface morphology of the samples, but decreases bandgap values.

INTRODUCTION

Very thin CdS films are commonly used as window layers in thin-film solar cells. Because light absorbed in CdS does not significantly contribute to the collected photocurrent, it is desired that this layer have the minimum thickness possible. The minimum thickness should allow for a CdS conformal coverage of the substrate without formation of defects that could shunt the cell. Solution-grown CdS thin films offer the advantages of conformal coverage on rough surfaces at minimal thicknesses, ease of deposition, and low cost [1,2].

In this study, we investigate the growth of CdS deposited on SnO_2 and glass under different conditions. The primary analytical technique used was atomic force microscopy (AFM), which provides the following desired characterization: extremely high magnifications, high-resistivity sample analysis, and determination of roughness values. We have also performed transmittance and reflectance measurements to obtain optical bandgap values of the deposited films.

EXPERIMENTAL

CdS films were deposited by the chemical solution growth technique. Two different processes were used, based mainly on the quantities of ammonium hydroxide and ammonium acetate used. In both processes an initial solution of de-ionized water, ammonium acetate, and cadmium acetate (the source of Cd) was prepared. In process A, thiourea (the source of S) was then added, and, at last, the reaction was initiated with a solution of ammonium hydroxide in de-ionized water. Two deposition temperatures were used, 70°C and 85°C. The solution was slightly basic, with pH just above 7. In process B, the concentration of ammonium hydroxide and ammonium acetate were increased many times. In this process, thiourea was the last chemical added, and the one to start the growth reaction. The films were deposited at 90°C. The solution was highly basic, with pH close to 10. Process A is similar to the one used by Devaney [3], and process B is similar to the one used by Chu [4].

In the solution growth method, CdS can grow on the substrate (heterogeneous process) or in the solution itself (homogeneous process). The heterogeneous process in general gives rise to films with quality suitable for photovoltaic application. The homogeneous process, which can be minimized by reducing the rate of formation of CdS, gives rise to CdS precipitates that deposit loosely on the substrate. These precipitates may come out of the film after deposition, giving rise to pinholes, as been observed by Danaher [5]. At early deposition stages, the solution is clear, but as homogeneous reaction takes place, it begins to get an orange coloration. Experimentally, one can determine when the reaction should be stopped, to prevent significant incorporation of CdS (coming from homogeneous reaction) in the film. This criterion was used to determine when to stop the deposition.

Besides borosilicate and sodalime glass, two structures were used as substrates:

- LOF SnO_2/sodalime glass
- Intrinsic SnO_2/Solarex SnO_2/borosilicate glass.

For each deposition, the substrates were removed from the solution at different times so that films with different thicknesses could be obtained. Film thickness varied from 10 nm to 150 nm.

Some CdS films were heat-treated in hydrogen to promote recrystallization and to remove oxygen from the films, which increases carrier concentration and mobility [6,7].

AFM analysis [8] was performed using a Park Scientific Autoprobe LS instrument in contact mode, using Si cantilevers. Transmittance and reflectance analyses were done in a Cary 2300 spectrophotometer equipped with integrating sphere.

RESULTS AND DISCUSSION

AFM images of CdS films deposited on SnO_2 revealed the surface morphology of both films. The CdS formed a secondary structure over the SnO_2 film. At early stages of growth, CdS films already show complete conformal coverage. This is an important result, because the thinner the CdS layer, the smaller the optical loss will be in the cell. The surface morphology of a sample after 15 minutes into growth is shown in Fig. 1. The SnO_2 structure, with large grains, is clearly distinguishable underneath the small-grain CdS thin film. The thickness of the CdS layer was about 30 nm. All films deposited on SnO_2, independent of growth process, showed complete coverage at thicknesses of 40 nm or less. We also found that grain growth occurs much faster horizontally than vertically in the initial stages. This is clearly seen in Table 1, when one compares grain size and thickness for the thinnest films. Another observation is that the average grain size of the films are defined at early deposition times. Later grain growth, when it occurs, is not significant, as also shown in Table 1.

We have not found many differences in surface morphology in samples grown by different processes and/or deposited on different SnO_2 films. The average grain size for most films was around 60 nm, with the exception of films grown at 70°C, which had an average grain size close to 35 nm. For the latter, it seems that the lower temperature favored a higher density of nucleation sites, and as a result, the smaller grain size.

After the initial nucleation process, the grains seem to grow independently of each other in a 3-dimensional process, while new grains are generated on the existing structure. This explains why the average grain size does not change after early deposition times, because new grains will prevent the growth of adjacent ones. It also explains the large variation in grain size observed, because old larger grains, as well as new smaller grains, are present. In a sample with an average grain size of 60 nm, grains as small as 30 nm and as large as 90 nm are observed. This is shown in Fig. 2.

Another important parameter shown in Table 1 is the rms roughness. The roughness values for all films agree well with the ones for the respective SnO_2 substrate. This is a very important result because it indicates that the growth is conformal and that the CdS thickness is uniform. If the growth were not conformal, for instance, with films growing preferentially at grain boundaries, the roughness values for the films would probably be smaller than the ones for the substrates.

It is important to note that the values obtained for grain size and roughness are averages and that there is a statistical variation associated with them, which depends on the location on the sample where the measurement was performed. To minimize these errors, we have done many measurements of each parameter. However, we still estimate an uncertainty around 10% and 15% in the reported values for roughness and grain size, respectively, due mainly to statistical fluctuations in the value for these parameters from point to point in the sample.

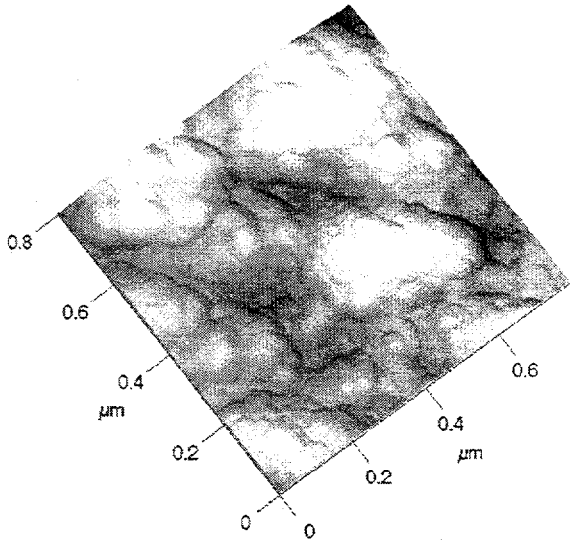

Fig. 1. CdS thin film (approximately 30 nm thick) deposited on SnO_2.

Table 1. Average grain size (GS), rms roughness (R), and film thickness (d) for CdS films deposited with different parameters on SnO_2. LOF means LOF SnO_2 deposited on sodalime glass. Sol means Solarex SnO_2 deposited on borosilicate glass, with an intrinsic SnO_2 layer on top. Last two lines show values of GS, R, and d for both SnO_2 used in the depositions.

Growth Process	Substrate	T (°C)	GS (nm)	R (nm)	d (nm)
A	LOF	70	31	34	10
			36	35	17
			34	33	50
A	LOF	85	56	33	10
			57	34	36
			61	36	100
A	Sol	85	56	23	10
			61	23	36
			62	23	120
B	LOF	90	52	33	21
			60	34	75
			59	32	138
B	Sol	90	59	22	45
			55	24	89
			62	22	140
LOF SnO_2			210	34	-
i-SnO_2			95	23	-

CdS films were also deposited on sodalime and borosilicate glass substrates. Because these substrates

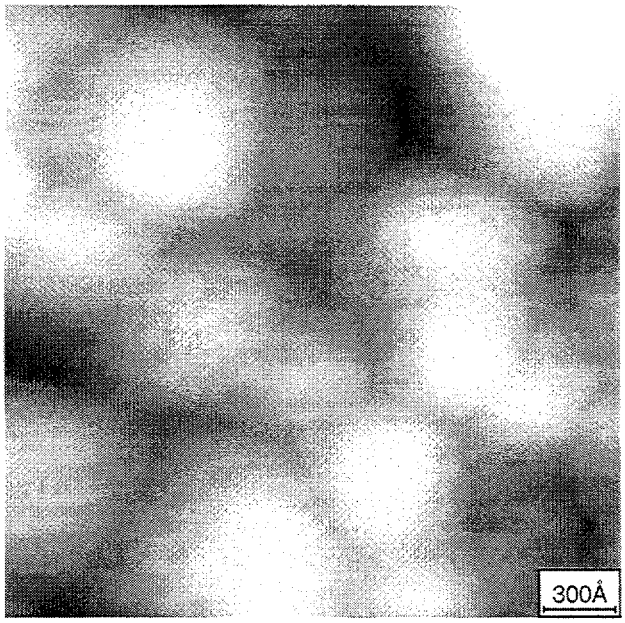

Fig. 2. AFM image of a CdS thin film grown on SnO_2 showing a large variation of grain sizes.

are much smoother than SnO_2, it is easier to observe the nucleation process. The nucleation and growth is very different than in films deposited on SnO_2. For glass substrates, complete coverage does not occur at early times, and nucleation and growth takes place through 3-dimensional islands.

Films deposited on sodalime substrates using process B showed scattered 3-dimensional islands with diameters varying from 27 nm to 92 nm, and height from 3 nm to 17 nm, at 10 minutes into growth. The subsequent films showed a continuous grain structure with the film grown for 40 minutes showing average grain size of 80 nm.

For the borosilicate substrate (also deposited using process B), nucleation was first observed at 15 minutes into growth, with very few islands with diameters varying from 60 nm to 90 nm and height from 5 nm to 15 nm. As deposition time increased, the number of islands also increased, as well as their maximum size. At 25 minutes, a non-continuous structure was observed, as shown in Fig. 3. The CdS grain size varied from 80 nm to 110 nm and the height from 50 nm to 60 nm. At 40 minutes, the CdS structure was almost continuous, but some very small open areas, with depth varying from 50 nm to 60 nm, were still visible. The average grain size was 88 nm.

The roughness measured for the borosilicate substrate was 0.8 nm and for the continuous CdS film was 7 nm. This low value for the CdS roughness indicates that the roughness of CdS deposited on SnO_2 is mainly due to the substrate structure, which reinforces our argument that the CdS coverage on SnO_2 is comformal and uniform.

The differences in nucleation and growth mechanisms observed in samples deposited on SnO_2 and glass are attributed to the fact that the rough SnO_2 provides many more nucleation sites than the very smooth glass. Because of this, films deposited on SnO_2 nucleate faster, show complete coverage at earlier times, have smaller grain sizes, and seem to be thicker.

Pinholes were not observed in any CdS film deposited on SnO_2. However, because peak-to-valley distances in these films are on the order of film thickness, pinholes may be camouflaged. This problem does not exist on the smoother films deposited on borosilicate and sodalime substrates. For these films, most samples did not show pinholes, and the few pinholes observed seemed to be due to incomplete coverage, other than a result of cluster deposition from homogeneous reaction. Because nucleation is much slower in these films, the observations are a good indication that films deposited on SnO_2 indeed do not have pinholes. This result was expected and shows that the precautions we took to keep the homogeneous reaction to a minimum during film growth were effective.

Four CdS films with thicknesses over 100 nm, two deposited by each process and using both types of SnO_2, were heat-treated in 30-torr hydrogen atmosphere at 400°C for 15 minutes. Contrary to what we expected, the AFM images showed the same kind of grain structure as before treatment, including grain size. These results indicate that the changes in properties observed in these films after this kind of treatment are probably related to chemical and/or intragranular structural changes.

To complement the AFM analyses, we have done reflectance and transmission measurements. With these values, absorption coefficients (α) were calculated, and the bandgap values (E_g) of the CdS films were determined. The bandgap values were obtained from the graph of $(\alpha E)^2$ vs. E, where E is the energy of the

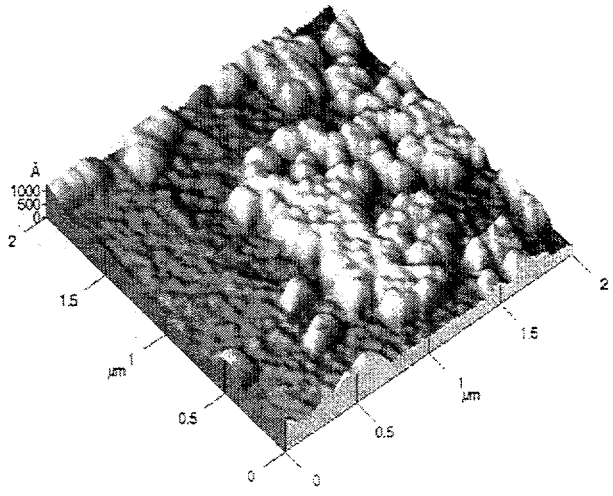

Fig. 3. CdS thin film deposited on borosilicate glass by process B, after 25 minutes deposition.

analyzing radiation [9]. The value of E_g was obtained by the intersection of the extrapolated linear part of the curve with the energy axis. To remove substrate effects from our analysis, the measurements were done on complete structures (film and substrate) and substrate structures without film.

The absorption coefficient of CdS in the region near to the bandgap, for all the films, was above 10^4 cm^{-1}, as observed previously by Danaher [5]. We found that the substrate structure is the most important factor affecting E_g, as shown in Fig. 4. The influence of the deposition process is not clearly evident. Films deposited on LOF SnO_2/sodalime presented bandgaps between 2.43 eV and 2.44 eV, whereas films deposited on intrinsic SnO_2 had bandgaps between 2.45 eV and 2.48 eV. The reasons for this behavior are not well understood at the present time, but are possibly associated with different stress states in the films. It was also observed that films deposited on LOF SnO_2 had larger values of absorption coefficient than films deposited on intrinsic SnO_2, for all the range of wavelengths used in the analyses.

Transmittance and reflectance measurements were also done on hydrogen heat-treated samples. The results for all the samples was a reduction in bandgap value. The new values ranged from 2.33 eV (previously 2.43 eV) to 2.42 eV (previously 2.48 eV). One effect of H_2 treatment in CdS is the preferential loss of S. The defects generated by this process can create shallow levels close to the conduction band, possibly being responsible for the observed decrease in bandgap. Another indication of the presence of such levels is that the absorption curves are not as smooth as before the treatment, pointing to the possible existence of more than one type of transition for charge carriers between bands. The main problem with the apparent reduction in bandgap is the increase in the optical loss in the CdS film. This can be observed even visually, with the darkening of the films. Finally, it was observed that films deposited by process B presented larger shifts in bandgap. This is probably associated with a different rate of S release during H_2 treatment compared to films deposited by process A.

CONCLUSIONS

- CdS thin films deposited by solution growth under normal device-processing conditions on SnO_2 films present complete conformal coverage even for small thicknesses (40 nm or less). Final average grain size is established at early deposition times. No defects, such as pinholes, were observed in such films.
- Nucleation of CdS films on glass occurs by the formation of 3-dimensional islands, which grow and increase in number as deposition proceeds.
- The bandgap of CdS films deposited on SnO_2 is influenced by the substrate structure.
- No effects of hydrogen heat treatment were found on the surface morphology of CdS films. However, effects of the treatment were observed in optical measurements by the reduction of bandgap values.

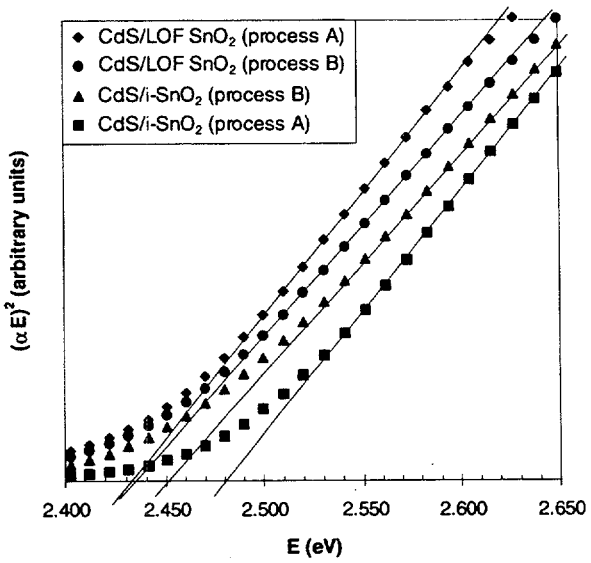

Fig. 4. $(\alpha E)^2$ curves showing bandgap values for CdS deposited with different parameters.

ACKNOWLEDGMENTS

The authors would like to thank Libbey-Owens-Ford and Solarex for providing the substrate samples used in this study. This work was performed, in part, under U.S. Department of Energy contract No. DE-AC36-83CH10093 with the National Renewable Energy Laboratory.

REFERENCES

[1] R.L. Call, N.K. Jaber, K. Seshan, and J.R. Whyte, Jr., *Solar Energy Materials* **2**, 373 (1980).
[2] A. Mondal, T.K. Chaudhuri, and P. Pramanik, *Solar Energy Materials* **7**, 431 (1983).
[3] W.E. Devaney, W.S. Chen, J.M. Stewart, and R.A. Mickelsen, *IEEE Trans. Electron Dev.* **37(2)**, 428 (1990).
[4] T.L. Chu, S.S. Chu, N. Schultz, C. Wang, and C.Q. Wu, *J. Electrochem. Soc.* **139(9)**, 2443 (1992).
[5] W.J. Danaher, L.E. Lyons, and G.C. Morris, *Solar Energy Materials* **12**, 137 (1985).
[6] Y.Y. Ma and R.H. Bube, *J. Electrochem. Soc.* **124(9)**, 1430 (1977).
[7] R. Sudharsanan and A. Rohatgi, *Proc. 21st IEEE Photov. Spec. Conf.* (IEEE, New York, 1990) p. 504.
[8] J. Frommer and E. Meyer, *J. Phys.: Condens. Matter* **3**, S1 (1991).
[9] E.J. Johnson, In: *Semiconductors and Semimetals* Vol. 3, R.K. Willardson and A.C. Beer eds. (Academic Press, New York, 1967) p. 168.

DETERMINATION OF THE VALENCE-BAND OFFSET OF CdS/CIS SOLAR CELL DEVICES BY TARGET FACTOR ANALYSIS

D. W. Niles, M. Contreras, K. Ramanathan, and R. Noufi
National Renewable Energy Laboratory
1617 Cole Boulevard, Golden, CO 80401

ABSTRACT

X-ray photoemission spectroscopy (XPS) is used to determine and compare the valence-band offsets (ΔE_V) for CdS grown by chemical bath deposition on single-crystal and thin-film $CuInSe_2$ (CIS). The thin-film CIS device was suitable for photovoltaic energy production. By sputtering through the CdS/CIS interface and reducing the depth profile with target factor analysis, the magnitude of ΔE_V was determined to be $\Delta E_V = 1.06 \pm 0.15$ eV for both the single-crystal and thin-film interfaces. This determination of ΔE_V is about 0.25 eV larger than many previously reported estimations CdS grown by physical vapor deposition on CIS and helps explain the record performance of CdS/CIS photovoltaic devices.

INTRODUCTION

Solar-cell devices made from the CdS/$CuInSe_2$ (CdS/CIS) heterojunctions are promising candidates for thin-film photovoltaic (PV) energy production.[1] The current record efficiency for CIS-based solar-cell devices exceeds 17%.[2] Despite progress in the efficiency of CdS/CIS-based solar-cell devices, a complete understanding of the electronic structure of the CdS/CIS interface remains elusive. In this manuscript, we attempt to resolve the controversy involving the magnitude of the valence-band offset (ΔE_V) and conduction-band offset (ΔE_C) between CdS and CIS in thin-film devices.[3-6]

The difference in the optical bandgaps of CdS and CIS must be shared by ΔE_V and ΔE_C. For efficient PV performance, ΔE_V must be large (approaching E_g[CdS]–E_g[CIS] = 1.38 eV) and ΔE_C must be small. In fact, early indirect photoemission measurements gave $\Delta E_V = 1.4$ eV in support of efficient PV performance.[3]

Subsequent direct photoemission measurements yielded $\Delta E_V = 0.8 \pm 0.1$ eV.[6] Our own photoemission measurements have shown the $\Delta E_V = 0.8 \pm 0.1$ eV for CdS on both single-crystal $CuInSe_2$ and thin-film CIS.[7] The inconsistency between the photoemission-measured ΔE_V and the required ΔE_V for effective solar-cell performance has led to other models for the CdS/CIS interface.[4,5]

A fundamental difference between the idealized photoemission experiments and the real world of CdS/CIS devices is the method of producing the CdS layer: whereas record-setting CIS devices employ a CdS layer made by chemical bath deposition (CBD), photoemission measurements have been made on CdS grown in vacuum by physical vapor deposition (PVD). The purpose of these experiments is to bridge the gap between measured valence-band offsets and record device performance by measuring the band alignment for CBD CdS deposited on CIS. To this end, we have deposited CBD CdS onto both single-crystal and thin-film CIS and then performed XPS depth-profiles to determine ΔE_V.

EXPERIMENT

CdS layers 50 nm thick were grown by CBD onto two substrates: one single-crystal CIS (SC-CIS) and one thin-film CIS (TF-CIS) several microns thick suitable for a high-efficiency photovoltaic device. The details of the thin-film CIS growth and CBD processes are described elsewhere.[8,9] We then sputtered through the CdS/CIS interface while monitoring core levels and valence bands with X-ray photoemission spectroscopy (XPS). The XPS system was a Physical Electronics 5600 XPS equipped with a monochromated Al Kα source operating at 350 W and hemispherical analyzer operated at 12 eV pass energy and 800 μm spot size.

We used 3 kV Ar^+ ions at ~30° from normal incidence to sputter through the interface while rotating the sample and rastering the ion beam over a 4x4 mm area. We determined the average sputter rate by measuring the sputter crater depths with a profilometer to be 1.8 nm/min. Aside from <1 at.% O in the CdS thin-film, we did not observe any residual contaminants from the CBD growth process at the CdS/CIS interface. All atomic concentrations were determined using standard sensitivity factors from Ref. 10. All spectra were aligned to the Fermi level of a metallic In sample.

After obtaining depth profiles from the CdS/SC-CIS and CdS/TF-CIS interfaces, we reduced the depth-profile spectra with target factor analysis (TFA) and determined

the ΔE_V from the reconstructed data.[11] TFA is a matrix-based algorithm that is becoming a standard data-reduction technique in the analysis of depth profiles. Ref. 11 presents a thorough discussion of TFA.

RESULTS AND DISCUSSION

Preferential sputtering was not apparent through the CdS overlayer. The atomic concentrations of sputtered thin-film and single crystal CdS were Cd = 51 ± 2 at.% and S = 49 ± 2 at.%. We did not observe any evidence for metallic Cd from high-resolution core line spectra or Fermi-level spectra.

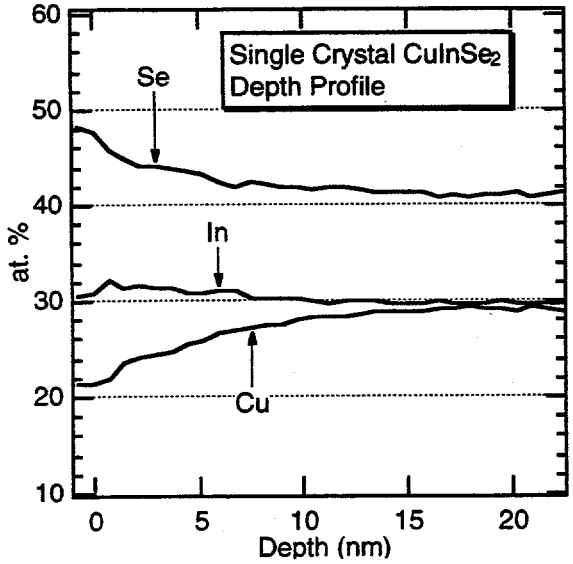

Fig. 1: Atomic concentrations for sputtered single-crystal CIS.

Preferential sputtering was a problem for the CIS substrate. Fig. 1 shows the atomic concentrations of SC-CIS cleaved in an N_2 ambient, inserted immediately into the analysis chamber, and then sputtered at 3 kV. The O signal was < 1 at.% and the C signal was imperceptible. The average atomic concentrations of the bulk were Cu = 25 at.%, In = 25 at.%, and Se = 50 at.% as determined by electron microprobe analysis. The crystal appeared to cleave along an imperfection and leave a surface that did not have the same atomic concentrations as the average. Sputtering further decreased the Se content of the CIS surface region and left behind metallic In and Cu.

The metallic behavior of the cations was visible in the In 3d spectrum shown in Fig. 2 and the presence of Fermi level emission (not shown here). Compared to the cleaved crystal, sputtering broadens the In 3d toward lower binding energy and makes a clear metallic In shoulder. The broadening indicates numerous chemical environments for the In, ranging from relatively unperturbed CIS to metallic In.

From nuclear stopping cross-section theory, we estimate a dose of ~10^{15} ions/cm^2 and an Ar^+ ion penetration depth of 20 nm. Therefore, all of the intensity in the measured photoemission signal stems from the interface region potentially damaged by the ion-beam.

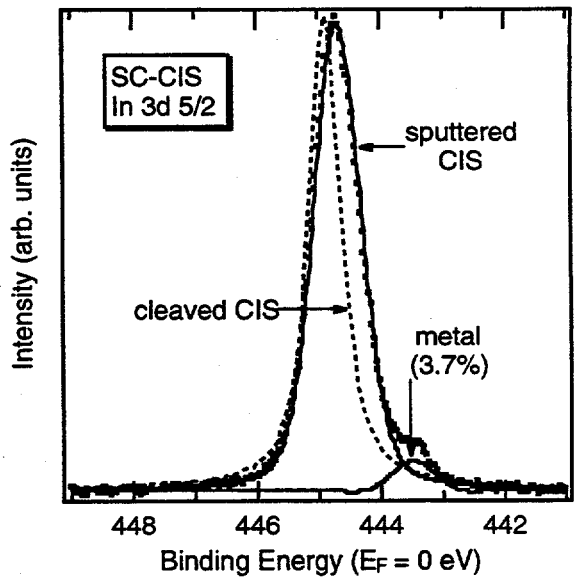

Fig. 2: In 3d 5/2, showing metallic In formation.

Fig. 3 shows the eigenvalue analysis of the depth profiles for both the CdS/SC-CIS and CdS/TF-CIS interface obtained through factor analysis. One can see from the Fig. 3 two primary eigenvalues followed by smaller ones that are about 3 orders of magnitude smaller that the two primary ones. Analysis of the residual error, the IND function, and eigenvectors associated with the eigenvalues support the conclusion that only two factors are needed to describe the depth profiles.[11]

Fig. 4 shows these two factors for the CdS/SC-CIS interface after target rotation: obviously, they correspond to the CdS overlayer spectrum and the CIS substrate spectrum. The conclusion is that every spectrum of the depth profile is a linear superposition of the spectrum of the CdS overlayer and the ion-damaged CIS substrate.

In Fig. 4, one can see embedded Cd in the CIS substrate, metallic In, and Fermi-level emission (not visible in the spectra as plotted) from the metallic cations. The amount of Cd in the CIS film is difficult to determine because the intensity is weak, but is less than 1 at.%. To within experimental error, the valence-band emission after

sputtering with Ar^+ was not significantly different from the the SC-CIS factor shown in Fig. 4. The fact that we need only two factors to describe the depth profile despite the problems brought about by preferential sputtering is somewhat perplexing. One would expect a priori to need three factors: one for the CdS, one for the CIS before sputtering created significant damage, and one for the heavily damaged CIS at the end of the depth profile. Our conclusion is that the shape of the CIS valence-band emission is relatively insensitive to the level of sputter-induced damage.

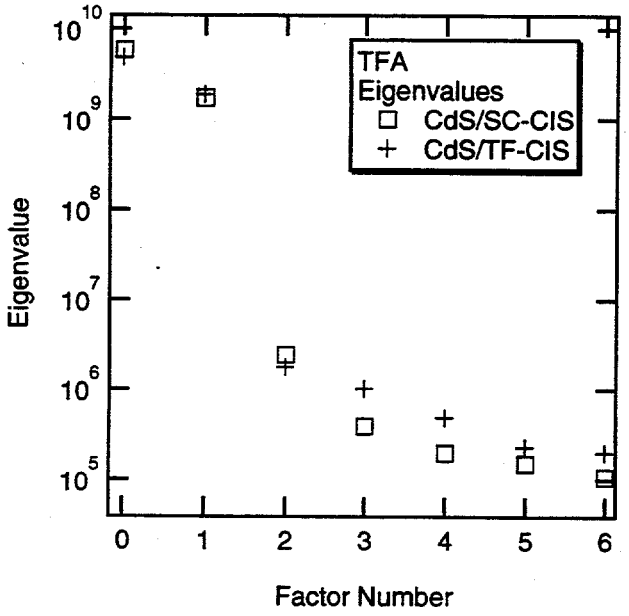

Fig. 3: Eigenvalues for both interfaces, showing that only two factors are necessary reconstruct the depth profile.

Further support for this conclusion comes from reducing the valence-band emission of the depth profile on the cleaved single-crystal (atomic concentrations shown in Fig. 1). We first measured a spectrum from a metallic In sample, and used it to subtract the metallic In signal from the cleaved, sputtered SC-CIS spectra. We then reduced the remaining emission with TFA, and found that one factor accounted for the signal, to within experimental error.

We used reconstructed data from the factors in Fig. 4 and the loading factors to determine ΔE_V for the system as a function of sputter depth. To determine the VBM, we linearly extrapolated the leading edge of the valence-band signal. We also determined the accuracy by taking the largest and smallest acceptable extrapolations consistent with the data. Fig. 4 is a plot of ΔE_V and the loading factors.

The data points and the smooth curve in Fig. 5 represent the position of the valence-band maximum (VBM) as a function of sputter depth. The dashed curves in Fig. 5 are the CdS and CIS loading factors as a function of depth. At depths less that 40 nm, the photoemission signal looks like the CdS factor seen in Fig. 4, without any signal from the CIS present. Between 40 and 60 nm, the depth-profile spectra change from appearing like CdS to appearing like CIS (with some embedded Cd). Within this transition region the position of the VBM moves towards the Fermi level. ΔE_V = 1.01 eV is the total change in the position of the VBM .

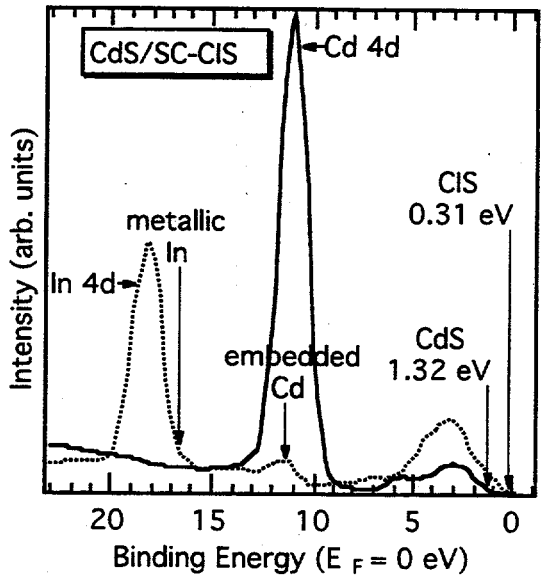

Fig. 4: CdS and CIS factors for the CdS/SC-CIS interface.

The results from the CdS/TF-CIS interface are essentially identical in all respects, except we measure ΔE_V = 1.11 eV. Fig. 6 shows the results. To within experimental error, this measured ΔE_V is that same as for the SC-CIS substrate. We conclude that ΔE_V for CBD CdS on both thin-film and single-crystal CIS is $\Delta E_V = 1.06 \pm 0.15$ eV.

In an earlier set of experiments, we deposited CdS by PVD at room temperature on both SC-CIS and TF-CIS while monitoring the valence-band emission with synchrotron radiation photoemission. For these systems, we found $\Delta E_V = 0.8 \pm 0.1$ eV in agreement with other measurements.[6,7] Although the error bars on the CBD and PVD results prohibit absolute confirmation of a larger ΔE_V for CBD devices, the data for the CBD CdS were reproducible and consistently showed a larger ΔE_V.

A possible explanation for the difference is the

presence of interface contaminants. Except for a small O signal (≤ 1 at. %), we did not see any contamination. Another possible explanation is that CBD and PVD CdS are chemically different. However, we carefully analyzed the atomic compositions, high-resolution photolines, and Auger parameters of CBD, PVD, and single-crystal CdS without uncovering any fundamental differences.Our present thesis for the difference in ΔE_V is that the

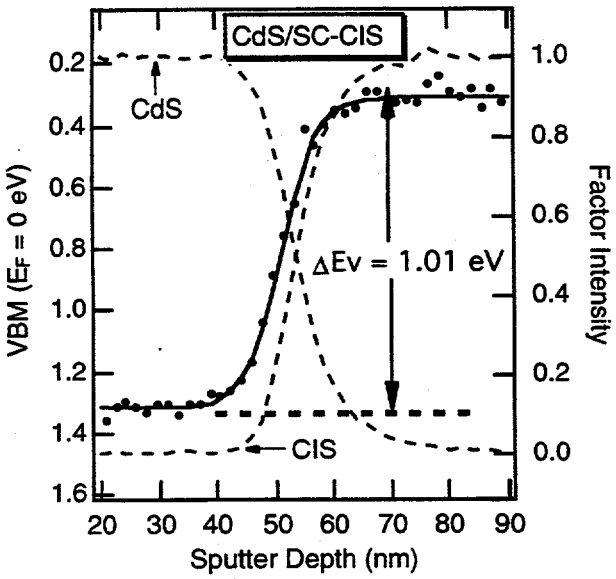

Fig. 5: Loading factors and ΔE_V for the CdS/SC-CIS interface.

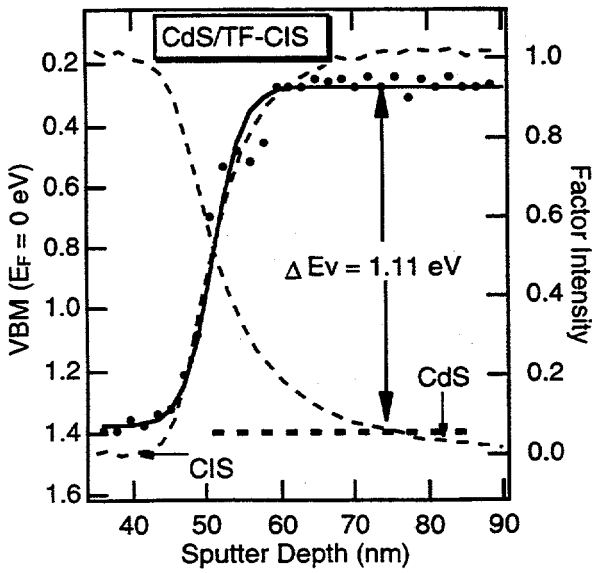

Fig. 6 Loading factors and ΔE_V for the CdS/TF-CIS

CdS/CIS interface chemistry is different between CBD and PVD CdS, but ion-beam damage obscures the chemistry of the interface and renders our data insufficient to prove this thesis.

The important quantity with regard to the performance of photovoltaic devices is the conduction band offset (ΔE_C) rather than the valence band offset. The general assumption within the photovoltaic community is that ΔE_C < 0.3 eV is necessary to understand the flow of charge across the CdS/CIS interface.[12] Using our measured ΔE_V, Eg(CdS) = 2.42 eV and Eg(CIS) = 1.04 eV , we calculate $\Delta E_C = 0.32 \pm 0.15$ eV. Our calculated value of ΔE_C for a real device supports the traditional model for CdS/CIS-based solar cells.

[1] H. Ullal et al., *Twenty--fourth IEEE PVSC* , 1994, v. 1, p. 266.

[2] M. A. Green et al., *Prog. Photovoltaics* **3**, 229 (1995).

[3] M. Turowski et al. , *Phys. Rev. B* **31**, 1022 (1985).

[4] D. Schmid et al., *J. Appl. Phys.* **73**, 2902 (1993).

[5] S.-H. Wei et al., *Appl. Phys. Lett.* **63**, 2549 (1993).

[6] T. Löher et al., *J. Appl. Phys.* **77**, 731 (1995).

[7] D. W. Niles, unpublished.

[8] M. Contreras et al., *Twenty--fourth IEEE PVSC* , 1994, v. 1, p. 68.

[9] J. Kessler et al., *Sixth International PVSEC* 1992, p. 1005.

[10] Jill Chastain, ed., *Handbook of X-Ray Photoelectron Spectroscopy*, edited by (Physical Electronics, Eden Prairie, MN,1992).

[11] E. R. Malinowski, *Factor Analysis in Chemistry* by (Wiley and Sons, Inc., 1991).

[12] J. L. Gray et al., *AIP Conference Proceedings* 353, 1995 p. 345.

RESULTS OF THE PEP'93 INTERCOMPARISON OF REFERENCE CELL CALIBRATIONS AND NEWER TECHNOLOGY PERFORMANCE MEASUREMENTS

C.R. Osterwald, National Renewable Energy Laboratory, Golden, Colorado, USA
S. Anevsky, All-Union Research Institute for Optophysical Measurements, Moscow, Russia
A.K. Barua, Indian Association for the Cultivation of Science, Calcutta, India
J. Dubard, Laboratoire Central des Industries Electriques, Fontenay-aux-Roses, France
K. Emery, National Renewable Energy Laboratory, Golden, Colorado, USA
D. King, Sandia National Laboratories, Albuquerque New Mexico, USA
J. Metzdorf, Physikalisch-Technische Bundesanstalt, Braunschweig, Germany
F. Nagamine, Japan Quality Assurance Organization, Tokyo, Japan
R. Shimokawa, Electrotechnical Laboratory, Ibaraki, Japan
N. Udayakumar, Udhaya Semiconductors (P) Ltd., Coimatore, India
Y.X. Wang, Tianjin Institute of Power Sources, Tianjin, China
W. Zaaiman, European Solar Test Installation, Ispra, Italy
T. Wittchen, Physikalisch-Technische Bundesanstalt, Braunschweig, Germany
A. Zastrow, Fraunhofer-Institut für Solare Energiesysteme, Freiburg, Germany
J. Zhang, National Institute of Metrology, Beijing, China

ABSTRACT

This paper presents the results of an international intercomparison of photovoltaic (PV) performance measurements and calibrations. The intercomparison, which was organized and operated by a group of experts representing national laboratories from across the globe (i.e., the authors of this paper), was accomplished by circulating two sample sets. One set consisted of twenty silicon reference cells that would, hopefully, form the basis of an international PV reference scale. A qualification procedure applied to the calibration results gave average calibration numbers with an overall standard deviation of less than 2% for the entire set. The second set was assembled from a wide range of newer technologies that present unique problems for PV measurements. As might be expected, these results showed much larger differences among laboratories. Methods were then identified that should be used to measure such devices, along with problems to avoid.

INTRODUCTION

Under the auspices of the seven-nation Photovoltaic Energy Project (PEP), an international round-robin of reference cell calibrations and performance measurements of Newer Technology (NT) PV devices was initiated in 1993. The round-robin was preceded by two other PEP-sponsored projects in 1984 [1] and 1987 [2]. The objectives of the intercomparison were threefold: (1) establish the World PV Scale (WPVS) by comparing primary reference cell calibrations traceable to national metrology programs, (2) identify problems with emerging technology measurements and propose recommendations for suitable measurement procedures to be considered by standardization organizations, and (3) recommend methods of qualifying calibration data in publications. Thirteen laboratories from eight nations participated in the intercomparison, which required more than two years to complete.

WPVS SAMPLE SET

A major recommendation of the PEP'87 intercomparison was that a single primary calibration method should not be adopted for international standardization, but rather, the total uncertainty of acceptable reference cell calibrations should be less than ±2% [2]. The WPVS sample set, which required the participants to calibrate 20 2×2 cm packaged silicon devices using the best method available to them that is traceable to national standards, was an attempt to act on this recommendation. Each participant provided at least one reference cell to the sample set that was returned at the conclusion of the intercomparison.

A number of calibration methods were used by the participating laboratories, including: outdoor primary calibration against a cavity radiometer (A), indoor primary with absolute simulator spectral irradiance (C), differential spectral responsivity with variable bias light (D1), differential spectral responsivity with no bias light (D2), indoor primary with a standard irradiance lamp (L), absolute spectral responsivity (R), and secondary calibration against a primary reference cell (S). All of these methods involve spectral corrections of some kind to the standard global air mass 1.5 spectral irradiance [3]. The letter codes, similar to those used in reference [2], identify the methods used in the plot of the normalized short-circuit current calibration results from ten laboratories, Fig. 1. For this data set, the overall 2σ standard deviation is 7.6%, a large value.

We adopted the following procedure to qualify the WPVS calibrations. First, it was decided that only primary calibration methods should be allowed to contribute to the WPVS. Thus, laboratories 1, 9, and 10 were removed as these were secondary calibrations. Second, any laboratories with 50% or more of their data points in Fig. 1 outside of 1.0 ± 0.02 were excluded. This criterion resulted in the removal of laboratories 3, 5, and 7. The normalized short-circuit currents were then recalculated, and individual points that exceeded 1.0 ± 0.02 were removed. The remaining data were averaged to obtain the final WPVS short-circuit current values. These results are presented in Fig. 2, where the overall 2σ standard deviation is now 1.9%. Although space does not allow presentation here, qualified spectral responsivity and short-circuit current temperature coefficients are also included as part of the World PV Scale.

The WPVS effort revealed several drawbacks to implementing such a program in its current state. First, the length of time needed to circulate all the cells among all laboratories traceable to the WPVS is excessive. The first attempt

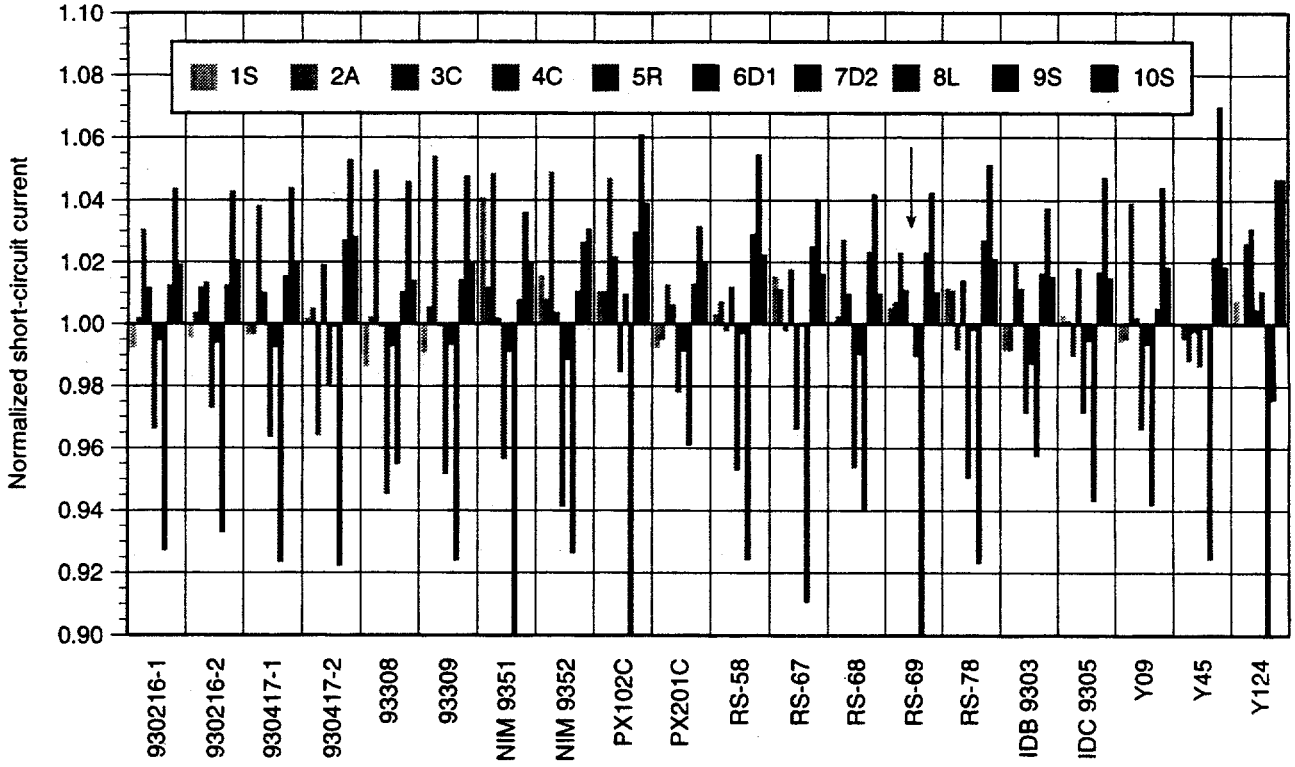

Fig. 1. Normalized 2×2 cm Si reference cell calibration results for the WPVS sample set. The 2σ standard deviation is 7.6%. The laboratory designations indicate the order in which the samples were circulated and the calibration methods used (see text). The vertical arrow marks a missing data point.

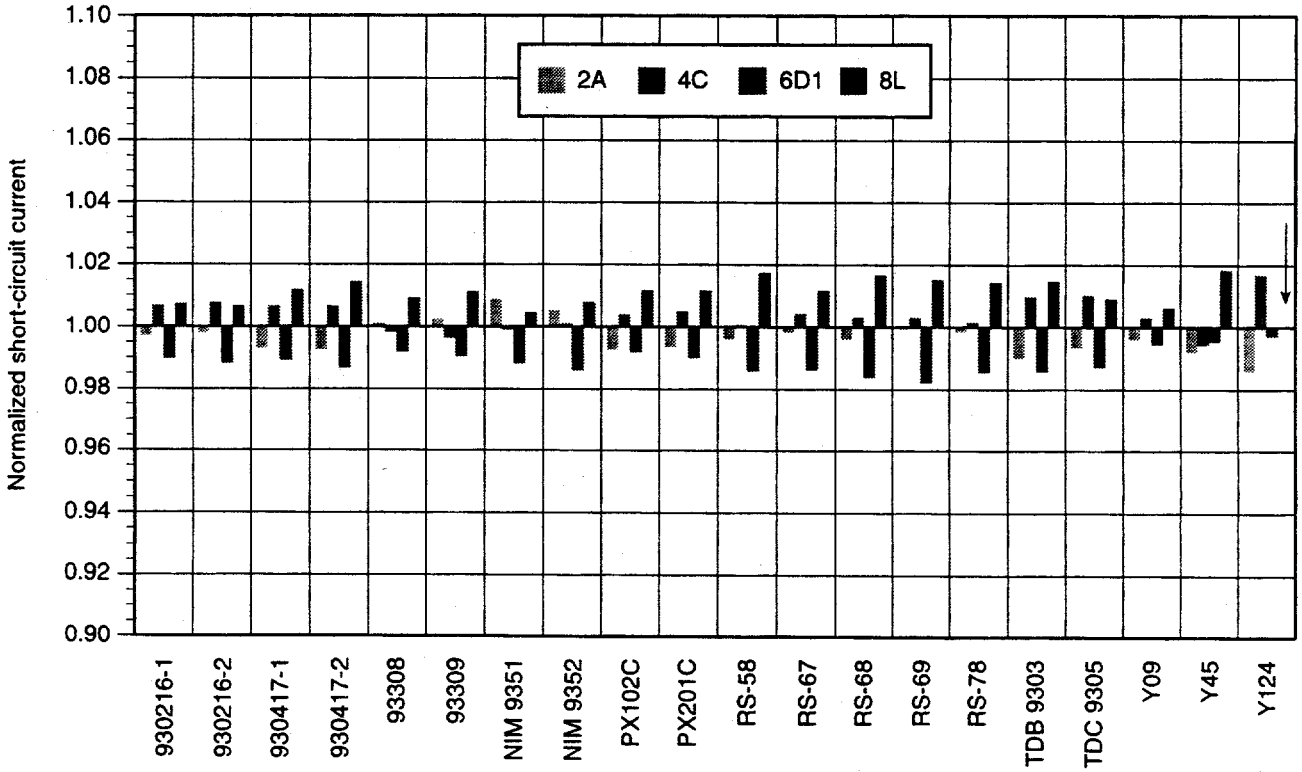

Fig. 2. Normalized reference cell calibration results for the WPVS sample set following removal of secondary calibrations (1, 9, and 10) and laboratories with 50% or more data points exceeding 1.0 ± 0.02 (3, 5, and 7). The 2σ standard deviation is 1.9%. The point marked with a vertical arrow was removed as an outlier.

required almost 3 years. During this time, the cells are unavailable and thus cannot be used as reference cells. Also, the risk of losing the entire set at once in shipment between laboratories is unacceptably high. Second, the cells currently in the WPVS are themselves problematic. The only restriction placed on the cells was that they meet the requirements of reference [4], which are fairly minimal. Several cells developed bubbles in encapsulation, and the cover windows of three cells were cracked during the calibrations. Moreover, the twenty WPVS cells represent a total of seven different package designs with a wide variety of temperature sensors, cables and connectors, and physical sizes. This variety caused logistical problems for the participants during the calibrations. Third, procedures for adding new cells to the WPVS set must be developed.

NT SERIES SAMPLE SET

The NT sample set consisted of two cells from each of the following categories: ESTI sensor, CuIn(Ga)Se_2, CdTe, a-Si bi-cell (two-cell minimodule), low-pass (300-800 nm) filtered Si, high-pass (600-1200 nm) filtered Si, GaAs, 10×10 cm bare Si, a-Si two-terminal tandem, and a two-cell GaAs concentrator module with fixed optics. All of the devices were packaged as reference cells except for the large-area silicon cells. Because of the objective to identify measurement problems, the participants were free to measure these samples by whatever methods they chose. The majority of the measurements were performed in solar simulators against reference cells, using spectral corrections to the global spectral irradiance. A notable exception was the GaAs concentrator module which several laboratories measured outdoors against blackbody detectors.

Overall, the nature of the NT series samples posed problems for all the laboratories. Also, no instructions were provided about how to measure the devices, except for necessary information about contacts and connectors. For example, the ESTI sensors consist of two 50-cm^2 silicon cells inside a module-laminated package. One cell is loaded with a 20-mΩ resistance for short-circuit current measurement, and the other cell is intended as a temperature sensor using the cell's open-circuit voltage. Because they are not intended to be operated at maximum power, a four-wire connection is not provided to the temperature cell. Most of the laboratories did not know how to calibrate these devices and measured the current-voltage curve of the open cell. Therefore, the ESTI sensor data are not reported.

Fig. 3 presents the normalized maximum-power results for the NT series. Maximum-power data were used for the comparison instead of efficiency because maximum-power is independent of cell area and because some laboratories did not measure cell areas. After the reported data were normalized, individual points that exceeded 1.0 ± 0.08 were removed and the normalization factors recalculated. The 2σ standard deviation of the remaining data is 5.7%, which is probably about what might be expected from such a diverse group of samples. The outlying data points were also re-normalized and appear in Fig. 3, even though most exceed the plot vertical limits.

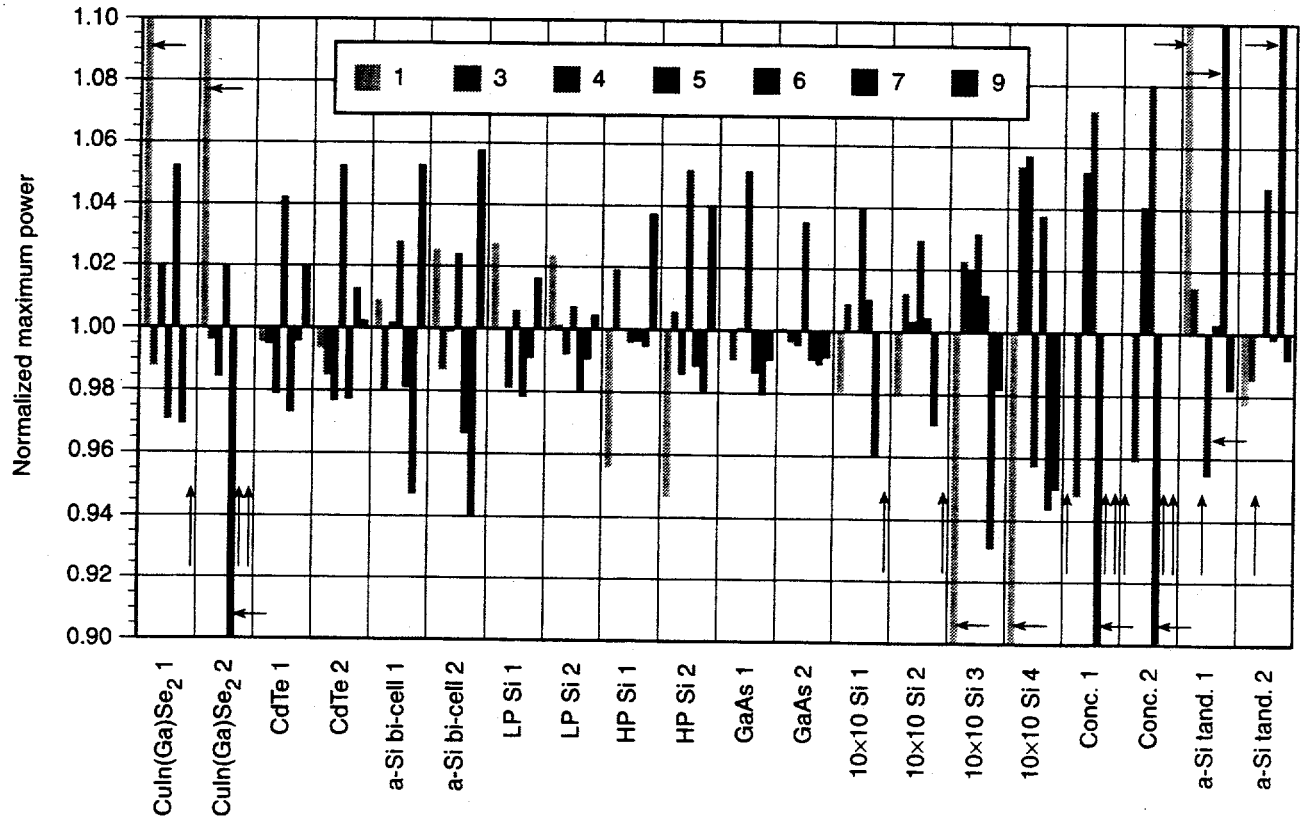

Fig. 3. Normalized maximum-power results for the NT series sample set. The 2σ standard deviation is 5.7%. The vertical arrows mark missing data points, and the horizontal arrows indicate data points that exceeded 1.0 ± 0.08. All but one of these points exceeded 1.0 ± 0.1 and were clipped to the plot edges. These outliers were not used to calculate the overall standard deviation.

Subsequent analysis and discussion of the results revealed a number of problems encountered by the participating laboratories. Contacting problems were uncovered by the large-area Si cell samples, two of which had four-terminal connector blocks provided (1 and 2), and two that had only two sockets for connections (3 and 4). Cells 3 and 4 therefore show more deviation caused by fill factor differences. The results for the CuIn(Ga)Se_2 devices indicate there is a strong possibility that the contacts of these devices degraded during the intercomparison. Laboratory 5 determined from the WPVS results that the reference cell used for this laboratory's measurements was out of calibration (about 4% high), which resulted in correspondingly higher values. The large-area devices caused temperature control problems for several laboratories. Laboratory 1 allowed large-area cells 3 and 4 to reach temperatures of approximately 40°C. Only three laboratories used multiple-source simulator measurement techniques on the a-Si tandem cells. A major problem was spectral response measurements of these cells. Half the participants did not attempt to measure the subcells individually, thus producing a composite spectral response. One laboratory could not measure the maximum power of the tandem cells because the higher open-circuit voltage of these devices exceeded the maximum limits of the instrumentation. Spatial non-uniformities may be responsible for the higher differences observed for the a-Si minimodules.

The analysis showed that differences in short-circuit current (not reported here) are not accounted for by differences in spectral response measurements. These differences must therefore be caused by reference cell calibrations.

RECOMMENDATIONS

A number of recommendations for performance measurements of newer technology devices were made. First, tandem-cell measurements are difficult, especially spectral response, and need to be done with multijunction techniques. Second, problems inherent with newer technology devices that can cause unexpected errors should be carefully considered. These include (a) area measurement, (b) temperature measurement and control, (c) device stability, (d) contacting and wiring, (e) pulsed light versus steady-state measurements, and (f) sweep speed of the current-voltage measurements. Third, reference cell calibration is vitally important, and adoption of the World PV Scale should help reduce differences.

After spending a great deal of time discussing the problems with the WPVS identified above, the following recommendations for future WPVS calibrations were made. First, circulation of the entire set among all the laboratories traceable to WPVS will no longer be performed. Intercomparisons will be replaced with recalibration at a single laboratory. The recalibration events should take place every 1 ½ to 2 years at different laboratories. Laboratories eligible for recalibration events will initially be those whose data were selected for the final WPVS average (laboratories 2, 4, 6, and 8 in Fig. 2). Second, new cells must undergo an extensive series of acceptance tests prior to being qualified for subsequent calibration. These acceptance tests include (a) meeting physical requirements, (b) light soaking, (c) current-voltage characteristics, (d) visual inspection, (e) temperature sensor integrity, and (f) temporal stability. Third, new cells that have passed the acceptance tests are circulated informally among several laboratories traceable to WPVS prior to the next calibration event. The new cells may then be brought to the next event for calibration with the other WPVS cells. Fourth, following the calibration event, the results of the recalibration and data from any new cells are considered and analyzed by the participating laboratories at a post-calibration meeting. The new qualified average for each cell is determined at this time. Also, laboratories that have improved their calibrations are considered for admittance to the recalibration group at this time. Finally, a new reference cell package design that should minimize logistical problems that can occur when calibrating a large number of devices from around the world was developed.

CONCLUSIONS

For the first time, a group of worldwide national laboratories have agreed on a single scale for PV reference cell calibrations. The 2σ standard deviation of the normalized short-circuit currents from four laboratories for 20 2×2 cm Si reference cells was 1.9%. Although each of the laboratories have different bias and random errors, this result appears to achieve the recommendation of the previous PEP'87 round-robin, that the total uncertainty for primary calibrations should be ±2%. Procedures for maintenance and recalibration for the World PV Scale have also been recommended.

A second sample set of newer technology PV devices circulated worldwide gave a 2σ standard deviation of 5.7% for the normalized maximum power, after removal of obvious outliers. This study has shown a number of problems associated with these measurements that must be dealt with if this uncertainty is to be reduced in the future.

ACKNOWLEDGMENT

This work was supported by the U.S. Department of Energy under contract No. DE-AC36-83CH10093.

REFERENCES

[1] H. Ossenbrink, R. Van Steenwinkel, K. Krebs, "The Results of the 1984/1985 Round-Robin Calibration of Reference Solar Cells for the Summit Working Group on Technology, Growth, and Employment," Joint Research Centre, Ispra Establishment, PREPRINT EUR 10613 EN, April 1986.

[2] J. Metzdorf, T. Wittchen, K. Heidler, K. Dehne, R. Shimokawa, F. Nagamine, H. Ossenbrink, L. Fornarini, C. Goodbody, M. Davies, K. Emery, R. DeBlasio, "Objectives and Results of the PEP'87 Round-Robin Calibration of Reference Solar Cells and Modules," *Proc. 21st IEEE PV Spec. Conf.*, Kissiminee, FL, 1990, pp. 952-959. See also "The Results of the PEP'87 Round Robin Calibration of Reference Solar Cells and Modules -Final Report-," *PTB report PTB-Opt-31*, ISBN 3-89429-067-6, Braunschweig, 1990, 174 p.

[3] "Photovoltaic Devices—Part 3: Measurement Principles for Terrestrial Photovoltaic (PV) Solar Devices with Reference Spectral Irradiance Data," *International Electrotechnical Commission Standard 904-3*, Geneva, Switzerland, 1989.

[4] "Photovoltaic Devices—Part 2: Requirements for Reference Solar Cells," *International Electrotechnical Commission Standard 904-2*, Geneva, Switzerland, 1989.

SPECTROSCOPIC, SCANNING LASER OBIC, AND I-V/QE CHARACTERIZATIONS OF BROWNED EVA SOLAR CELLS

F. J. Pern, Center for Performance Engineering, Qualification, and Reliability; National Renewable Energy Laboratory (NREL), Golden, CO 80401.
I. L. Eisgruber, Materials Research Group, Inc.; Wheat Ridge, CO 80033.
R. H. Micheels, Polestar Technologies, Inc.; Needham Hts, MA 02194.

ABSTRACT

The effects of ethylene-vinyl acetate (*EVA*) discoloration due to accelerated field or laboratory exposure on the encapsulated silicon (Si) solar cells or EVA/glass laminates were characterized quantitatively by using non-invasive, non-destructive ultraviolet-visible (UV-vis) spectrophotometry, spectrocolorimetry, spectro-fluorometry, scanning laser OBIC (optical beam induced current) spectroscopy, and current-voltage (*I-V*) and quantum efficiency (*QE*) measurements. The results show that the yellowness index (*YI*) measured directly over the AR-coated solar cells under the glass superstrate increased from the range of -80 to -90 to the range of -20 to 15 as the EVA changed from clear to brown. The ratio of two fluorescence emission peak areas generally increased from 1.45 to 5.69 as browning increased, but dropped to 4.21 on a darker EVA. For a solar cell with brown EVA in the central region, small-area grating QE measurements and scanning laser OBIC analysis between the brown and clear EVA regions showed that the quantum efficiency loss at 633 nm was 42%-48% of the loss at 488 nm, due to a reduced decrease of transmittance in browned EVA at the longer wavelengths. The portion of the solar cell under the browned EVA showed a decrease of ~36% in efficiency, as compared to the cell efficiency under clear EVA. Transmittance loss at 633 nm was 38% of the loss at 488 nm for a light yellow-brown EVA/glass laminate that showed a small increase of 10 in the yellowness index.

INTRODUCTION

EVA encapsulants of two commercial formulations, the slow-cure EVA A9918 and fast-cure EVA 15295 with or without a primer (*P*), are widely used for the encapsulation of crystalline Si and some thin-film photovoltaic (*PV*) modules. Weathering of EVA-encapsulated PV modules or accelerated exposure of EVA laminated in glass to UV light can result in EVA discoloration from light yellow to dark brown. Consequently, the light transmittance through the EVA decreases, resulting in reduced photocurrent generation and PV module efficiency [1-4]. This work was conducted as part of a continuing effort to characterize, identify, and correlate quantitatively the extent and the mechanisms of degradation in materials contributing to the performance loss in EVA-encapsulated PV cells. We used non-invasive, non-destructive analytical methods, including UV-vis spectrophotometry, spectrocolorimetry, spectro-fluorometry, scanning laser OBIC spectroscopy, I-V, and QE measurements. This paper describes the results of our study about the effect of EVA browning on solar cell performance.

EXPERIMENTAL

Samples of EVA/glass laminates were made by curing A9918 films between glass slides at 145°C for 40 min. Solar cell samples were already encapsulated and provided by a commercial source. They were made of polycrystalline (*pX*), edge-defined, film-fed-growth (*EFG*) ribbon Si solar cells with a dark-blue anti-reflection (*AR*) coating in a common encapsulation configuration of glass/EVA/pX-Si cells/EVA/ Tedlar™. The PV cells that received simulated, accelerated degradation (*Type I*) were of 5-cm x 10-cm in size; each cell was laminated between a 12.5-cm x 12.5-cm glass superstrate and black Tedlar film substrate. The cell coupons weathered outdoors (*Type II*) consisted of two 4.4-cm x 4.8-cm pX-Si cells connected in parallel and encapsulated to a size of 9.4-cm x 11.8-cm with EVA A9918P between an AFG Solatex™ glass superstrate and a semitransparent polymer film substrate.

Accelerated testing in the laboratory was conducted for Type I cell samples at 85°C ± 2°C for 198 days in room humidity (typically 20%-25% relative humidity). UV exposure under three GE 100-W, RS-4 UV lamps on a turntable in a tabletop chamber yielded a uniformly brown EVA in the cells, whereas thermal degradation by heating in dark ovens produced uniformly light-yellow EVA [2]. The samples of EVA/glass laminates were discolored either by exposing to a concentrated 1-kW Xe light at a black panel temperature (*BPT*) of 54°C ± 2°C or to an enhanced-UV light from an Oriel 1-kW Xe solar simulator at BPT=44°C ± 2°C [4].

Samples of Type II cell coupons were received only for analytical measurements. Except for the unexposed controls, initial conditions of the exposed samples were not available. The coupons received various doses of UV exposure (295 nm to 385 nm) up to 1100 kWh in an EMMA™ mirror concentrator apparatus at the DSET

Laboratories in Arizona. The coupon temperatures were kept below 65°C by forced-air cooling. The EMMA-exposed cells exhibit either partially browned EVA or almost completely browned EVA over the cell areas; the EVA over the unexposed controls is clear.

Fluorescence [5,6], scanning laser OBIC [7,8], I-V, QE, and UV-vis transmittance measurements were performed for the respective samples. Small area grating QE measurements were performed with a light beam of ~1-mm x 2-mm in size. In the color index measurements [4], the reflectance mode with a 10-mm port was used for the solar cells and the transmission mode for the EVA/glass laminates.

RESULTS AND DISCUSSION

Figure 1 shows the results of (a) color indices and (b) transmittance spectra measured for an EVA A9918 film that was laminated and cured between two quartz slides and then discolored by a concentrated 1-kW Xe light for 451 h. The A9918 film rapidly lost the UV absorber [4], Cyasorb UV 531™, while developing a light

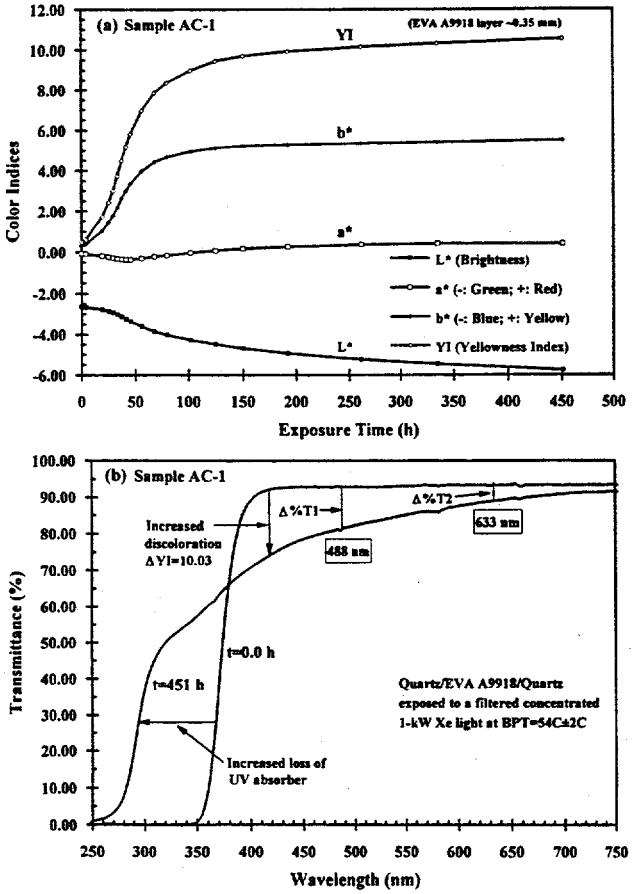

Figure 1. Changes in the (a) color indices and (b) transmittance spectra from t=0 h to t=451 h measured for a discoloring EVA A9918 laminated between two quartz slides and exposed to a filtered, concentrated 1-kW Xe light at a black panel temperature (*BPT*) of 54°C ± 2°C.

yellow-brown color with a small increase of $\Delta YI=10$ as seen in Fig. 1a (curve YI) and Fig. 1b. The transmittance spectrum decreased in the broad region from ~375 nm to ~800 nm as a result of the yellowing. As seen in Fig. 1b, the ratio of transmittance loss at 633 nm to that at 488 nm, $\Delta\%T_2/\Delta\%T_1$, is 38%. The two wavelengths are of the two lasers used in the scanning OBIC analysis discussed below. Fluorescence analysis indicates a new broad emission peak (not shown here) that is attributed primarily to the formation of conjugated polyenes [4-6]. Factors that affect the EVA discoloration *rate* have been reported elsewhere [4].

We demonstrated for the first time the usefulness of spectrocolorimetry in assessing the degree of EVA discoloration directly over glass/EVA-encapsulated solar cells with a dark-blue AR coating. Measurements were performed for the EMMA-exposed cells and compared to the controls. Figure 2 shows the results of (a) the yellowness index, *YI*, and (b) the fluorescence spectra measured for these samples. For the EVA that remained visually clear over the dark-blue areas of AR-coated solar cells (either exposed or unexposed), we obtained a YI in the range of -80 and -90 with a standard deviation (*SD*) of ~1 to ~8. Surface unevenness and reflection from the silver (Ag) gridlines on the EFG ribbon pX-Si cells contributed to the higher SD in the measurements for some cells. For the areas where EVA was browned to varying degrees, measured YI ranged from -18 to +11, also with a SD of ~1 to ~8. The large increases in YI from clear EVA to brown EVA are also evident in the fluorescence spectra (Fig. 2b), where the peak region (375-442 nm) is assigned to the original chromophores that existed after encapsulation curing, and the peak region (442-685 nm) to the degradation-produced chromophores that gave the brown color. The ratio of the integrated peak area over these two peak regions, PAR=PA(443-685 nm)/PA(375-442 nm), shows a general increase from 1.45 for unexposed controls to 5.69 for a fairly brown EVA, but decreases as the brown color darkened further (Fig. 2b). The ratio trend would be more accurate if the peaks were deconvoluted and background emission subtracted.

The optical effect of EVA browning on cell efficiency loss is illustrated in Fig. 3. For a Type I cell exposed to the RS-4 UV light and resulted in visibly brown EVA, the measured cell efficiency decreased by 19.3% (Fig. 3a), primarily due to EVA browning because no obvious changes in the cell's series and shunt resistance were observed [2]. The gradual decreases in the cell's absolute quantum efficiency (or spectral response) due increased EVA browning are shown in Fig. 3a. For an EMMA-exposed Type II cell with brown EVA in the central region and clear EVA around the brown rectangular area (area ratio ~1:1), the results from small-area grating QE measurements are shown in Fig. 3b. The cell shows a decrease of ~36% in the efficiency under brown EVA as compared to that under clear EVA, as determined by measuring the I-V for the cell portion under brown EVA region while masking clear EVA region, and vice verse.

The optical effect of EVA browning on PV cell efficiency loss can be better resolved spatially by using

scanning laser OBIC analysis, which can perform line-scan measurements as well as mapping of the current response for entire cell or module [7,8], as illustrated in Fig. 4. An Ar laser of 488 nm was used for the "blue" scan (Fig. 4, top) and a He-Ne laser of 633 nm for the "red" scan (Fig. 4b, bottom). The decrease in the photocurrent response (or quantum efficiency) over the browned EVA region in each type of scan should correspond in principle to the transmittance loss, Δ%T, due to EVA browning as indicated in Fig. 1b; i.e.,

$$\Delta\%T(633nm)/\Delta\%T(488nm) \sim [\Delta QE(633nm)/\Delta QE(488nm)] \times [QE(488nm)/QE(633nm)]$$

The results are 42%-48% from the small-area grating QE measurements and ~46% from the scanning laser OBIC measurements, calculated for the ratio of quantum efficiency loss at the two wavelengths between the brown EVA and clear EVA by using the right-half cell areas seen in Fig. 4. A 38% was obtained for $\Delta\%T_2/\Delta\%T_1$ between %T at 633 nm and at 488 nm for the light yellow-brown EVA/glass laminate that showed only a small increase of 10 in YI (see Fig. 1b). These results appear to correspond well quantitatively. The discrepancy between the values from the Δ%T and ΔQE calculations (38% vs. 42%-48%) is attributed primarily to the obvious difference in the EVA color between the two samples.

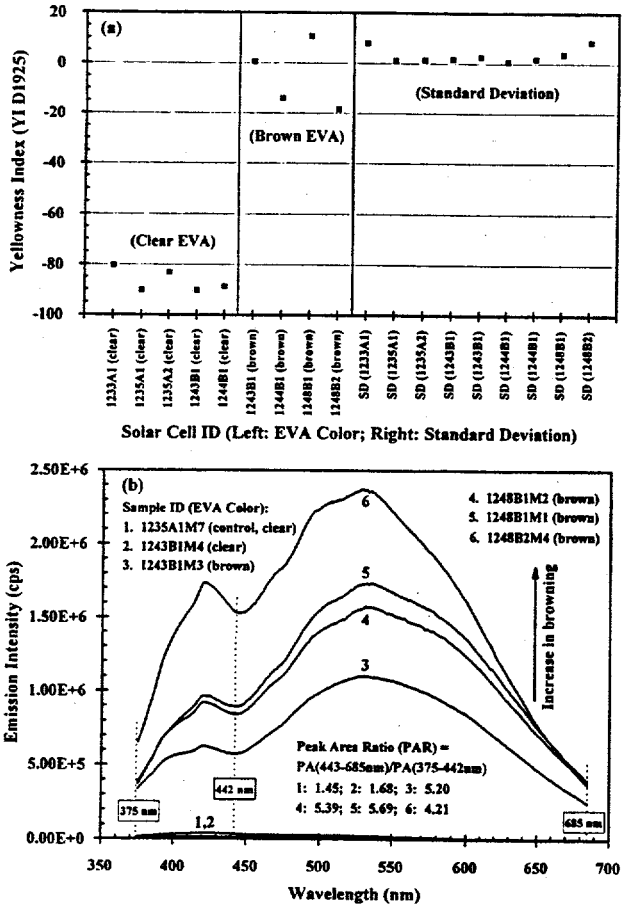

Figure 2. (a) Yellowness index (*YI*) measured for clear, partially brown, and mostly brown EVA over the encapsulated pX-Si solar cells with and without accelerated natural weathering in an EMMA™ mirror concentrator apparatus. The samples are code-numbered as indicated in the figure. The standard deviations from multiple spot measurements are shown on the right half of the figure for each solar cell. (b) Fluorescence spectra obtained with an excitation wavelength of 350 nm for the clear and brown EVA regions over three solar cells from (a), with the code-numbers indicated. The ratios of integrated peak area over two peak regions, PAR= PA(443-685 nm)/PA(375-442 nm), are indicated.

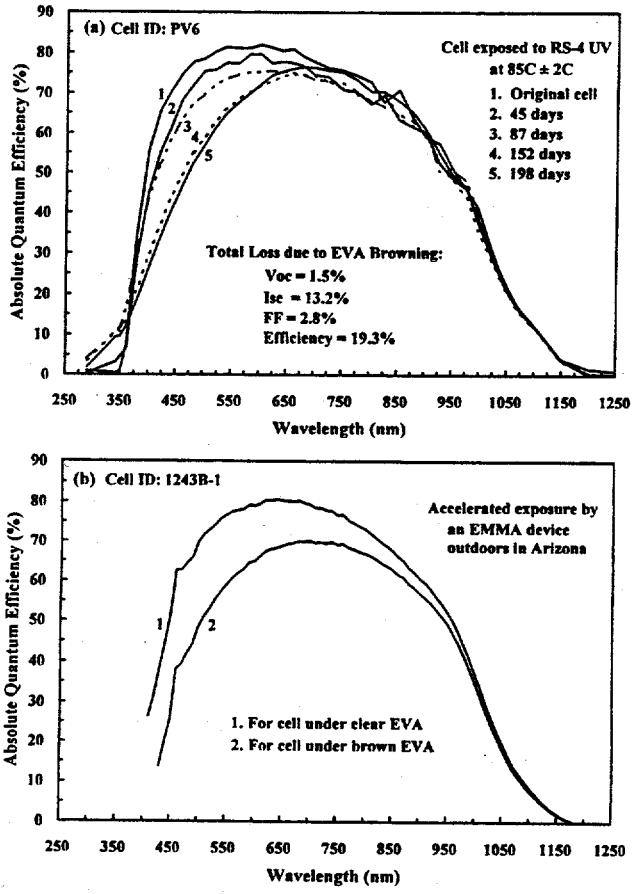

Figure 3. The wavelength dependence of the absolute quantum efficiency (i.e., spectral response) determined for (a) a Type I cell exposed to RS-4 UV light at 85°C ± 2°C for 198 days that produced a uniform brown EVA over the entire cell (curves 1-5), and (b) small-area grating quantum efficiency (*QE*) measured without light and voltage bias for a Type II cell (as shown in Fig. 4) that exhibits brown EVA in the central region (curve 1) and clear EVA in the perimeter around the brown region (curve 2). A light beam of ~1-mm x 2-mm in size was used in the grating QE measurements between two gridlines on the cell.

CONCLUSION

We have shown that several non-invasive, non-destructive analytical methods can be conveniently applied to characterize *quantitatively* the optical effect of EVA browning on PV cell efficiency. However, a good correlation among *all* of these spectroscopic and I-V/QE results still requires a more systematic study with a greater number of PV cells and EVA/glass laminates that are prepared through careful experimental design. Work in this area is now in progress at NREL.

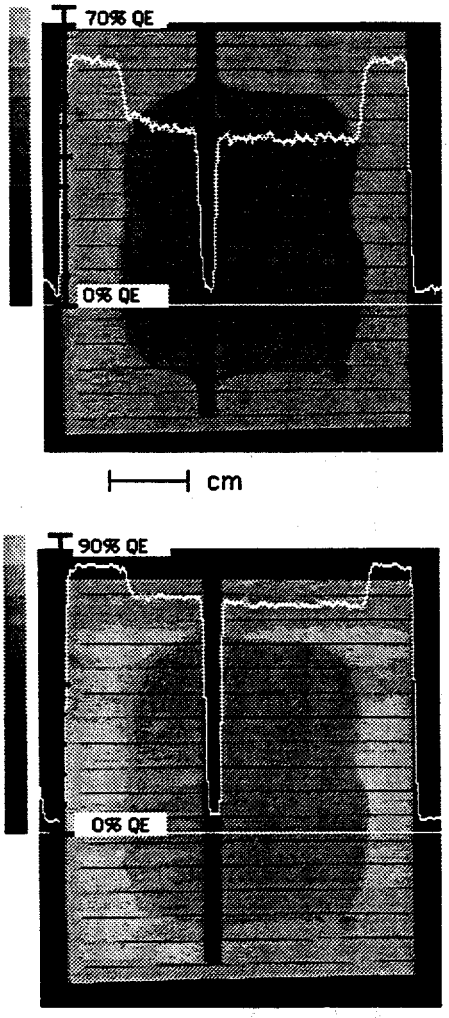

Figure 4. Scanning laser OBIC maps of the photocurrent responses for a Type II cell in Fig. 3b; (top) a "blue" scan with a 488-nm Ar laser beam, and (bottom) a "red" scan with a 633-nm He-Ne laser beam. The shaded areas in the central regions of the figures indicate the brown EVA. The horizontal white lines at 0 %QE indicate the positions of the line scan and the curves indicate the corresponding photocurrent with the OBIC response scales on the left. The QE% in the scanning laser OBIC was corrected with a monocrystalline-Si reference solar cell.

ACKNOWLEDGMENTS

The authors thank D. Dunlavy, H. Field, K. Emery, and R. Matson of the Center for Measurements and Characterization at NREL for their assistance and discussion in the I-V, QE, and laser OBIC measurements. We also thank A. W. Czanderna and R. DeBlasio for their support. This work was performed as part of the task entitled "Reliability Science of Encapsulated PV Cells" with the support by the U. S. Department of Energy under contract No. DE-AC36-83CH10093.

REFERENCES

1. A. W. Czanderna and F. J. Pern, "Encapsulation of PV Modules Using Ethylene Vinyl Acetate Copolymer as a Pottant: A Critical Review," *Solar Energy Materials and Solar Cells*, **43**, 1996, In press. (NREL/TP-412-7359)

2. F. J. Pern, "A Comparative Study of Solar Cell Performance under Thermal and Photothermal Tests," *Proc. PV Performance and Reliability Workshop*, Golden, CO, Sept. 16-18, 1992, pp. 326-44. (SERI/CP-411-5184)

3. F. J. Pern, A. W. Czanderna, K. A. Emery, and R. G. Dhere, "Weathering Degradation of EVA Encapsulant and The Effect of Its Yellowing on Solar Cell Efficiency," *Proc. 22nd IEEE PVSC*, Las Vegas, Nevada, Oct. 7-11, 1991, pp. 557-561.

4. F. J. Pern, "Factors That Affect The EVA Encapsulant Discoloration Rate Upon Accelerated Exposure," *Proc. 24th IEEE PVSC, First WCPEC*, Waikoloa, Hawaii, Dec. 4-9, 1994, pp. 897-900. For an expanded version, *Solar Energy Materials and Solar Cells*, **41/42**, 1996. In press.

5. F. J. Pern, "Luminescence and Absorption Characterization of The Structural Effects of Thermal Processing and Weathering Degradation on Ethylene Vinyl Acetate (EVA) Encapsulant for PV Modules," *Polym. Deg. and Stab.*, **41**, 1993, 125-139. (NREL/TP-213-4605)

6. F. J. Pern and S. H. Glick, "Fluorescence Analysis as a Diagnostic Tool for Polymer Encapsulation Processing and Degradation," in R. Noufi and H. Ullal ed. *AIP Conference Proceedings* no. 306, American Institute of Physics, NY, 1994, pp. 573-585. (NREL/TP-412-5996)

7. R. J. Matson, K. A. Emery, I. L. Eisgruber, and L. L. Kazmerski, "The Large-Scale Laser Scanner: Milli-Characterization of Photovoltaic Devices and Modules," *Proc. 12th Euro. PVSEC*, Amsterdam, The Netherlands, April 11-15, 1994, **II**, pp. 1222-1225.

8. I. L. Eisgruber, R. J. Matson, J. R. Sites, and K. A. Emery, "Interpretation of Laser Scans from Thin-Film Polycrystalline Photovoltaic Modules," *Proc. 24th IEEE PVSC, First WCPEC*, Waikoloa, Hawaii, Dec. 4-9, 1994, pp. 283-286.

THERMAL PROCESSING OF EVA ENCAPSULANTS AND EFFECTS OF FORMULATION ADDITIVES

F. J. Pern and S. H. Glick

Center for Performance Engineering, Qualification, and Reliability
National Renewable Energy Laboratory
Golden, Colorado

ABSTRACT

We investigated the *in-situ* processing temperatures and effects of various formulation additives on the formation of ultraviolet (*UV*) excitable chromophores in the thermal lamination and curing of ethylene-vinyl acetate (*EVA*) encapsulants. A programmable, microprocessor-controlled, double-bag vacuum laminator was used to study two commercial as-formulated EVA films, A9918P and 15295P, and solution-cast films of Elvax™ (*EVX*) impregnated with various curing agents and antioxidants. The results show that the actual measured temperatures of EVA lagged significantly behind the programmed profiles for the heating elements and were affected by the total thermal mass loaded inside the laminator chamber. The antioxidant Naugard P™, used in the two commercial EVA formulations, greatly enhances the formation of UV-excitable, short chromophores upon curing, whereas other tested antioxidants show little effect. A new curing agent chosen specifically for the EVA formulation modification produces little or no effect on chromophore formation, no bubbling problems in the glass/EVX/glass laminates, and a gel content of ~80% when cured at programmed 155°C for 4 min. Also demonstrated is the greater discoloring effect with higher concentrations of curing-generated chromophores.

INTRODUCTION

EVA copolymer encapsulant is widely used for the encapsulation of crystalline silicon (*Si*) and some thin film photovoltaic (*PV*) modules. Two commercial formulations are available: EVA A9918 using a slow-curing agent Lupersol 101™ (*L-101*) and EVA 15295 using a fast-curing agent Lupersol TBEC™ (*L-TBEC*) with or without adding a primer (*P*). Specific processing conditions, i.e., temperature, time, and pressure, are not readily known because they are considered proprietary information by PV manufacturers. The two EVA formulations have been confirmed to turn yellow to brown as a result of photothermal degradation in the field or accelerated exposure in the laboratory [1-4]. EVA browning can reduce PV module efficiency because of decreased light transmittance [3,4]. Both of the formulation additives and curing-generated chromophores contribute to EVA discoloration [2]. In addition, if not carefully processed, EVA 15295 has a tendency to generate bubbles in modules during encapsulation because of thermal decomposition of L-TBEC to produce CO_2 and other gaseous organics at the curing temperatures.

This work is part of our continuing effort to improve the photostability of EVA with modified formulations [5]. The purposes of this work are to (1) investigate and monitor in-situ the actual temperatures of the EVA film and the heating elements in the laminator chamber during the thermal lamination and curing processes, (2) determine the thermal and chemical factors that affect formation of chromophores in curing the EVA films, and (3) determine the usefulness of the new additives used--a curing agent and antioxidants in particular--in the improved EVA formulations that achieve simultaneously faster curing, no bubbling problems, and minimum formation of UV-excitable chromophores. We also demonstrated experimentally the discoloring effect of curing-generated chromophore concentration.

EXPERIMENTAL

Extruded films of as-formulated, commercial EVA A9918P and 15295P were provided by vendors. Solution-cast films were prepared by drying in Petri dishes ~40 ml of cyclohexane or tetrahydrofuran solutions of Du Pont's Elvax™ (*EVX*) at a concentration of 50 mg/ml that were addeded with predetermined concentrations of various curing agents and stabilizers. The films were laminated/cured between two soda lime glass microslides or borosilicate slides using programmed temperature-pressure-time profiles on a custom-built, lab-scale, microprocessor-controlled, programmable, double-bag vacuum laminator. Sturdy aluminum spacer frames and plates were used to allow good control of the cured EVA layer thickness. Several thermocouples were installed to control and monitor *in-situ* the temperatures of the heating elements, heating rates, and EVA laminates inside the chamber. Emphasis was placed on fast-curing to reduce the PV encapsulation time. All laminates were analyzed for fluorescence characteristics with a SPEX Fluorolog-II spectrofluorophotometer [6,7] and some for their gel content. To demonstrate the discoloring effect of curing-generated chromophores, one set of samples containing increased concentrations of both the UV light

stabilizer, Tinuvin 770™ (*T-770*), and the antioxidant, Naugard P (*Na-P*), was exposed to enhanced UV light from an Oriel 1-kW Xe solar simulator at a black panel temperature (*BPT*) of 44°C ± 2°C for over 1500 h.

RESULTS AND DISCUSSION

I. *In-situ* monitored EVA temperatures during lamination and curing processes

Figure 1a shows the typical temperature-time profiles programmed for the heating elements and used for processing the slow-cure and fast-cure EVA in this work to study the chromophore formation at various temperatures. The vacuum-pressure controls were "built-in" in the programs and were activated when certain temperature-time set points were reached. However, the temperature-time profiles can be altered easily so that the lamination and curing steps are done in a "one-step, high temperature" manner to reduce the processing time. The actual temperatures monitored for the heating elements, EVA 15295P, and EVA A9918P are shown in Figs. 1b and 1c, respectively. The results show that the actual EVA temperatures lagged significantly behind the programmed profiles for the heating elements. The thermal lagging was noticeably affected further by total thermal mass loaded inside the laminator chamber. Furthermore, in fast curing the EVA temperatures barely reached the programmed set point (Fig. 1b), whereas in slow curing the EVA temperatures exceeded the set point significantly (Fig. 1c). The consequence of a lagging or uncertainty in curing temperature is a lack of precise control of temperature for producing the desired gel content in the EVA laminates. A minimum gel content of ~70% is required to provide sufficient mechanical strength to support the solar cells in a PV module.

II. Effect of antioxidants and curing agents on the formation of chromophores by curing

The effect of the antioxidant Naugard P (*Na-P*) on increasing the formation of chromophores was verified for the first time in this study. Na-P is used in both A9918P and 15295P EVA formulations. The results of fluorescence analysis seen in Fig. 2a show that a large increase in the chromophore concentration was observed for the EVX films cured with L-101 in the presence of Na-P (curves 1/A vs. 3/C). Without Na-P, the EVX films cured with a curing agent or "pseudo-cured" under conditions as if with L-101 (curves 2/B) show little change in the chromophore concentrations. Similar results are obtained for the EVX films cured with Lupersol TBEC as shown in Fig. 2b (curves 1/A vs. 4/D). Accordingly, curing of the two commercial EVA formulations in the presence of Na-P will inevitably increase the concentration of UV-excitable chromophores, which can lead to enhanced Norrish degradation reactions [4,8].

In principle, greater polymer photostability can be realized if the concentrations of degradation-inducing chromophores can be minimized [8]. We have identified

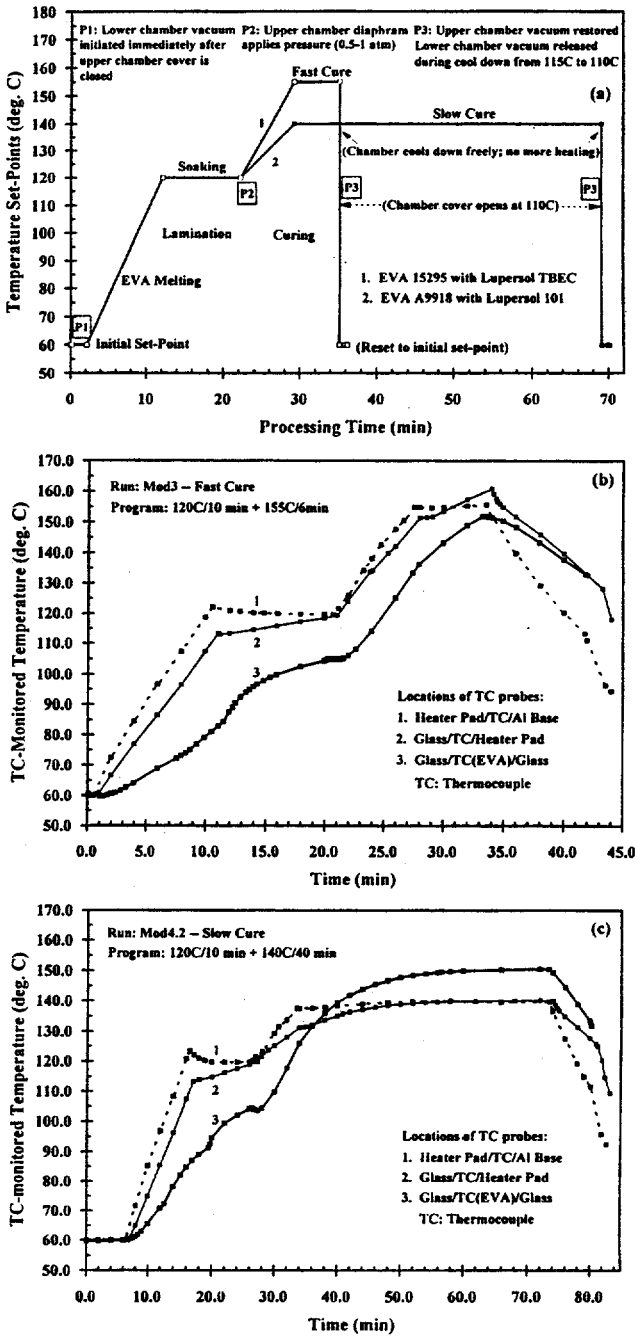

Figure 1. (a) Programmed temperature-time profiles for fast-cure EVA 15295 formulation using Lupersol TBEC (*L-TBEC*) and slow-cure EVA A9918 formulation using Lupersol 101 (*L-101*). The temperatures are programmed for the heating elements in the vacuum laminator. The vacuum-pressure controls are "built-in" to the programs and are activated automatically at certain temperature-time set points. (b) The *in-situ* monitored actual temperature-time profiles for the heating elements and EVA 15295 laminates. (c) Same as (b) but for EVA A9918.

a fast-curing agent that performs better than L-TBEC and a number of antioxidants that are better than Na-P with results illustrated in Figs. 2b and 2c. Figure 2b (curves 6/F) shows that very low chromophore concentration was present in the films laminated at 80°C (no curing yet). But as mentioned above, the presence of Na-P in fast-curing with L-TBEC or a new curing agent (labeled as "L-X" here) greatly increased the concentration of UV-excitable chromophores (curves 1/A and 2/B). The chromophore concentration decreased noticeably when Na-P was replaced by a new antioxidant AO-1 (curves 3/C). In the absence of Na-P, L-TBEC produced somewhat higher concentration of the chromophores than L-X (curves 4/D vs. 5/E). Figure 2c shows that, as compared to the plain EVX films, the L-X curing agent and other chosen antioxidants (labeled as AO-2, -3, and -4) have a minimal effect on chromophore formation. In addition, L-X and the antioxidants (AO-1, 2, 3, and 4), chosen specifically for modifying the EVA formulations, do not cause bubbling problems in the glass/EVX/glass laminates and gave a gel content of ~80% when cured at programmed 155°C for 4 min. Bubbling problems are well known when using L-TBEC in the EVA 15295 as are frequently encountered by PV manufacturers.

III. Discoloring effect of curing-generated chromophores at high concentrations

The effect of a high concentration of curing-generated chromophores on the discoloration of cured EVX laminates is demonstrated in Fig. 3, where a set of samples that contained increasingly greater amounts of Na-P and T-770 were exposed to enhanced UV light. The two additives were maintained at a fixed molar ratio. Fig. 3a shows the fluorescence excitation and emission spectra for the samples before UV exposure, and Fig. 3b shows the spectra after 1104 h of exposure. Figure 3c shows the net change in yellowness index (*YI*) for the samples as a function of exposure time. The discoloration rate is greater for the samples with higher chromophore concentrations produced from curing. On the other hand, results from previous study indicate that high concentration of T-770 can facilitate photodecomposition of the UV absorber, Cyasorb UV 531™ [5]. Thus, the contribution of T-770 at higher concentrations in Fig. 3 to the EVA discoloration remains to be determined.

CONCLUSION

By processing EVA between glass slides, we have shown that processing EVA during simulated encapsulation of PV cells can be adversely affected by a lagging laminator temperature and uncertainty in temperature control. The effect of antioxidant Naugard P on forming and increasing the concentration of UV-excitable chromophores upon curing is verified for the first time. We found that the concentrations of curing-generated, UV-excitable chromophores can be reduced significantly by using curing agent and antioxidants other than those used in the the current commercial EVA formulations. We also showed that the chromophores at

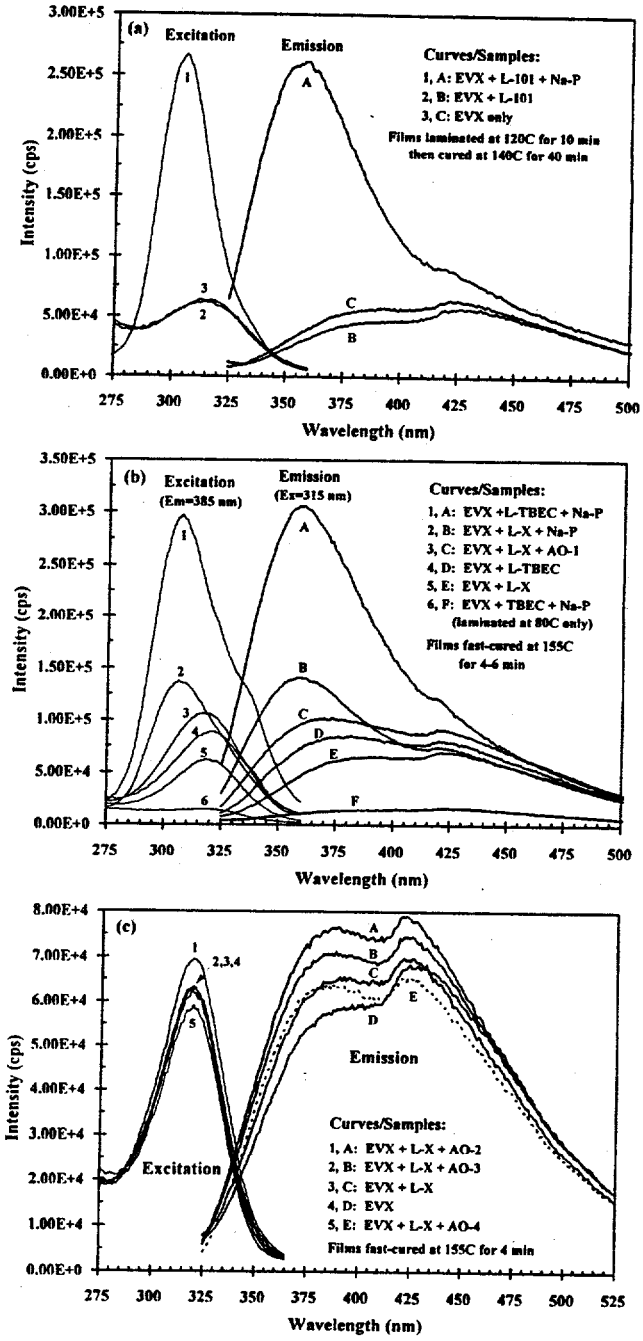

Figure 2. Fluorescence excitation and emission spectra (a) for cured EVX films that were prelaminated at 120°C for 10 min; (1, A): EVX added Naugard P (*Na-P*) and cured with L-101; (2, B): EVX cured with L-101; and(3, C): plain EVX but "pseudo-cured" as if with L-101; (b) laminated and cured EVX films impregnated with curing agents L-TBEC and L-X (see text) with or without antioxidant Na-P or AO-1, before and after curing at programmed 155°C for 4 min to 6 min; and (c) laminated and cured EVX films with or without the curing agent L-X and antioxidants, AO-2, -3, and -4. The spectra are not subtracted from those of microslide.

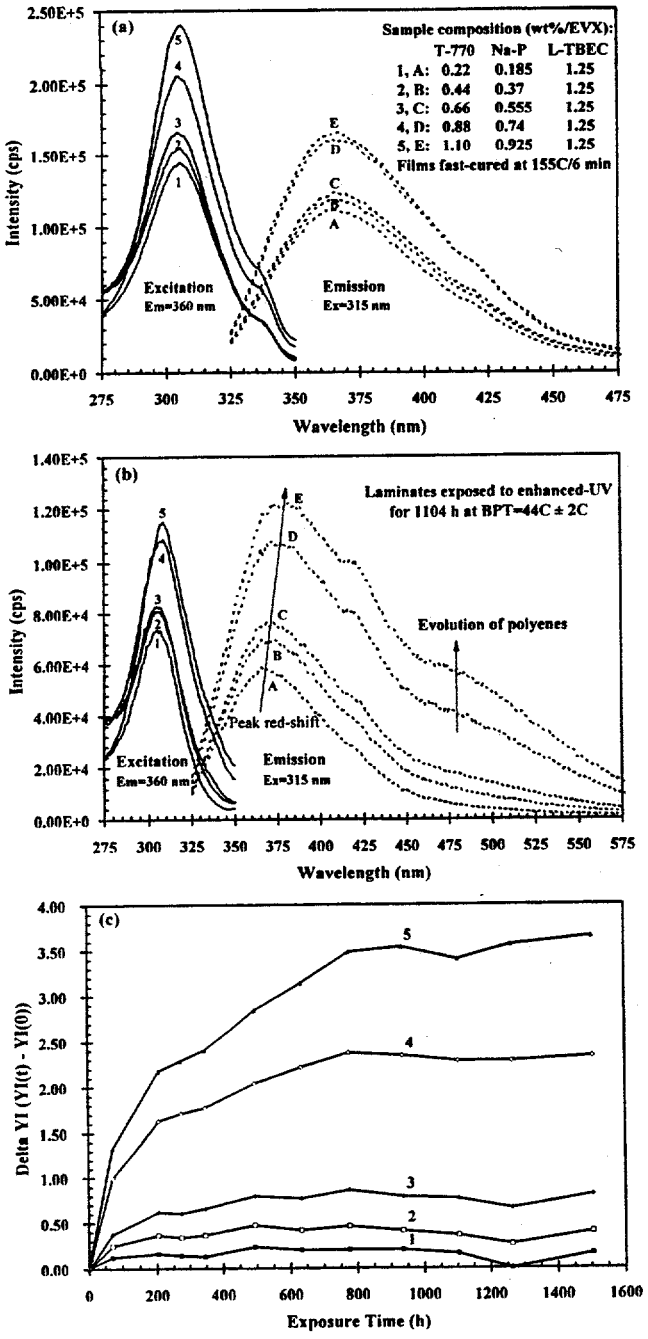

Figure 3. Fluorescence excitation and emission spectra for (a) as-cured EVX films laminated between two borosilicate slides and (b) UV-exposed at BPT=44 °C ± 2°C for 1104 h. The EVX films were impregnated with increasing concentrations of both Tinuvin 770 and Naugard P from sample 1 to 5 at a fixed molar ratio, as indicated in the figure, and cured with 1.25 wt% L-TBEC. (c) Net change in yellowness index (*YI*) measured as a function of UV exposure time for the set of samples.

higher concentrations can induce a higher discoloration rate.

ACKNOWLEDGMENTS

The authors thank the support of their team leader, A. W. Czanderna, and project manager, R. DeBlasio. This work was performed as part of the task entitled "Reliability Science of Encapsulated PV Cells" with the support by the U.S. Department of Energy under contract No. DE-AC36-83CH-10093.

REFERENCES

1. F. J. Pern, "Comparison of The Photostability for Two Common EVA Formulations: EVA A9918 and EVA 15295", *Proc. of 6th PV Performance and Reliability Workshop*, Sept. 21-23, 1994, Lakewood, CO, pp. 329-347. (NREL/CP-411-7414).

2. F. J. Pern, "Factors That Affect the EVA Encapsulant Discoloration Rate Upon Accelerated Exposure," *Proc. of 24th IEEE PVSC at the First World Conference on Photovoltaic Energy Conversion*, Dec. 4-9, 1994, Waikoloa, Hawaii, pp. 897-900. (NREL/TP-412-7425).

3. F. J. Pern, "A Comparative Study of Solar Cell Performance under Thermal and Photothermal Tests," *Proc. PV Performance and Reliability Workshop*, Golden, CO, Sept. 16-18, 1992, pp. 326-44. (SERI/CP-411-5184)

4. A. W. Czanderna and F. J. Pern, "Encapsulation of PV Modules Using Ethylene Vinyl Acetate Copolymer as a Pottant: A Critical Review," *Solar Energy Materials and Solar Cells*, **43**, 1996, In press. (NREL/TP-412-7359)

5. F. J. Pern, "Modification of EVA Formulation for Improved Stability," *Proc. PV Performance and Reliability Workshop*, Golden, CO, Sept. 8-10, 1993, NREL, pp. 358-74. (NREL/TP-410-6033)

6. F. J. Pern, "Luminescence and Absorption Characterization of The Structural Effects of Thermal Processing and Weathering Degradation on Ethylene Vinyl Acetate (EVA) Encapsulant for PV Modules," *Polym. Deg. and Stab.*, **41**, 1993, pp. 125-139.

7. F. J. Pern and S. H. Glick, "Fluorescence Analysis as a Diagnostic Tool for Polymer Encapsulation Processing and Degradation," in Noufi R, Ullal H (Eds), *AIP Conference Proceedings for the 12th NREL PV Program Review Meeting*, book no. 306, American Institute of Physics, NY, 1994, pp.573-585. (NREL/TP-412-5996)

8. (a) J. F. McKellar and N. S. Allen, "*Photochemistry of Man-Made Polymers*," Applied Science, London, 1979. (b) N. M. Emanuuel and A. L. Bucgachenko, "*Chemical Physics of Polymer Degradation and Stabilization*," VNU Science Press, Utrecht, The Netherlands, 1987.

EFFECT OF HEAT TREATMENTS AND WINDOW LAYER PROCESSING ON THE CHARACTERISTICS OF $CuInGaSe_2$ THIN FILM SOLAR CELLS

K. Ramanathan, M. A. Contreras, J. R. Tuttle, J. Keane, J. Webb, R. Dhere, A. L. Tennant, F. S. Hasoon, and R. Noufi
National Renewable Energy Laboratory, 1617 Cole Blvd., Golden CO 80401.

ABSTRACT

Interaction between chemical bath deposited CdS and ZnO window layers are a focus of this paper. Low temperature anneals were used to follow the changes at the interface. Optical absorption spectra show that CdS and ZnO intermix upon annealing. When applied to ZnO/CdS/ $CuInGaSe_2$ thin film solar cells, changes in the short and long wavelength response were observed. The latter is attributed to an increase in the energy gap of the absorber by diffusion of S. The interdiffusion is shown to increase the short wavelength collection, and hence the current density of the devices. Photoluminescence data provides some indication of the quality of the interface.

INTRODUCTION

Thin film solar cells based on $CuInSe_2$ and its alloys with Ga and S have demonstrated excellent efficiencies in the laboratory scale. In our laboratory, a 17.7% efficiency device based on $CuInGaSe_2$ absorber has been recently demonstrated [1]. The devices are fabricated by depositing a thin layer of CdS by chemical bath deposition (CBD), followed by a bilayer of sputtered ZnO. The first layer adjacent to the CdS is typically 50 nm thick, and it is sputtered in a slight oxygen partial pressure using an undoped ZnO target to a resistivity of 10-50 Ω-cm. The second layer is subsequently deposited from an alumina doped ZnO target in pure argon atmosphere to produce a conductive, transparent contact. Typical thickness and resistivity of this layer are 350 nm and 5 x 10^{-4} Ω-cm, respectively.

Much attention has been paid to the reaction chemistries and the absorber formation via different routes, but there has not been a similar dedicated effort in the junction area. There are many fundamental questions that demand attention. For example, the reactive nature of the chemical bath and the possibility of an intermediate compound formation during the CBD has been suggested, but it requires more serious incorporation into modeling and in explaining the observed heterojunction phenomena. Chemically grown CdS is known to exhibit a mixture of cubic and hexagonal phases [2]. The crystal structure of the CdS and the consequence of a lattice mismatch between CdS and ZnO is an important issue. There is a significant difference in the lattice constants between ZnO and CdS. For the wurtzite form, a = 4.14 Å and 3.25 Å; and c = 6.72 Å and 5.2 Å for CdS and ZnO, respectively. For the cubic CdS, a = 5.82 Å. Although the polycrystalline nature of the interfaces involved will relax the lattice mismatch to some extent, the implications cannot be dismissed outright. Given the compatibility of crystal structures and chemical nature of the CdS and ZnO, the two can be expected to react, forming solid solutions. Finally, the use of a high/low resistivity ZnO combination and its effect on the device performance has not been thoroughly studied.

In this paper, we have attempted to study the interaction between the CBD CdS and the ZnO deposited on glass and on $CuInGaSe_2$ thin films. We have used a set of annealing conditions to identify the changes that take place. Optical absorption, device current-voltage and spectral response measurements have been used to study the effect of heat treatment on solar cell properties.

EXPERIMENTAL

The $CuInGaSe_2$ thin films used in this study were prepared by elemental coevaporation by the method described previously [3]. The substrates were soda lime silicate glass onto which a 1 μm thick Mo had been sputter deposited. The Ga/(Ga+In) ratio was 0.28-0.3. The films were specular and free of defects. CdS was grown to a thickness of 50 nm by the reaction of $CdSO_4$ and thiourea in an ammoniacal bath. The bath composition was 0.0015 M $CdSO_4$, 1.5 M NH_4OH and 0.15 M thiourea. Thiourea was added when the bath temperature was 40°C, and the reaction proceeded as the temperature rose to 70°C in about 5 min. This allowed the deposition of about 50 nm thick CdS layer. Clean borosilicate glass substrates (Corning 7059) were also used for depositing the CdS for optical absorption experiments. For all the standard device data, the CdS coated $CuInGaSe_2$ films were annealed at 200°C for 2 min. in air. The standard procedure for ZnO deposition, described above, was modified for the purposes of the experiments performed here. In many cases, the samples were brought out of the sputter system after only the undoped ZnO had been deposited. They were annealed at different conditions, and the doped ZnO layer was deposited subsequently to fabricate devices. The intention here was to minimize the increase in sheet resistance of the conductive ZnO layer,

described below.

First, we examine the effect of heat treatments on the CdS/ZnO structures on glass. The CdS was deposited in the usual manner, and a ZnO bilayer was sputtered onto the CdS layer. Optical reflectance and transmittance data were taken in the wavelength range 300-1300 nm at every stage of the heat treatment. Absorption was deduced from the measured reflectance and transmittance data. Sheet resistance of the ZnO layer was also measured. We expect the current flow to be confined mainly to the conductive ZnO layer because the undoped ZnO and the CdS layers are more resistive. An increase in sheet resistance of the structure was observed upon heating at modest temperatures and short durations. The as deposited sample had a sheet resistance of 18 Ω/sq, and this quickly increased to about 60 Ω/sq after 2 min. anneal in air at 200°C, and to about 100 Ω/sq after a 2 min. anneal at 250°C. This increase was also observed for anneals in argon, and this points to a thermal rather than oxygen related phenomenon. Identical ZnO bilayers on glass, annealed under the same conditions, did not exhibit any change in sheet resistance The resistance increase is attributed to a compensation of the donors in the ZnO:Al layer by an element or species diffusing from below. This is likely to be sulfur from the CdS, but no confirmation has been obtained.

Optical spectra (see Figure 1) show that there is a significant reduction in the absorption due to the anneals. In this spectral region, ZnO is non-absorbing,

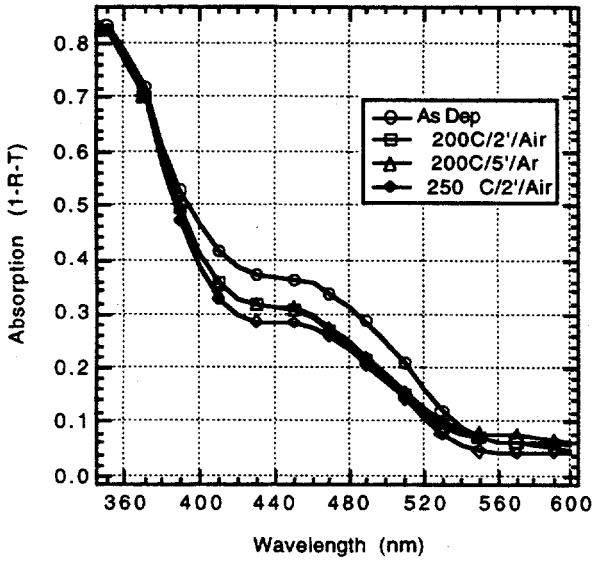

Fig. 1. Optical absorption of glass/CdS/ZnO structures annealed at different conditions.

and the CdS is strongly absorbing. A reduction in the absorption can be explained by the formation of an intermediate layer between CdS and ZnO that is of an energy gap higher than that of CdS. The candidate materials are $Cd_{1-x}Zn_xS$ and $ZnO_{1-x}S_x$, the exact nature of which was not determined in this study. Nevertheless, it is reasonable to argue that the heat treatment causes an intermixing between CdS and ZnO, with a possibility of a

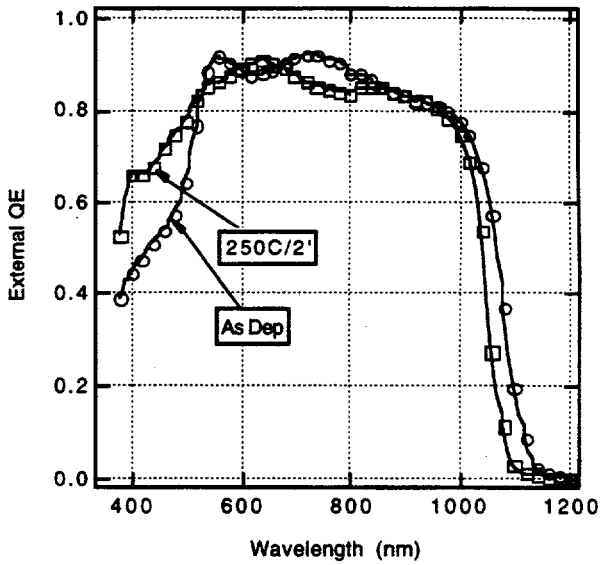

Fig. 2. Spectral response of ZnO/CdS/CuInGaSe$_2$ devices. Heat treatments were made after the undoped ZnO was deposited.

reduced CdS thickness. If this effect can be used in a ZnO/CdS/CuInGaSe$_2$ solar cell, it is likely to demonstrate a better short wavelength response.

Fig. 2. shows the spectral response of two ZnO/CdS/CuInGaSe$_2$ cells fabricated on absorbers prepared in the same run but from different parts of the substrate. They were annealed differently following the undoped ZnO deposition. Open circles correspond to the case where the ZnO bilayer was deposited on the CdS and

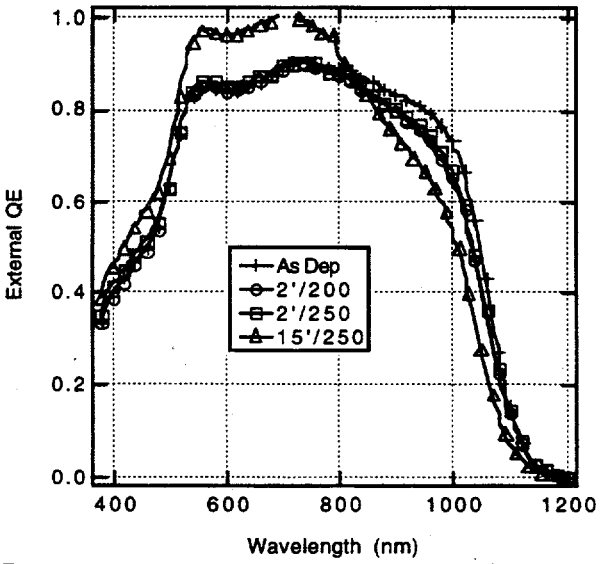

Fig. 3. Spectral response of a ZnO/CdS/CuInGaSe$_2$ device at various stages of anneal.

no further heat treatment was given. Open squares

represent a device where the undoped ZnO was deposited on the CdS, the sample was heat treated at 250°C for 2 min., followed by the deposition of ZnO:Al. We find that the blue response of the heat treated device is significantly improved. The gain in the current density was estimated to be 1.2 $mA.cm^{-2}$. Also, the long wavelength edge of this device has moved to shorter wavelengths, indicating an increase in the bandgap of the absorber itself. This is possibly caused by the diffusion of sulfur into the absorber. Ga diffusion to the surface of the absorber, another possibility that can account for the bandgap increase, is considered unlikely due to the low temperatures and short times involved in the heat treatments.

Fig. 3. shows the spectral response of the same device that was subjected to repeated anneals. Major changes are observed for a prolonged anneal at 250°C. The long wavelength edge moves to shorter wavelengths or higher energies, an effect similar to that shown in Fig. 2. The improvement in the short wavelength region is also evident. More interesting is the gain in the spectral response in the visible region which enhances the collection to near unity. This can be attributed to the reduction of recombination in the junction/ depletion region by affording better passivation. It is conceivable that, in addition to interdiffusion between CdS and ZnO, significant changes can occur at the CdS/$CuInGaSe_2$ interface.

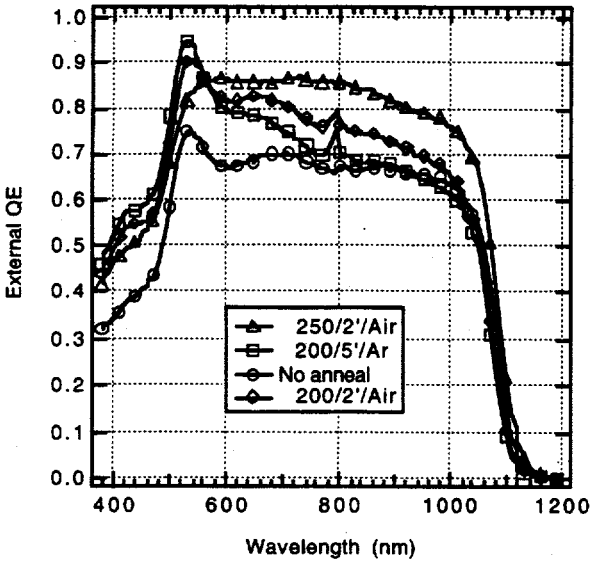

Fig. 4. Spectral response of ZnO/CdS/$CuInGaSe_2$ devices. Heat treatments were made after the undoped ZnO was deposited.

Figs. 4 and 5 show the spectral response and current voltage characteristics of four devices where the $CuInGaSe_2$/CdS/ZnO structures were annealed at different temperatures following the undoped ZnO deposition. In all but the 250°C anneal, we find that the response peaks around the CdS bandgap value, and it tails off in the red region. The corresponding device parameters are poor, ranging from 5%-9%, characterized by low voltages and poor fill factors. There appears to be a voltage dependent collection loss, as evidenced by the soft I-V in the forward bias region.

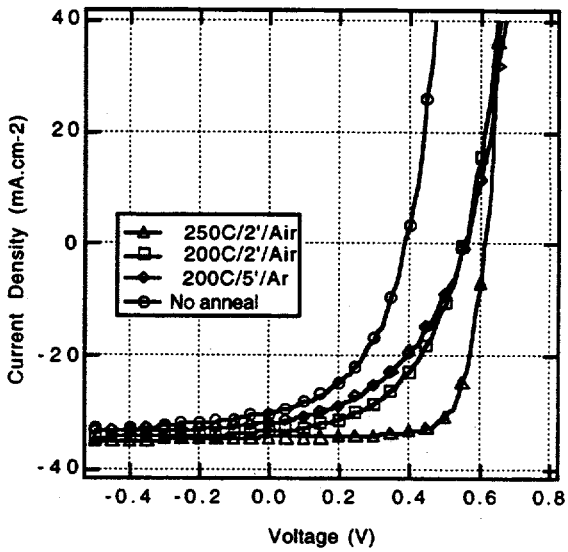

Fig. 5. Illuminated I-V curves for the devices shown in Fig. 4.

Modeling efforts [4,5] have shown that surface and interface states can have a profound influence on the diode characteristics. In particular, the addition of trap states in the CdS and acceptor like states at the CdS/ZnO interfaces are shown to produce anomalous I-V curves. A similar explanation is invoked here, although the mechanisms may be quite different. The 250°C anneal seems to have annealed out the interface states, as inferred from the I-V curve (14.8% efficiency) and the panchromatic spectral response.

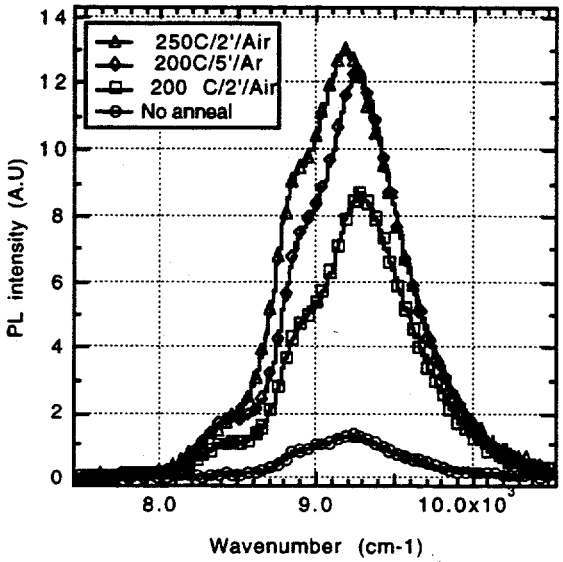

Fig. 6. PL emission spectra of devices shown in Fig. 4.

Photoluminescence (PL) spectra taken at room

temperature for the four devices are shown in Fig. 6. The most noticeable difference is the higher intensity of the higher efficiency devices. There are two peaks observed in the low energy side of the main peak. The peaks on the lower energy side (lower wavenumbers) have been assigned to donor-acceptor pair transitions [6]. There appears to be a shift in some of the peak positions as well, but we have not attempted a deconvolution of the spectra. A detailed publication on this subject will be forthcoming.

CONCLUSIONS

We have shown that modest heat treatments to CdS/ZnO structures produces significant changes in the optical and electrical properties. A reduction in the CdS related absorption points to the formation of an interdiffused region with a wider band gap. This effect translates, rather beneficially, to ZnO/CdS/$CuInGaSe_2$ thin film cells where the short wavelength response is improved. The bandgap of the absorber is also increased as a result of the heat treatment, and we speculate that the diffusion of sulfur in the $CuInGaSe_2$ could be the cause. A wide range of current-voltage and spectral response behaviors are observed that can be accounted for by invoking bulk and/or interface states. PL spectra show an approximate correlation between device efficiency and the PL intensity.

ACKNOWLEDGMENTS

The authors acknowledge the help of Brian Keyes and Don Dunlavy. This work is supported by the U. S. Department of Energy under Contract No. DE-AC36-83CH10093 to the National Renewable Energy Laboratory.

REFERENCES

1. J. R. Tuttle, J. S. Ward,A. Duda, T. A. Berens, M. A. Contreras, K. Ramanathan, A. L. Tennant, J. Keane, E. D. Cole, K. Emery, and R. Noufi, *Materials Research Society Meeting*, San Francisco, March 1996, to be published.
2. T. Nakanishi and K. Ito, *Solar Energy Mater.* 35, 171 (1994).
3. M. A. Contreras, J. Tuttle, A. Gabor, A. Tennant, K. Ramanathan, S. Asher, A. Franz, J. Keane, L. Wang, and R. Noufi, *Proc. 1st WCPEC*, Hawaii, Dec. 1994, p. 68.
4. Y. J. Lee and J. L Gray, *Proc. 1st WCPEC*, Hawaii, Dec. 1994, p.287.
5. T. Walter, D. Hariskos, R. Herberholz, V. Nadenau, R. Shaffler and H. Schock, *13th European PVSEC*, Nice, Oct. 1995, to be published.
6. S. Zott, K. Leo, M. Ruckh and H. W. Schock, Appl. Phys. Lett., **68**, 1144 (1996).

THE ROLE OF OXYGEN IN CdS/CdTe SOLAR CELLS DEPOSITED BY CLOSE-SPACED SUBLIMATION

Doug H. Rose, Dean H. Levi, Rick J. Matson, David S. Albin, Ramesh G. Dhere, and Peter Sheldon
National Renewable Energy Laboratory, 1617 Cole Blvd., Golden, CO 80401

ABSTRACT

The presence of oxygen during close-spaced sublimation (CSS) of CdTe has been previously reported to be essential for high-efficiency CdS/CdTe solar cells because it increases the acceptor density in the absorber. We find that the presence of oxygen during CSS increases the nucleation site density of CdTe, thus decreasing pinhole density and grain size. Photoluminescence showed that oxygen decreases material quality in the bulk of the CdTe film, but positively impacts the critical CdS/CdTe interface. Through device characterization we were unable to verify an increase in acceptor density with increased oxygen. These results, along with the achievement of high-efficiency cells (13% AM1.5) without the use of oxygen, led us to conclude that the use of oxygen during CSS deposition of CdTe can be useful but is not essential.

INTRODUCTION

CdS/CdTe solar cells are notable contenders in the race for inexpensive, high-efficiency photovoltaics [1]. The breakthrough that created much of the current interest in n-CdS/p-CdTe thin-film cells was the use of oxygen ambient during close-spaced sublimation (CSS) of CdTe by researchers at Eastman Kodak. Through this innovation, they were able to break the 10% efficiency barrier for thin-film CdTe solar cells [2]. The use of oxygen during CSS deposition of CdTe culminated at the University of South Florida with a 15.8% cell, the current world record for CdTe cells [3,4].

To date, research on oxygen ambient has focused on its effect as a dopant. It has been reported that oxygen is essential to high-efficiency cells because it increases the acceptor density in the CdTe absorber thus preventing buried homojunction formation [5-8]. Such junctions have low photon collection due to the high absorption coefficient of CdTe.

The presence of oxygen during deposition has some disadvantages. Depositions in an oxygen ambient cause CdTe sources to non-uniformly oxidize, reducing the source flux [9]. Additionally, oxygen can cause surface features of 0.5 to 10 μm in height on the CdTe film, most likely through ejection of particles from the source material [9]. These effects can reduce device efficiency and run-to-run reproducibility, which could present problems for high-volume manufacturing.

Because the use of oxygen has disadvantages, we were led to the questions, " What is role of oxygen in CSS CdTe cells, and is it truly essential?" In this paper we describe some effects of oxygen other than doping. We also report high-efficiency CdS/CdTe solar cells made without oxygen in any stage of production and present a plausible alternative to the theory that oxygen acts as an acceptor in CSS-deposited CdTe.

EXPERIMENTAL DESCRIPTION

Solar cells were fabricated with a superstrate structure consisting, in most cases, of the following layers: glass/SnO_2/CdS/CdTe/back contact material (HgTe:Cu-doped graphite or multilayer metal). The substrate used for the majority of experiments was Corning 7059 glass, with a SnO_2 layer (Solarex) serving as the transparent front contact. A thin (600-1200 Å) CdS layer was applied by chemical bath deposition [9] and then annealed at 400°C in 30 torr H_2 for 15 minutes. CSS deposition of the CdTe was accomplished by placing a CdTe source plate in close proximity (2-6 mm) to the substrate. The source was heated to 630°-680°C and the substrate to 500°-620°C. This arrangement causes Cd and Te to sublime from the source and diffuse to the substrate. The ambient used during CdTe deposition was a mixture of O_2 and He, with O_2 partial pressures of 0-24 torr and He partial pressures of 0-45 torr.

A post-deposition anneal was performed on most of the samples by soaking in $CdCl_2$ dissolved in MeOH, then annealing at 400°C for 40 minutes in a He or a He+O_2 ambient. A back contact was then applied. Additional details of processing CdS/CdTe cells by this method can be found in other publications [9].

Source and substrate temperature control for the CdTe deposition was accomplished by heating graphite susceptors with quartz-halogen lamps. We have previously reported that the graphite susceptors that have typically been used for CSS deposition (Poco Graphite DFP-3-2) can react with oxygen in the deposition chamber at a high enough rate to convert a large portion of the oxygen to CO and CO_2 [9]. The rate of reaction depends on the condition of the graphite susceptors and can change with use. The graphite susceptors used in the experiments for this paper had a pyrolytic graphite coating (Fabmate® from Poco Graphite) that reduced the reaction of the ambient oxygen with the susceptors to a negligible amount, thus providing a constant and reproducible ambient.

RESULTS

Nucleation and Growth

We determined that oxygen increases CdTe nucleation site density, based on the following evidence:

1. Decreased grain size and reduced faceting of CdTe films grown on CdS with oxygen ambient.
2. Improved CdTe coverage of bare glass and SnO_2 substrates with oxygen ambient.
3. Decreased pinhole density of CdTe films grown on CdS in oxygen ambient or on oxidized CdS films.

Grain size tends to scale with film thickness, and the presence of oxygen decreases the sublimation rate from the source; therefore, it was necessary to adjust deposition parameters to achieve similar film thicknesses to legitimately determine the effect of oxygen on grain size and faceting. Figures 1a and 1b are scanning electron micrographs of two films grown using deposition time to achieve similar CdTe thicknesses. The film grown in oxygen clearly has smaller, less-faceted grains.

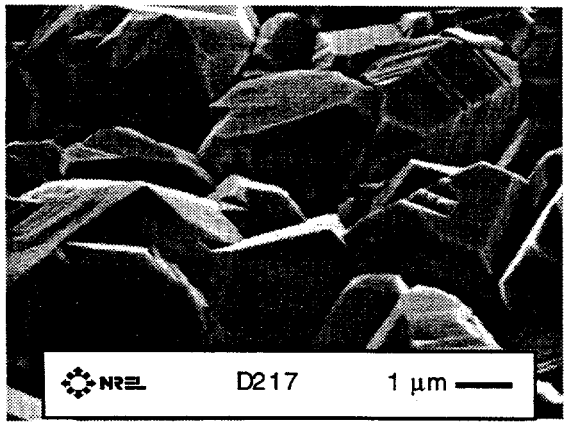

Fig. 1a. CdTe film grown in 15 torr He (source = 640°C, substrate = 600°C, separation = 2 mm, deposition time = 1 minute; film is 4.3 μm thick).

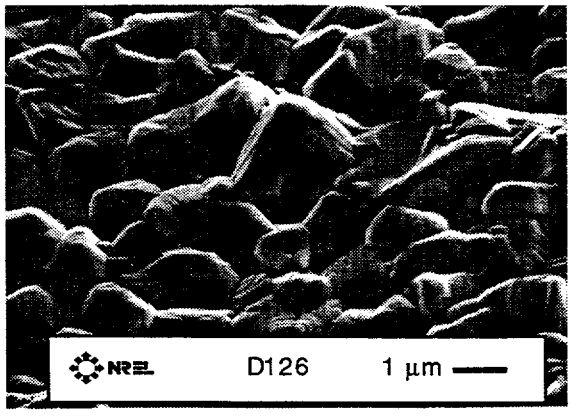

Fig. 1b. CdTe film grown in 2 torr O_2 and 13 torr He (source = 640°C, substrate = 600°C, separation = 2 mm, deposition time = 5 minutes; film is 4.8 μm thick).

The trend of smaller, less-faceted grains with increasing O_2 partial pressure during deposition also holds when the adjustment to achieve similar thickness is done with source temperature or with source/substrate separation.

The ability of oxygen to improve initiation of CdTe growth on bare glass and SnO_2-coated glass is clear. At high substrate temperatures, attempts to deposit CdTe on bare borosilicate glass in the absence of oxygen result in incomplete coverage. To achieve full coverage without oxygen, the substrate temperature must be well below 500°C (low temperature also increases nucleation site density). We found that high levels of oxygen (greater than 4 torr) are capable of producing complete CdTe coverage on bare glass at 600°C. The improvement of nucleation with oxygen is not as dramatic on SnO_2 as it is on bare glass, but it is still evident.

The tendency of oxygen to suppress pinholes can be witnessed by backlighting films with a strong, small light (e.g., a fiber-optic light source). We found that films grown in the absence of oxygen had to be very thick (10-20 μm) to prevent pinholes, whereas films grown in 0.5 to 2 torr oxygen could be free of pinholes at less than 3 μm.

We also found that oxidized CdS can suppress pinhole formation. A CdTe film was grown in the absence of oxygen on a CdS film that had been oxidized at 600°C in 1 torr oxygen for 20 seconds. This CdTe film had fewer pinholes than a film grown under similar circumstances without the prior oxidation of the CdS film. This result provides evidence that the effect of oxygen at the location of growth, and not changes in vapor constituents from source oxidation, is the cause of increased nucleation attributed to the presence of oxygen.

Material Quality As Determined by PL

Through its effect on nucleation, grain size, and defect chemistry, oxygen ambient also affects the minority carrier lifetime in CdTe. We used time-resolved photoluminescence (PL) and PL spectroscopy to probe CdS/CdTe samples made at a range of oxygen partial pressures. Laser excitation at 600 nm allowed us to selectively probe within 1 μm of the surface from either the front (i.e., the CdS/CdTe side) or the back (i.e., the CdTe side) of the cell.

Our measurements indicate that, for as-deposited films, the bulk CdTe (near the back of the cell) is higher quality when growth takes place in the absence of oxygen, as evidenced by lower non-radiative recombination. We took the PL intensity (which indicates the radiative recombination) as a measure of material quality. Figure 2 shows the inverse relationship of the relative PL intensity for as-deposited bulk CdTe to the oxygen partial pressure during growth. In contrast, the intermixed CdS_xTe_{1-x} near the CdS/CdTe junction has improved quality with increasing oxygen. Figure 2 shows the direct relationship of the relative PL intensity from the CdS/CdTe interface to the oxygen partial pressure during growth.

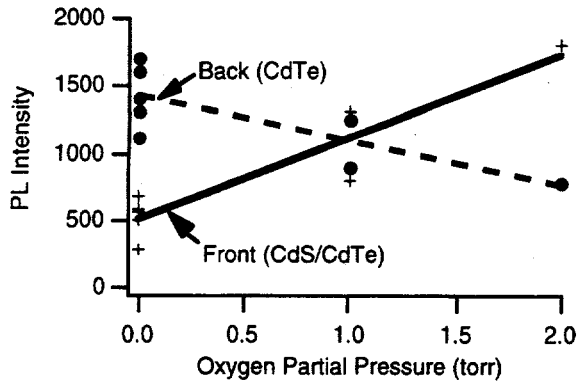

Fig. 2. Relative PL intensity of as-deposited CdTe on CdS films. "Front" indicates illumination of the CdS/CdTe interface. "Back" indicates illumination of the CdTe side.

Like the as-deposited films, films treated by a $CdCl_2$ anneal showed decreased PL intensity with increasing O_2 for the bulk CdTe. For the CdS/CdTe side, a relationship between O_2 partial pressure and PL intensity after the $CdCl_2$ anneal was not evident; however, the PL intensity did increase to an average of 5000 (arbitrary units).

The peak wavelength of the photoluminescence also exhibited a dependence on oxygen partial pressure for as-deposited films. Increasing oxygen shifted the PL peak from 853 nm to 850 nm.

Doping

Device characterization has not as yet corroborated the assertion, made in literature, that oxygen increases the acceptor density in CdTe. Our Capacitance-Voltage (CV) measurements have not shown a correlation between oxygen partial pressure during deposition and doping in the absorber. In addition, electron-beam-induced current (EBIC) and quantum efficiency (QE) measurements were not as conclusive regarding the correlation between the buried homojunction formation and reduced oxygen partial pressure as has been previously reported. Of the many cells that we have fabricated without oxygen, only a few exhibited the deeply buried junction phenomenon described in literature, as evidenced by a QE showing significantly lower collection of 650-nm light relative to the collection of 800-nm light.

EBIC line scans were performed on device cross-sections. Using peak collection to indicate junction location we have seen both shallow and deeply buried (> 1 μm) homojunctions in cells made without oxygen. Variation of junction depth from shallow to deep was also found within a given sample.

The most remarkable result concerning the doping effects of oxygen was the ability to make high-efficiency cells (13% AM1.5) without oxygen, thus countering the contention that oxygen during CSS deposition of CdTe is essential for high-efficiency cells. Many high-efficiency cells were made by depositing CdTe films in the absence of oxygen. These films were deposited to thicknesses of 15 μm to prevent pinholes, and the $CdCl_2$ anneal was done in a He ambient. There is, of course, the possibility that the previously reported benefit of increased acceptor density has been replaced in these cells by some unintended dopant.

CdTe is an efficient self-compensator, thus reducing the likelihood that low-level unintended dopants would have a large impact. Still, we performed several experiments to reduce the likelihood that an unintended dopant was present and was responsible for the shallow junction depositions despite the absence of oxygen.

The majority of high-efficiency, no-oxygen depositions were done using source plates of polycrystalline CdTe (99.999%, Johnson Matthey) on borosilicate glass or SnO_2-coated glass. To reduce the possibility of benefits from the use of a source plate or unknown dopants in the CdTe source material, we made a cell using high-purity CdTe (99.99999%, Alfa Aesar) directly from sintered powder. This cell, after application of a MgF anti-reflection coating, had an AM1.5 efficiency of 13.0% (V_{oc} of 0.799 V, J_{sc} of 22.54 mA/cm^2, FF of 70.84%), as verified by the National Renewable Energy Laboratory.

To determine if the $CdCl_2$ dip/anneal step was doping the absorber and preventing deep junction formation, we made a cell without the $CdCl_2$ dip/anneal step and without oxygen during deposition. This cell had an efficiency of more than 6% and a QE indicative of a shallow junction.

To determine if the HgTe:Cu-doped graphite back contact we normally use was doping the absorber and preventing deep junction formation, we made a cell with a back contact similar to that used in literature [7]. Using a 1:88:35 nitric acid / phosphoric acid / deionized water etch followed by a deionized water rinse, then room temperature sputter deposition of 0.6 μm Ni on a film deposited without oxygen produced a cell with an efficiency of 9.7%.

These results indicate that high-efficiency cells are possible without extrinsic doping of the absorber. The ability of CdTe to self-compensate and its tendency to grow slightly p-type under some growth conditions support this possibility.

Interaction with Substrate

The characteristics of the CdS layer appear to have a large impact on the CdTe growth in the absence of oxygen. On some of the SnO_2-coated glass substrates used in these experiments, we deposited a thin layer (500-3000 Å) of not-intentionally doped tin oxide by sputtering in an O_2/Ar ambient. Historically, this layer is added to increase the open-circuit voltage (V_{oc}), with one possible explanation of its value being that it introduces a finite resistance in any shunt paths (pinholes), thus reducing their degradation of V_{oc}. Although our studies have shown this layer to have marginal effect (+ or -) on cells deposited with oxygen ambient, this layer has a stark detrimental effect on cells made without oxygen. CdTe films made using substrates with this "intrinsic" SnO_2 layer (thus, glass/SnO_2/i-SnO_2/CdS/CdTe) tend to have pinholes,

reduced adhesion to the substrate, and a higher CdS/CdTe defect density as evidenced by PL measurements. These films also tend to produce low-efficiency devices. One intriguing explanation could be a strong dependence of growth and interdiffusion characteristics for different CdS films, where those differences are caused by differences in CdS nucleation for different substrates.

We also found that oxidation of the CdS on these substrates prior to CdTe deposition not only decreased the pinhole density, but allowed cells with greater than 10% efficiency to be produced without oxygen during the CdTe deposition.

DISCUSSION

The nucleation and growth effects described in this paper have profound implications for solar cells. Decreased grain size will tend to increase recombination in the bulk of the CdTe; however, this negative effect could be outweighed by the benefits of reduced pinhole density and better coverage with thin films. The effect of oxygen on growth also impacts the most critical region of the cell, the CdS/CdTe interface. This concept, that oxygen can benefit the CdS/CdTe interface while reducing the quality of the bulk CdTe, was corroborated by the PL measurements and substrate interaction effects described in this paper.

What remains a question is whether or not oxygen acts as a dopant in CSS CdTe. Oxygen has previously been shown to compensate donors in CdTe deposited by a variety of methods [9]. However, prior to the ground-breaking work at Kodak, oxygen was not known to act as an acceptor in CdTe. The conclusion that oxygen acted as an acceptor in CSS CdTe was based primarily on device characterization [5], principally EBIC, QE, and CV. More fundamental studies were less conclusive. PL investigation of CSS CdTe showed no additional shallow acceptor level when illumination was from the CdTe side of the device [8]. Characterization of films on bare glass showed a carrier concentration of less than 3×10^{12} cm^{-3} with an oxygen concentration of 10^{19}-10^{20} cm^{-3} [6].

The conclusion that oxygen was essential because it acts as an acceptor in CSS CdTe was thus based primarily on device results. The devices we produced for this paper exhibited very different characteristics. For our cells, oxygen was not essential for producing high-efficiency cells, but was still useful for its effect on nucleation.

From the above results it appears plausible that oxygen does not act as an acceptor in CdTe, but instead, as a reactive gas that can alter the deposition conditions in a favorable manner. Thus, if the desired conditions can be achieved by means other than oxygen, such as through control of the characteristics of the CdS, then high-efficiency cells might be achieved reproducibly without the disadvantages, such as irreproducibility and material waste from source oxidation, that oxygen ambient during growth presents for high-volume manufacture.

CONCLUSION

We have described several effects of oxygen, most notably the benefits of improved nucleation and improved CdS/CdTe junction formation. We have also produced high-efficiency devices without oxygen and proposed that oxygen may not, in fact, act as acceptor in CSS CdTe. We will continue study the effects of oxygen with the intent of developing fabrication techniques that can provide the benefits attributed to oxygen without the manufacturing problems associated with its use.

ACKNOWLEDGMENTS

This work was supported by the U.S. Department of Energy under contract No. DE-AC36-83CH10093 to NREL.

REFERENCES

1. K. Zweibel, *Intl. J. Solar Energy*, **12**, 1992, pp. 285-292.

2. Y.S. Tyan and E.A. Perez-Albuerne, "Efficient Thin-Film CdS/CdTe Solar Cells," *Proceedings of the 16th IEEE Photovoltaic Specialists' Conference*, 1982, pp. 794-800.

3. J. Britt and C. Ferekides, *Appl. Phys. Lett.*, **62** (22), 31 May 1993, pp. 2851-2852.

4. T. Chu and S. Chu, *Final Letter Report, EAT-3-13159-01-104149*, Oct. 1993.

5. Y.S. Tyan, F. Vazan, and T.S. Barge, "Effect of Oxygen on Thin-Film CdS/CdTe Solar Cells," *Proceedings of the 17th IEEE Photovoltaic Specialists' Conference*, 1984, pp. 840-845.

6. M. Hsu, R. Jih, P. Lin, H. Ueng, Y. Hsu, and H. Hwang, "Oxygen Doping in Close-Spaced-Sublimed CdTe Thin Films for Photovoltaic Cells," *J. Appl. Phys.*, **59** 1986, pp. 3607-3609.

7. Y.S. Tyan, "Topics on Thin Film CdS/CdTe Solar Cells," *Solar Cells*, **23**, 1988, pp. 19-29.

8. C.W. Tang and F. Vazan, "Effect of Oxygen on the Photoluminescence of CdS/CdTe Thin Films," *J. Appl. Phys.*, **55** (10), 15 May 1984, pp. 3886-3888.

9. D.H. Rose, D.S. Albin, R.J. Matson, A.B. Swartzlander, X.S. Li, R.G. Dhere, S. Asher, F.S. Hasoon, and P. Sheldon, "Effects of Oxygen During Close-Spaced Sublimation of CdTe Solar Cells," To be published in *Proceedings of the Materials Research Society, Volume J*, April 8-12,1996, and references therein.

HIGH-QUALITY CdTe FILMS FROM NANOPARTICLE PRECURSORS

Douglas L. Schulz, Martin Pehnt, Ed Urgiles, David W. Niles, Kim M. Jones, Calvin J. Curtis, David S. Ginley
National Renewable Energy Laboratory, 1617 Cole Blvd., Golden, CO 80401-3393

ABSTRACT

In this paper we demonstrate that nanoparticulate precursors coupled with spray deposition offers an attractive route into electronic materials with improved smoothness, density, and lower processing temperatures. Employing a metathesis approach, cadmium iodide was reacted with sodium telluride in methanol solvent, resulting in the formation of soluble NaI and insoluble CdTe nanoparticles. After appropriate chemical workup, methanol-capped CdTe colloids were isolated. CdTe thin film formation was achieved by spray depositing the nanoparticle colloids (25-75 Å diameter) onto substrates at elevated temperatures (T = 280-440°C) with no further thermal treatment. These films were characterized by x-ray diffraction (XRD), x-ray photoelectron spectroscopy (XPS), and atomic force microscopy (AFM). Cubic CdTe phase formation was observed by XRD, with a contaminant oxide phase also detected. XPS analysis showed that CdTe films produced by this one-step method contained no Na or C and substantial O. AFM gave CdTe grain sizes of ~0.1-0.3 μm for film sprayed at 400°C. A layer-by-layer film growth mechanism proposed for the one-step spray deposition of nanoparticle precursors will be discussed.

INTRODUCTION

CdTe represents one of a few polycrystalline thin film photovoltaic technologies presently being investigated by industry for terrestrial solar cell application. With a bandgap energy (1.5 eV) that nearly matches the solar spectrum, CdTe-based solar cell efficiencies as high as 15.8% have been reported for small area cells (1.08 cm^2) [1]. Nearly all thin film CdTe solar cells are composed of a multilayer structure with a p-type CdTe/n-type CdS heterojunction as the active part of the device.

There have been relatively few reports of spray pyrolysis of CdTe solar cells [2-4]. In 1981, Serreze et al. fabricated a very small area (2.4 mm^2) CdTe/CdS solar cell with an efficiency of 4.0% [2]. This was the first documentation of a CdTe/CdS solar cell where the CdTe layer was deposited by spray deposition. Subsequently, researchers at Photon Energy Inc. (now Golden Photon Inc.) reported a 12.3% efficiency for small area (31.3 mm^2) spray deposited CdTe solar cells [3,4]. The fabrication of larger CdTe solar cells by the same process produced modules with active area (754 cm^2) efficiencies up to 8.1% and a 6.1 W power output [3,4]

The science of semiconductor nanoparticle materials has developed rapidly over the past 10 years [5-8]. One novel property associated with nanoparticles is a reduction in melting point versus the bulk material. Alivisatos et al. have provided transmission electron microscopy selected area diffraction evidence that semiconductor nanoparticles exhibit reduced melting temperature with decreasing particle size [9].

The use of nanoparticle precursors for thin film spray deposition might offer significant advantages over conventional spray pyrolysis routes. As a consequence of higher surface diffusivities [10] and reduced melting temperatures, nanoparticle precursor routes potentially offer the advantage of lower processing temperatures. Beyond the inherent savings with respect to thermal budget, decreased growth temperatures might also allow the use of low-cost substrates such as soda-lime glass while alleviating substrate outdiffusion and relieving thermal stress. In addition, the improved packing during deposition inherent with the small particle diameter can produce smoother, denser films. This approach has the potential to yield films similar in quality to those obtained by vacuum techniques but without the expense and complexity.

We have recently reported the spray deposition of CdTe films using a nanoparticle CdTe colloid precursor [11,12]. The reduced melting temperature associated with nanoparticles was used in the reported studies with phase-pure CdTe film development observed at temperatures as low as 240°C. These routes to CdTe films suffered from substantial C contamination, likely due to the non-volatile trioctylphosphine (TOP) and/or trioctylphosphine oxide (TOPO) nanoparticle surface capping agents. In this report, we present the synthesis of methanol-capped CdTe nanoparticles and the use of these nanoparticles as precursors to CdTe thin film growth by spray deposition. These CdTe thin films show a reduction in C contamination versus the TOP/TOPO-capped precursors. We expect the

technology presented in this manuscript to be transferable directly to the CdTe solar cell device community.

EXPERIMENT

CdTe nanoparticle colloids were prepared by the reaction of Na_2Te with CdI_2 in methanol at -78°C by modification of a literature preparation [13]. After appropriate chemical workup, yields for this metathesis reaction are typically greater than 90% [14]. Nanoparticle characterization has been described elsewhere. We refer to CdTe nanoparticles prepared via this route as "methanol-capped" where "capped" refers to the bonding of solvent and/or ligand molecules to the nanoparticle surface. Prior to spray deposition, the nanoparticle solution was loaded into a Paasche VL-Set™ airbrush and sonicated for 20 minutes to reduce agglomeration of the nanoparticles. The solution was then transferred to the Plas-Labs glove box and sprayed onto heated substrates using nitrogen as a carrier gas. Corning 7059 glass substrates were cleaned with Liquinox and rinsed with distilled water prior to use.

Using a one-step method, the CdTe nanoparticle colloid was sprayed onto substrates that were heated to relatively high temperatures (T_{dep} = 280-440°C) with no further thermal treatment. During deposition, the distance from the sprayer nozzle to the substrate was adjusted such that initial impingement of the colloid spray onto the heated substrate led to wetting of the substrate followed by rapid evaporation of the methanol solvent. Upon spraying too close to the substrate, the ink tended to run giving poor film morphologies. Spraying too far from the substrate provided no film growth due to the low sticking coefficient due to premature solvent evaporation. For these CdTe samples, film growth occurs as the preformed CdTe nanoparticles, upon interaction with the hot substrate, coalesce to form a CdTe thin film. Processing conditions employed in this study are summarized in Table 1.

Table 1. Processing Conditions and Characterization of Spray Deposited CdTe Thin Films.

Film ID	T_{dep} (°C)	XRD: phases	XRD: FWHM (°)[a]	XRD: Grain Size (Å)[b]	AFM: Roughness (Å)[c]	AFM: Grain Size (Å)[d]
280	280	cubic CdTe (broad)	1.70	50		
350	350	cubic CdTe >> $CdTe_2O_5$	0.70	120		
400	400	cubic CdTe > $CdTe_2O_5$	0.45	200	437	60-300
440	440	cubic CdTe > $CdTe_2O_5$	0.35	280		

a: full-width at half-maximum of the (111) reflection; b: diameter calculated using the Scherrer equation; c: root mean square; d: grain size refers to diameter.

RESULTS AND DISCUSSION

Crystalline phase development of the CdTe films was determined by XRD (Fig. 1). A significant increase of CdTe crystallinity with increasing deposition temperature was noted as follows: XRD full-width at half maximum (FWHM) values for the (111) peak decrease from 1.7° for Film 280 (T_{dep} = 280°C) to 0.35° for Film 440 (T_{dep} = 440°C). Applying the Scherrer equation to these FWHM values gives grain sizes from 50 Å for Film 280 to 280 Å for Film 440 (Table 1). Also apparent in the XRD characterization of these CdTe films is the development of a contaminant oxide phase with several XRD reflections that we attribute to $CdTe_2O_5$ (PDF No. 36-345). An increase in the XRD intensity of the oxide phase occurs with increasing deposition temperature. The evolution of this phase may be a consequence of incomplete exclusion of air from the ink reservoir in the Paasche sprayer during sonication or from the nitrogen-purged spraying box. This oxide formation during one-step spraying of methanol-capped CdTe nanoparticle precursor colloids contrasts with results using TOP/TOPO-capped CdTe nanoparticles where no Te/Cd oxide phase formation was observed given a nearly identical one-step spray deposition approach. This observation provides a measure of the relative stability of the capping agent for methanol- versus TOP/TOPO-capped CdTe nanoparticles as applied to one-step spray deposition of CdTe films.

The surface morphology of a film sprayed at 400°C, Film 400, was measured using AFM. An overall smooth morphology was observed with a root mean square (RMS) surface roughness value of 437 Å. Grain sizes from about 60-300 Å were measured. These grain sizes are comparable, on a qualitative scale, to those obtained by XRD (Table 1).

The elemental composition of Film 400 was determined using XPS. Prior to data collection, the surface of this film was sputtered to a depth of 500 Å. There are two observations that are noteworthy regarding the chemical composition of this film. First, the Cd and Te are nearly stoichiometric; which likely reflects the relatively fixed Cd:Te ratio within the crystalline CdTe nanoparticle precursor. Second, although no C or Na are noted, an O contamination is observed. This observation is consistent with XRD data for this film.

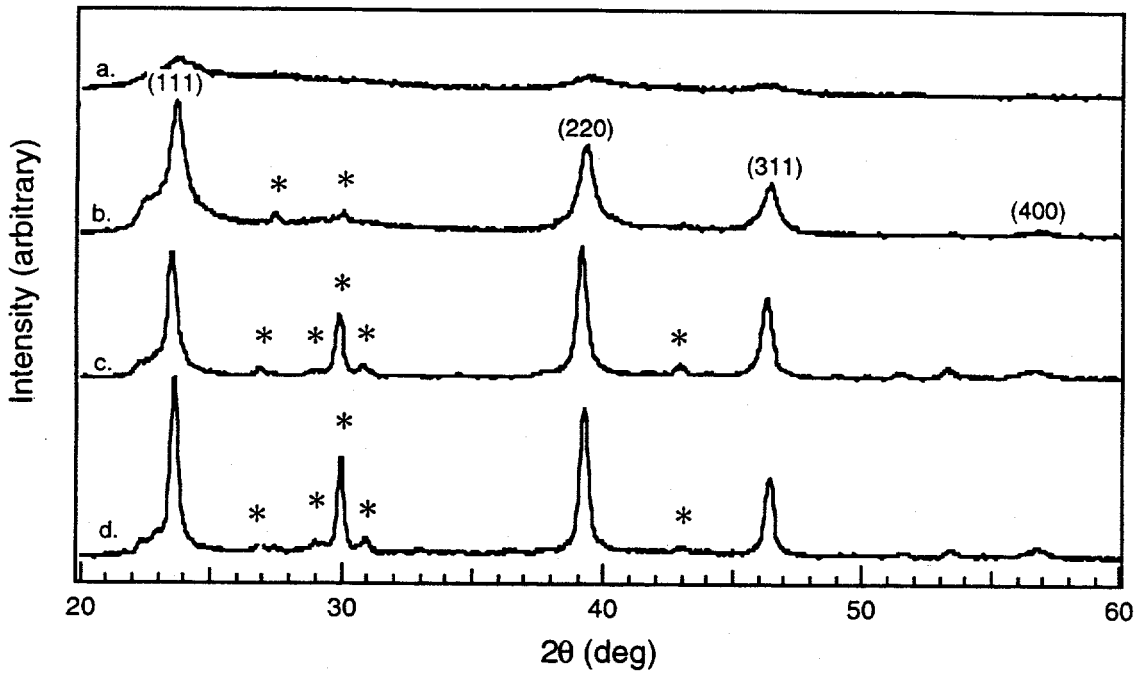

Figure 1. XRD θ/2θ data of CdTe films deposited by the one-step approach using substrate temperatures of (a) 280°C, (b) 350°C, (c) 400°C, and (d) 440°C. (* denotes $CdTe_2O_5$)

Growth Process Comment

Figure 2 is a schematic diagram of CdTe film growth via one-step spray deposition of a colloidal precursor showing one possible layer-by-layer growth process. Accordingly, pressurized CdTe colloidal ink is sprayed from a spray nozzle onto a heated substrate at elevated temperature. The sprayer head traverses the substrate at a given rate at a distance from the substrate such that the surface becomes wetted initially. Heat from the substrate is transferred to the growth layer until the temperature of the growth layer becomes equal to the boiling temperature of the solvent. At this point, the solvent evaporates, leaving capped nanoparticles on the film surface. As more heat is transferred from the substrate to the growth layer, the growth layer temperature exceeds the temperature for ligand desorption and the cap is volatilized with film growth occurring concomitantly.

According to this proposed layer-by-layer process, several variables exist with respect to overall film growth. First, the instantaneous cooling of the substrate is affected by the flow rate of the colloid and the carrier gas as well as their associated heat capacities. These variables can be modified using different types of sprayer heads, solvents, or carrier gases. Second, the overall system pressure during film growth affects both the solvent evaporation and the cap volatilization processes. At lower pressures, the solvent evaporation and cap volatilization would occur at lower temperatures. Finally, the condition and heat capacity of underlying growth layers clearly affect the kinetics of the growth mechanism of subsequent layers.

CONCLUSIONS

Nanoparticle CdTe colloids have been synthesized by reacting CdI_2 with Na_2Te in methanol solvent. Although methanol-capped nanoparticle CdTe materials exhibit less stability toward oxidation than other materials such as TOP/TOPO-capped CdTe, the evolution of the capping agent seems to occur much more readily for the former versus the latter. The metathetic synthesis presented herein offers economic, as well as synthetic, advantages compared to other reported procedures, and yields greater than 90% are obtained.

Nanoparticle CdTe colloids have been employed as precursors for the spray deposition of CdTe thin films according to a one-step method. XRD characterization of CdTe films processed accordingly showed cubic zincblende CdTe phase formation along with a contaminant phase, $CdTe_2O_5$. This oxide phase, comprising 4 wt.% of the film by XPS, is thought to be a consequence of incomplete exclusion of air from the system. AFM characterization of a film sprayed at 400°C showed the film possessed 60-300 Å grains with a RMS

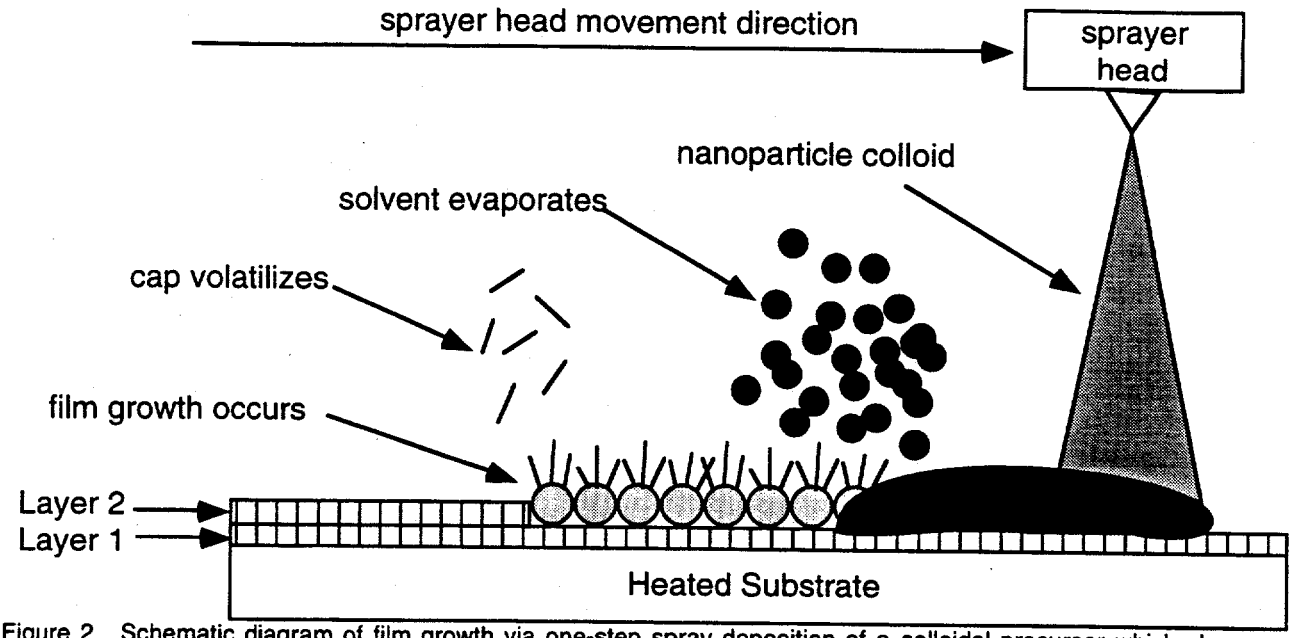

Figure 2. Schematic diagram of film growth via one-step spray deposition of a colloidal precursor which shows one possible layer-by-layer growth process.

surface roughness of 437 Å. XPS analysis showed a nearly stoichiometric ratio of Cd:Te with no C or Na contamination.

A layer-by-layer growth mechanism has been proposed for the one-step spray deposition of nanoparticle precursors. Factors influencing this proposed mechanism include solvent flow rate, solvent heat capacity, carrier gas flow rate, carrier gas heat capacity and sprayer head type. In-depth thermal analysis experiments are planned to probe the mechanisms by which the methanol capping agent is evolved from the nanoparticle CdTe precursor during thin film growth. We expect that a more thorough understanding gained therein should provide the appropriate growth conditions whereby impurity contamination may be minimized with the maintenance of good film properties.

We envision this one-step approach to be amenable to a wide variety of electronic materials, limited only by the ability to synthesize a nanoparticle precursor colloid of the material of interest. In the short term, we hope to extend this methodology to the industrial synthesis of CdTe-based solar cells.

ACKNOWLEDGMENTS

This research was funded by the U.S. Department of Energy, Office of Energy Research, Chemical Sciences Division and Materials Science Division and the U.S. Department of Energy National PV Program.

REFERENCES

1. C. Ferekides, J. Britt, Y. Ma, and L. Killian, *Proc. 23rd IEEE Photovoltaic Spec. Conf.* 389 (1993).
2. H. B. Serreze, S. Lis, M. R. Squillante, R. Turcotte, M. Talbot, and G. Entine, *Proc. 15th IEEE Photovoltaic Spec. Conf.* 1068 (1981).
3. S. P. Albright, J. F. Jordan, B. Ackermann, and R. R. Chamberlin, *Solar Cells* **27**, 77 (1989).
4. S. P. Albright, B. Ackermann, and J. F. Jordan, *IEEE Trans. Electron Dev.* **37**, 434 (1990).
5. M. L. Steigerwald, and L. E. Brus, *Annu. Rev. Mater. Sci.* **19**, 471 (1989).
6. H. Weller, *Adv. Mater.* **5**, 88 (1993).
7. H. Weller, *Angew. Chem. Int. Ed. Engl.* **32**, 41 (1993).
8. R. F. Service, *Science* **271**, 920 (1996).
9. A. N. Goldstein, C. M. Echer, and A. P. Alivisatos, *Science* **256**, 1425 (1992).
10. R. P. Andres, R. S. Averback, W. L. Brown, L. E. Brus, W. A. Goddard, A. Kaldor, S. G. Louie, M. Moscovits, P. S. Peercy, S. J. Riley, R. W. Siegel, F. Spaepen, and Y. Wang, *J. Mater. Res.* **4**, 704 (1989).
11. M. Pehnt, D. L. Schulz, C. J. Curtis, K. M. Jones and, D. S. Ginley, *Appl. Phys. Lett.* **67**, 2176 (1995).
12. M. Pehnt, D. L. Schulz, C. J. Curtis, H. R. Moutinho, A. Schwartzlander, and D. S. Ginley, *Mat. Res. Soc. Symp. Proc.* (in press).
13. M. Müllenborn, R. F. Jarvis, B. G. Yacobi, R. B. Kaner, C. C. Coleman, and N. M. Haegel, *Appl. Phys. A* **56**, 3217 (1993).
14. D. L. Schulz, M. Pehnt, D. H. Rose, E. Urgiles, A. F. Cahill, D. W. Niles, K. M. Jones, C. J. Curtis, and D. S. Ginley, *Chem. Mater.* (submitted for publication).

A COMPARISON OF GETTERING IN SINGLE- AND MULTICRYSTALLINE SILICON FOR SOLAR CELLS

B. L. Sopori*, L. Jastrzebski** and T. Tan***
* National Renewable Energy Laboratory, ** University of South Florida, ***Duke University

ABSTRACT

The differences in the impurity gettering between single and multicrystalline silicon are discussed. These differences arise from impurity-defect interactions that occur during thermal processing of multicrystalline material. A gettering model is proposed to explain the observed behaviour of gettering in multicrystalline cells.

INTRODUCTION

Impurity gettering is an essential process step in fabricating silicon devices. In integrated circuit (IC) fabrication, gettering primarily removes impurities that may have diffused into the wafers during one or more previous process steps [1]. However, in solar-cell fabrication, the role of gettering is quite different—it aims to upgrade the lower-quality material to enable fabrication of high-efficiency devices on low-cost substrates. Furthermore, gettering in solar cells is intended to be a byproduct of cell-fabrication processes. Although much information exists on the gettering effects in IC devices, this information cannot be directly applied to low-cost (both single- and multicrystalline) silicon. This is so because in low-cost silicon, many impurity and defect interactions are activated during a gettering process that do not occur in the IC device fabrication. These interactions occur for the following reasons: (a) effective removal of impurities from the entire bulk of the solar cell requires extended gettering, involving long times and higher temperatures; (b) the concentrations of various impurities in solar-cell substrates are considerably higher than that of IC devices; and (c) solar-cell substrates have high densities of crystal defects.

In this paper, we discuss results of studies carried out to identify mechanisms that cause these differences and to find methods that can produce wafers/devices with a uniformly high minority-carrier diffusion length (MCDL) and solar-cell response. These investigations have led to a gettering model for multicrystalline silicon that explains results observed by us, as well as results reported by other researchers.

GETTERING METHODS/ANALYSES

The gettering studies were done on both high-quality single-crystal and multicrystalline (MC) commercial solar-cell silicon wafers, using phosphorus, chlorine, and aluminum gettering. We have also investigated two new gettering schemes that show excellent promise for solar cells. These methods are back-side hydrogen gettering and ultrasound treatments.

Phosphorus diffusions were performed using either SiP_2O_7 solid source or $POCl_3$ source. Effective gettering by P requires its concentration at the wafer surface to be high. This is because the mechanisms of P gettering involve higher solubility of metallic impurities in the heavily P-diffused region, and impurity segregation at the Si_3P_4 precipitates and dislocation loops produced by heavy diffusions. Consequently, P diffusions must be carried out at high temperatures. In our experiments, the diffusions were typically done in the temperature range of 850°-1025°C for 60-120 minutes. These diffusion conditions were selected because the lower range of temperature is generally used for solar-cell fabrication, whereas the upper temperatures gave best gettering results on single-crystal float-zone (FZ) wafers. Chlorine gettering was performed using tricholoroethane (TCA) Source/O_2 in the temperature range of 1000°-1150°C for 30-90 minutes. It is known that chlorine gettering occurs via formation of volatile metal chlorides, a process whose efficiency decreases with temperature. Aluminum gettering was performed by depositing a thin layer, typically 1 μm, of Al on the wafer and performing a subsequent anneal, either in a conventional furnace at 700°-900°C, for 60-120 minutes or in an RTA furnace at 600°-900°C for 0.5 to 5 minutes [1,2].

Hydrogen gettering uses hydrogen-induced defects as the gettering sites. The technique uses a low-energy hydrogen implant to produce specific defects known as platelets on the back side of the wafer. These defects have been identified as having cores of vacancy-type defects that can capture and trap interstitial impurities like transition metals. In a typical gettering process, the hydrogenation is followed by a low-temperature process in which the sample is illuminated with intense light from a bank of tungsten-halogen lights. Fast-diffusing impurities such as transition metals are trapped at the platelets, leaving the bulk of the wafer devoid of these impurities. Ultrasound gettering uses ultrasonic energy, coupled to the wafer by means of a transducer, to produce a dissociation of impurities from dislocated regions. This technique appears primarily to improve regions of low MCDL [3]. Solar cells were gettered by phosphorus diffusions and Al treatments by the conventional processes.

A surface photovoltage (SPV) technique was used to monitor the MCDL before and after gettering. In some cases, the Fe and Cr concentrations were measured before and after gettering using a technique that is also based on the SPV principles. Finished solar cells were analyzed by I-V characterization and mapped by light-beam-induced current (LBIC) using PVSCAN 5000 [4].

RESULTS

The gettering procedures described above produced expected improvements in the MCDL in single-crystal material. Generally, in the case of an IC-quality single-crystal wafer, the gettering efficiency increases both with time and temperature, and impurity removal is

spatially uniform. However, in MC materials, the gettering results differ in many ways. Here, we only emphasize the aspects that relate to a better understanding of the mechanisms responsible for causing differences between single-crystal and MC silicon. These mechanisms are then used to develop a gettering model for MC silicon. These features are briefly described below.

Interactions of Impurities with Crystal Defects

Our analyses have shown that commercial silicon wafers for photovoltaic applications have high concentrations of Fe and Cr. Typical densities of these impurities range from 10^{11} to 10^{12}/cm^3. Furthermore, it is observed that a well-defined correspondence between Fe (or Cr) concentration and MCDL does not exist. This may be attributed to impurity-defect interactions that can cause nonuniformities in the concentration of dissolved impurities.

Figure 1 shows diffusion length and Fe concentration distribution in a commercial multicrystalline material before and after Cl gettering. These data were taken from many wafers and show several important features.

1. The diffusion lengths are below the theoretical limit set by the formation of Fe-B pairs in a single-crystal material. The solid line identifies this limit on the diffusion length for various Fe concentrations. This result demonstrates that in multicrystalline wafers, the MCDL is controlled by other impurities and/or defects.

2. Figure 1a shows that the data are concentrated primarily in two groups—region I, where the diffusion length is considerably lower than the Fe-B limit and shows low Fe concentration, and region II, where MCDL is close to the Fe-B limit. Our studies on the comparison of spatial maps of Fe/Cr and defect density shows that region I corresponds to heavily dislocated areas of the wafers.

3. Figure 1b shows that region I is nearly unchanged by gettering whereas region II shows significant improvement in the diffusion length. We believe that region 1 has precipitated Fe—this was supported by the observation that dissolved Fe concentration as measured by the SPV technique was lower at high-dislocation-density sites.

4. Similar results are also observed in solar cells. Figure 2 shows LBIC maps at the excitation wavelength (λ=0.905 μm) of two solar cells fabricated on adjacent wafers. In one case, the cell was fabricated using a single phosphorus diffusion for junction formation (Figure 2a). In the other case (Figure 2b), phosphorus gettering was performed before cell fabrication. The legend on the maps shows the response of the cell in mA/mW. Gettering is shown to improve most of the cell area except localized regions near the middle of the cell. From defect maps produced by PVSCAN 5000, these regions are identified as having high dislocation density.

The results described above demonstrate that impurity removal by external gettering has much lower efficiency in the regions of high dislocation density compared to regions with low or zero dislocation densities. Interestingly, as described above, the dissolved Fe and Cr concentrations at the defected regions, in the as-grown material, are lower than in the low-defect regions. This implies that precipitation of metallic impurities occurs at the defect sites during the growth process. This explains why gettering of impurities that have precipitated at defects is difficult by conventional gettering procedures. Lower gettering efficiency in the defected regions is observed in all gettering processes, except by the ultrasound technique.

Al Gettering by RTA Processing

The impurity gettering by Al treatment is thought to be a result of impurity dissolution in liquid Al. This process can occur at temperatures lower than for phosphorus or Cl gettering and can be effective for a variety of different impurities because the solubility of nearly all metallic impurities is quite high in liquid Al. In a high-quality single-crystal wafer, the dependence of gettering efficiency on the process temperature (above 700°C) is not expected to be strong. Similar to the P gettering, where one would expect release of impurities from gettering sites at higher temperatures, the Al gettering can be very effective provided slow cooling is used in this process. Slow cooling ensures that the residual impurity concentration in the gettered region is

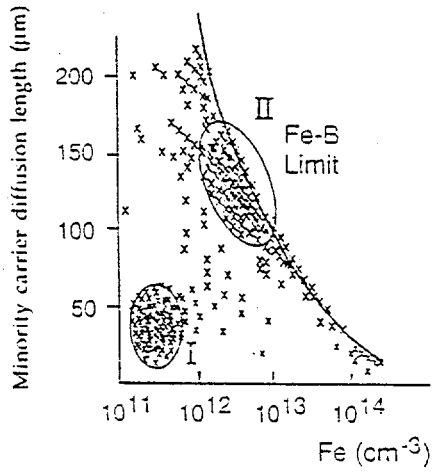

Figure 1a

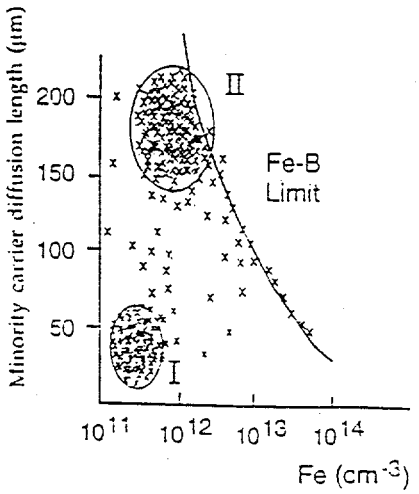

Figure 1b

Figure 1: Diffusion length and Fe concentration distribution before (1a) and after (1b) Cl gettering. The solid line indicates the limit of MCDL due to Fe-B recombination.

much below the solubility limit at the maximum process temperature.

Effects of cooling rate can easily be seen in Al gettering of a ribbon material performed in an RTA set-up. Figure 3 shows the ratio of (diffusion length after gettering)/(diffusion length before gettering) for two cooling rates of 125°C/s and 30°C/s. Al gettering was done under different process conditions that included changing heating and cooling rates. It was found that the gettering efficiency depends on the heating/cooling rates as well as on the maximum temperature. The optimum maximum temperature was found to be 700°C. The optimum heating /cooling rate was determined to be 30°C/s.

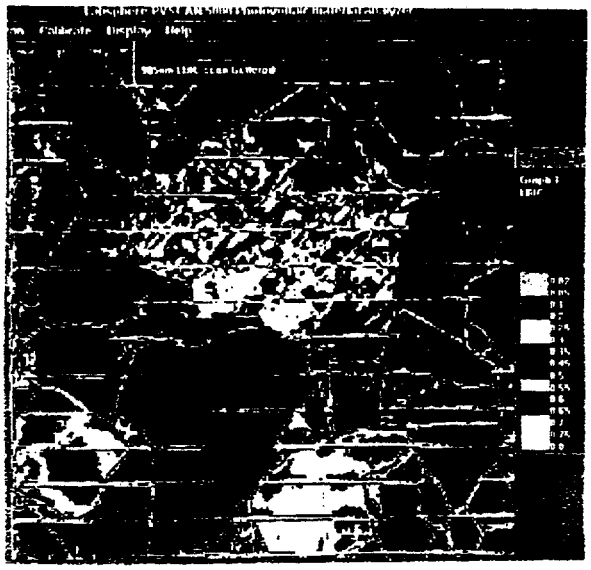

Figure 2a. LBIC map, at λ = 0.905 µm excitation of ungettered cell

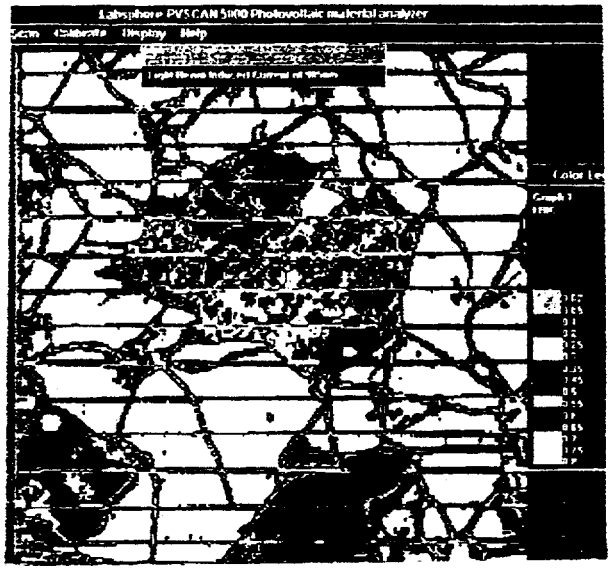

Figure 2b. LBIC map, at λ = 0.905 µm excitation of gettered cell

The optimum time for Al gettering varies for different materials. Figure 4 shows the average increase in diffusion length for a ribbon sample and a cast wafer. In this case, the cast wafer requires longer gettering. We believe that optimum values for both the time and temperature depend strongly on the nature and concentration of the impurities in the material. These effects can be inferred from the gettering model presented in the next section.

Saturation of Gettering Region(s)

High concentrations of impurities present in the solar-cell substrate can saturate the gettering regions. Hence, sequential gettering steps such as Al treatment following a phosphorus treatment can be additive in improving the material quality. Our Al gettering has shown that, when the impurity concentration is high, multiple gettering using thinner gettering layers can be more effective than a single-step gettering using a thicker Al film.

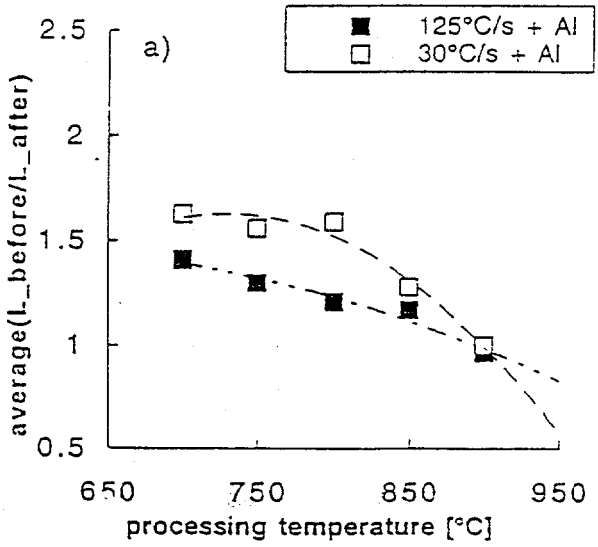

Figure 3. Fractional improvement in the MCDL by an RTA Al-gettering as a function of processing temperature for two different cooling rates.

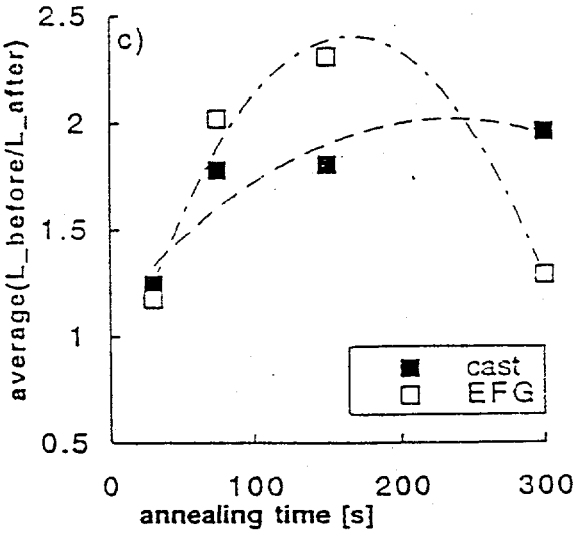

Figure 4. Fractional 1mprovement in the MCDL by an RTA Al-gettering as a function of processing time for two differentmulticrystalline substrates

Effect of High Temperature Processing

In some cases of higher-temperature processing, gettering can lower the MCDL. We believe that this effect is produced by initiation of dissolution of precipitated impurities. When the dissolution rate of a precipitated impurity is higher than its gettering rate, a net accumulation of the dissolved impurity can occur that leads to a reduction in the MCDL. Point-defect injection, accompanying phosphorus diffusion and/or Al treatment, can accelerate the dissolution process.

It is interesting that Al gettering appears to have the same limitations as phosphorus or chlorine gettering in being less efficient in the regions of high-dislocation density. Ultrasound treatment offers some promise as a technique for improving high dislocation regions. It is expected that hydrogen gettering may also provide some added advantage by producing passivation of defected regions.

GETTERING MODEL

Our analyses of the gettering results suggest that there are a number of impurity-defect interactions that occur during gettering of a multicrystalline silicon wafer. These interactions are time- and temperature-dependent and are also influenced by point-defect injection that accompany each gettering process. Many observed results of gettering, passivation, and thermal processing on the solar-cell performance can be explained by considering such interactions between defects and impurities that take place during a gettering or a thermal process. A model that illustrates these interactions is shown in Figure 5. This figure depicts a multicrystalline silicon sample containing grain boundaries, dislocations, impurities, and point defects such as interstitials and vacancies. The impurities are shown to be in two states—dissolved, and precipitated at grain boundaries and dislocations. This model can be used to explain qualitatively why gettering does not improve the regions of high dislocations and why processing at temperatures higher than about 950°C can result in degradation of the material quality. The former is related to the fact that precipitation of impurities at the defect sites takes place at high temperatures during the cool down of the crystal. Experimental results suggest that during the crystal growth, impurities precipitate on dislocations and grain boundaries with the formation of silicides. Because precipitated impurities cannot migrate, a conventional gettering process does not effectively remove impurities from heavily dislocated regions. On the other hand, point-defect injection that can take place during a gettering process can enhance impurity dissolution. If the impurity dissolution rate is greater than the gettering rate, the gettering step can result in an increase in the concentration of the dissolved impurities, accompanied by a degradation in the cell performance. This process is likely to occur at higher temperatures.

DISCUSSION

All gettering processes seem to work well on multicrystalline wafers if the gettering temperatures are below about 900°C. It is known from results of FZ single-crystal wafers that gettering by P diffusion improves with temperature. However, in the case of CZ single-crystal silicon this feature may not be true because at higher temperatures some precipitation of oxygen can occur. In the MC wafers, the mechanism appears to be different, as discussed in the above model. This difference arises primarily because the existing bulk crystal defects can participate in precipitation/dissolution of impurities. Consequently, crystal defects are a major mechanism for solar cell nonuniformity. It is determined that these nonuniformities can cause power loss within the cell. Thus, the effectiveness of any gettering process for improving large-area cell performance will be limited by how well it can getter heavily dislocated regions.

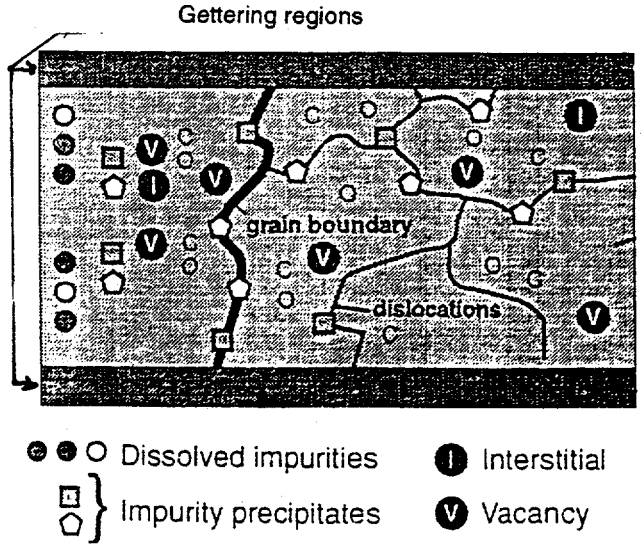

Figure 5. A schematic illustrating various processes that take place in a multicrystlline silicon solar-cell substrate during gettering.

ACKNOWLEDGMENT

This work was supported by the U. S. Department of Energy under contract No. DE-AC36-83CH10093.

REFERENCES

[1] L. Jastrzebski, S. Ostapenko, W. Henley, D. Schielieu, G. Nowak, and L. Lagowski, "Improvement of Diffusion Length in Photovoltaic Poly-Silicon by Various Gettering Approaches," *13th NREL Photovoltaic Program Review*, AIP Conference Proceedings, **357**, 1996, pp135-149, and references there-in.

[2] S. M. Joshi, R. Gafiteanu, U. M. Gosele, and T. Y. Tan, "Simulations and Experiments on External Gettering of Silicon," *13th NREL Photovoltaic Program Review*, AIP Conference Proceedings, **357**, 1996, pp527-534.

[3] K. Carr, N. Carlson, P. Weitzman, B. L. Sopori, C. Marshall, and L. Allen,"Applications of Scanning Defect Mapping System for Semiconductor Characterization," *Symposium on Defects and Impurity Engineered Semiconductors and Devices*, MRS **378**, 1995, pp 579-585.

[4] S. S. Ostapenko, L. Jastrzebski, J. Lagowski, and B. Sopori, "Increasing short minority carrier diffusion length in solar grade polycrystalline silicon by ultrasound treatment," *Appl. Phys. Lett.* **65**, 1555(1994).

SIEMENS SOLAR CIS PHOTOVOLTAIC MODULE AND SYSTEM PERFORMANCE AT THE NATIONAL RENEWABLE ENERGY LABORATORY

Troy Strand, Benjamin Kroposki, and Robert Hansen
National Renewable Energy Laboratory
Golden, CO USA

Dennis Willett
Siemens Solar Industries
Camarillo, CA USA

ABSTRACT

This paper evaluates the individual module and array performance of Siemens Solar Industries' copper indium diselenide (CIS) polycrystalline thin-film technology. This is accomplished by studying module and array performance over time. Preliminary temperature coefficients for maximum power, maximum-power voltage, maximum-power current, open-circuit voltage, short-circuit current, and fill factor are determined at both the module and array level. These coefficients are used to correct module/array performance to 25°C to evaluate stability. We show that CIS exhibits a strong inverse correlation between array power and back-of-module temperature. This is due mainly to the narrow bandgap of the CIS material, which results in a strong inverse correlation between voltage and temperature. We also show that the temperature-corrected module and array performance has been relatively stable over the evaluation interval (≈2 years).

INTRODUCTION

The Engineering and Technology Validation Team at the National Renewable Energy Laboratory (NREL) conducts in situ technical evaluations of photovoltaic (PV) modules and arrays at NREL's Photovoltaic Outdoor Test Facility (OTF) in Golden, CO. The OTF is located at 39.7°N latitude, 105.2°W longitude, at an elevation of 1,782 meters. Siemens Solar Industries' polycrystalline thin-film technology is the focus of the research presented here.

The module structure is $Cu(In,Ga)Se_2$ (CIS) [1]. These modules are vintage CIS modules and do not represent the current state-of-the-art for Siemens Solar. Furthermore, all modules were subjected to accelerated testing at Siemens Solar before deployment at NREL. Note that these are research modules, so they do not all come from a common process or production stream, and this may be the source of some variation in the data.

The research team is attempting to correlate individual module performance with array performance. Also, temperature coefficients (TCs) are determined at the module, array, and system level. Results presented here are based on the outdoor performance of an individual module and of an array consisting of 34 modules (≈1 kW). Figure 1 shows the Siemens Solar 1-kW PV array being evaluated at NREL's OTF.

Fig. 1. The Siemens Solar 1-kW PV array.

EXPERIMENTAL PROCEDURE

Long-term performance data are acquired at the individual module, array, and system levels. Individual module, array, and system data are then evaluated and compared for correlation.

Individual Module Data Acquisition

Individual module performance is monitored with an RD-1200 multi-tracer. The module is loaded at its maximum power (max-power) point, except when current versus voltage (I-V) curves are taken. I-V curves are swept from short-circuit current (I_{sc}) to open-circuit voltage (V_{oc}) and are acquired every half-hour. The module data presented in this paper were restricted to plane-of-array (POA) irradiances between 950 and 1050 W/m^2. Data were collected over a period of about 1-1/2 years for this module.

Array/System Data Acquisition

In monitoring and evaluating system performance, two sets of data are collected. The two data sets include instantaneous measurements and real-time data acquisition. The instantaneous array performance is monitored via a portable I-V curve tracer and is termed "array performance" for this paper. These I-V traces are acquired once a month (weather permitting) at POA irradiances between 900 and 1100 W/m^2. Real-time array/system performance is monitored via a Campbell

Scientific CR10 datalogger, and these results are termed "system performance" here. Data collected include array current and voltage, back-of-module and ambient temperatures, and POA irradiance. Data are sampled every 5 s and are stored as 15-min. averages.

RESULTS AND DISCUSSION

Module Performance

One Siemens Solar CIS module was used for the module performance evaluation. The module's aperture-area was measured to be 3946.3 cm^2 (127.3 cm x 31.0 cm). This module is from a process or production stream similar to those deployed in the system. The module was installed at a 40° tilt and is loaded at maximum power during the day, except when I-V curves are taken. Data collection for this study started July 11, 1994, and ended December 13, 1995. Figure 2 shows maximum power (P_{max}) normalized to 1000 W/m^2 and back-of-module temperature versus time. In Fig. 2, the CIS module shows a strong inverse correlation between P_{max} and back-of-module temperature. This effect can be attributed to the narrow (about 1 eV) bandgap of the CIS material. V_{max}, V_{oc}, I_{max}, I_{sc}, and temperature were plotted against time. V_{max} and V_{oc} exhibited a strong inverse correlation with back-of-module temperature. I_{max} exhibited a larger inverse correlation with back-of-module temperature than that of I_{sc}. This is the result of an inverse correlation between fill factor (FF) and back-of-module temperature (see Table 1). Gaps in the data occur because the multi-tracer was unavailable when being used for other experiments.

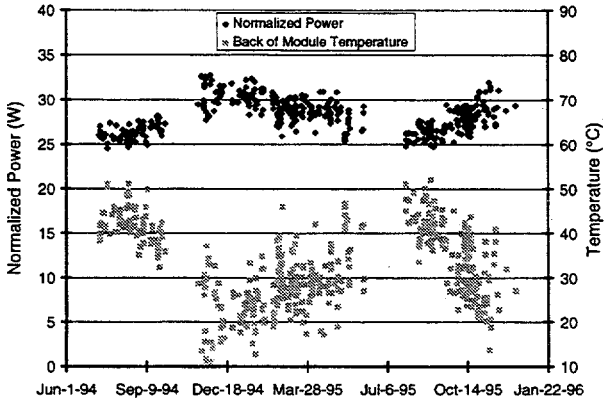

Figure 2. Normalized power and back-of-module temperature versus time.

To examine the long-term stability of this module, we corrected the performance data to a 25°C reference temperature by calculating TCs for the module. For example: using a linear regression of power (normalized to 1000 W/m^2) versus back-of-module temperature, the TC for P_{max} was determined to be -0.67%/°C, with an R^2 of 0.96 (Fig. 3). This R^2 indicates that P_{max} is well-correlated with temperature. The TC of -0.67%/°C is consistent with previously reported results for the CIS material [2].

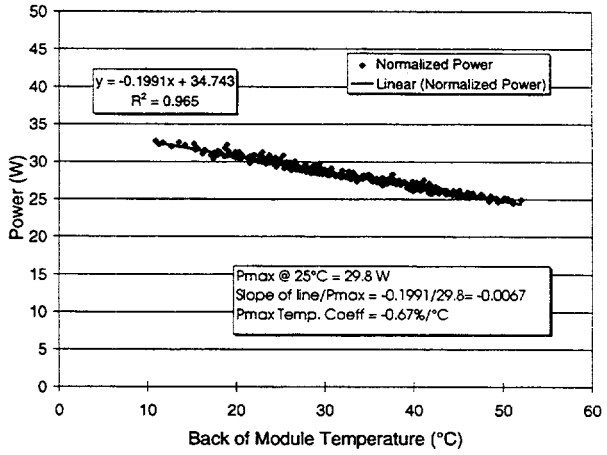

Figure 3. Normalized power versus module temperature.

Figure 4 shows P_{max} corrected to 25°C versus time for the CIS module. In this figure, note that the scatter due to temperature is greatly reduced (indicating a valid TC) and that the module shows good stability over time.

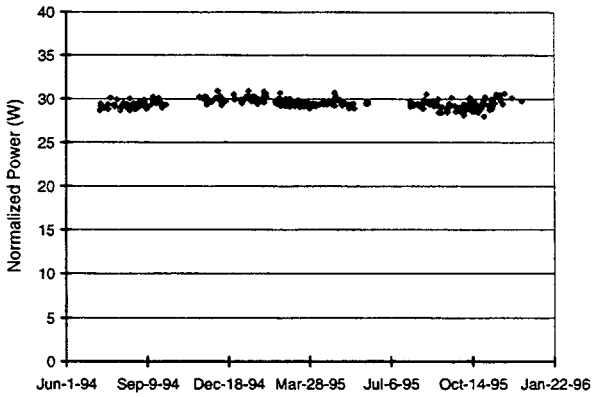

Figure 4. Normalized and temperature-corrected power versus time.

In a similar manner, TCs were calculated for V_{max}, V_{oc}, I_{max}, I_{sc}, and FF for the CIS module. These were also found to be consistent with previously reported results [2] and are summarized in Table 1.

Table 1. CIS Module Temperature Coefficients

	P_{max}	I_{max}	V_{max}	I_{sc}	V_{oc}	FF
TC	-0.67	-0.07	-0.60	0.00	-0.54	-0.15
R^2	0.96	0.21	0.96	0.00	0.98	0.85

Using the coefficients presented in Table 1, V_{max}, V_{oc}, I_{max}, and I_{sc} for the CIS module were also corrected for temperature and plotted against time. This exercise

revealed that these coefficients greatly reduced the scatter in the module data due to temperature, thus indicating their validity. These graphs were omitted from the paper for brevity.

Array/System Performance

The Siemens Solar CIS array comprises 34 modules located at NREL's PV Outdoor Test Facility. The average module from this group had the following electrical characteristics (measured at NREL before deployment): P_{max}= 28.3 W, V_{max}= 15.56 V, V_{oc}= 22.38 V, I_{max}= 1.832 A, and I_{sc}= 2.264 A. Using the average max-power, the summation of module max-powers at STC is 962 W. Array installation was completed September 15, 1993, and data acquisition began April 1, 1994. The evaluation period for this data set covers about 2 years.

The array is fixed at a 40° tilt and is aligned true south. The array is divided into three separate subarrays. Two of the subarrays (1 and 3) are each composed of six parallel strings of two modules in series. Subarray 2 is composed of five parallel strings of two modules in series. Each subarray feeds dc power to a separate max-power tracker. The outputs of the three max-power trackers are paralleled and tied to a 0.95-ohm, 2-kW fixed resistive load. Subarrays 1 and 2 contain modules that have been physically damaged. These two subarrays have been showing a degradation trend in both power and current. Discussion of the system performance is therefore limited to subarray 3 (≈340 W at STC).

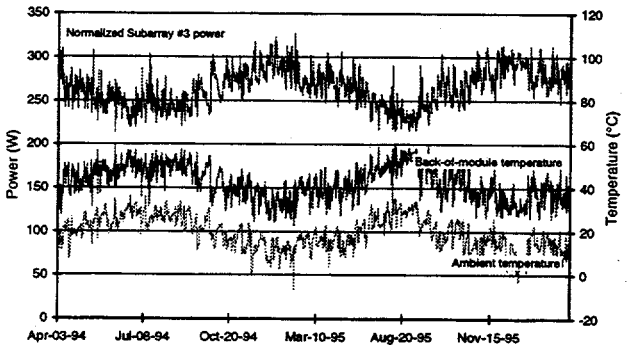

Figure 5. Normalized subarray power, back-of-module temperature, and ambient temperature versus time.

Figure 5 shows subarray 3 power, back-of-module temperature, and ambient temperature versus time. The data in this chart were restricted to POA irradiances between 900 and 1100 W/m^2. Power is normalized to 1000 W/m^2. The figure shows a strong inverse correlation between subarray power and back-of-module temperature. The max-power current (normalized to 1000 W/m^2), max-power voltage, and back-of-module temperature for subarray 3 were also plotted against time. We observed that both max-power current and max-power voltage exhibited a notable inverse correlation with temperature.

The array performance is monitored via a portable I-V curve tracer. Based on this data set, preliminary TCs for P_{max}, V_{max}, V_{oc}, I_{max}, I_{sc}, and FF were calculated. The data were not corrected for spectral effects. Figure 6 presents the TC calculation for P_{max}, -0.79%/°C, with an R^2 of 0.89. Table 2 presents the TCs calculated from the I-V curve-trace data. These TCs are also consistent with previously reported results [2]. The TC for FF was determined to be -0.25%/°C, again showing that fill factor for this material is influenced by temperature [2].

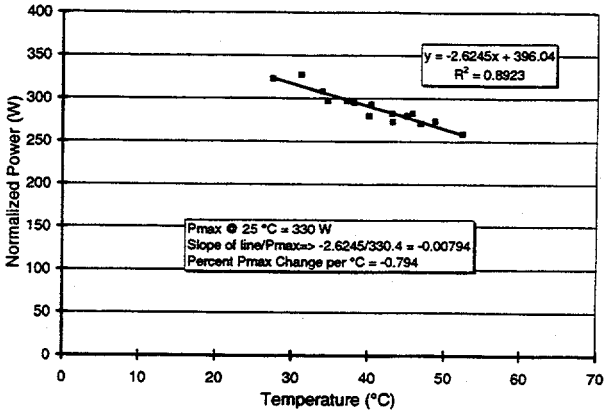

Figure 6. Array P_{max} temperature coefficient derivation.

Table 2. CIS Array Temperature Coefficients

	P_{max}	I_{max}	V_{max}	I_{sc}	V_{oc}	FF
TC	-0.79	-0.19	-0.63	-0.03	-0.56	-0.25
R^2	0.89	0.43	0.86	0.05	0.94	0.80

The subarray power presented in Figure 5 was corrected for temperature based on the TC of -0.79%/°C. The subarray performance, normalized to 1000 W/m^2 and corrected to 25°C back-of-module temperature, is shown in Figure 7. The temperature-corrected power is shown to be relatively stable, with only slight fluctuations that still follow temperature inversely. This indicates that the temperature coefficient for power may be slightly larger than that used here.

Table 3. CIS System Temperature Coefficients

	P_{max}	I_{max}	V_{max}
TC	-0.89	-0.53	-0.43
R^2	0.97	0.88	0.93

In an attempt to further mitigate the fluctuations in Fig. 7, we calculated TCs based on the system performance data. Using these TCs, shown in Table 3, subarray P_{max}, I_{max}, and V_{max} were corrected for temperature. Figure 8 shows the temperature-corrected power (using the larger coefficient of -0.89%/°C) for subarray 3. The amplitude of the variation in power due to temperature is slightly less than that seen in Fig. 7.

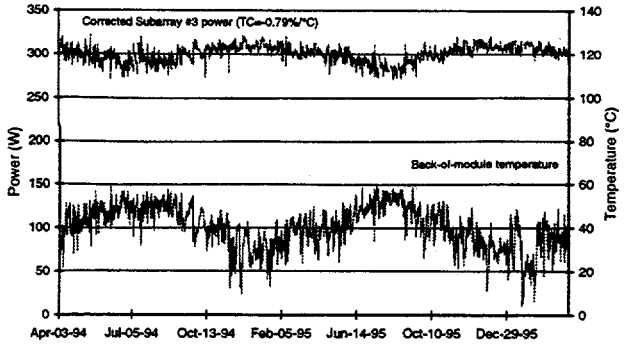

Figure 7. Normalized and temperature-corrected subarray power versus time (array temperature coefficient).

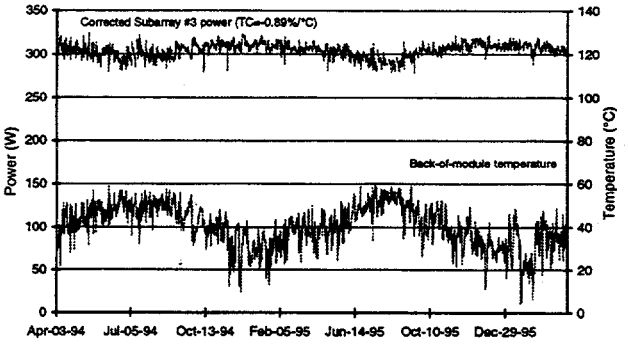

Figure 8. Normalized and temperature-corrected subarray power versus time (system temperature coefficient).

We also found that the TCs calculated at the system level, when applied to the real-time data, were far better at smoothing the variation in V_{max} and I_{max} due to temperature than those determined at the module and array level. Therefore, we conclude that using temperature coefficients calculated from the I-V characteristics of an individual module in predicting array performance may lead to discrepancies with actual system performance. This is due in part to the accuracy at which the max-power tracker finds the max-power point and the accuracy at which the temperature sensor measures the junction temperature (i.e., back-of-module temperature measurements versus imbedded-junction temperature measurements). Here, the accuracy at which the max-power tracker finds the max-power point was determined to be the major cause of variations in TCs among those calculated at the module and array levels (I-V curve-trace data) versus the system level (real-time data).

State-of-the-Art Cu(In,Ga)(Se,S)$_2$

The current state-of-the-art polycrystalline thin-film technology from Siemens Solar is a graded alloy with the notable addition of sulfur. This material is most properly designated as Cu(In,Ga)(Se,S)$_2$. By adding sulfur, the V_{oc} of the device was increased. This increased V_{oc} has the net affect of decreasing the TC for voltage, thus decreasing the TC for P_{max} to -0.55%/°C.

CONCLUSIONS

Preliminary temperature coefficients for P_{max}, V_{max}, I_{max}, V_{oc}, I_{sc}, and FF based on individual module, array, and system data were calculated. Table 4 summarizes these results. Note that the data were not corrected for spectral effects; thus, these preliminary coefficients may be influenced by spectrum. The cause of the elevated P_{max} temperature coefficient determined at the system level is attributed to max-power-point tracking error.

Max-power current was found to exhibit a weaker inverse correlation with temperature at the module level than at the array level. Power and voltage exhibited a strong inverse correlation with back-of-module temperature at both the module and array levels. This is mainly due to the narrow (about 1 eV) bandgap of the CIS material, which results in a strong inverse correlation between voltage and temperature. Fill factor was shown to exhibit an inverse correlation with temperature. Finally, the temperature-corrected module and array powers are shown to be relatively stable over the period of evaluation.

Table 4. Temperature Coefficients

	Module		Array		System	
	TC	R^2	TC	R^2	TC	R^2
P_{max}	-0.67	0.96	-0.79	0.89	-0.89	0.97
I_{max}	-0.07	0.21	-0.19	0.43	-0.53	0.88
V_{max}	-0.60	0.96	-0.63	0.86	-0.43	0.93
I_{sc}	0.00	0.00	-0.03	0.05	na	na
V_{oc}	-0.54	0.98	-0.56	0.94	na	na
FF	-0.15	0.85	-0.25	0.80	na	na

ACKNOWLEDGMENTS

The authors thank Siemens Solar Industries for samples and support of this work. This work was supported by the U.S. Department of Energy under contract No. DE-AC36-83CH10093.

REFERENCES

[1] D. Tarrant, A. Ramos, D. Willett, and R. Gay, "CuInSe$_2$ Module Environmental Durability," *22nd IEEE PVSC*, **V1**, 1991, pp. 553-556.

[2] C. R. Osterwald, T. Glatfelter, and J. Burdick, "Comparison of the Temperature Coefficients of the Basic I-V Parameters for Various Types of Solar Cells," *19th IEEE PVSC*, 1987, pp. 188-193.

OPPORTUNITIES AND ISSUES IN INTERNATIONAL PHOTOVOLTAIC MARKET DEVELOPMENT

Roger Taylor, Doug Arent, Sam Baldwin, Robert McConnell, Jack Stone, Harin Ullal, Cecile Warner, William Wallace
National Renewable Energy Laboratory, 1617 Cole Blvd., Golden, CO 80401

Paul Klimas, Elizabeth Richards, Charles Hanley, and John Strachan
Sandia National Laboratories, Albuquerque, NM 87185-0704

ABSTRACT

The confluence of technology development and market readiness is opening up major business opportunities for photovoltaic (PV) systems throughout the developing world. The National Renewable Energy Laboratory (NREL) and Sandia National Laboratories in Albuquerque (Sandia), working on behalf of the U.S. Department of Energy, have launched pilot projects in several countries throughout the world over the past 3 years. The focus of these pilot projects has been the development of in-country institutional capabilities necessary to deliver the promise of PV electricity to the rural populations. In addition to country-specific activities, NREL is conducting several technology, information, and partnership projects focused on further accelerating the education, training, business, and technology developments necessary to bridge the gap between promise and reality. This paper summarizes these efforts.

COUNTRY PROJECTS

Country-specific, pilot-project partnerships have been developed and are being carried out in Brazil, India, China, South Africa, Mexico, and elsewhere. A common theme in all these country collaborations has been to team up with strong in-country affiliates to build on the existing in-country institutional capability.

Brazil

In Brazil, the Joint U.S./Brazilian Renewable Energy Rural Electrification Project was established following the Earth Summit in Rio de Janeiro in June 1992. In collaboration with the Centro de Pesquisas de Energia Eletrica (CEPEL) and the local state-owned electric utilities, installation of the hardware for Phase 1 of the project was completed in 1994 and nearly 800 PV lighting systems are continuing to operate successfully. Installation of Phase 2 hardware is now nearing completion in 5 additional states, where emphasis has expanded into other applications (water pumping by both PV and small wind-electric systems, stand-alone home electrification with basic ac power, two 50-kW village-scale hybrid power systems for diesel-fuel displacement in the Amazon Basin, and additional home, school, and health clinic dc power systems). The objectives of these pilot projects are to establish technical, institutional, and economic confidence in using renewable energy (PV and wind) systems to meet the needs of the citizens of rural Brazil.

Of particular interest both in Brazil and elsewhere (particularly Indonesia) is the nearly economic opportunity for village-power retrofits. The northern region of Brazil, including most of the Amazon Rain Forest, is sparsely populated—10 million people living in 5 million km^2, or less than 7% of the country's population in 56% of its total area. Electricity generation, where it exists, is mainly based on isolated thermal-electric systems ranging from a few kilowatts, in small villages, to tens of megawatts in the capital cities. There are more than 300 of these mini-grid systems operated by local utilities and thousands of privately owned systems. The cost of electricity from these systems is high and strongly dependent on system size. In the villages with diesel systems under 100 kW, the cost can be more than US$ 0.50/kWh. These high costs are due more to operation and maintenance costs and low capacity factor than to high fuel costs. The two hybrid power systems being installed in Joanes (Para) and Campinas (Amazonas) will demonstrate the technical opportunities (and problems) of operating PV-wind-battery-diesel hybrid power systems in remote locations in Brazil [1].

India

In India, activities are under way with the Ministry of Non-Conventional Energy Sources (MNES) and the West Bengal Renewable Energy Development Agency (WBREDA) to supply technical and economic support to the Ramakrishna Mission. The Mission is a well-respected humanitarian organization working in the general area of rural and subsistence-level dwellers. The Mission has identified the Sundarbans, the delta region of southern Bengal, where the Ganges River meets the Bay of Bengal, as an ideal area for the pilot project. The Mission will be responsible for educating and training the users of PV systems and for collecting the revenues from system owners.

Three hundred homes in seven villages will be provided with electric lights and auxiliary power sockets. In addition, a clinic, weaving facility, and youth club will receive lights and a vaccine refrigerator. Several battery-charging stations will be built, and a spice grinder and water pump will be PV powered. The villages will also receive street lights. Approximately 30kW of PV panels (polycrystalline silicon) will be deployed.

This project is cost-shared 50-50 with the Ministry of Non-Conventional Energy Sources in India, who will provide batteries, compact fluorescent lamps, and other balance-of-system components. MNES will pay for custom duties and a

technical consultants WBREDA and Exide Industries, Ltd. to assist in installation and maintenance. The Government of India will provide a 50% subsidy to purchase the home lighting systems and the system owners will be required to provide the remaining amount in the form of a down payment and future payment of a long term, low interest loan. By requiring direct user investment in the systems, a pride of ownership should provide a more serious interest in keeping the systems well maintained. In addition the owners will be required to pay a small amount into a maintenance fund which will be used to provide door-to-door service for maintaining the systems. The Ramakrishna Mission will use the down payment money to establish a revolving line of credit so that the systems can be replicated for other users in the area. It is expected that entrepreneurs will be attracted to invest in home lighting systems expansion and that the battery charging stations will represent an opportunity for a revenue producing venture. The Mission will provide the banking and revenue collection functions in the area. By involving the women of the village in the use of the systems, their empowerment in being actively involved in caring for the systems will be a positive force in the villages.

Based on the success of this project, the Mission will raise additional funds to purchase and promote cost-effective system installations.

China

Rapid growth in economic development coupled with the absence of an electric grid in large areas of the rural countryside have created a need for new energy sources both in urban centers and rural areas in China. The Ministry of Electric Power in China has announced that China needs to install 100 to 130 GW of new electric generating capacity by the year 2000 to meet the demands of the growing economy. Concerns over environmental pollution from the increased use of coal-fired steam turbines to meet this capacity expansion is a growing concern. As a consequence of these factors, there is a growing interest in China for the development of renewable energy resources and technologies to meet energy demands and help mitigate pollution problems. Interest in the use of renewable energy is reflected both at the central government level in Beijing and at the local level in the provinces and autonomous regions of China.

China has an abundance of renewable energy resources in the form of solar, wind, biomass, hydro, geothermal, and ocean tidal resources. China is also already one of the world's largest users of renewables, primarily in the form of hydropower and biomass. The solar resource of the country is also enormous and is strategically located in areas of the greatest need in terms of rural energy development. There are more than 120 million rural people in northern and western China and over 300 coastal islands that currently have no access to the electric power grid and no near-term prospects for grid connection. There is an excellent match of solar and also wind resources to meet the rural electrification needs of these people.

The current installed capacity of PV systems in China is small, but growing rapidly. In 1993, the installed capacity of PV systems was about 3.5 MW_p, and by 1995 the installed capacity was about 5 MW_p. Most of this capacity (60%) is power for telecommunications applications. About 1.5 MW_p is installed in remote, agricultural, and village power applications, for which opportunities exist throughout China. There are more than 10,000 rural household systems already installed, mostly in Inner Mongolia, Tibet, and Qinghai. Household systems are generally in the range of 20 to 80 W and are used for lighting and small consumer electronics. The largest PV systems are in the range of 10 to 25 kW, most of which are village demonstration systems in Tibet. There is experience with wind/PV hybrid systems in the range of 200 W to 35 kW. There is at present no experience with grid-connected PV systems in China. However, the quality of grid power is a pervasive problem, and the use of PV for grid-support, uninterruptible power supplies, and peak-shaving applications in the potential urban market is of high interest in China.

In the central government of the People's Republic of China, there are three commissions under the State Council that are actively involved in renewable energy: the State Planning Commission (SPC), the State Economic and Trade Commission (SETC), and the State Science and Technology Commission (SSTC). The SPC is in charge of planning and budget approval for large infrastructure projects. The SETC is in charge of industrialization and retrofitting existing industries. The SSTC is in charge of planning and program administration of scientific research and development projects. Project implementation and management are the responsibilities of various ministries, such as the Ministry of Electric Power (MEP) and the Ministry of Agriculture (MOA). In February, 1995, Hazel O'Leary, Secretary of the U.S. Department of Energy (DOE), signed the Energy Efficiency and Renewable Energy protocol agreement with the State Science and Technology Commission in Beijing that established a broad umbrella for Sino/American cooperation to develop renewable energy technologies and markets in China.

Prior to and since the signing of the protocol agreement, DOE has been working closely with key departments in the SPC, SSTC, and SETC to provide assistance and support for China's renewable energy planning activities. Such activities include preparation of the Agenda 21, "White Paper on China's Population, Environment, and Development in the 21st Century," and encouragement for renewable energy project development for China's Ninth Five-Year Plan, for the period of 1996 to 2000. Under the framework for cooperation established by the protocol agreement, DOE is pursuing development of three project annexes: (1) with the Chinese Ministry of Agriculture for rural energy development, (2) with key organizations for wind energy and hybrid system cooperation, and (3) for business development activities in cooperation with the SETC. NREL is providing assistance to DOE for implementing projects under the protocol agreement in China.

The high cost, lack of a marketing and distribution infrastructure, and variable quality of modules and balance-of-system components are barriers to the widespread deployment of photovoltaics in China. Several cooperative projects are being conducted in China to address these problems. Under the protocol agreement, NREL is working with the MOA and the Chinese State Council Office of Poverty Alleviation and Rural Development to develop a cost-shared program to provide household PV electricity systems to rural families in Western China. This project is being conducted with the Solar Electric Light Fund (SELF) in Washington, D.C., and is designed to expand and strengthen the

distribution infrastructure previously established in Gansu province in China. This infrastructure involves a partnership between the rural energy offices at the county level (under the MOA), provincial government agencies associated with poverty alleviation, and local PV system integrators in China. Rural energy offices exist at the district and county level in almost every province in China and can help facilitate rural electrification projects throughout China, providing a widespread infrastructure for technology deployment. The use of revolving credit funds for financing the purchase of household systems to expand the market for PV is a critical component of the project.

In collaboration with the Chinese Academy of Science in Beijing and the Center for Energy and Environmental Policy at the University of Delaware in the United States, NREL is also working with several agencies of the Inner Mongolian government and several key investors in Inner Mongolia to develop PV and PV/wind hybrid projects in Inner Mongolia. A series of case studies is being conducted for household and village-power systems to develop technical and economic performance data and information. The government of Inner Mongolia is committed to a village electrification program over the next 5 years, which will involve a number of villages that will be electrified using renewable energy technologies. Inner Mongolia also has an established distribution infrastructure for rural energy-system deployment at the county and village level that can provide an infrastructure for PV market development. Involvement of the local electricity bureau is a key component of this project. Local electricity bureaus at the provincial and county level potentially represent a national infrastructure for technology deployment throughout China [2].

South Africa

Dramatic political changes in South Africa have prompted an unprecedented effort to improve social equity of the majority of South Africans. A vital component of this effort addresses the energy requirements of the poor. This includes providing power for basic lighting and for productive uses to some 20 million citizens who do not currently have access to the existing transmission and distribution system. Aggressive programs are currently under development in South Africa for the electrification of rural clinics, schools, and homes. Although basic lighting for improved quality of life, health, and education are critical near-term efforts, long-term sustainable development requires improved economic development. Renewable energy resources offer tremendous benefits to the energy, economic, and social challenges South Africa faces.

The South African photovoltaic market is multi-dimensional, with an existing commercial sector that serves the game reserves, national parks, telecommunications network, and farmers. Additionally, and with the new government, three programs have been developed for rural electrification: schools, medical clinics, and domestic systems.

The schools program has been funded initially by the Government of National Unity (GNU) and is administered by Eskom, the national parastatal electricity utility. The program hopes to electrify 16,000 schools over 5 years at about 500 W each, with associated building wiring and audio-video equipment.

The medical clinics program is run by the Independent Development Trust (IDT) and has a target of about 2000 clinics. This program is fully functional and electrifies about 10 clinics per month through an extensive network of field agents, many of whom also work with other development portfolios such as agriculture and small business development. A typical clinic system is rated at 900 W, and about 200 installations have already been completed.

The domestic households program began in 1995 and is formulated under a new company called Renewable Energy for South Africa (REFSA), which is a subsidiary of the Central Energy Fund, and under the oversight of the Department of Mineral and Energy Affairs. The DOE brokered US AID (U.S. Agency for International Development) funding of $1.1 million as a cost-share of the pilot phase, now administered by ECRE/REFAD (the U.S. Export Council for Renewable Energy/Renewable Energy for African Development). DOE has also been instrumental in developing implementation ideas and bringing international financing institutions into the discussions. REFSA has received technical assistance from NRECA (the National Rural Electric Cooperative Association), Sandia, and NREL.

DOE has a broad and coordinated effort looking at the complete energy sector in South Africa. The Department's efforts also include strong efficiency components, capacity building programs, technical exchange, and policy development. For renewable energy, the DOE has worked in partnership with both NREL and Sandia National Laboratories on a multi-tiered program that includes building manufacturing capability, market development, technical interchange for R&D, and pilot testing of a variety of technologies.

Cooperation between Spire Corporation and in-country partners Renaissance (a South African empowerment and investment company), AEG (Pty) Limited (affiliated with ASE Americas), the University of Port Elizabeth, and others has led to the establishment of Suncorp, a black-owned business for PV module assembly and solar system supply to a wide variety of emerging PV markets in South Africa. Suncorp will provide locally manufactured product that will help meet the needs of the South African Reconstruction and Development Programme's efforts to stimulate the socio-economic development of disadvantaged communities in South Africa. A key to successful expansion of rural electrification is the development of a local marketing, distribution, maintenance, and financing infrastructure. Independent of the Suncorp efforts, NREL and Sandia are also working with local in-country affiliates to pilot a Solar Enterprise Initiative that will establish local franchises with commercial financing as part of the REFSA program.

Mexico

Mexico represents a major potential market for photovoltaics. Mexico has more than 80,000 villages, representing 7 million people with no access to grid-supplied electricity or its associated economic opportunities; a potential market on the order of $1 billion. Over 100,000 communities are without potable water, another $1billion potential market. The agricultural sector offers even larger opportunities; as examples, there are 600,000 cattle ranches in need of water pumping, representing a $6 billion potential market, as well as a great need for irrigation systems for citrus and other crops. The Mexican government has recently shown considerable interest in renewables, subsidizing the purchase of more than 30,000 solar home-lighting systems over the last few years and incorporating renewables components into some of its

federal agencies. However, aside from the solar home systems, the other market sectors remain largely untapped, and Mexico is implementing a variety of development programs, particularly in the agricultural sector, that offer excellent opportunities for PV if the agencies involved can acquire the capabilities necessary for accessing and using the technology. The North American Free Trade Agreement and Mexico's proximity to the United States offer special advantages to the U.S. industry.

Sandia and NREL are implementing a multi-year program in Mexico to facilitate the use of renewable energy, primarily PV and wind, in rural, off-grid, productive-use applications. This program is co-sponsored by the DOE and the USAID. Like other programs described in this paper, the approach by Sandia and NREL emphasizes sustainability and the development of in-country institutional capacity. The program team is working with established Mexican organizations and within established and funded programs to incorporate the use of renewable energy technologies where they are the best technical and economic solution. The team provides training and technical assistance and uses the implementation of pilot projects as a tool to institutionalize the use of renewable-energy technologies. About 30 cost-shared PV systems have been installed to date, and more than 100 systems will be installed by the end of 1996. Also, significant near-term replication of these projects is under way, as the Fideicomiso de Riesgo Compartido (FIRCO - a federal shared-risk trust fund under Mexico's agriculture department) initiates a major $225 million development program. Sandia and NREL are providing technical assistance as FIRCO begins to implement hundreds of PV and wind projects, with equipment purchases made entirely with Mexican funds (no U.S. cost share).

Productive-use applications are those that provide an economic or social benefit to the end-user. They have a high degree of sustainability and replicability because a means for paying for the systems is builtin. Examples include water pumping for livestock or crop irrigation, lighting for commercial or business activities, communications, power for grain-grinding or carpentry, and ecotourism.

The Sandia/NREL Mexico program is divided into specific projects and cross-cutting activities. The projects include working with FIRCO at both the state and national levels, along with state-agency activities in several states, including Chihuahua, Sonora, Baja California Sur, and Quintana Roo. In addition, the program has cooperative projects under way with Conservation International, The Nature Conservancy, World Wildlife Fund, and their local Mexican partner organizations to incorporate the use of renewable energy into ongoing protected-areas management activities in Mexico. Cross-cutting activities include solar and wind resource assessment, training, technical and economic analysis, financing mechanisms, industry interactions, project monitoring and evaluation, and environmental assessments.

DEVELOPMENT STRATEGY

A common theme in all these country collaborations has been to team up with strong in-country affiliates to build on the existing in-country institutional capability. Different types of organizations have emerged in each country. In Brazil, the electric utility industry is a key player. In China, the rural energy offices of the Chinese Ministry of Agriculture are key players. In India, the non-governmental Ramakrishna Mission is a key player. In South Africa, diverse governmental and private-sector capabilities are being focused on developing new institutions. And in Mexico, federal and state agricultural development agencies have emerged as strong partners. The key issue in PV commercialization is the development of these institutional capabilities as rapidly as possible.

Toward that end, our efforts are increasingly focused on developing in-country institutional capability. Activities include the following:

- Internships to train in-country professionals
- System design software for renewable energy and hybrid-system analysis
- Educational and media communication tools to train local experts in effectively relaying the renewables message
- Policy consultation to facilitate informed decision-making by local officials
- Academic programs to further educate engineers and scientists, in cooperation with U.S. colleges and universities
- Financial support through linkages with international financing institutions
- Development of local in-country centers of excellence to facilitate technology transfer and project expertise
- Electronic information access to provide rapid, up-to-date information on products, literature, projects, design tools, financing, and contacts
- Specialized technology consultation for country-specific needs
- Testing and evaluation services to ensure reliable systems and components under local conditions.

International partnerships are helping to accelerate both the development and the implementation of renewable energy technologies. Although these efforts span across the entire range of renewable technologies, PV is often the entry point. Moving into the next century, it is increasingly important to work more closely with government agencies, utilities, businesses, research laboratories, development and investment organizations, and consumer and community groups to support sustainable economic development through the worldwide use of renewable-energy technologies.

REFERENCES

[1] C. Warner, R. Taylor, M. Moszkowicz, and C. Ribeiro, "PV-Hybrid Village Power Systems in Amazonia," *Twenty-fifth IEEE PVSC*, 1996.

[2] W. Wallace and S. Tsuo, "Sino/American Cooperation for PV Development in the People's Republic of China," *Twenty-fifth IEEE PVSC*, 1996.

[3] J. L. Stone and H. S. Ullal, "PV Opportunities in India," *13th NREL Photovoltaics Program Review, AIP Conference Proceedings 353*, 1995.

POROUS SILICON GETTERING

Y.S. Tsuo, P. Menna,* J.R. Pitts, K.R. Jantzen, S. Asher, M. Al-Jassim, and T.F. Ciszek
National Renewable Energy Laboratory, 1617 Cole Blvd., Golden, Colorado 80401, USA
*ENEA-Centro Ricerche Portici, Localite Granatello 80055, Portici, Italy

ABSTRACT

We have studied a novel extrinsic gettering method that uses the large surface areas produced by a porous-silicon etch as gettering sites. The annealing step of the gettering used a high-flux solar furnace. We found that a high density of photons during annealing enhanced the impurity diffusion to the gettering sites. We used metallurgical-grade Si (MG-Si) prepared by directional solidification casting as the starting material. We propose to use porous-silicon-gettered MG-Si as a low-cost epitaxial substrate for polycrystalline silicon thin-film growth.

BACKGROUND

Photovoltaic (PV) solar cells made using thin-film crystalline silicon on a low-cost substrate have the potential for low cost, high efficiency, and long-term stability [1]. However, the lack of a suitable low-cost substrate that can be used for epitaxial growth of thin-film silicon at temperatures of 600°C or above without contaminating the film has, so far, prevented the development of truly low-cost, thin-film crystalline silicon for solar-cell fabrication [2-4]. The objective of this study is to develop such a low-cost, high-temperature, epitaxial substrate for polycrystalline silicon thin-film growth. Our approach is to make such a substrate by using a novel porous-silicon gettering method to create low-impurity layers on both surfaces of a metallurgical-grade silicon (MG-Si) wafer. The novel porous-silicon gettering method involves a simple stain etching for generating a porous silicon layer on both surfaces of the MG-Si wafer and a high-temperature (1000°C) annealing step using a high-flux solar furnace (HFSF) [5]. The porous silicon layers are removed, along with the gettered impurities, after gettering. If the subsequent epitaxial thin-film silicon growth is done on this substrate at a temperature lower than the annealing temperature, then the low-impurity layers can serve as diffusion barriers to prevent impurities in the bulk of the MG-Si substrate from contaminating the film.

Gettering reduces impurities in a wafer by localizing the impurities in regions away from the active device regions. The effectiveness of gettering depends on the establishment of gettering sites for absorbing impurities, the diffusion coefficients of the impurities in bulk Si, and the segregation coefficient of the impurities at the gettering sites. Using electrochemically etched porous silicon to getter impurities and other defects in electronic-grade silicon has been studied previously using conventional furnaces [6-9]. The significant increase of the surface area achieved with the porous silicon (nearly 600 m^2/cm^3), as well as the larger lattice parameter of porous silicon compared with that of bulk Si, greatly enhance the probability of tying up the contaminants during the annealing step. Recent studies of enhanced impurity gettering by nanometer-scaled cavities in silicon also indirectly confirmed that porous silicon should provide effective gettering sites [10,11]. These studies showed that metallic contaminants react with Si dangling bonds present on the internal surface of the nanometer-scale voids created within Si crystals. The resulting cavity-trapped impurity states of the metal are more stable than the silicide phase. For instance, the binding energy of Cu within the cavity traps is 0.5 eV larger than in the Cu_3Si phase.

The intense incoherent light irradiation in a HFSF may also enhance the diffusion of metallic impurities. In a study using an artificial light source, Borisenko and Dorofeev [8] showed that intense photoelectronic excitations caused by light absorption generate excess impurity interstitials in the surface layer. This enhances the diffusivity of impurities, because the diffusion of interstitial metallic atoms is an order of magnitude faster than that of substitutional atoms [12].

EXPERIMENTAL METHODS

The MG-Si was prepared by directional solidification casting. Wafer-sawing damage was chemically removed using an HF and HNO_3 solution before porous-silicon etching. A simple and low-cost chemical etching is used to generate porous silicon layers on both front and back surfaces of the silicon wafers. A high-flux solar furnace [5] is used to provide high-temperature annealing. The porous-silicon gettering sites, along with the gettered impurities, can be easily removed by oxidation followed by a HF dip or a silicon chemical etch. Each porous-silicon gettering process removes up to about 10 μm of wafer thickness. This gettering process can be repeated so that the desired purity level is obtained.

NREL's high-flux solar furnace uses an off-axis design. A flat, tracking heliostat 32 m^2 in area reflects sunlight onto a faceted primary concentrator of 25 curved, hexagonal mirrors with a 7-m focal length. Both the heliostat and primary concentrator are front-surface aluminum mirrors coated for enhanced-ultraviolet-reflectivity. The primary concentrator focuses the light to a position inside the target bay, where 94% of the energy falls inside a 10-cm-diameter circle. The wafer under HFSF processing is positioned in the

center of the sample chamber, facing the incident sunlight and supported by three point contacts at the edge and a thermocouple tip touching the back surface. For annealing, an argon atmosphere of 600 torr is used in the sample chamber. For diffusion, an atmosphere of 2% oxygen and 98% argon of 600 torr is used. To determine the wafer temperature during HFSF processing, we used a type K, thin-wire, inconel sheathed thermocouple in direct contact with the back surface of the 300-micron-thick wafer. The temperature difference between the front and back surfaces of the wafer is calibrated by observing the temperature difference (78°C) of the melting point (801°C) of a NaCl paste painted on the front surface of the wafer and the temperature of the back surface measured by the thermocouple. For all the experiments reported in this paper, we use the front surface temperature as the sample temperature. The maximum possible systematic error of the temperature at the front surface of the wafer should be less than 20°C. Conventional furnace annealings were done in a Tempress 8-inch-diameter quartz tube furnace. The sample-temperature accuracy should be well within 5°C.

The depth profiles of impurities before and after gettering were measured using secondary-ion mass spectroscopy (SIMS). The junction profiles after phosphorus diffusion were measured using a Solid State Measurements, Inc., computerized, spreading resistance probe.

POROUS SILICON GETTERING

We used an HNO_3/HF (1:100) etching solution for the porous-silicon etching of MG-Si wafers [13]. This chemical etching method (also known as stain etching) is very simple, requiring no electrodes and no applied voltage; fast, taking 10 minutes or less; and produces porous silicon on both sides of the silicon wafer. The resulting porous silicon layers are about 2-μm thick and are strongly photoluminescent [14]. The porous-silicon-etched Si wafers were then annealed in an HFSF for 15 to 30 min. at a sample temperature of 1000°C.

SIMS depth-profiling measurements done from the front (illuminated) and back surfaces of the MG-Si wafers showed that the HFSF annealing treatments caused impurities in the bulk of the wafers to diffuse and segregate at the porous-silicon-etched surfaces. The effectiveness of this impurity gettering process increases with the HFSF treatment time. Strong gettering effects were observed for Al, B, Fe, Cu, and Cr impurities. For example, Figure 1 shows the copper impurity levels as a function of the sputtering time (which is proportional to the distance from the surface) for the front surface of an as-polished MG-Si

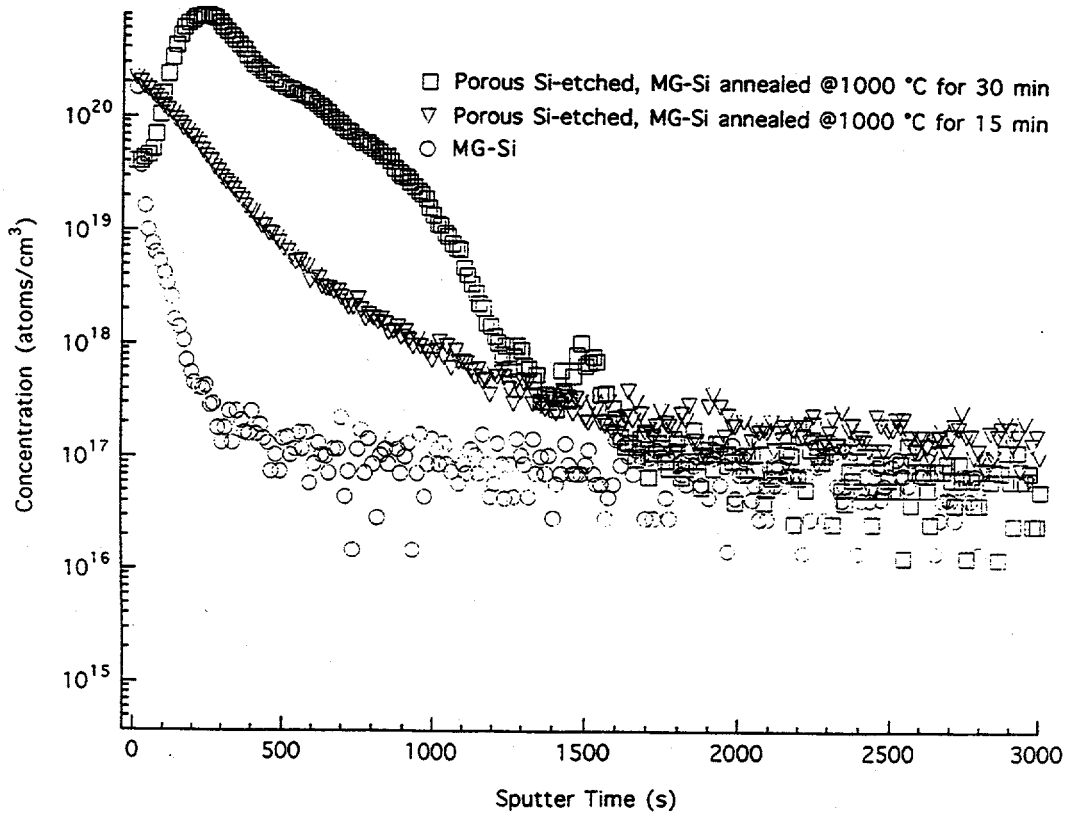

Fig. 1 SIMS depth profiles of the Cu impurity of (1) an as-polished cast MG-Si, (2) the same sample after porous-silicon etch and a 1000°C, 15-min. HFSF anneal, and (3) the same sample after porous-silicon etch and a 1000°C, 30-min. anneal.

wafer, the identical wafer after porous-silicon etching and a 1000°C, 15-min. HFSF annealing treatment, and the same wafer after porous-silicon etching and a 1000°C, 30-min. HFSF annealing treatment. The sharply increasing or decreasing Cu profiles very close to the surface region obtained during about the first 200 seconds of sputtering are most likely due to measurement errors caused by variations in surface morphology and cleanliness. The high-copper-concentration region near the surface of the wafer corresponds to the porous-silicon-etched region, which is about 2-μm thick (about 1500 s of sputtering time). Copper has a very high diffusion coefficient, and there is even a slight copper gettering effect (not shown) at the surface region after porous-silicon etching but before annealing. The amount of surface gettering significantly increases with high-temperature annealing and with annealing time, as shown in Fig. 1. Clearly, the combination of a porous-silicon etch and an HFSF annealing treatment effectively getters impurities to the porous-silicon-etched surface layers.

PHOTON-ENHANCED DIFFUSION

To heat a silicon wafer in a HFSF to 1000°C, we need concentrated sunlight of about 40 W/cm^2. Such intense illumination can increase the ratio of interstitial impurities over substitutional impurities [8]. The diffusion of interstitial impurities is faster than substitutional impurities, because substitutional diffusion requires additional intrinsic defects such as vacancies or silicon self-interstitials. Furthermore, the diffusion of interstitials into the silicon is promoted along the direction of heat flow, from the irradiated front surface to the back of the wafer. We observed higher levels of gettered impurities in the front surface than in the back surface, especially in the grain-boundary regions. However, there is a significant temperature difference between the front and back surfaces during HFSF annealing: 78°C at the front-surface temperature of 801°C.

To more positively identify the photon-induced effects, we compared the phosphorus diffusion properties of HFSF-processed, single-crystal silicon wafers against conventional furnace-processed wafers in the temperature range of 775°C to 950°C. The two groups of samples used the same 300-μm-thick, 0.2-ohm-cm-resistivity, float-zone growth, boron-doped, single-crystal silicon wafers, same spin-on phosphorus dopants from Emulsitone Co., and same diffusion temperatures and diffusion time (20 min.). The long diffusion time of 20 min. is chosen to reduce the effects of minor variations in heating and cooling rates. The junction profile measurements after diffusion show that HFSF-diffused samples have considerably deeper junctions than conventional-furnace-diffused samples (see Figure 2). The difference in the junction depths is equivalent to a temperature difference of 25°C on the low-temperature side and 75°C on the high-temperature side. These temperature differences are larger than the maximum possible error (20°C) in our estimation of the front-sample surface temperature during HFSF annealing. Comparisons of the peak surface phosphorus concentrations for the two groups of samples (See Figure 3) show that HFSF-annealed samples have higher peak surface phosphorus concentrations at temperatures below 875°C. At temperatures above 875°C, the peak phosphorus doping concentrations for the two groups of samples are about the same. We believe the enhanced phosphorus diffusion in HFSF-annealed samples is due to photon-related effects.

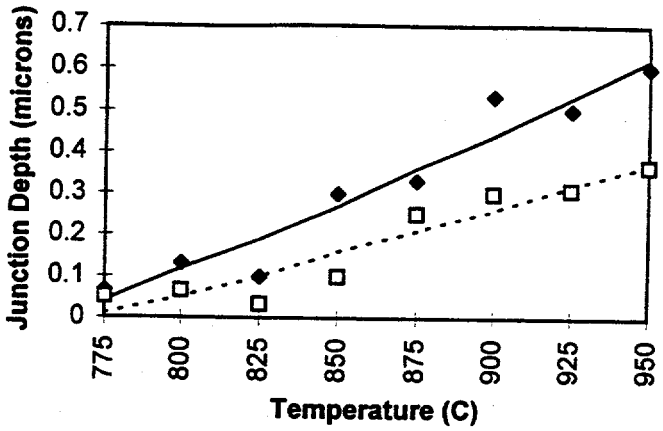

Fig. 2 Junction depth vs. diffusion temperature for solar-furnace-diffused samples (solid line) and conventional-furnace-diffused samples (dotted line).

Hartiti et al. [15] obtained similar effects of photon-enhanced diffusion of phosphorus when comparing rapid thermal processing (RTP) and conventional thermal processing (CTP) methods between temperatures of 800°C and 1000°C. However, the difference between RTP and CTP decreases with temperature and disappears above 900°C, whereas the difference in the junction depths between HFSF- and CTP-processed samples observed by us increases with temperature. Hartiti et al. attributed the enhancement they observed to photon-enhanced Si-Si bond-breaking, which reduced the surface barrier for phosphorus diffusion.

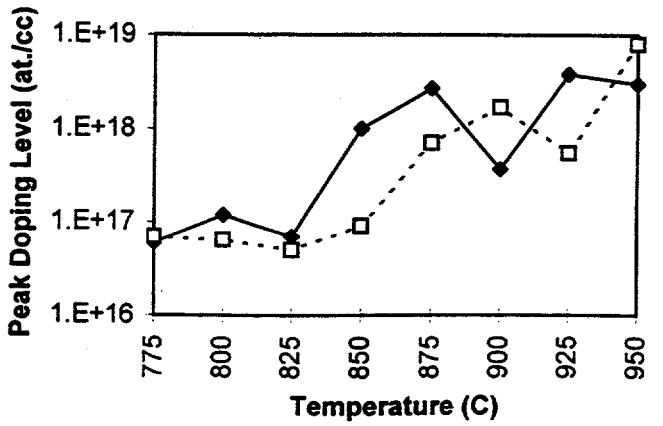

Fig. 3 Peak phosphorus doping concentration vs. diffusion temperature for solar furnace-diffused samples (solid line) and conventional-furnace-diffused samples (dotted line).

CONCLUSIONS

We have proposed here a new type of low-cost substrate that can be used for epitaxial growth of thin-film polycrystalline silicon without impurity contamination. We have demonstrated how such a substrate can be made from metallurgical-grade silicon wafers by showing that the large surface area created by a porous-silicon etch provides effective gettering sites and that the presence of photons during HFSF annealing enhances gettering efficiency. A porous-silicon-gettered MG-Si substrate has several advantages: (1) It is suitable for epitaxial polycrystalline silicon growth because the substrate itself is also polycrystalline silicon; (2) The film contamination from the substrate can be avoided if the film growth temperature is less than the gettering temperature of 1000°C because the gettered surface layers can serve as diffusion barriers; (3) It is a highly conductive substrate; (4) The substrate can be textured before film deposition; and (5) The porous-silicon etching and HFSF annealing can be done in large areas at low cost.

We have also demonstrated that porous-silicon gettering is a very effective extrinsic gettering technique for Al, B, Fe, Cu, and Cr impurities. The special features of porous-silicon gettering include: (1) A simple and low-cost chemical etching is used to generate the porous layers on both sides of the Si wafer to provide a large number of efficient gettering sites; (2) Porous-silicon etching causes no permanent damage to the substrate; (3) A high-flux solar furnace is used to provide low-cost, low-contamination, high-temperature annealing; (4) Impurity diffusion is enhanced by incident photon flux during annealing; (5) The gettering sites, along with the gettered impurities, can be easily removed at the end the process; and (6) The gettering process can be repeated to obtain the desired purity level, with a loss of only 10 μm of wafer thickness for each gettering cycle.

ACKNOWLEDGEMENTS

We thank Dr. T. Wang of NREL and Dr. C.J. Huang of the Industrial Technology Research Institute for helpful discussions. This work was supported by the U.S. Department of Energy under contract No. DE-AC36-83CH10093 through an NREL Director's Development Fund.

REFERENCES

1. A. Wang, J. Zhao, S.R. Wenham, and M.A. Green, "21.5% Efficient Thin Silicon Solar Cell," *Progress in PV: Res. & Appl.*, 4, pp.55-58, 1996.

2. A.V. Shah, R. Platz, and H. Keppner, "Thin-Film Silicon Solar Cells: A Review and Selected Trends," *Solar Energy Mat. & Solar Cells*, 38, pp. 501-520, 1995.

3. S.R. Wenham and M.A. Green, "Silicon Solar Cells," *Progress in PV: Res. & Appl.*, 4, pp.3-33, 1996.

4. M.J. Stocks, A. Cuevas, and A.W. Blakers, "Theroretical Comparison of Conventional and Multilayer Thin Silicon Solar Cells," *Progress in PV: Res. & Appl.*, 4, pp.35-54, 1996.

5. Y.S. Tsuo, J.R. Pitts, M.D. Landry, P. Menna, C.E. Bingham, A. Lewandowski, and T.F. Ciszek, "High-Flux Solar Furnace Processing of Silicon Solar Cells," to be published in *Solar Energy Materials and Solar Cells.*

6. Y.S. Tsuo, Y. Xiao, and C.A. Moore, "Device Applications of Porous and Nanostructured Silicon," in *Porous Silicon*, edited by Z.C. Feng and R. Tsu, World Scientific Publishing: NY, 1994.

7. M.R. Poponiak, "Method of Gettering Contaminants in Monocrystalline Silicon," U.S. Patent 3,929,529, (1975).

8. V.E. Borisenko and A.M. Dorofeev, *MRS Symp. Proc.* 13, p. 375, 1983.

9. S.Y. Shieh and J.W. Evans, "Some Observations of the Effect of Porous Silicon on Oxidation-Induced Stacking Faults," *J. Electrochem. Soc.*, 140, pp. 1094-1096, 1993.

10. S.M. Meyers, D.M. Follstaedt, D.M. Bishop, and J.W. Medernach, in *Proceedings of Semiconductor Silicon*/1994, Eds. H.R. Huff, W. Bergholz, K. Sumino, The Electrochemical Society Inc., (1994), p. 808.

11. J. Wong-Leung, C.E. Ascheron, M. Petravic, R.G. Elliman, and J.S. Williams, "Gettering of Copper to Hydrogen-Induced Cavities in Silicon," *Appl. Phys. Lett.*, 66, pp. 1231-1233, 1995.

12. C.S. Chen and D.K. Schroder, "Kinetics of Gettering in Silicon," *J. Appl. Phys.*, 71, pp. 5858-5864, 1992.

13. P. Menna, G. Di Francia, and V. La Ferrara, "Porous Silicon in Solar Cells - A Review and a Description of Its Applications as an Anti-Reflection Coating,"*Solar Energy Materials and Solar Cells*, 37, pp. 13-24, 1995.

14. P. Menna, Y.S. Tsuo, M. Al-Jassim, S. Asher, F.J. Pern, and T.F. Ciszek, "Light-Emitting Porous Silicon from Cast Metallurgical-Grade Silicon," to be published in *J. Electrochemical Soc.*

15. B. Hartiti, R. Schindler, A. Slaoui, B. Wagner, J.C. Muller, I. Reis, A. Eyer, and P. Siffert, "Towards High-Efficiency Silicon Solar Cells by Rapid Thermal Processing," *Prog. in PV: Res. & Appl.*, 2, pp.129-142, 1994.

INVESTIGATIONS INTO ALTERNATIVE SUBSTRATE, ABSORBER, AND BUFFER LAYER PROCESSING FOR $Cu(In,Ga)Se_2$-BASED SOLAR CELLS

John R. Tuttle, T.A. Berens, J. Keane, K.R. Ramanathan, J. Granata,*
R.N. Bhattacharya, H. Wiesner, M.A. Contreras, and R. Noufi
National Renewable Energy Laboratory, Golden, Colorado USA
* Colorado State University, Fort Collins, Colorado USA

ABSTRACT

High-performance $Cu(In,Ga)Se_2$(CIGS)-based solar cells are presently fabricated within a narrow range of processing options. In this contribution, alternative substrate, absorber, and buffer layer processing is considered. Cell performance varies considerably when alternative substrates are employed. These variations are narrowed with the addition of Na via a Na_2S compound. Sputtered and electrodeposited CIGS precursors and completed absorbers show promise as alternatives to evaporation. A recrystallization process is required to improve their quality. $(In,Ga)_ySe$ buffer layers contribute to cell performance above 10%. Further improvements in these alternatives will lead to combined cell performance greater than 10% in the near term.

INTRODUCTION

High-efficiency $Cu(In,Ga)Se_2$ (CIGS)-based solar cells exhibit performance approaching 18% [1]. They are readily made within a narrow range of processing parameters. These include a single substrate type (soda-lime glass), a single heterojunction partner/buffer layer and method to make it (CdS by chemical-bath deposition [CBD]), and absorber fabrication by either evaporation methods or selenization of metal precursors.

In this contribution, we report on efforts that diverge from this mainstream and create more flexible opportunities for CIGS-based solar-cell and module processing. The alternatives are listed in Table 1. They include back-electrode/substrate systems that may be chemically decoupled from the absorber by the introduction of impurity-gettering barrier layers. Required impurities, such as Na, are introduced controllably. Alternative substrates to soda-lime glass are investigated. Alternative absorber processing, such as sputtering or electrodeposition, has successfully produced nearly 10% device performance to date [2,3]. These material delivery techniques are considered to be more transferable to production-scale systems than is the vacuum co-evaporation process. We report here on the evolution from the CIGS bulk material to the thin-film product.

Finally, several non-CBD, non-CdS heterojunction partners have been investigated and show promise [4,5]. The $(In,Ga)_y(Se,S)_x$ material system is especially attractive because buffer-layer formation can occur in-line with the absorber. Success in these areas depends on a high level of understanding of the physical and chemical operation of the conventional, high-efficiency, CIGS-based device structure.

Table 1. Alternatives to conventional CIGS absorber-based cell components.

Cell Component	Alternative
Substrate/ Mo back-contact (w/ & w/o Na_2S)	Soda-lime glass Soda-lime glass w/ 1000Å of SiO_x Smooth Al_2O_3 7-mil Stainless Steel 20-mil Pilkington Glass
Absorber	DC Sputtering Electrodeposition
Junction Buffer	$(In,Ga)_ySe$ In_ySe

EXPERIMENTAL

Alternative 5-cm x 5-cm substrates described in Table 1 are prepared by depositing a 1-μm Mo film by DC sputtering at 4-mTorr operating pressure. In some cases, a 100-Å Cr layer is evaporated prior to Mo deposition. On soda-lime glass (SLG) substrates, a 400-Å SiO_x barrier layer is first evaporated on a 2.5-cm x 5-cm section to getter Na out-diffusing from the SLG. In the experimental matrix, CIGS absorbers were deposited on these substrate configurations with and without the incorporation of 200 Å of Na_2S. The recipe for the deposition of the absorber is described in detail elsewhere [5]. The devices were completed with standard CBD of 500 Å of CdS, followed by RF sputtering of 500 Å intrinsic and 3500 Å Al-doped ZnO layers.

Alternative CIGS thin-film absorbers are deposited on standard Mo/SLG substrates. Precursor films are prepared by DC sputtering at 150-200 W from a CIGS target fabricated at Target Materials Inc., from bulk material synthesized at ASARCO, Inc. Electrodeposited (ED) precursors are synthesized at NREL by a proprietary technique developed for Davis, Joseph, and Negley Corp. Precursor films are subsequently recrystallized by exposure to either Se or Cu-Se under a temperature profile up to 550°C [2]. The absorber is completed with an (In,Ga,Se) vapor treatment at 550°C to bring the composition from the two-phase Cu-rich region to the single-phase In-rich region. Devices are completed in the conventional manner described

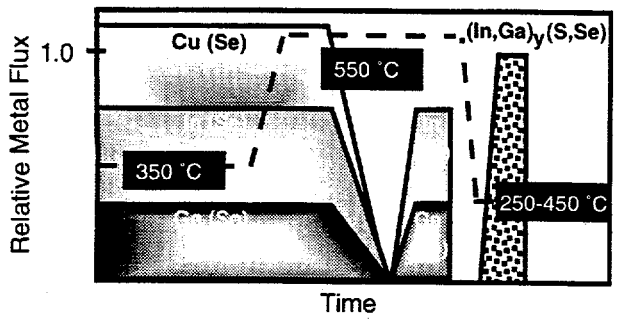

Fig. 1. Deposition profile for in-situ, alternative buffer layer using (In,Ga)y(S,Se).

above.

Alternative buffer layers are introduced in-situ following the deposition of a conventional graded CIGS absorber described in detail elsewhere [6]. In Fig. 1, the processing scheme is illustrated. The surface of the absorber is terminated by lowering the temperature and continuing with a vapor activity of (In,Ga,Se) for a period of 2 and 4 min. The lower the temperature, the less in-diffusion of Cu into the layer from the absorber. These structures were subsequently completed in one of three ways: (a) CBD CdS/i-ZnO/Al:ZnO, (b) chemical-bath treatment (CBT) in NH_4OH and a Cd salt, followed by the bi-layer ZnO, and (c) bilayer ZnO.

3-μm Ni/Al evaporated grids completed all of the above structures with about 4% coverage. Current-Voltage (I-V) characterization is carried out at AM1.5 illumination, and device efficiencies are quoted as total-area to include grid losses. Quantum-efficiency (QE) measurements are made in the dark and under voltage and light-bias in the wavelength range 380-1500 nm. Capacitance-Voltage (C-V) is conducted at 100 kHz from -2.0 to 0.5 V. Film characterization is accomplished by scanning-electron microscopy (SEM) to investigate morphology issues and by X-ray diffraction (XRD) to look at structural changes in the evolution of the precursor to the completed absorber.

RESULTS

Substrate

The purpose of looking at alternative substrates is two-fold. The first is to understand the role of the SLG, with the hope of decoupling the absorber quality and device performance from what is intended to be the cheapest and lowest-quality component of the cell. The second is to create opportunities for replacing the SLG in applications that require mechanical flexibility, improved thermal conductivity, or electrical coupling to an interconnect structure.

In Fig. 2, data are presented for the open-circuit voltage (V_{oc}) and conversion efficiency (η) of devices fabricated on five substrate configurations, with and without the addition of Na_2S as a sodium source [7]. For cells that do not contain Na, or that have a SiO_x barrier layer between the SLG and Mo, V_{oc}'s range from 550-580 mV. For cells that contain Na and/or upon the introduction of the Na_2S, V_{oc}'s range from 600-670 mV. The exception in this case is the cell fabricated on Al_2O_3. This corresponds to $+\Delta V_{oc}$'s of 20-50 mV with the introduction of additional Na into the absorber. Even more dramatic, and yet unexplained, is the general, and sometimes drastic, improvement in fill-factor (FF) with the addition of the Na_2S. For the cells on SLG, the anomalous FF behavior (22% and 40 %) is believed to be related to the ZnO processing [1]. The addition of Na appears to neutralize this phenomenon.

One significant result here is the 13.2% cell fabricated on a flexible 7-mil. stainless-steel (SS) substrate. This opens up applications where either flexible and/or conducting substrates are advantageous. A flexible substrate would have advantages from a specific power (W/kg) perspective or from a manufacturing perspective, where roll-to-roll processing would offer cost advantages.

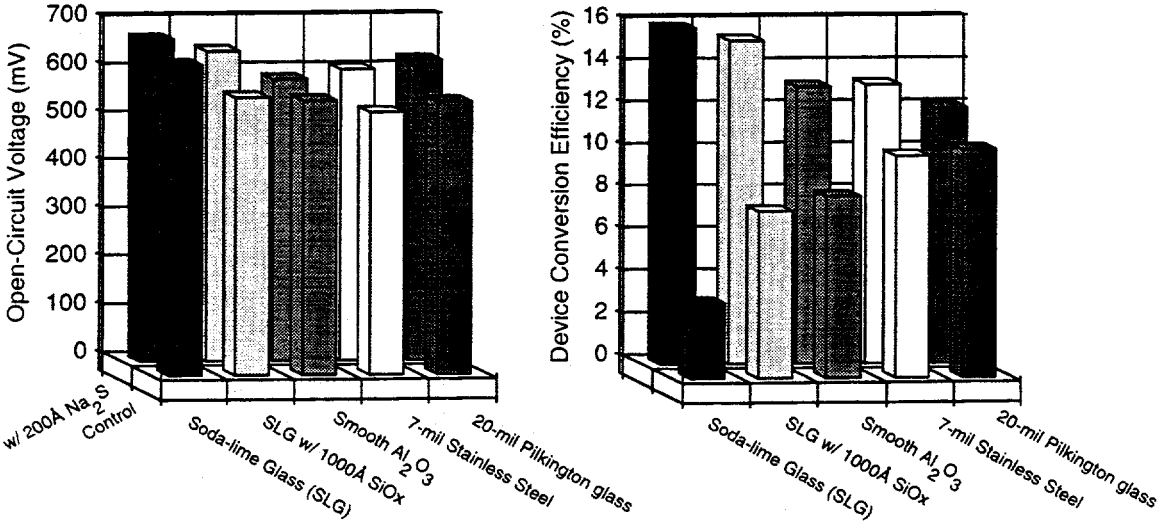

Fig. 2. Comparison of V_{oc} and device efficiency for cells fabricated on different substrates, with and without the addition of Na_2S as a sodium source. Devices incorporating Na_2S include an MgF_2 anti-reflection coating.

Table 2. Parameter space for sputtered precursors and general recrystallization processes.

Processing Parameter	Variable Space
Sputter Pressure (mTorr)	20:8 cycles 8 8:3 cycles 3
Substrate Temp. (°C)	Plasma ambient (50° - 80°C) 200°C
Precursor Processing	(a) None (b) Cu (25°C) -> Se anneal @ 550°C (c) Cu,Se @ 550°C (d) Cu_2Se (sputtered) -> Se anneal @ 550°C (e) Se only @ 550°C (for Cu-rich precursor)

Absorber

The purpose of this effort was to look at sputtering from a compound CIGS target and electrodeposition of a CIGS precursor as alternative delivery techniques to co-evaporation of the elemental constituents. A matrix approach to the sputter deposition process, and subsequent processing of both sputtered and ED precursors was pursued (Table 2). The goal was to create an absorber that exhibits similar structure and morphology to that of an evaporated film. In Fig. 3, XRD data for the as-deposited sputtered precursors are shown. The observed trend is that precursor films deposited at ambient temperature (AT) and at higher pressure exhibit no crystalline behavior, whereas those deposited at 200°C and at higher pressure exhibit crystallinity and preferred orientation. In the sputtering process, the kinetic energy of the species arriving at the substrate depends on the background pressure and decreases approximately by an order of magnitude in going from 3 to 20 mTorr [8]. For a CIGS molecule, the energies may roughly be 200 and 20 meV, respectively, at those pressures. Therefore, a preliminary explanation for

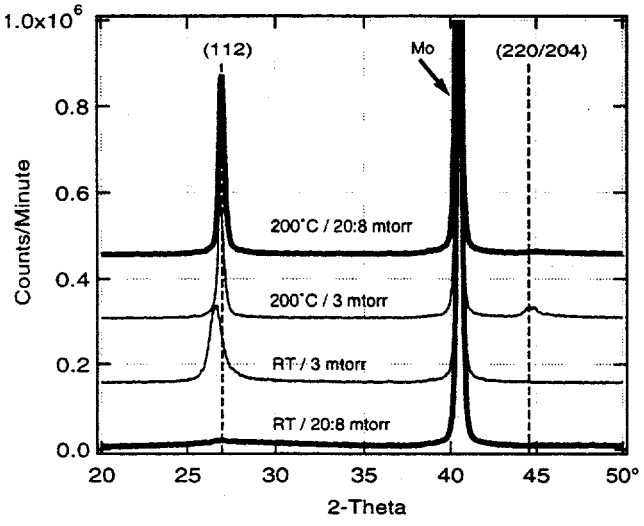

Fig. 3 Structural comparison by XRD of CIGS thin-film sputtered precursors deposited under different conditions.

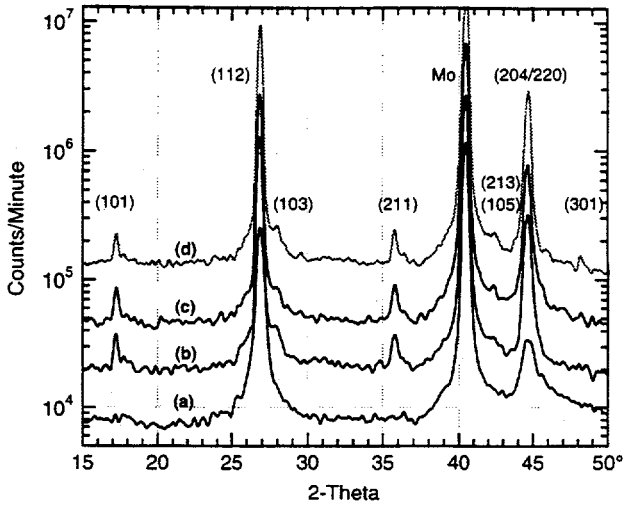

Fig. 4. Structural comparison by XRD of CIGS thin-film sputtered precursors deposited at 3 mtorr and recrystallized according to the conditions of Table 2. (a)-(d) reference Table 2.

Table 3. Parameter space for precursor sputtering and recrystallization processes. Bold lettering implies as-deposited condition.

Process	V_{oc} (mV)	J_{sc} (mA/cm²)	FF (%)	η (%)	Comments
Sputtering	508	24.3	57	7.0	**CIGS** + Cu + Se + (In,Ga,Se
Electrodeposition	545	34.0	66	12.3	**CIGS:CS** + (In,Ga,Se)

the observed phenomena is that the kinetic energy of the sputtered material influences the degree of crystallinity in the absence of substrate heat, whereas the energy imparted to the arriving species by the substrate at 200°C dominates growth kinetics in that scenario. It is unclear, however, why the sample deposited under a higher sputtering pressure would exhibit exclusive (112) orientation, a higher total energy state, whereas the lower pressure produces a film with both (112) and (220) orientations.

The purpose of the recrystallization process is to take the poorly crystallized precursors and convert them to high-quality CIGS thin-film absorbers. Cu_xSe has previously been identified as a suitable material, under the appropriate temperature and chemical conditions, to act as a fluxing agent for the recrystallization process. We have considered three mechanisms for introducing the Cu and Se, and one for activating excess Cu already in the film, described in Table 2. Of the four techniques (b)-(e), the simple selenization process and the sequential processes (Cu_xSe or Cu followed by Se) are the most applicable to a manufacturing environment.

In Fig. 4, XRD analysis of recrystallized sputtered precursors suggests that all processes are similar in their impact on a minimally crystallized film. The analysis identifies the chalcopyrite phase and a slight preferred (112) orientation. After the film sees an excess of Cu, Devices can then be fabricated. In Table 3, we present our best results to date. The 12.3% device by electrodeposition is

very encouraging. The sputtering results continue to be preliminary. Carrier collection within the absorber appears to be poor as observed by the low short-circuit current density (J_{sc}). This study, however, has proven to be fruitful in elucidating the relationship between the sputtering process and the final product.

Buffer Layer

The purpose of this effort is to replace the CBD CdS with an in-situ process for forming the junction in CIGS-based cells. This would allow continuous vacuum processing from the absorber through to the ZnO deposition. In Fig. 1, the process for the creation of an $(In,Ga)_ySe$ buffer layer is described. In Fig. 5, data are presented for devices fabricated with such a structure. Completed CIGS absorbers were exposed to (In,Ga,Se) vapor for an additional 2- or 4-min. at either 300°C, 400°C, or 500°C. The temperature influences the in-diffusion of Cu from the absorber which, in turn, influences the bandgap and conductivity type of the surface layer. The data (I-V and QE not shown) suggest the formation of a discrete n-type layer at 300°C, producing a buried junction and poor spectral response. At 500°C, there is sufficient Cu in the layer to consider it an extension of the p-type absorber. It consequently is a poor heterojunction partner to ZnO. The intermediate temperature appears to create a buffer layer that is neither isotype to the absorber nor sufficiently n-type to move the junction away from the heterointerface. This recipe has succesfully produced a device with total-area performance of near 11%. Continued optimization of the

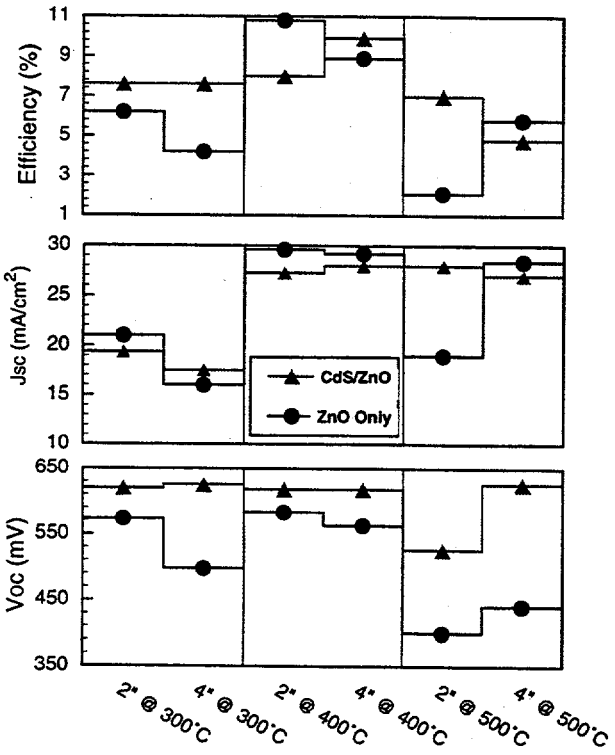

Fig. 5. V_{oc}, J_{sc}, and device efficiency for devices made with modified buffer layers fabricated in-situ with the absorber.

properties of this layer, as well as the properties of the ZnO window layer, will drive the performance well above the present benchmark.

FINAL REMARKS

This contribution has initiated work on creating more flexible and potentially manufacturable processes to fabricate high-quality, CIGS-based solar cells. Although far from optimized, we have identified alternatives to SLG substrates, evaporated absorbers, and CdS buffer layers. Individual substitution of each of these processes has produced devices with performance over 10%. It is now our intent to optimize the individual processes and combine them into one simple, reproducible, high-yield process that may easily be scaled to a manufacturing environment.

ACKNOWLEDGEMENTS

The authors thank United Solar Systems Corp. for the stainless-steel substrates, and James Dolan and Jeff Alleman for technical assistance. This work was supported by the U.S. Department of Energy under Contract No. DE-AC36-83CH10093 to NREL.

REFERENCES

1. J.R. Tuttle, J.S. Ward, A. Duda, T.A. Berens, M.A. Contreras, K.R. Ramanathan, A.L. Tennant, J. Keane, E.D. Cole, K. Emery, and R. Noufi, *Proceedings of the 1996 Spring MRS Meeting*, San Fran., CA, 8-12 April, 1996 (in press).
2. J.R. Tuttle, M.A. Contreras, K.R. Ramanathan, A.L. Tennant, S.A. Asher, D. Niles, R. Matson, J. Keane, and R. Noufi, *Proceedings of the 13th European Photovoltaic Solar Energy Conference*, Nice, France, 23-27 Oct., 1995, p. 2131.
3. R.N. Bhattacharya, A.M. Fernandez, M.A. Contreras, J. Keane, A.L. Tennant, K.R. Ramanathan, J.R. Tuttle, R. Noufi, and A.M. Hermann, *J. Electrochem. Soc.*, **143**(3), March 1996, p. 854.
4. J.R Tuttle, M. Contreras, A. Tennant, R. Matson, A. Duda, J. Carapella, D.S. Albin, and R. Noufi, *Proceedings of the NREL Photovoltaic Advanced Research and Development 11th Review Meeting*, AIP Conf. Proc. 268, May 13-15, 1992, Denver, CO, 268, p178.
5. Y. Ohtake, M. Ichikawa, A. Yamada, and M. Konagai, *Proceedings of the 13th European Photovoltaic Solar Energy Conference*, Nice, France, 23-27 Oct., 1995, p. 2088.
6. J.R. Tuttle, A.M. Gabor, M.A. Contreras, A.L. Tennant, K.R. Ramanathan, A. Franz, R. Matson, and R. Noufi, *Proceedings of the 13th NREL Photovoltaic Program Review*, AIP Conf. Proc. 353, Lakewood, CO, May 17-19, 1995, p.47.
7. M. Bodegard, J. Hedstrom, K. Granath, A. Rockett, and L. Stolt, *Proceedings of the 13th European Photovoltaic Solar Energy Conference*, Nice, France, 23-27 Oct., 1995, p. 2080.
8. Y. Yamamura and M. Ishida, *J. Vac. Sci. Technol. A*, 13(1), Jan/Feb, 1995, p. 101.

TECHNICAL EVALUATION OF TWO 6-kW MONO-Si PHOTOVOLTAIC SYSTEMS AT THE NATIONAL RENEWABLE ENERGY LABORATORY

E. Ernest van Dyk,* Troy Strand, and Robert Hansen

National Renewable Energy Laboratory, 1617 Cole Boulevard, Golden, CO 80401, USA

* On leave from the Department of Physics, University of Port Elizabeth, PO Box 1600, Port Elizabeth, 6000, South Africa.

ABSTRACT

This paper presents an analysis of performance data on the two 6-kW_{ac} grid-connected photovoltaic systems at the National Renewable Energy Laboratory (NREL). The performance parameters analyzed include dc and ac power, aperture efficiency, energy, capacity factor and performance index which are compared to plane-of-array irradiance, ambient temperature, and back-of-module temperature as a function of time, either daily or monthly. Power ratings of the systems were also obtained for data corresponding to different test conditions. This study has shown, in addition to expected seasonal trends, that system monitoring is a valuable tool in assessing performance and detecting faulty equipment. In addition, methods applied for this study may be used to evaluate and compare systems employing different cell technologies.

INTRODUCTION

The goal of this study was to evaluate and compare the performance of two identical 6-kW_{ac} grid-connected photovoltaic (PV) systems located on the roof of the Solar Energy Research Facility (SERF) building at NREL in Golden, Colorado. The systems began operation on March 23, 1994. The evaluation was done by the analysis of performance data obtained by continuous system monitoring for the period August 1, 1994, to July 31, 1995. The performance parameters analyzed include dc and ac power, aperture area efficiency, energy, capacity factor, and performance index. These parameters are compared to plane-of-array (POA) irradiance, ambient temperature, and back-of-module temperature as a function of time, either daily or monthly. The energy output of the systems was also simulated using PVFORM, a simulation program. The power ratings of the systems were also obtained for data corresponding to different test conditions. Finally, system losses were determined.

The results show, in addition to expected seasonal trends, that system monitoring is a valuable tool in assessing performance and detecting faulty equipment. Each system was given an estimated rating of 6 kW_{ac} based on Photovoltaics for Utility-Scale Applications (PVUSA) test conditions (PTC).† The systems were found to produce a similar amount of total energy, but were operating at approximately 7% below their estimated rating. This may be attributed to the design inverter efficiency being estimated at 95% (compared with the measured value of 88%) and the module aperture-area efficiency being estimated at 12.8% (compared with the measured value of 11.0%). The continuous monitoring also revealed faulty software in the peak-power-point tracking equipment. Furthermore, the methods applied in this study may be used to evaluate and compare systems employing different cell technologies.

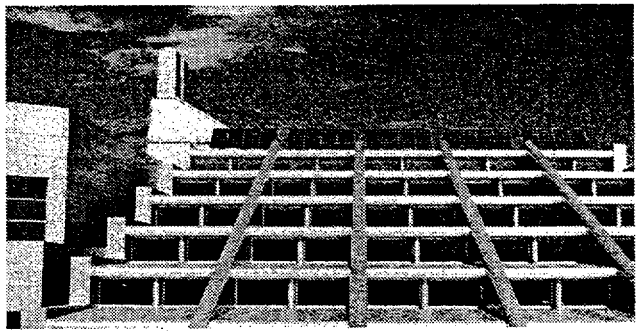

Fig. 1. Photograph showing the SERFEAST array.

SYSTEM DESCRIPTION

Each system, comprising a monocrystalline Si array, was estimated at 6 kW_{ac} under PTC when deployed. The SERF arrays each consist of 140 PV modules connected with the following configuration: 5 source circuits, each with one positive and one negative monopole; each monopole consists of 14 series-connected modules. The

† PTC: PVUSA test conditions - 1000 W/m^2 POA irradiance, 20°C ambient temperature, and 1 m/s wind speed.

dc rating of each array at standard test conditions (STC)‡ is 7.43 kW. This dc rating was obtained by summation of module peak power at STC. The arrays are mounted on the roof of the SERF building at a fixed tilt of 45° from the horizontal and aligned with the building, approximately 15° east of true south. The SERF building is located at 39.7°N latitude and 105°W longitude and the elevation is approximately 1800 m [1]. The systems are identified as SERFEAST and SERFWEST, corresponding to their position on the SERF building. The SERFEAST array is shown in Figure 1.

DATA ACQUISITION

The data acquisition is centered around Campbell Scientific data loggers connected to a computer via modem link, with data sampled every 5 s and stored as 15 min averages. The data are estimated to be accurate to ± 1%. For the purposes of this study, the performance data were restricted to those collected between August 1, 1994, and July 31, 1995.

RESULTS AND DISCUSSION

Figure 2 shows the dc and ac power (normalized to 1000W/m^2), back-of-module temperature, aperture efficiency, and inverter efficiency as a function of time over the period monitored for the SERFWEST system. The data were restricted to POA irradiance greater than 850 W/m^2 for analysis of power and associated parameters. The heavy solid lines represent a 50-point moving average for each parameter and are included to serve merely as a guide to the eye. From the figure, the expected inverse correlation between system output and back-of-module temperature is clearly demonstrated.

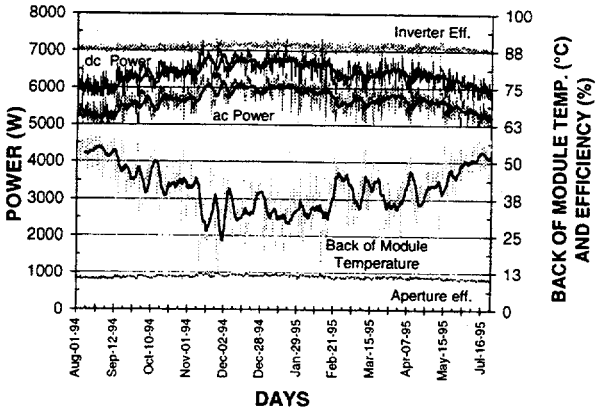

Fig. 2. Normalized dc and ac power, back-of-module temperature, aperture-area efficiency, and inverter efficiency vs. time for the SERFWEST system.

The aperture-area efficiency is defined as the ratio P_{out}/P_{in}, where P_{in} is the POA irradiance for net module aperture area (module area excluding frame) of system and P_{out} is the dc power output. The annual average aperture area efficiency was determined to be 11.0%, compared with the design value of 12.8%. This discrepancy may be attributed, in part, to various array losses that were not adequately accounted for and to prevailing weather conditions. It should be noted that the annual average aperture efficiency based on all the data collected was determined to be 10.5%.

The system losses, which ultimately determine system performance, may result from array losses and those associated with dc to ac conversion. The array losses are caused by wiring, module shadowing, soiling, degradation, reflection, and effects related to temperature and spectral variations. The energy lost because of array losses, excluding temperature, was determined to be 10.6% as measured relative to the STC array rating. The temperature losses were found to be as high as 13% when modules operate at 55°C. The losses associated with dc to ac power conversion on power conditioning equipment used are easily quantified by direct measurement of dc- and ac-power outputs. These losses are illustrated in Figure 2 by the inverter efficiency, defined as the ratio P_{ac}/P_{dc}. The annual average inverter efficiencies determined using POA irradiances above 850 W/m^2 were 88.6% and 88.3% for the SERFWEST and SERFEAST systems, respectively. This is approximately 7% below the design inverter efficiency of 95%. At 75% of full load (6kW$_{ac}$), the inverter should run at 95%. It should, however, be noted that the annual inverter efficiencies based on all data collected were 86.7% and 86.4% for the SERFWEST and SERFEAST systems, respectively. The cumulative effect of all the system losses is about 30% of possible energy generation as determined by the array STC ratings of 7.43 kW per system.

The total annual dc energy produced by the two systems was 12.0 MWh and 11.8 MWh for SERFEAST and SERFWEST, respectively. The monthly energy produced shows variation caused by seasonal insolation and prevailing weather conditions. These variations, spring and fall maxima and corresponding winter and summer minima, are depicted in Figure 3, together with energy production as predicted by a modeling program, PVFORM [2]. PVFORM uses actual radiation and meteorological data to simulate output based on system parameters and typical system losses. The radiation and meteorological data used are direct radiation, global horizontal radiation, ambient temperature and wind speed. These data were obtained from the Reference Meteorology and Irradiance Station (RMIS) at NREL [3,4]. The RMIS irradiance data is accurate to ± 3% for global horizontal, ± 1% for direct normal, and ± 5% modeled irradiance [4,5]. The total dc energy as obtained by the simulation differs from the actual SERFWEST energy produced by 1.5%, thereby indicating the significance of performing a simulation. It must, however, be stressed that by performing a simulation many input parameters influence the ultimate output and may therefore be misleading. During the months in which a significant difference between measured and simulated energy is observed, the

‡ STC: Standard test conditions -1000 W/m^2 POA irradiance, 25°C cell temperature, and air mass 1.5 global spectrum.

difference may be attributed to either temperature effects or snow on the arrays. More specifically, the lower measured energy in September, June, and July could be attributed to temperature and weather patterns, while the March difference may be ascribed to snow on the arrays. It is worth noting that the unusually low energy production of the SERFEAST system in July 1995 may be accounted for by the fact that the peak-power tracking equipment had a software error. This error resulted in the low energy production and does, in part, account for the difference in total energy production. The error was corrected in August 1995.

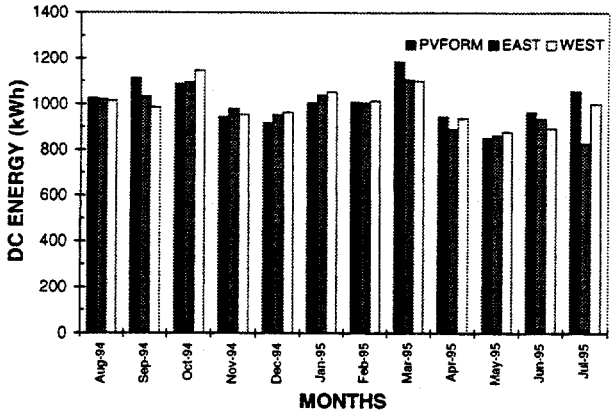

Fig. 3. Comparison of actual dc energy with simulated dc energy for both systems. The simulation was performed using PVFORM and employing RMIS data.

Seasonal trends in performance are also depicted in Figure 4 by the monthly capacity factors and performance indices, calculated using the estimated PTC system rating of 6 kW_{ac} and shown as percentages. The low SERFEAST system performance in July may be accounted for by the faulty peak-power tracker as discussed above. The capacity factors for May are the lowest, excluding July SERFEAST data. This may be attributed to adverse weather conditions. The performance index, however, shows that May is a good month. This is because the reduced irradiance in May is accounted for in determining the performance index; this may be misleading as it could be assumed that May is a high energy producing month, which is not the case. The performance index does, however, show that in May the systems performed well under the prevailing conditions.

Outdoor power ratings were obtained for the systems relative to STC, PTC, and Nominal Operating Cell Temperature (NOCT)§ under the conditions of the Nominal Terrestrial Environment (NTE). For these calculations the data were restricted as follows:

STC: POA irradiances > 750 W/m^2 and back-of-module temperature between 23°C and 27°C,

PTC: POA irradiances > 750 W/m^2 and ambient temperature between 18°C and 22°C and 1 m/s wind speed, and

NOCT: POA irradiances between 750 W/m^2 and 850 W/m^2, ambient temperature between 18°C and 22°C and wind speed between 0.8 m/s and 1.2 m/s.

§ NOCT: Nominal Operating Cell Temperature - cell temperature at NTE - 800 W/m^2 POA irradiance, 20°C air temperature, and 1m/s wind speed.

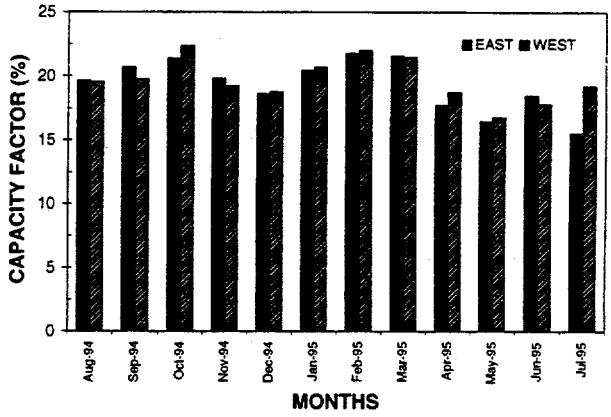

Fig. 4 (a). Monthly capacity factor for both SERFEAST and SERFWEST systems.

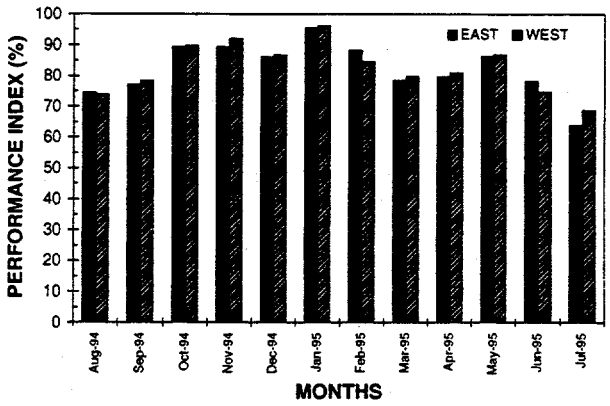

Fig. 4 (b). Monthly performance index for both SERFEAST and SERFWEST systems.

The dc and ac power, as a function of POA irradiance for the SERFEAST system, is shown in Figure 5 for PTC. The solid lines represent a least-squares fit to each data set, with the appropriate equation also shown. The outdoor ratings at the above-mentioned test conditions are summarized in Table 1 below.

Table 1. Outdoor rating of systems at different test conditions. The NOCT values are normalized to 1000 W/m^2 for comparison.

Ref. Condition	DC POWER (W)		AC POWER (W)	
	East	West	East	West
STC	6851	6857	6140	6157
PTC	6260	6287	5509	5563
NOCT	6408	6463	5720	5814

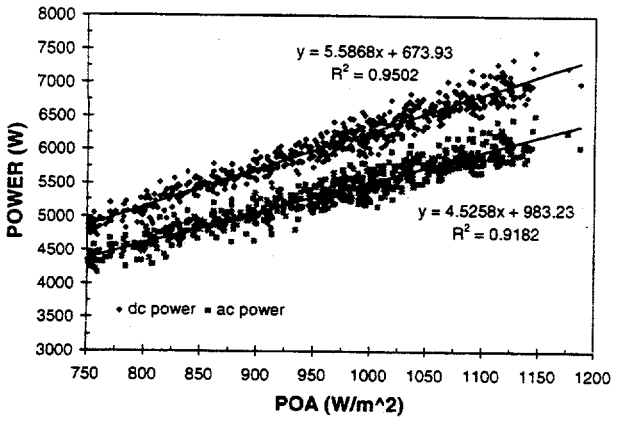

Fig. 5. SERFEAST dc and ac power as function of POA irradiance for PTC outdoor rating.

From Table 1, it is evident that the systems do not perform as predicted. The PTC estimate of the systems is 6 kW_{ac}, and the measured outdoor rating is lower than this by 7.3% and 8.2% for the SERFEAST and SERFWEST systems, respectively. This lower outdoor rating may be attributed, in part, to the fact that the inverters operate at lower annualized efficiencies of about 88% compared to the rated 95%.

SUMMARY AND CONCLUSIONS

The data obtained from continuous system monitoring used to evaluate and compare performance of the two systems showed that the systems operated in a similar manner. The expected seasonal fluctuations for mono-crystalline Si were also observed. These seasonal variations (spring and fall maxima and corresponding winter and summer minima) are clearly illustrated by analyzing energy production data and associated parameters. The analysis of energy produced also illustrated the value of continuous monitoring to detect faulty equipment, as was the case for the peak-power tracking software. Furthermore, the energy produced was also modeled using a simulation program. This simulation, using system design parameters, yielded a total dc energy that is comparable with that measured, thereby illustrating the value of modeling system energy output. When modeling system performance, the application of system derating was found to be critical.

The analysis of system power output showed that the systems were overrated (at PTC) by approximately 7% to 8%. This may be attributed to the design inverter efficiency being estimated at 95%, compared with the measured value of approximately 87%, as well as the aperture-area efficiency being overestimated. The average measured aperture-area efficiency was 11.0%, which is significantly lower than the design value of 12.8%.

The annual average capacity factor and performance index were determined to be 19.6% and 82.5%, respectively. The performance index was, however, found to be misleading for the months with adverse weather conditions, as was the case for May 1995.

An analysis of the system losses revealed that, when excluding the effect of temperature, the average array losses amounted to 10.6% of potential energy production as measured relative to STC array rating. The temperature losses may be as high as 13% when modules operate at elevated temperatures. The annual average of dc to ac conversion losses was found to be about 13% of the generated dc power. The cumulative effect of all the system losses is about 30% of the dc array rating at STC.

Finally, the methods of analysis, as applied in this study, may be used to evaluate different systems comprising different cell technologies.

ACKNOWLEDGMENTS

The authors wish to thank Roland Hulstrom and Dick DeBlasio for their support. The assistance of Daryl Myers in supplying RMIS data and for many useful discussions is acknowledged. Ben Kroposki is acknowledged for supplying temperature coefficient data and useful discussions.

This work was supported by NREL under Contract No. DOE-AC36-83CH10093 to the U.S. Department of Energy.

The work was also conducted as part of a joint project between NREL and the University of Port Elizabeth, South Africa.

REFERENCES

[1] T. Strand, L. Mrig, and R. Hansen, "Technical Evaluation of Photovoltaic Systems at NREL," PV Performance and Reliability Workshop, Lakewood, CO, September 1994

[2] D.F. Menicucci, J.P. Fernandez, "User's Manual for PVFORM: A Photovoltaic System Simulation Program for Stand-Alone and Grid-Interactive Applications," SAND85-0376, April 1991.

[3] D.R. Myers, private communication.

[4] D.R. Myers and T.W. Cannon, "Photovoltaic Solar Radiometric Measurements and Evaluation," 13th NREL Photovoltaics Program Review, Lakewood, CO. AIP Conference Proceedings 353, America Institute of Physics, Woodbury, NY.

[5] D.R. Myers, "Uncertainty Analysis for Thermopile Pyranometer and Pyrheliometer Calibrations Performed by SERI," SERI TR/215-3294. Solar Research Institute, Golden, CO, April 1988.

SINO/AMERICAN COOPERATION FOR PV DEVELOPMENT IN THE PEOPLE'S REPUBLIC OF CHINA

William L. Wallace and Y. Simon Tsuo
National Renewable Energy Laboratory, 1617 Cole Blvd., Golden, Colorado 80401, USA

ABSTRACT

Rapid growth in economic development, coupled with the absence of an electric grid in large areas of the rural countryside, have created a need for new energy sources both in urban centers and rural areas in China. Environmental pollution from the increased use of coal-fired steam turbines to meet this capacity expansion is a concern. There is a growing interest in China to develop renewable-energy resources and technologies to meet energy demands and help mitigate pollution problems. In February 1995, Secretary Hazel O'Leary of the U.S. Department of Energy signed an Energy Efficiency and Renewable Energy Protocol Agreement with the Chinese State Science and Technology Commission in Beijing, China. Under this agreement, projects using photovoltaics for rural electrification are being conducted in Gansu Province in western China and Inner Mongolia in northern China, providing the basis for much wider deployment and use of photovoltaics for meeting the growing rural energy demands of China.

BACKGROUND

Recently, the Ministry of Electric Power in China announced that China must install 100 to 130 gigawatts of new electric generating capacity by the year 2000 to meet the demands of the rapidly growing economy and to provide electricity to a large number of rural people presently without access to the electric grid [1]. Environmental pollution from the increased use of coal-fired steam turbines to meet this capacity expansion is a serious concern. As a consequence of these factors, there is growing interest in China to develop renewable-energy resources and technologies to meet energy demands and help mitigate pollution problems. Interest in renewable energy is reflected both at the central government level in Beijing and at the local level in the provinces and autonomous regions of China.

China has an abundance of renewable-energy resources in the form of solar, wind, biomass, hydro, geothermal, and ocean tidal resources. China is also already one of the world's largest users of renewables, primarily in the form of hydropower and biomass [2]. The solar resource of the country is also enormous and is strategically located in areas of greatest need in terms of rural energy development. More than 120 million rural people in northern and western China and more than 300 coastal islands currently have no access to the electric power grid and no near-term prospects for grid connection. There is an excellent match of solar and wind resources to meet these rural electrification needs. For example, the richest solar-energy resources in China are located in Inner Mongolia, Qinghai-Tibet Plateau, Northern Ningxia and Gansu Provinces. These are regions where population density is low, and it is often too costly or impractical for grid extension to reach many of the potential users.

In the central government of the People's Republic of China, three commissions under the State Council are actively involved in renewable energy: the State Planning Commission (SPC), the State Economic and Trade Commission (SETC), and the State Science and Technology Commission (SSTC). The SPC is in charge of planning and budget approval for large infrastructure projects. The SETC is in charge of industrialization and retrofitting existing industries. The SSTC is in charge of planning and program administration of scientific research and development projects. Project implementation and management are the responsibilities of various ministries, such as the Ministry of Electric Power (MEP) and the Ministry of Agriculture (MOA). In February 1995, Hazel O'Leary, Secretary of the U.S. Department of Energy (DOE), signed the Energy Efficiency and Renewable Energy Protocol Agreement with the SSTC in Beijing that established a broad umbrella for Sino/American cooperation to develop renewable-energy technologies and markets in China.

Prior to and since the signing of the protocol agreement, DOE has been working closely with key renewable-energy departments in the SPC, SSTC, and SETC, in providing assistance and support for China's renewable-energy planning activities. Such activities include preparing the Agenda 21, "White Paper on China's Population, Environment, and Development in the 21st Century," and encouraging renewable-energy project development for China's Ninth Five-Year Plan, for the period of 1996 to 2000. Under the framework for cooperation established by the protocol agreement, DOE is developing three project annexes: (1) with MOA, for rural energy development, (2) with MEP and other key organizations, for wind energy and hybrid system cooperation, and (3) with SETC, for business development activities. National Renewable Energy Laboratory (NREL) is assisting DOE in implementing projects under the protocol agreement in China.

PHOTOVOLTAIC DEVELOPMENT IN CHINA

The People's Republic of China has a long history of research and development of photovoltaic (PV) solar cells. PV solar-cell research for space applications began in China in 1958. The first space PV power system for a Chinese satellite (SJ-1) was deployed in 1971. There are now two organizations that specialize in manufacturing space PV power systems: Tianjin Institute of Power Sources and Shanghai Xin Yu Power Supply Factory. Terrestrial applications of PV in China began more than 20 years ago, in 1974, when China installed a Pvpowered, navigation beacon light system in the Bohai Ocean. Commercial production of terrestrial solar cells began in 1976. The current installed capacity of PV systems in China is small, but is growing rapidly. In 1993, the installed capacity of PV systems was about 3.8 MW_p ; in 1994, the installed capacity was about 5.1 MW_p ; and in 1995, the installed capacity was about 6.3 MW_p [3]. Some 60% of this capacity is power for telecommunications applications.

About 1.5 MW_p of the PV generating capacity is installed in remote, agricultural, and village power applications, for which opportunities exist throughout China. There are more than 10,000 rural household systems already installed, mostly in Inner Mongolia, Tibet, and Qinghai. Household systems generally range from 20 to 80 W and are used for lighting and small consumer electronics. The potential is excellent for increased use of PV solar home systems in China's northwest provinces. For example, according to the Qinghai Provincial Electric Power Bureau, there are 107,000 unelectrified households in the province, and the Bureau plans to subsidize the electrification of 15,000 households using PV solar home systems by the year 2000. There are six 7- to 25-kW, stand-alone PV power stations in China, five in Tibet, and one in Gansu. A 30-kW, stand-alone power station is under construction in Tibet. China also has experience with wind/PV hybrid systems in the range of 200 W to 35 kW, but at present China has no experience with grid-connected PV systems. However, the quality of grid-connected electricity is a pervasive problem, and the use of PV for grid-support, uninterruptible power supplies and peak-shaving applications in the potential urban market is of great interest.

At least 16 organizations in China have manufactured and sold crystalline or amorphous silicon PV modules for terrestrial applications, with a total manufacturing capacity of about 5.5 MW_p. However, many of them have either stopped production or are not manufacturing at full capacity because of a combination of the following: (1) outdated equipment (All of China's PV cell and module production lines were imported before 1991.), (2) high manufacturing costs due to lack of automation and small-scale production, and (3) shortage of silicon wafers. Presently, only five organizations in China have an annual production level of PV modules of more than 200 kW_p: Qinhuangdao Huamei Photovoltaics Electronics, Corp. Ltd.; Yunnan Semiconductor Device Factory; Kaifeng Solar Cell Factory; Ningbo Solar Power Supply Factory; and Harbin-Chronar Solar Energy Electricity Corp. Chinese-made modules have a significant price advantage over American-made modules when the module size is less than 50 W_p because of lower labor costs and the 30% import tariff and value-added tax. Presently, Chinese module production cannot keep up with demand, and the average sales price has steadily increased during the last 2 years.

RURAL ELECTRIFICATION IN WESTERN CHINA

The high cost, lack of a marketing and distribution infrastructure, and variable quality of modules and balance-of-system components are barriers to the widespread deployment of photovoltaics in China. Several cooperative projects are being conducted in China to address these problems. Under the protocol agreement, NREL is working with the MOA and the Office of Poverty Alleviation and Rural Development of the Chinese State Council to develop a cost-shared program to provide household PV electricity systems to rural families in Western China. This project is being conducted with the Solar Electric Light Fund (SELF), a non-profit organization in Washington D.C. This DOE-funded project is designed to expand and strengthen the distribution and postsales support infrastructure previously established in the Gansu province in China. This infrastructure involves a partnership between rural energy offices at the county and township level (under the MOA), provincial government agencies associated with the Poverty Alleviation program, and local PV system integrators in China. Rural energy offices exist at the township, district, and county level in all the provinces of China, and they can help facilitate rural electrification projects throughout China, providing a widespread infrastructure for technology deployment. The use of revolving credit funds for financing the purchase of household systems to expand the market for PV is a critical component of the project.

Fifty percent of the cost of the project is provided by the Chinese government through the Gansu Provincial Poverty Alleviation and Rural Development Office, Gansu Planning Commission, and Gansu Economic and Trade Commission. The China side of the project is managed by the Gansu Solar Electric Light Fund (GSELF), which was established in 1993 for the specific purpose of promoting solar home systems in Western China. In MaGiacha village in Tonwei County, Gansu Province, GSELF installed 112 solar home systems of 20 W each in 1993, with partial financial support from the Rockefeller Foundation through SELF. In the MaGiacha project, each householder provided a 300 Yuan down payment and agreed to pay 12 Yuan/month for 12 years, which totals 80% of the cost with no interest charge. Additionally, GSELF is installing 172 solar home systems financed by the United Nations Development Program. Because the loan collections in previous GSELF projects have been difficult, the current DOE project is based on cash sales, with a 80% overall cost recovery. A revolving-fund account will be set up at the Lanzhou Branch of the China Construction Bank for purchasing additional systems. During the project cycle of 18 months (April 30, 1996 to

October 31, 1997), PV solar home systems will be expanded from 400 sets at the start to at least 600 sets by project's end (based on nominal 20-watt systems at a selling price of 2,400 Yuan per system).

PV panels and sealed lead-acid batteries will be purchased from the United States and other balance-of-system components (including charge controllers, compact fluorescent lights, and wiring) will be provided by three local system integrators: Gansu PV Company, Gansu Natural Energy Research Institute PV Company, and Zhong-Xing Electronic Instruments Factory. The training of 100 rural technicians and management staff of local service networks is included in the project. A "train the trainers" training session will be conducted jointly by U.S. and China technical experts. From this base, we hope to strengthen and expand the sales and service infrastructure, and to gradually build service networks for PV solar home systems in the provinces, counties, townships, and villages in western China. At the same time, we hope to increase market acceptance of American-made components.

PV CASE STUDIES IN INNER MONGOLIA

In collaboration with the Chinese Academy of Science (CAS) in Beijing and the Center for Energy and Environmental Policy (CEEP) at the University of Delaware in the United States, NREL is also working with several agencies of the Inner Mongolian government and several key investors in Inner Mongolia to develop PV and PV/wind hybrid projects in Inner Mongolia. The government of Inner Mongolia is committed to a village electrification program over the next 5 years, which will involve a number of villages that will be electrified using renewable-energy technologies. Inner Mongolia also has an established distribution infrastructure for rural energy system deployment at the county and village level that can provide an infrastructure for PV market development. Involvement of the local electricity bureau is a key component of this project. Local electricity bureaus, at the provincial and county levels, potentially represent a national infrastructure for technology deployment throughout China.

A series of case studies is being conducted by CAS, CEEP, and NREL for household and village power systems in Inner Mongolia, to develop technical and economic performance data and information. A report, "Levelized Cost Analyses of Small-Scale, Off-Grid Photovoltaic, Wind and PV-Wind Hybrid Systems for Inner Mongolia, China," was recently published [4]. This report summarizes levelized cost analyses performed on household-scale PV (22 W to 1 kW), wind (100 W to 2 kW), and PV-wind hybrid systems operating in four counties in Inner Mongolia. The report concludes that from a systems and users perspective, levelized costs of stand-alone, renewable-energy home systems are lower than gen-sets. This signals a sizable market opportunity for household-scale renewable-energy systems in Inner Mongolia.

REFERENCES

[1] Y. Lian, *Renewable Energy Programs and Projects in China*, published in 1994 by the Division of Renwable Energy Power, Ministry of Electric Power, The People's Republic of China.

[2] See, for example, *Solar Energy in China*, Yan Luguang and Kong Li, editors, Chinese Academy of Sciencies, Beijing, China; 1995.

[3] Wang Sicheng, Energy Research Institute of the State Planning Commission, "Current Status of PV in China and Typical PV System Analysis," 1996, unpublished.

[4] John Byrne, et. al., "Levelized Cost Analyses of Small-Scale, Off-Grid Photovoltaic, Wind, and PV-Wind Hybrid Systems for Inner Mongolia, China," March 1996, Center for Energy and Environmental Policy, University of Delaware, Newark, Delaware.

FIELD COLLAPSE DUE TO BAND-TAIL CHARGE IN AMORPHOUS SILICON SOLAR CELLS

Qi Wang and Richard S. Crandall
National Renewable Energy Laboratory, Golden, CO

Eric A. Schiff
Syracuse University, Syracuse, NY

ABSTRACT

It is common for the fill factor to decrease with increasing illumination intensity in hydrogenated amorphous silicon solar cells. This is especially critical for thicker solar cells, because the decrease is more severe than in thinner cells. Usually, the fill factor under uniformly absorbed red light changes much more than under strongly absorbed blue light. The cause of this is usually assumed to arise from space charge trapped in deep defect states. We model this behavior of solar cells using the Analysis of Microelectronic and Photonic Structures (AMPS) simulation program. The simulation shows that the decrease in fill factor is caused by photogenerated space charge trapped in the band-tail states rather than in defects. This charge screens the applied field, reducing the internal field. Owing to its lower drift mobility, the space charge due to holes exceeds that due to electrons and is the main cause of the field screening. The space charge in midgap states is small compared with that in the tails and can be ignored under normal solar-cell operating conditions. Experimentally, we measured the photocapacitance as a means to probe the collapsed field. We also explored the light intensity dependence of photocapacitance and explain the decrease of *FF* with the increasing light intensity.

INTRODUCTION

The key feature of a-Si:H *p-i-n* solar cells is that photogeneration occurs in the region with a high electric field (i.e., the i layer). The carrier drift length is a unique parameter in the operation of *p-i-n* solar cells that distinguishes them from the other types of solar cells. To achieve a high-efficiency solar cell, it is highly desirable that the drift length be greater than the i-layer thickness so that photogenerated carriers can be collected effectively. Therefore, a probe of the electric field in the i layer is crucial because the drift length is proportional to the electric field. We observe that the fill factor (*FF*) of a-Si:H *p-i-n* solar cells decreases as the light intensity increases. As we increase the illumination intensity from low levels to one-sun, we observe a decrease in fill factor of approximately 15% in as-grown cells.

Illumination generates electrons and holes. The recombination of electron and hole leads to a loss of carriers. The drift of carriers and the nature of blocking contacts lead to the photogenerated space charge. The space charge is mainly due to the free carriers, to the trapped charge in the midgap states, and to the trapped charge in band-tail states. This space charge screens the applied field and reduces the internal field. As the light intensity increases, more electrons and holes are produced. This causes more photogenerated space charge, further decreasing the electric field in the i layer. We propose that a decrease in the electric field causes the *FF* to decrease with increasing light intensity. Photogenerated space charge in traps is the main cause of the electric field reducing. We use AMPS modeling and photocapacitance experiments to verify this.

SIMULATION

In general, a complete approach to this problem entails solving the transport equations of electrons and holes in an a-Si:H solar-cell device. Although a simple closed-form solution is not available, we could solve the transport equations numerically [1,2]. We model the behavior of a-Si:H *p-i-n* solar cells using the AMPS simulation program [2]. The details of the use of AMPS has been published elsewhere [3]. To test our hypothesis, we model the light intensity dependence of *p-i-n* solar cells and emphasize the effect on *FF* due to the band-tail states and the midgap states.

The modeled devices have a homojunction *p-i-n* structure with the energy gap of 1.72 eV. The thickness of the p layer is 100 Å, the thickness of thei layer is 5000 Å, and the thickness of the n layer is 250 Å. The thicknesses are close to the experimental solar cells fabricated at the National Renewable Energy Laboratory (NREL). The modeling uses a Gaussian distribution of midgap states and an exponential distribution of the band-tail states in the i layer. The simulated experiment is to simulate the modeled cell with increasing light intensity from 1/1000 th of a sun to 8 suns. We change only i layer parameters, such as the band-tail width and the density of the midgap state, for each simulation.

Figure 1 summarizes the modeling results. We plot the *FF* as a function of the short-circuit current (J_{sc}) for three experiments. We use the short-circuit current to reflect the light intensity. For example, a current of 12 mA/cm^2 corresponds to 1-sun light intensity. The parameters of the i layer used in each experiment is listed in the table below the figure.

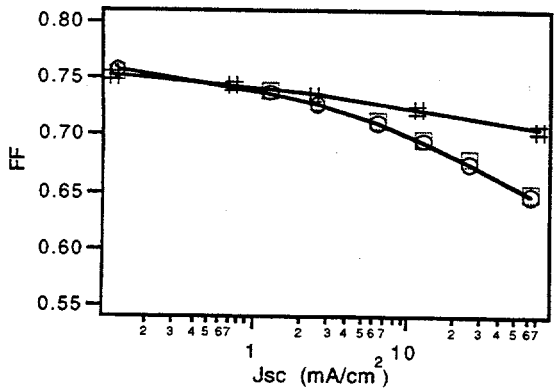

	Cell □	Cell ○	Cell #
Nd	$5x10^{15}$	0	0
Ea (meV)	27	27	0
Ed (meV)	44	44	0

Figure 1. The simulation results of fill factor as a function of illumination intensity for three experiments. The designed cell has a *p-i-n* structure with i layer thickness of 0.5 mm. The table shows the i layer parameters for each experiment.

The first experiment is to run a standard cell with i-layer parameters close to the real cell. For example, the conduction-band tail width (Ea) is 27 meV, and the valence-band tail width (Ed) is 44 meV. We choose a midgap defect density (Nd) of 5×10^{15} cm^{-3} ,which is close to the defect density in an as-grown cell. As expected, we observe a decrease of *FF* with increasing light intensity, as in the actual cell. The symbol □ represents this experiment.

To test whether or not this decrease in *FF* is caused by the space charge trapped in the midgap defects, we remove the defects. We do the second experiment on this new cell without the defect states. We use symbol ○ to denote this run. We find that it has little effect on *FF*. It also shows a decrease of *FF* with the increasing of light intensity. The data of the second experiment are almost identical to the first one. This implies that the space charge in midgap defect states is so small that it causes insignificant changes in the electric field in the dark. In fact, we find that the midgap defect density must be as high as 1×10^{17} to reduce the fill factor below that in the standard cell for just AM1 illumination (J_{sc}=12 mA/cm^2) from the simulation.

We proposed that the decrease in *FF* is mainly caused by the space charge in the band-tail states. We hypothesized that if the cell has no band-tails, there is no light dependence of the fill factor. The third designed cell is the one without the midgap defects and band-tails. The third experiment is denoted by the # symbol. The results support our ideas. It really shows less dependence on light intensity than the standard cell. This indicates that most photogenerated space charge is trapped in the band-tails. On the other hand, there is a slight but significant illumination dependence of *FF* at high light intensity. We attribute this effect to the space charge of free carriers.

EXPERIMENTAL

Experimentally, we cannot easily measure the electric field in the i layer, but we can measure the effect of space charge using the well-established capacitance technique. We can measure the photocapacitance (C_{ph}) [4-6], which is a sensitive probe of the i-layer field distortion. It measures the response of space charge to the applied voltage. We measure capacitance in the dark and under illumination. We define the photocapacitance by subtracting the capacitance in the dark (C_{dk}) from its value in the light. In the following section, we address the photocapacitance theory first and then show the experimental results.

It is well known that any space charge has an associated capacitance [7]. There are two capacitances in the *p-i-n* configuration: one for electrons and one for holes. For simplicity, one can think of the total photocapacitance as the two capacitances added in series. Crandall modeled the photocapacitance previously [8,9]. The Regional Approximation was applied to solve the transport equations and analytical solutions could be obtained only for two extreme cases. If perturbation to the system is small, the photogenerated space charge is so small that the electric field is little changed from its dark value. In this case, C_{ph} is given by

$$C_{ph} = \frac{ed^3}{2(\mu_h + \mu_e)} \frac{G}{V^2}. \qquad (1)$$

If the perturbation to the system is large enough that it determines the shape of the electric field, C_{ph} is given by

$$C_{ph} = c \frac{\mu_h^{0.75}}{\mu_e^{0.5}} \frac{G^{0.25}}{V^{0.5}}, \qquad (2)$$

where e is the electron charge, G is the photogeneration rate, V is the applied voltage plus the built-in voltage, d is the sample thickness, μ_e is the electron drift mobility, μ_h is the hole drift mobility, and c is a constant. The beauty of having an analytical solution is that the relationship between the cause and effect is clearly presented. The theory predicts that at low light intensity, C_{ph} increases linearly with the generation rate and is reciprocal to the square of the applied voltage. At high light intensity, C_{ph} increases with a quarter power of the generation rate and is reciprocal to the square root of the applied voltage. Photocapacitance also depends on the drift mobility, but that is not the subject of this study. Unfortunately there is not an analytic expression to connect the two regimes.

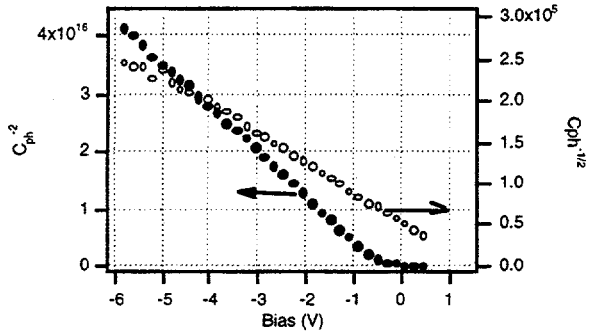

Figure 2. The voltage dependence of photocapacitance plotted as $C_{ph}^{-1/2}$ and C_{ph}^{-2} versus voltage. The sample has a *n-i-p* structure with i-layer thickness of 1.5 μm, and the measurement is done at room temperature with a modulation frequency of 10 kHz.

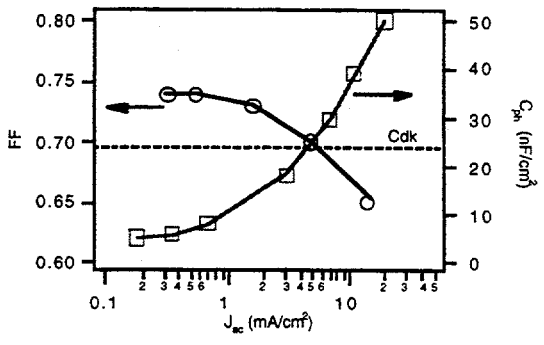

Figure 3. The light-intensity dependence of FF and photocapacitance in one sample. The sample has a *p-i-n* structure with i-layer thickness of 0.5 μm. The photocapacitance is measured at zero bias.

In Figure 2 we select two extreme cases to test the theory. The theory also works for the *n-i-p* structure sample. The sample has a nip structure and is deposited on a transparent conductive oxide (TCO) coated glass substrate with an i-layer thickness of 1.5 μm. We chose a thicker sample than the normal solar cell because it is more affected by the space charge. The open circles are the data measured at low red-light intensity. The ratio of C_{ph} to C_{dk} is about 4%, which is a small perturbation. We plot $C_{ph}^{-1/2}$ versus voltage using the right-hand axis. The linear relation is what we expected from Eq. (1). The solid circles are the data taken at high red-light intensity. The ratio of C_{ph} to C_{dk} is about 650% and the perturbation is large. We plot C_{ph}^{-2} versus voltage using the left-hand axis. It also shows a linear dependence on the voltage. The data support the theoretical prediction of the voltage dependence of C_{ph}. It is worth mentioning that C_{ph} can be greater than C_{dk} for moderate light intensity although an analytical solution is not available in that case.

DISCUSSION

In this section, we first discuss the qualitative explanation for the decrease of *FF* with increasing light intensity in a-Si:H solar cells. We use photocapacitance as an indicator of the electric-field distortion in the i layer. The larger is C_{ph}, the more field distortion. Then we discuss the effect of recombination on the *FF*.

In Figure 3, we plot the *FF* and C_{ph} measured at zero bias as a function of the short-circuit current measured in one sample. A current of 14 mA/cm^2 corresponds to AM1 light intensity. The sample has a structure of glass/TCO/p/i/n/Pd. The p-layer thickness is about 150 Å. The i-layer thickness is about 4500 Å, and the n-layer thickness is about 300 Å. The cell has an efficiency over 8 % in the as-grown state. We show the dark capacitance to indicate the thermal equilibrium condition. At low light, C_{ph} is only a small fraction of C_{dk}. This implies that at these light intensities, the system is near its equilibrium condition and the perturbation of the electric field is small. As the light intensity increases, C_{ph} increases and is comparable to C_{dk}. In this case, the perturbation is no longer small. At high light intensity, C_{ph} is many times larger than C_{dk}. In this case the perturbation is enormous. The electric field is near collapse.

This observation and interpretation agrees well with our idea that the decrease of electric field causes the decrease of *FF* with the increase of light intensity, as we see in Fig. 3. We interpret the small *FF* change at low light intensity as a result of a small perturbation of the electric field by photogenerated space charge. We explain the *FF* decrease at high light intensity as a result of a large perturbation of the field.

To conclude, we have studied the field collapse in a-Si:H *n-i-p* and *p-i-n* solar cells. The simulation shows that the decrease in fill factor is caused by photogenerated space charge trapped in the band-tail states rather than in defects. The photocapacitance measurement clearly demonstrates the effect of the photogenerated space charge. Photocapacitance theory in two extreme cases has been successfully tested on one sample at room temperature. We qualitatively explain the decrease of *FF* with increasing light intensity, using C_{ph} as a measure of electric-field distortion. We expect this technique will become a useful diagnostic tool for a-Si:H solar cells.

ACKNOWLEDGMENTS

The authors thank E. Iwaniczko and Yueqin Xu for the sample preparation and S. J. Fonash for helpful discussions. This work is supported by the U.S. Department of Energy under contract No. DE-AC36-83CH10093.

REFERENCES

1. M. Hack and M. Shur, *J. Appl. Phys.* **58**, 997 (1985).
2. J. K. Arch and S. J. Fonash, *Appl. Phys. Lett.* **60**, 757 (1992).
3. F. A. Rubinelli, S. J. Fonash, and J. K. Arch, *Proceedings of the 6th International PVSEC*, 851 (1992).
4. R. S. Crandall, *Appl. Phys. Lett.* **42**, 451 (1983).
5. R. S. Crandall, J. Kalina, and A. Delahoy, in *Amorphous Silicon Technology*, edited by A. Madan, M.J. Thompson, P.C. Taylor, P. G. LeComber and Y. Hamakawa, MRS Symposia Proceedings No. 118 (Materials Research Society, Pittsburgh, 1988), p. 593.
6. Qi Wang and R. S. Crandall, in *Amorphous Silicon Technology 1996*, edited by M. Hack, E. Schiff, S. Wagner, R. Schropp, and A. Matsuda, MRS Symposia Proceedings No. 420 (Materials Research Society, Pittsburgh, 1996), in press.
7. A. Rose, *Concepts in Photoconductivity and Allied Problems*, Krieger, Huntington, 1978.
8. R. S. Crandall, *J. Appl. Phys.* **54**, 7176 (1983).
9. R. S. Crandall, *J. Appl. Phys.* **55**, 4418 (1984).

SURFACE SEGREGATION AS A MEANS OF GETTERING Cu IN LIQUID-PHASE-EPITAXY SILICON THIN LAYERS GROWN FROM Al-Cu-Si SOLUTIONS

T.H. Wang, T.F. Ciszek, R. Reedy, S. Asher, and D. King
National Renewable Energy Laboratory, Golden, CO 80401

ABSTRACT

We demonstrate that, by using the natural surface segregation phenomenon, Cu can be gettered to the surface from the bulk of silicon layers so that its concentrations in the liquid-phase-epitaxy (LPE) layers are much lower than its solubility at the layer growth temperature and the reported 10^{17} cm^{-3} degradation threshold for solar-cell performance. Secondary-ion mass spectroscopy (SIMS) analysis indicates that, within a micron-deep sub-surface region, Cu accumulates even in as-grown LPE samples. Slower cooling after growth to room temperature enhances this Cu enrichment. X-ray photoelectron spectroscopy (XPS) measurement shows as much as 3.2% Cu in a surface region of about 50 Å. More surface-sensitive, ion-scattering spectroscopy (ISS) analysis further reveals about 7% of Cu at the top surface. These results translate to an areal gettering capacity of about 1.0×10^{16} cm^{-2}, which is higher than the available total-area density of Cu in the layer and substrate (3.6×10^{15} cm^{-2} for a uniform $1.2 \times 10^{17} cm^{-3}$ Cu throughout the layer and substrate with a total thickness of 300 μm).

INTRODUCTION

Cu-Al has been found to be a good solvent system to grow macroscopically smooth Si layers with thicknesses in tens of microns on cast metallurgical-grade (MG) Si substrates by liquid-phase epitaxy (LPE) at temperatures near 900 °C [1]. This solvent system uses Al to ensure good wetting between the solution and substrate by removing silicon native oxides, and it uses Cu to control Al-doping into the layers. Isotropic growth is achieved because of a high concentration of solute silicon in the solution and the resulting microscopically rough interface. The incorporation of Cu in the Si layers, however, was a concern because Cu is a major solution component and is generally regarded as a bad impurity for silicon devices due to its fast diffusivity and deep energy levels in the bandgap. One study[2] shows that Cu nonetheless will not degrade solar-cell performance until above a level of 10^{17} cm^{-3}. This threshold is expected to be even higher for thin-layer silicon solar cells owing to the less-stringent requirement on minority-carrier diffusion length. But to ensure long-term stability of solar cells, lower Cu concentrations in the thin layers are still preferred.

When grown under near-equilibrium conditions from a Cu-Si melt, the silicon crystal is expected to be saturated with Cu to its solid solubility limit at the growth temperature (1.2×10^{17} cm^{-3} for 900°C). More components in the melt will slightly change Cu incorporation about this level because of the change in free energy in the melt. Using Al-Cu-Si solutions, Cu incorporation will be a little less from experiments and calculation with the multi-component regular solution model. During post-growth cool-down, the Cu will become supersaturated and segregate to the surface or precipitate at the defect sites. The free-silicon surface is the preferred escape site for the supersaturated Cu atoms because the high free energy in the bulk will be spent on creating a new Cu-terminated surface if Cu has lower surface energy than silicon. This indeed is the case: Cu aggregates to the surface during cool-down after layer growth. We may incorporate this surface segregation phenomenon to effectively getter fast-diffusing Cu from the bulk of silicon without using a dedicated gettering procedure.

LPE GROWTH OF SILICON

The liquid phase epitaxial growth setup and procedure is described elsewhere [1]. Thin silicon layers of 10-30-μm thickness were grown at temperatures around 900 °C on pure Czochralski(CZ) single crystal substrates in this study. The solution compositions were kept nearly constant at 23%Si-28%Al-49%Cu for the growth runs to minimize their effects on Cu incorporation in solid silicon. After a sample is withdrawn from the solution, a free silicon surface is exposed and the sample temperature is gradually reduced to room temperature. It is during this cool-down period that surface segregation occurs for various impurities in silicon crystals (both the layer and substrate) depending on their relative surface energy to silicon.

SURFACE SEGREGATION

Surface segregation is a redistribution of solute atoms (e.g., Cu) between the surface and bulk of a (Si) crystal from the as-grown uniform distribution until the total energy of the crystal becomes a minimum. The equilibrium surface composition (mole fraction in the

surface monolayer), x^{ϕ}_{Cu}, of Cu as a function of temperature is described by the Bragg-Williams equation [3]. The equation predicts a full surface coverage at temperatures somewhere below the growth temperature,

$$\frac{x^{\varphi}_{Cu}}{1-x^{\varphi}_{Cu}} = \frac{x^{B}_{Cu}}{1-x^{B}_{Cu}} \exp\left[\frac{\Delta G + 2\Omega^{S}_{SiCu}\left(x^{\varphi}_{Cu} - x^{B}_{Cu}\right)}{RT}\right],$$

where $\Delta G=(\mu_{Si}^{0\Phi}-\mu_{Si}^{0B})-(\mu_{Cu}^{0\Phi}-\mu_{Cu}^{0B})$, μ's are the surface and bulk chemical potential of pure Si and pure Cu, x^{B}_{Cu} is the bulk mole fraction of Cu, and Ω^{S}_{SiCu} is the interaction parameter between Si and Cu in the solid. For the grown Si crystal, a binary Si-Cu consideration (excluding Al) leads to $\Omega^{S}_{SiCu} = 12.81RT_e$, where T_e is the growth temperature.

Due to the residual stress near the surface region even in as-grown layers, segregation to the surface is not limited to the top monolayer. Thus, combined with the fast diffusivity and relatively low solubility of Cu in silicon, this surface segregation effect may be used to effectively getter Cu from the bulk of the silicon thin layers and substrates.

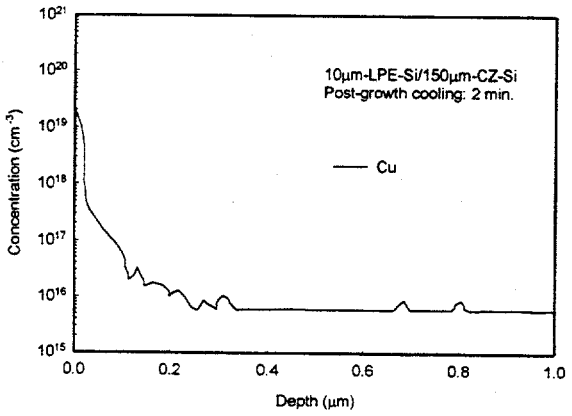

Fig.1. SIMS depth profile of Cu with a total sample thickness ≈ 160 µm.

The significance of surface segregation is evidenced by the depth profiling of Cu obtained with secondary-ion mass spectroscopy (SIMS) analysis in thin-layer silicon grown on high-purity single-crystal silicon substrates (Figs. 1 and 2). Because of the dynamic nature of SIMS measurements, the signal in the first 100 Å is not accurate, but both samples show Cu enrichment in the 0.3-0.4-µm surface region. One can easily notice the difference in the bulk Cu concentrations between the two samples. A logical explanation is the difference in total Cu content due to different substrate thicknesses. Both samples are expected to be saturated with Cu at the growth temperature of 900°C. The sample in Fig. 2 is thicker and would gather more Cu during growth from in-diffusion of Cu than the sample in Fig. 1. During the sample cool-down period after growth, Cu out-diffuses to the surface and results in different levels of reduction in bulk Cu concentrations.

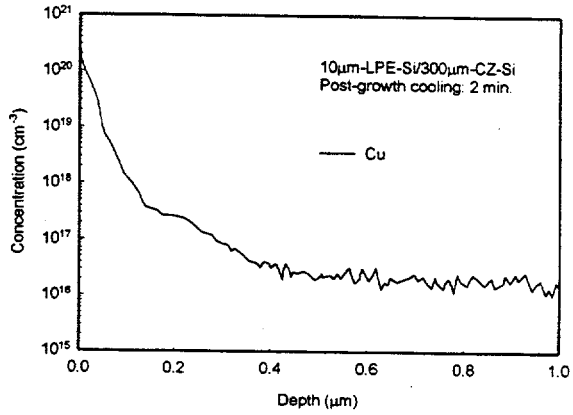

Fig.2. SIMS depth profile of Cu with a total sample thickness ≈ 310 µm.

GETTERING OF Cu

To fully use this Cu sink near the surface, a slower cooling after layer growth can be done to speed up the segregation process (Fig. 3). The same sample was analyzed with X-ray photoelectron spectroscopy (XPS), which shows as much as 3.2% of Cu in a surface region of about 50 Å. More surface-sensitive, ion-scattering spectroscopy (ISS) analysis reveals about 7% Cu at the top surface as shown in Fig. 4. Surface contaminants (e.g., O, C) prevented accurate measurement at the top monolayer, but this composition represents the minimum amount of Cu at the surface.

The slow diffusers (like B shown in Fig. 3) also exhibit surface segregation, yet the effects were limited to much smaller regions, indicating that surface segregation for slow-diffusing impurities is farther away from reaching the equilibrium state during the sample cooling period. Otherwise, one would expect it to extend to a depth and exhibit a profile similar to Cu.

According to the Bragg-Williams equation, the amount of Cu segregating to the surface would follow the curves in Fig. 5, where ΔG is the driving force

arising from the difference between the chemical potential differentials (surface to bulk) of pure Si and Cu, and Ω is the interaction parameter (regular solution model) between Si and Cu in the solid silicon, which we determined experimentally to be $12.81RT_e$. Therefore, it is straightforward to apply surface segregation as a gettering step following the LPE growth process.

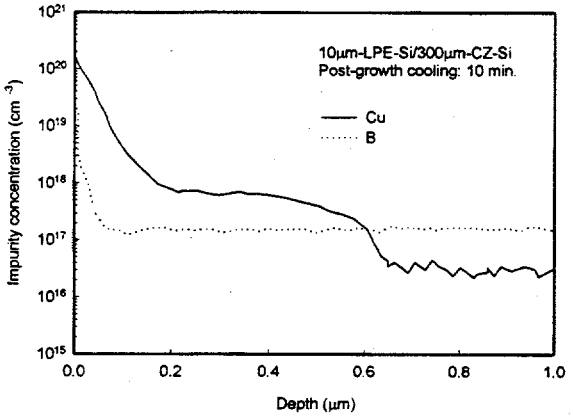

Fig. 3. Slower post-growth cooling as compared to Fig. 2.

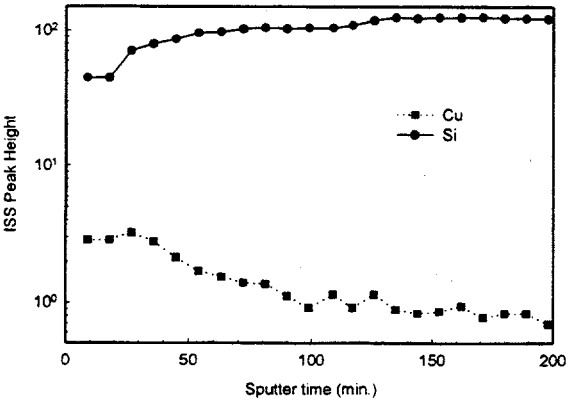

Fig.4. Cu depth profile by ISS.

Taking the Cu depth profiles in Fig. 3 and Fig.4 as nearly equilibrium, the gettering capacity is estimated to be about 1.0×10^{16} cm^{-2}, higher than a monolayer of Cu, owing to the extensiveness of Cu enrichment in the sub-surface region.

The total areal density of Cu in the layer and substrate is estimated to be 3.5×10^{15} cm^{-2} at the uniform concentration of 1.2×10^{17} for the total thickness of 300 μm, for example.

After removing the top Cu-enriched surface region by wet chemical etch, bulk concentration of Cu is typically about 1×10^{16} cm^{-3}, as seen in Fig. 6. Diagnostic solar cells made in such layers exhibit efficiencies as high as 15.3%, compared to 15.7% for Czochralski (CZ)-Si control cells.

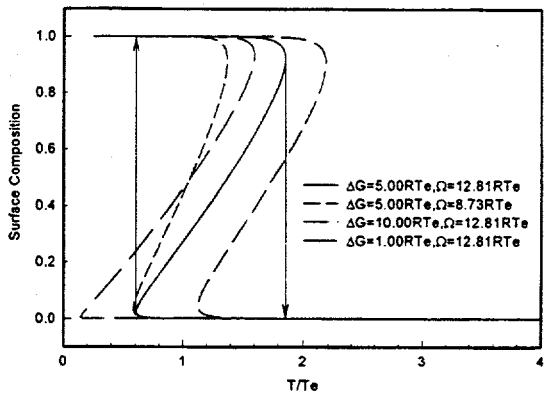

Fig.5. Equilibrium surface composition of Cu as a function of temperature. The upward and downward arrows are example paths for decreasing and increasing temperatures, respectively.

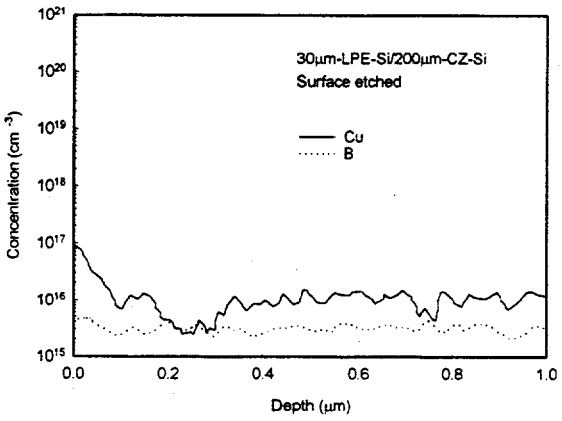

Fig.6. Cu depth profile after a surface etch in 3:1:2 mixture of nitric, hydrofluoric, and acetic acids. The boron profile is shown as a reference to indicate no significant surface segregation between the time of the acid etch and SIMS measurement.

Note that this surface segregation will have the same effect in gettering other fast-diffusing impurities like Ni or Fe. Due to their overall lower solubility in silicon (5×10^{16} cm^{-3} for Ni, 2.5×10^{15} cm^{-3} for Fe at 900°C), the bulk concentrations of these impurities after surface segregation should be low enough to not cause any device performance degradation, even if a low-purity metallurgical-grade-Si is used as LPE substrates. Slow diffusing impurities in a metallurgical-grade-Si substrate will not catch up the epitaxial growth front, thus they will not be of a concern.

For grain boundaries, the relative (to the bulk) chemical potentials of Si and Cu atoms at these locations are very likely to be lower than that of a free surface. This implies that the difference between the relative grain boundary energy of Si and that of Cu is smaller than the difference between the relative surface energy of Si and Cu. The same argument may be made for other defects in silicon. Experimental evidences are abundant, including SIMS analysis in which no significant impurity enrichment at grain boundaries was observed and the necessity of a thick sample in order to Cu-decorate defects in silicon [4]. Therefore, free silicon surface is the preferred escape site for fast diffusing impurities even for defected materials provided a small silicon thickness and sufficient time are given.

SUMMARY

Surface segregation can be used to effectively getter Cu and other fast-diffusing impurities (supposedly having lower surface energy than silicon) from bulk silicon when the impurity concentration exceeds its room-temperature solubility and when the silicon crystal is in thin (a few hundred microns) forms. When a free-silicon surface is available, this gettering process does not need special procedures, but only a prolonged cool-down step. The estimated total areal gettering capacity of 1.0×10^{16} cm^{-2} should be sufficient for Cu concentration up to 1.2×10^{17} cm^{-3} in a silicon wafer as thick as 800μm.

Silicon layers grown by LPE from Al-Cu solutions have shown below 1×10^{16} cm^{-3} in Cu concentration, and such a level of Cu impurity does not appear to degrade solar-cell performances.

This gettering procedure may be conveniently incorporated in many (sheet or ribbon) crystal growth and wafer processes, by using a slow cool-down and a surface-removal procedure. As a matter of fact, such a procedure may have already existed in many current processes naturally.

ACKNOWLEDGMENTS

We thank Dr. Y.S. Tsuo for diagnostic cell fabrications. Support for this work was provided by the U.S. Department of Energy under contract No. DE-AC36-83CH10093 to the National Renewable Energy Laboratory.

REFERENCES

[1] T.H. Wang and T.F. Ciszek, *Conference Record of the Twenty-Fourth IEEE Photovoltaic Specialists Conference*, Hawaii, 1994, p.1250.

[2] J.R. Davis, Jr., A. Rohatgi, R.H. Hopkins, P.D. Blais, P. Rai-Choudhury, J.R. McCormic, and H.C. Mollenkopf, *IEEE Trans. Electron. Devices*, **ED-27**, 1980, p.677.

[3] J.Du Plessis and G.N. Van Wyk, *J. Phys. Chem. Solids*, **49**(12), 1988, p. 1441 and p. 1451.

[4] T.F. Ciszek, in: *Semiconductor Silicon 1973*, Eds. H.R. Huff and R.R. Bugess (Electrochem. Soc., Pennington, NJ, 1973), p.150.

PV-HYBRID VILLAGE POWER SYSTEMS IN AMAZONIA

C. L. Warner, R.W. Taylor
National Renewable Energy Laboratory (NREL)
1617 Cole Blvd.,Golden, CO 80401, USA

C. M. Ribeiro, M. Moszkowicz, A. J. V. Borba
Centro de Pesquisas de Energia Elétrica (CEPEL)
Rio de Janeiro, Brazil

ABSTRACT

The Brazilian Amazon region is an ideal location for isolated mini-grid systems. Hundreds of diesel systems have been installed to supply electricity to this sparsely populated region. However, the availability of renewable energy resources makes the Amazon well-suited to renewable energy systems. This paper describes the technical aspects of two hybrid systems being installed in this region through the cooperative effort of multiple partners: U.S. Department of Energy, through NREL, and Brazilian CEPEL/Eletrobras and state electric utilities.

INTRODUCTION

The U.S. Department of Energy (DOE), through the National Renewable Energy Laboratory (NREL), is implementing a joint technology research and demonstration task with the Centro de Pesquisas de Energia Elétrica (CEPEL) in Brazil [1]. In this program, DOE is cost-sharing renewable-energy pilot projects with Brazilian state-owned utilities. As part of this program, two hybrid power systems were procured for villages in the Amazon region of Brazil (see Figure 1). This paper describes the design, present status of installation, and plans for the operation of these systems.

AMAZON REGION: ELECTRIC ENERGY ASPECTS

The Amazon region in Brazil is sparsely populated, with 17 million people living in 5 million km^2. This translates to less than 12% of the country's population in 58% of the total area. Electricity generation, where it exists, is based mainly on isolated diesel systems ranging from a few kilowatts in small villages, to tens of megawatts in some capital cities. Only 9% of Brazil's electric energy is consumed in Amazonia, but consumption has been increasing at a rate of about 18% per year for the last 20 years, while the national rate increased at only 8.2%. Over 30% of the population does not have access to electric energy [2].

More than 300 mini-grid systems are operated by local utilities, and thousands more are privately owned. Table 1 gives the distribution of system capacity for the 300 systems operated by utilities. Normally, the small systems operate for only 6 to 12 hours per day [3].

Figure 1. Map of South America indicating the Brazilian Amazon region.

Table 1. Distribution of Utility Diesel Systems, by Size [3]

System Size (kW)	% of Total # of Systems
0 - 100	10
100 - 500	37
500 - 1000	23
> 1000	30
Total	**100**

The cost of remote electricity is high and depends strongly on system size. In villages with diesel systems smaller than 100 kW, the cost can be greater than US$ 0.50/kWh. These high costs are due largely to operation and maintenance and low capacity factor, and secondarily, to high fuel costs. The small systems are normally very unreliable. As a result of the present situation, small remote villages experience both high electricity cost and very low-quality energy service, if any. High electric costs are not borne by villagers, however, due to fixed electric tariff rates mandated by the

government. Hence, such service, when provided, must be subsidized.

In 1995, the total Brazilian national budget for fossil fuel to run the utilities' isolated systems reached almost $250 million, which corresponds to more than 1 billion liters of diesel and 320,000 gross tons of oil. The planned budget for 1996 is $340 million. Recently, in a Brazilian national meeting, it was proposed that this budget be directed gradually to fund renewable-energy projects where- ever funds were subsidizing the operation of diesel systems.

AMAZON REGION: RENEWABLE RESOURCES AVAILABILITY

The Amazon region is extremely rich in renewable-energy resources. The average insolation is 5 kWh/m^2-day, with very little variation throughout the year. The wind regime has proven to be significant near the coast, and there are other promising locations as well. And biomass, either through planted wood or vegetable oil, and hydroelectric also have potential.

To quantify the availability of solar and wind resources at both hybrid power sites, measuring stations have been installed and resources monitored.

DESCRIPTION OF THE HYBRID SYSTEMS

Details of the two systems and their locations appear below. Apart from research and demonstration interests, both hybrid systems are expected to reduce fuel consumption, increase the lifetime of diesel generators currently installed at the sites, and improve service quality. The designs of the systems are significantly different. The Campinas system will meet the entire load requirement with PV-generated electricity, and the Joanes system will operate in a "peak shave" mode, transferring the peak demand of the village to "off peak" periods at the diesel generation plant. In this way, it will use the maximum energy available from renewable sources. In Joanes, renewable generation is expected to reach 115 MWh/year, or some 45% of the total present demand. A concurrent program for energy conservation in the village is expected to boost the fraction of the load met by renewable energy to over 60%.

Joanes

The first system, a 50-kW PV-wind-battery hybrid, is being installed in the village of Joanes, located at the municipality of Salvaterra, on Marajó Island, state of Pará (see Figure 1). The system design and control and the power- processor hardware were supplied by New World Village Power Company (NWVP) of Vermont. This system will operate either isolated or interconnected to the local grid. While in the interconnected mode, it will either deliver excess energy to or charge the battery bank from the grid.

One year of solar radiation (global horizontal, direct normal, and diffuse), ambient temperature, and wind (speed and direction) data at the site is available. During this period (May 1994 to April 1995), the average wind speed was 6.58 m/s, and the daily average global-horizontal radiation was 5.30 kWh/m^2. There is a good match of resource availability to the demand during a typical day. Figure 2 shows the average normalized daily profile of load, wind, and solar energy for Joanes.

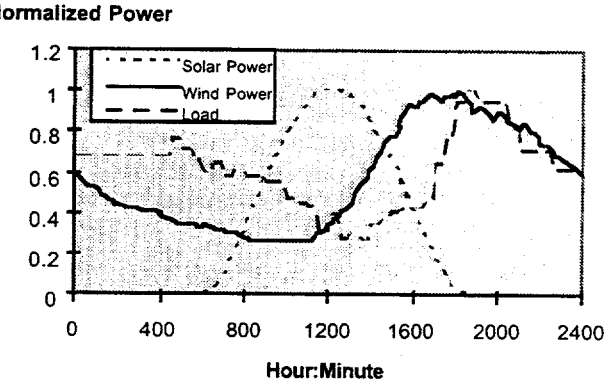

Figure 2. Daily load and generation profiles, village of Joanes - annual daily average (1994/1995).

The ratio of diffuse to global radiation ranged from 0.26 in July 1994, to 0.63 in February 1995, whereas the clearness index ranged from 0.40 in April 1995 to 0.60 in September 1994. The average temperature was approximately 27°C.

System Design, Configuration, and Grid Connection

This system is based on a rotary converter (shaft-coupled DC motor and synchronous alternator), rather than an electronic inverter, for power conversion. It comprises four 10-kW wind machines supplied by Bergey Windpower and 10 kW of PV modules from Siemens Solar Industries. A system schematic showing the connection to the Salvaterra grid is given in Figure 3.

PV structures were designed to allow monthly manual adjustment of the slope by the operator. The battery bank was sized to carry the load during a typical daily peak period (6:00 p.m. to 12:00 a.m.) without any real-time contribution from renewable sources. Control, data acquisition, fault detection, and diagnostics are primarily provided through programmable logic controllers (PLCs) connected via a serial link to a local operator interface (a computer running an algorithm based on the Wonderware Intouch software package).

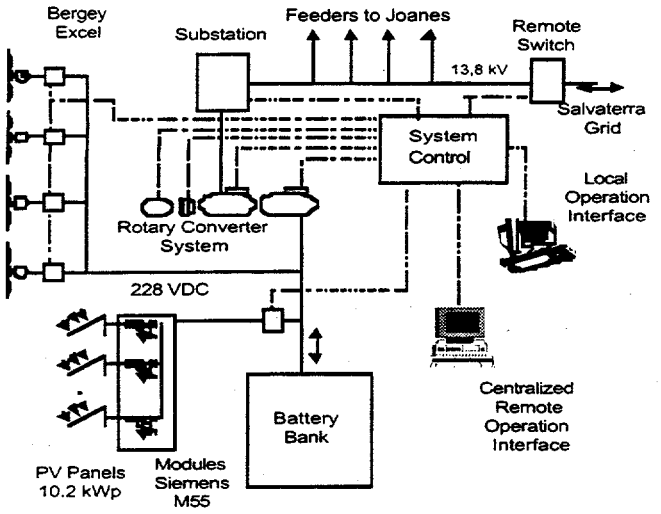

Figure 3. Simplified schematic drawing of Joanes hybrid system.

AC switches, PV contactor, and battery bank state-of-charge are controlled by the PLCs. Wind turbines have their own controllers and will be disconnected from the DC bus if the battery bank is fully charged or the system is off. Battery state-of-charge is assessed through terminal voltage monitoring, compensated by current and temperature. The battery will be recharged in a constant current/constant voltage sequence with temperature compensation. Equalization charges are also planned. Specific charge/discharge parameters are programmed for the characteristics of the selected battery bank.

Regarding grid connection, Joanes is connected to the Salvaterra power plant, one of 41 utility owned and operated diesel systems presently installed in Pará. The plant has a nominal capacity of 1.2 MVA. Joanes receives its electricity from this system, through a 17-km line operated at 13.8 kV. The village has 170 consumers, plus public lights. There are 4 transformers in Joanes with a total of 165 kVA, and distribution to consumers is at the line voltage, 110 V.

Operation Strategy

As envisioned, operation of the system is fundamentally driven by fuel displacement and peak load reduction at the Salvaterra power plant. The day is divided into key periods, as shown in Figure 4.

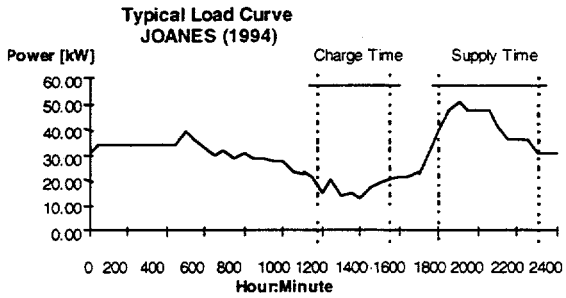

Figure 4. Operation of the Joanes hybrid system adjustable operation windows over typical load curve.

Two operation windows are defined: "Supply Time" and "Charge Time." During charge time, the system will be connected to the grid and the battery will be recharged to a maximum preset level. During supply time, the system will be isolated from the grid, carrying the village load. The windows will be defined by the operator in both relative position to the load curve and duration. Outside the defined windows, the village will be supplied by the grid, with renewables charging the battery bank.

Campinas

The second hybrid power system, a 50-kW PV-diesel-battery hybrid, is being installed in the village of Campinas, about 100 km upstream from Manaus, in the state of Amazonas, between the Solimoes and Negro rivers (see Figure 1). System controls and power processor for the Campinas plant were supplied by Advanced Energy Systems Ltd. (ASES), as a subcontractor to Bergey Windpower Corp. A 50-kW PV array was supplied by Solarex Corporation. Two existing diesel units, currently supplying the village load, are being modified to interface with this hardware.

System Design and Configuration

A system schematic is given in Figure 5. PV panels are fixed, tilted 8° toward the south. Control, data acquisition, fault detection, and diagnostics are primarily provided by the AES inverter's internal capabilities. A local operator interface is connected to the inverter via a serial link.

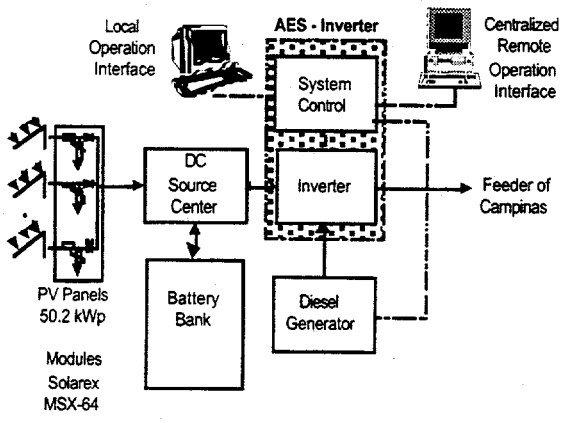

Figure 5. Simplified schematic of Campinas hybrid system.

Operation Strategy

This system will keep the diesel units from running, unless a sequence of cloudy days occurs that depletes the battery bank state-of-charge. In this case, the diesel will run to supply the load and recharge the battery bank to a preset maximum state-of-charge. While running, the diesel generators will be operated close to the nominal power rating to achieve high operating efficiency and to avoid damage to the units due to underload conditions. If the load requirement is greater than the nominal power of the inverter, the diesel generator will be turned on and the inverter will supply the remaining power requirement.

The Brazilian state electric utilities (CELPA in Pará and CEAM in Amazonas) are responsible for site preparation, village grid connection, system installation, operation, and maintenance, as well as for supply of the battery bank. System performance will be remotely monitored using a satellite communication system supplied by Ascension Technology.

PRESENT STATUS OF PROJECTS

Currently, site preparation at the two villages has been substantially completed, the equipment is in-country, and installation of the two hybrid power systems is slated for May 1996 [4,5].

CONCLUSIONS

The hybrid systems described here represent two significantly different approaches to the problem of remote power supply using renewable energy. Deployment of both systems is expected to provide the Brazilian utilities with installation and operating experience in hybrid power. Monitoring the performance of these systems will contribute significantly to the body of knowledge in hybrid power systems, influencing the design, implementation, and operating strategy of future projects.

Concurrent with this program, energy conservation measures are being implemented in both villages. Regardless of the specific design, energy costs are very high for these regions when compared to conventional, large grid- connected systems. This high cost reinforces the need for aggressive energy conservation measures and appropriate use of electricity.

This joint technology research and demonstration program has succeeded thus far because key institutional relationships between United States and Brazil have been developed. Furthermore, the necessary in-country training and manpower requirements for sustainable renewable-energy technologies, including hybrid village power systems, have been established. The project is yielding a number of benefits beyond the actual energy generated, including enhanced sales, profits, and employment opportunities for renewable-energy manufacturers; cost-competitive alternatives to diesel, kerosene, and grid-extension; and improvement of economic and social conditions for the rural population due to the availability of reliable electric power.

A new project headed by CEPEL has recently been launched to further evaluate the wind and solar potential of the Amazon region, as a follow-on to the current program. In this second step, each of the nine state utilities in the Amazon region will supply one village with centralized or distributed solar or wind systems, according to the availability of each resource and village load characteristics.

REFERENCES

[1] R.W. Taylor, C. Leboeuf (Warner), M. Moszkowicz, L.C. G. Valente, "Joint U.S./Brazilian renewable Energy Rural Electrification Project", *Twenty-fourth IEEE PVSC, Waikoloa, HI, December 1994.*

[2] Anuário Estatístico do Brasil, IBGE, 1993.

[3] Cadastro de Unidades Geradoras - Sistemas Isolados, Eletrobrás.

[4] C.M. Ribeiro, M.R.P. Araújo, A.Z. da Cunha, A.H.C. Ribeiro, "Implantação de Sistema Híbrido para Eletrificação da Vila de Joanes (Pará)," *XIII SNPTEE, 1995.*

[5] L.C.G. Valente, M.R.P. de Araújo, R. Hill, R.W. Taylor; "PV Power for Villages in the North Region of Brazil;" *XIII European PV Conference, Nice, October, 1995.*

PROGRESS AND ISSUES IN POLYCRYSTALLINE THIN-FILM PV TECHNOLOGIES

Ken Zweibel, Harin S. Ullal, Bolko von Roedern
National Renewable Energy Laboratory
1617 Cole Blvd., Golden, CO 80401 USA

ABSTRACT

Substantial progress has occurred in polycrystalline thin-film photovoltaic technologies in the past 18 months. However, the transition to first-time manufacturing is still under way, and technical problems continue. This paper focuses on the promise and the problems of the copper indium diselenide and cadmium telluride technologies, with an emphasis on continued R&D needs for the near-term transition to manufacturing and for next-generation improvements. In addition, it highlights the joint R&D efforts being performed in the U.S. Department of Energy/National Renewable Energy Laboratory Thin-Film Photovoltaic Partnership Program.

INTRODUCTION

Following are some highlights covered in this paper: (1) a record, total-area efficiency of 17.7% has been achieved for a thin-film $CuInGaSe_2$ (CIGS) solar cell fabricated by NREL scientists; (2) a total-area efficiency of 12.4% for a thin-film $CuInSe_2$ (CIS) solar cell fabricated by International Solar Electric Technology (ISET), where the CIS absorber layer was deposited by a non-vacuum technique; (3) an aperture-area efficiency of 13.0% for two thin-film CIGS minimodules (40.4 and 50 cm^2) fabricated by Solarex and jointly by Siemens Solar Industries and Showa-Shell, respectively; (4) fabrication by Solar Cells, Inc. of a 9.1% efficient, 6728-cm^2 area CdTe module; (5) installation of four nominal 1-kW and two nominal 10-kW thin-film CdTe grid-connected PV arrays by Solar Cells, Inc.; (6) installation of two nominal 25-kW thin-film CdTe PV arrays by Golden Photon Inc., and Solar Cells, Inc.; and (7) commissioning of a 2-MW thin-film cadmium telluride (CdTe) manufacturing plant by Golden Photon.

FILMS AND DEVICES

Higher Efficiency with Ga-Alloyed $CuInSe_2$

Since the last IEEE meeting in Hawaii, university and industry groups have focused their efforts on CIGS films and devices. Ga alloying made it much easier to achieve cells with higher open-circuit voltages (V_{OC}). However, short-circuit current densities (J_{SC}) have frequently suffered with Ga alloying [1]. Most groups obtained their own champion cell results with absorber layers having an effective bandgap of 1.1 to 1.2 eV. This corresponds to a Ga/(Ga+In) atomic ratio of 25% to 30%. In many instances, the Ga content of the absorbers is graded, either accidentally (the Ga tends to accumulate near the rear or Mo contact of the absorber) or deliberately, by introducing a Ga profile. Several Ga profiles, as well as absorbers with more or less Ga grading, have allowed researchers to achieve cells with high efficiencies. Table 1 summarizes selected results of cells from various university and industry groups measured at NREL. Aside from making it easier for all groups to obtain cells with high V_{OC}, Ga alloying has also improved the areal uniformity of cell efficiencies and the adhesion of the absorber layers to the Mo contacts, although Ga alloying has not completely eliminated all delamination problems. A highlight of Table 1 is the NREL world-record 17.7% CIGS cell, the highest efficiency for any thin-film cell. Details of the cell are covered elsewhere in this Proceedings.

Table 1: CIGS Solar-Cell Parameters (total-area efficiencies)

Group	Area [cm^2]	V_{OC} [mV]	J_{SC} [mA/cm^2]	FF [%]	η [%]	Comments
NREL	0.41	674	34.0	77.2	17.7	Record for all thin films
IEC	0.41	607	33.6	72.9	15.0	"Standard" CIGS absorber
IEC	0.40	746	25.2	69.7	13.1	High Ga content
WSU	0.44	500	34.7	65.5	11.3	SSI double-graded absorber, ZnO window (no CdS)
ISET	0.47	473	38.5	68.0	12.4	Non-vacuum deposited CIS, no Ga
Solarex	0.41	592	34.5	75.6	15.5	
EPV	0.42	507	31.6	69.6	13.9	
NREL	0.41	540	34.0	66.9	12.3	Electrodeposited precursor

Higher Ga alloy contents corresponding to absorber bandgaps >1.2 eV have in the past caused a more significant deterioration of the solar-cell currents and fill factors (FF) [2]. The group at the Institute of Energy Conversion (IEC, U. Delaware, Newark, DE) has been quite successful in limiting the worsening of device performance upon the incorporation of larger Ga concentrations (Ga/Ga+In >0.4). A cell with 13.1% efficiency and a V_{OC} of 745 mV was obtained. IEC concluded that the current-voltage dependence in this cell was limited by voltage-dependent collection mechanisms, resulting in effective diode quality factors >2 [3]. It is important to note that the inferior carrier collection not only occurs in CIGS, but also in

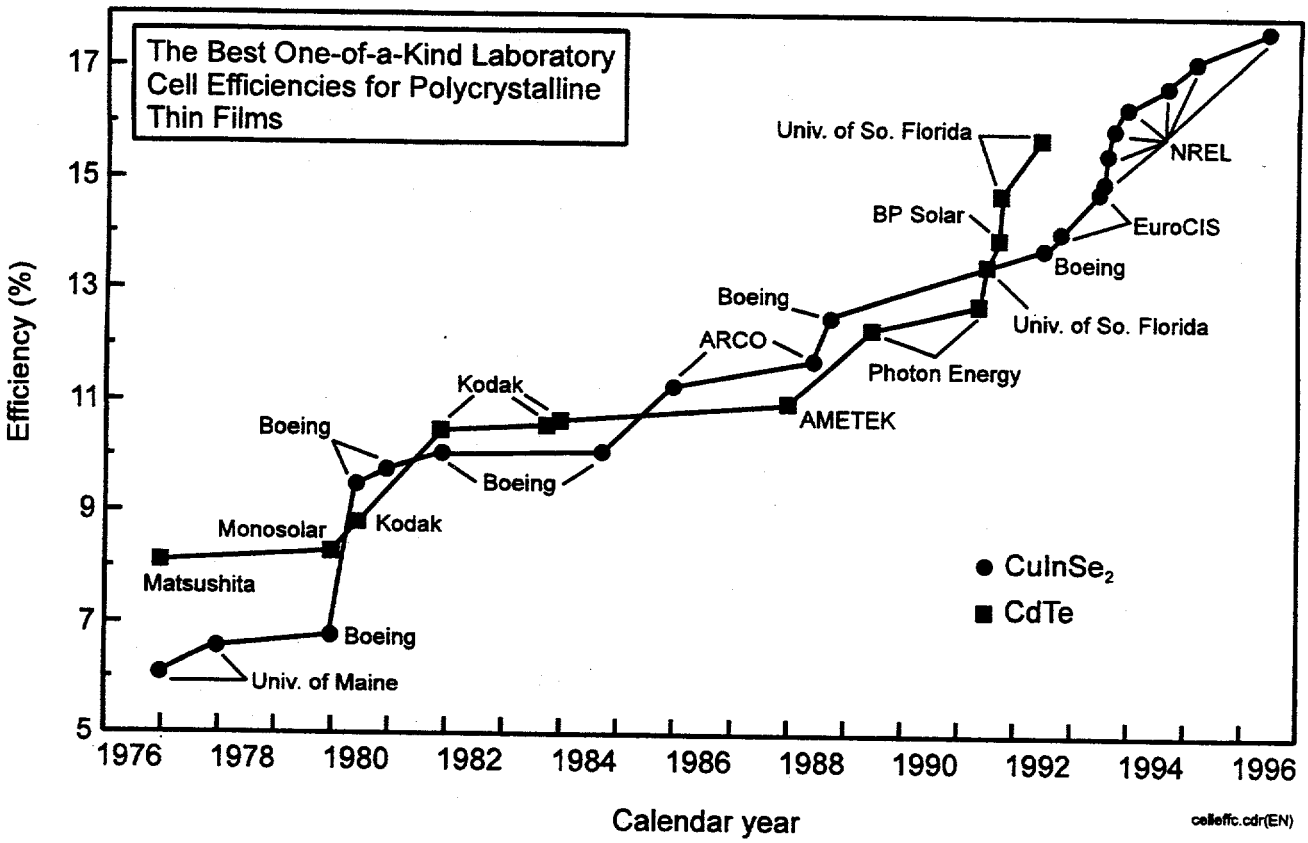

Fig 1. NREL researchers achieved 17.7% cell efficiency for CIGS in 1996. Progress toward high efficiency supports the idea that low-cost thin films will eventually reach 15% module goals.

$CuInS_2$ and in pentenary alloys. This raises the question whether the worsening of device performance with increasing bandgap or Ga- or S- alloying may be linked to something besides defects introduced by the alloying elements. In addition to progress within the individual research groups, there has also been a significant exchange of materials between university and industry groups. Although initially some university groups objected to investigating CIGS (arguing that it would make more sense to understand the CIS system first), the use of Ga alloys has advanced device performance at all levels for all groups. As an exception, ISET obtained remarkable cell results for an un-alloyed CIS cell deposited by a non-vacuum deposition process (see Table 1), and Siemens' standard absorber is a double-graded pentenary $Cu(In,Ga)(S,Se)_2$ alloy.

Thin-Film Partnership Teamed CIGS Research

The DOE/NREL's Thin-Film Partnership Program has organized two CIS research teams: the "junction" and the "absorber" teams. Table 2 lists the participating groups funded by the Partnership Program. Several other groups (e.g., ITN Energy Systems of Wheat Ridge, CO, and Corning of Corning, NY) outside the NREL Partnership Program have also regularly attended the team meetings and are considered team members.

Table 2: NREL-Funded CIS R&D Partners

Colorado State U. (CSU)	Device analyses, team leader "junction" team
Florida Solar Energy Center (FSEC)	CIGS from sputtered metal precursors and selenization
Institute of Energy Conversion (IEC, U. Delaware)	High Ga-content CIGS, material and device analyses, champion cells
Purdue U.	Numerical solar-cell modeling
U. of Florida (UF)	Selenization, S-alloys, single-crystal CIS, rapid thermal processing of CIS
U. of South Florida (USF)	Se vapor selenization, manufacturing-friendly process
Washington State U. (WSU)	Alternative heterojunction layers (CdS replacements)
U. of Toledo (UT)	Laser-scribing steps used in CIS (and CdTe) module manufacturing
National Renewable Energy Laboratory (NREL)	Absorber formation, junction formation, material and device analyses, champion cells, team leader "absorber" team
Siemens Solar Ind. (SSI)	Cell processing to test improved processes, round-robin cell processing, supplier of layers
Energy Photovoltaics (EPV)	Cell processing to qualify large-area deposition processes, non-H_2Se selenization
International Solar Electric Technology (ISET)	Cell work to qualify deposition processes, non-vacuum-deposited CIS
Solarex	High-efficiency cells

The two CIS teams have exchanged samples for analyses and device completion. Two comprehensive documents were generated that provide the structural, compositional, and luminescence properties of these absorbers. Despite the substantial compilation of materials data, it remains difficult to recognize material attributes that would predict good device performance. It also should be emphasized that the exercise of cross-processing layers into cells has revealed that each layer must be optimized in conjunction with the other layers. For example, although both NREL and Siemens Solar have obtained high-efficiency cells, the cell efficiencies were usually lower when NREL deposited its own ZnO on CIGSS-coated substrates provided by Siemens, or when Siemens deposited its ZnO on NREL absorbers. The current-voltage measurements for most samples were carried out at IEC, whereas the compositional and structural analyses were mostly done at NREL. To build on their early cross-cutting work, the Partnership's CIS teams are now being organized into smaller teams focused on specific problems.

The teams initiated a systematic study of investigating the advantages of the chemical bath deposition (CBD) process by replacing it with a physical vapor deposition process. It was found that the exposure to the bath's background solution (CBD solution without thiourea) alone (prior to the evaporation of the CdS layer) positively affects the performance [4]. In general, it appears much easier to obtain high CIS cell efficiencies using CBD CdS. Attempts to entirely eliminate the CdS layer are under way. A very remarkable result was achieved in the Siemens/ Showa-Shell collaboration described below. Presently, it is not clear whether eventually appropriately treated CIS/ZnO junctions will achieve the same device performance as can be obtained today only by using a CdS layer, or whether other buffer layers, such as those investigated by the Stuttgart group [5], will be needed.

Table 3: CdTe Solar-Cell Parameters (total-area efficiencies)

Group	Area [cm^2]	V_{oc} [mV]	J_{sc} [mA/cm^2]	FF [%]	η [%]	Comments
USF	0.928	853	21.7	76.5	14.2	CSS, soda-lime glass superstrate, $T_{deposition}$ <500°C
SCI	0.27	839	21.9	72.4	13.3	"CSS," soda-lime glass superstrate
CSM	0.10	778	22.4	74.0	12.9	Electro-deposited CdTe, USF SnO_2 superstrate
NREL	0.69	823	21.3	73.3	12.8	7059 superstrate
U. Toledo	0.12	806	19.7	73.3	11.6	Sputtered CdTe and CdS, commercial LOF superstrate

More Groups Fabricate High-Efficiency CdTe Cells

There has not been a new efficiency record for CdTe cells since the Hawaii meeting. This is because it was recognized that the process used by the USF group to fabricate the 15.8%-efficient [6] record cell was incompatible with low-cost, soda-lime glass substrates because of substrate temperatures ≥600°C. Instead, the work was focused on understanding the processing requirements for high-efficiency cells at lower (<550° C) substrate temperatures. The major accomplishment has been that more groups have been able to achieve total-area cell efficiencies in the 12%-14% efficiency range using processing temperatures compatible with low-cost glass. Also, the understanding of what affects the device performance appears to have advanced. Although a variety of deposition techniques have resulted in high-efficiency cells, the University of South Florida is leading the U.S. groups with a 14.2%-efficient cell prepared on a soda-lime glass superstrate. Table 3 gives the performance of several selected cells prepared by various groups. Table 4 lists the groups involved with CdTe solar-cell research.

Thin-Film PV Partnership Teamed CdTe Research

The Partnership CdTe researchers created two research teams: the "stability" team, which addresses cell and module stability issues, and a high-efficiency cell/thin CdS team. The stability team initiated a study of various minimodules. Light-soaking and measurements are carried out at NREL. IEC initiated light- and bias-stress experiments on solar cells. Several modules and arrays fabricated by SCI have demonstrated acceptable long-term performance when exposed to prevailing outdoor conditions. However, some experimental devices have shown significant degradation upon bias and light-stress. The analyses of the degradation phenomena are complicated because there are reversible and non-reversible changes in the device parameters that may either improve or degrade them.

Table 4: NREL-Funded CdTe Research Partners

U. South Florida (USF)	CSS of CdTe and CdS, high-efficiency/thin-CdS team leader
Colorado State U. (CSU)	Device analyses
Colorado School of Mines (CSM)	Electrodeposited CdTe
U. Toledo	Sputtered CdTe, CdTe alloys, laser scribing
National Renewable Energy Laboratory (NREL)	CSS deposition, rear contact, material characterization, CdS/CdTe interdiffusion, stability and module testing, team leader, stability team
Institute of Energy Conversion (IEC, U. Delaware)	PVD CdTe, rear contact, device measurements, cell stability
Golden Photon	Solar-cell work to improve stabilized performance of spray-deposited CdTe devices
Solar Cells Inc. (SCI)	Solar-cell work to improve stabilized cell performance

The thin-CdS team initiated a round-robin experiment where all groups provided cells with different CdS-layer thicknesses. This experiment was driven by the quest to reduce optical losses in the CdS, to increase J_{SC}. Also, the 15.8%-efficient USF cells (prepared at high temperatures) had successfully employed thin CdS layers. The results of the CdS-thickness study were that in most instances a thinning of the CdS layer increased the blue response of the cells. However, sometimes V_{OC} and FF were reduced in the cells with the thinner CdS. Further, an "unknown" loss of J_{SC} was frequently observed (typically 1-5 mA/cm^2), i.e., a reduction in quantum efficiency for all wavelengths greater than approximately 500 nm [7]. Presently it is unclear what is the mechanism for this loss and why this loss was minimized in the η = 15.8% USF cells. Recent cell processing has revealed that it is probably beneficial for the surface of the SnO_2 superstrate to be quite resistive. A dual SnO_2 layer had been used by the USF group for a long time. Other groups have adopted this processing. The main effect is an increase in V_{OC}, especially when the CdS layer is thin. It is presently not well understood why the resistive layer is beneficial, but it appears to be a genuine observation in all technologies that the emitter or window layer of the cells should be quite resistive to achieve good values for V_{OC} [8]. Significant effort was also devoted to improve the CdTe/metal-contact interface. In this area, several groups use proprietary recipes ("treatments" of the CdTe surface) or buffer layers that enhance cell performance and stability. IEC developed a new metallization procedure that involves the application of a thin Cu layer, low-temperature annealing, and an etch step to remove the excess Cu [9]. Cu "doping" of the rear contact improves the device performance, but also leads to cell degradation. As in the case of CIS, it was realized that the optimum rear contacting scheme depended on the other layers of the cell. Thus, during round-robin sample exchanges, IEC's contacting procedure produced device results that were sometimes superior and sometimes inferior to the results that other groups obtained using their own optimized CdS/CdTe/contact combinations.

MODULES AND TESTING

Progress at the minimodule and module level has also been encouraging. Tables 5 and 6 summarize the minimodule and module performance of several groups worldwide. Thus far, in a joint effort by SSI and Showa-Shell, an aperture-area efficiency of 13.0% has been verified by NREL. Graded CIGSS has been used as the absorber layer. The thin-CdS layer was replaced by a Zn-based buffer layer. A similar 13%-efficiency result, but *with* CdS, was achieved for a CIGS minimodule by Solarex, Newtown, PA. A process similar to NREL's was used for the Solarex minimodule fabrication. The Vapor-Phase Manufacturing Consortium, funded by the U.S. Advanced Research Projects Agency and led by ITN Energy Systems, has fabricated a minimodule with a reported aperture-area efficiency of 7.1% on a flexible substrate. For power modules, the most impressive performance improvement has been for a CdTe module fabricated by SCI. Their best aperture-area efficiency is 9.1%, with a power output of 61 W verified by NREL.

Table 5: CIGS Minimodule Performance

Manufacturer	Area [cm^2]	V_{OC} [mV]	J_{SC} [mA/cm^2]	FF [%]	η [%]	Comments
SSI/Showa Shell	50.2	6.74	2.81	0.69	13.0	Zn Buffer (no CdS)
Solarex	40.4	11.6	1.69	0.66	13.0	PVD absorber
ISET	144.9	9.45	1.62	0.64	9.8	Two-stage
EPV	202.3	11.5	1.23	0.64	9.0	Se vapor

Table 6: Module Performance

Company	Material	Area [cm^2]	η [%]	Power [W]
SCI	CdTe	6728	9.1*	61*
SSI**	CIS	3830	11.2	43.1
SSI**	CIS	3859	10.3*	39.7*
BP Solar***	CdTe	4540	8.4	38.2
SSI	CIS	3261	10.1*	35.7*
Golden Photon	CdTe	3528	7.7*	27.2*
SSI	CIS	938	11.1*	10.4*
Matsushita	CdTe	1200	8.7	10
BP Solar	CdTe	706	10.1	7.1
Golden Photon	CdTe	832	8.1*	6.8*
ISET	CIS	845	6.9*	5.8*
EPV	CIS	791	7.2	5.7
EPV	CIS	722	6*	4.3*

*NREL-measured;**Unencapsulated;***Not monolithic

After 7 years of testing of SSI's CIS modules at NREL's outdoor test facilities, the modules display remarkably robust performance. SCI's CdTe modules show good, stable performance after 2 years of testing at NREL [10].

Several companies are expanding their pilot line and manufacturing facilities. Golden Photon, Inc. (GPI), Golden, CO, has installed a 2-MW CdTe manufacturing line in Golden, CO (Figure 2). SCI plans to install a 10-MW CdTe manufacturing line in Toledo, OH, in late 1997. EPV is setting up a 200-kW CIS pilot line in Lawrenceville, NJ. ISET is setting up a 50-kW pilot line in Inglewood, CA, for CIS specialty products. Materials Research Group (MRG), Wheat Ridge, CO, is supplying equipment to Lockheed Martin (LM), Denver, CO, for LM's CIS pilot line. In Europe, the Center for Solar Energy, University of Stuttgart, and Phototronics Solartechnik/Putzbrunn, Germany, are jointly developing prototype 900-cm^2 CIGS modules using an evaporation technique. Nordic Solar Energy AB, Kista, Sweden, in collaboration with Uppsala University, Sweden, is also scaling up its activities to fabricate 900-cm^2 prototype CIGS modules. ITN Energy Systems and MRG are supplying equipment and plant design for a 1-MW CdTe manufacturing plant for Polyplex in New Delhi, India. In another joint effort EcoSolar (Pune, India), National Physical Laboratory (New Delhi, India) and Colorado State University (Fort Collins, CO), funded by the U.S. Agency for International Development, are setting up a pilot line to make CdTe modules in Pune, India.

TECHNICAL ISSUES

The CIS and CdTe technologies face a number of immediate and longer term issues and opportunities, compiled in Table 7.

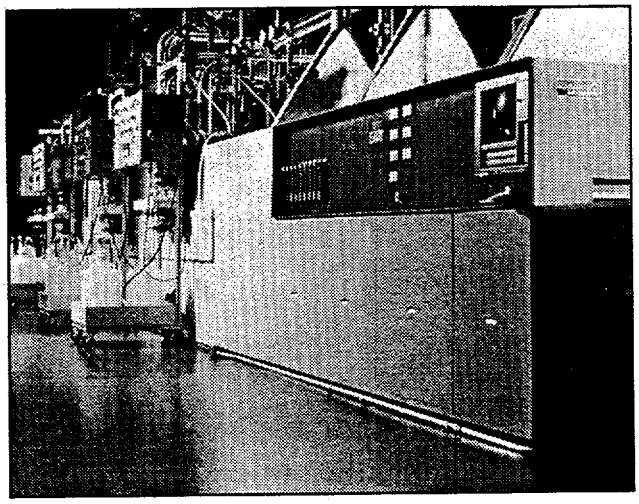

Fig 2. Golden Photon Inc., has installed a 2-MW CdTe production plant in Golden, CO, the first CdTe module manufacturing plant in the world.

Table 7. Issues and Opportunities

Issue/Opportunity	Material	Timeframe
Technology Base (materials, processes, devices)	Both	Immediate
Manufacturability (scale-up and yield)	Both	Immediate
Process Selection and Cost	CIS	Immediate
Adapting Lab-Cell Results to Module Prototypes	Both	Immediate
Intrinsic Stability	CdTe	Immediate
Encapsulation and Secondary Stability Interactions	Both	Immediate
In-Plant Environment, Safety, & Health	Both	Immediate
Product Recycling	Both	Mid-Term
Improved Lab-Cell Efficiency (thin CdS, alloys, gradients, contacts)	CdTe	Immediate
Lower-Cost Processes (rates, capital costs, materials use, thinner cells, encapsulation)	Both	Mid-Term
Higher-Bandgap Cells/Modules for Simplified Manufacturing and Better Outdoor Performance	CIS alloys	Mid-Term
Improved TCOs (performance and cost)	Both	Mid-Term
Flexible, Lightweight Modules (and Roll-to-Roll Processing)	Both	Mid-Term
Multijunctions (and efficiencies >20%)	Both	Mid-Term
Nontoxic, Highly Available Substitutes for In, Ga, Te, Cd, Se	Both	Long-Term

What are the critical-path issues in relation to "first-time" manufacturing success? Table 8 summarizes six of the key issues.

Success in resolving these issues will determine if either or both CdTe and CIS will be successfully manufactured. No timeframe is assumed for these activities. Those who are first to address them will carry the enhanced burden of facing them sooner than others. They will also own the business opportunity of leading those who do not follow aggressive commercialization paths.

An issue implicit in the above is that of "technology base." It is because the technology base of these innovative PV materials is relatively sparse that they sustain such high risks during important transitions (e.g., to first-time manufacturing). Although the sparse technology base cannot be identified as a "critical path" issue (due to its ambiguous nature), progress to improve it is highly important for manufacturing success.

Several of the issues/opportunities in the tables require further clarification. CIS and its alloys have been used with spectacular success to make solar cells. Numerous creative processes and device designs (including compositional and deposition temperature gradients) have been exploited, so that a goal of 20% efficiency now seems reasonable. However, scale-up to manufacturing has been slow and problematic. Amidst the wealth of CIS-alloy process choices, companies must find the right one. To this point, no one can be certain that they have chosen correctly.

The "champion" efficiency of CdTe has not improved lately. Although work to ensure the general use of thin CdS is important for moving the field toward 16%, something new—probably in terms of voltage, perhaps through alloy gradients and better contacts—will be needed to bring CdTe toward 20% efficiency.

It will be awhile before either CdTe or CIS can fully reach their cost potential. Both will be preoccupied with the transition to first-time manufacturing. However, once this transition is made, strong focus on process improvements will be essential. These should result in costs dropping below $\$100/m^2$, and eventually towards the $\$50/m^2$ level.

Table 8. Critical-Path Issues for First-Time Manufacturing

Critical Path Issue	Comments
CIS Process Selection	Selection from various forms of delivery, temperatures, and materials combinations
CIS Process Yield	At reasonable efficiencies (> 8%)
CdTe Process Yield	At reasonable efficiencies (> 7%)
CdTe Module Stability and Encapsulation	Contacting, water vapor, chemical interactions, diffusion; encapsulation design and cost
In-Plant ES&H, including off-spec disposal (both)	Worker safety and procedures, biomonitoring, regulations, return or processing of off-spec modules and process debris; cost
Demonstrated Outdoor Reliability	Small-scale (1- to 10-kW) systems in various climates

CIS alloys with Ga and S move the bandgap towards 1.5 eV. This not only has substantial cell-performance benefits, it has substantial manufacturing and outdoor module performance benefits. Manufacturing advantages from lower current densities are fewer scribes per module and better performance from typical TCOs. Although this research opportunity is not crucial in the near-term (and some work is already being done), it is likely that work in the future will move in the direction of higher-bandgap alloys.

Neither CIS nor CdTe is presently made on flexible substrates at performance levels near the state-of-the-art on glass. However, interest exists in CIS to develop flexible arrays, and progress is being made. Similar activity in CdTe is minimal due to the requirement for a glass superstrate. It remains to be seen whether the market and cost advantages claimed for roll-to-roll processing are valid.

After CIS and CdTe are established and 10% commercial modules are a reality, substantial privately funded research may be directed toward polycrystalline thin-film multijunctions and toward semiconductors without toxicity and availability problems. R&D sponsored by the public sector may begin to address these opportunities in the next few years.

APPLICATIONS

Several PV systems have been installed worldwide using CdTe modules. GPI has mainly installed CdTe PV arrays for water pumping. Cumulatively, GPI has installed less than 100 kW in the United States and overseas. Two 25-kW CdTe installations have recently been deployed at China Lake, CA. The arrays were supplied by GPI and SCI (see Figure 3). SCI has deployed two nominal 10-kW grid-connected arrays at PVUSA, Davis, CA, and in Toledo, OH. The PVUSA array was recently measured at 12 kW. In addition, SCI has supplied four nominal 1-kW arrays to NREL, Toledo Edison (2 arrays), and Tunisia. The SCI CdTe arrays have demonstrated stable performance at various locations.

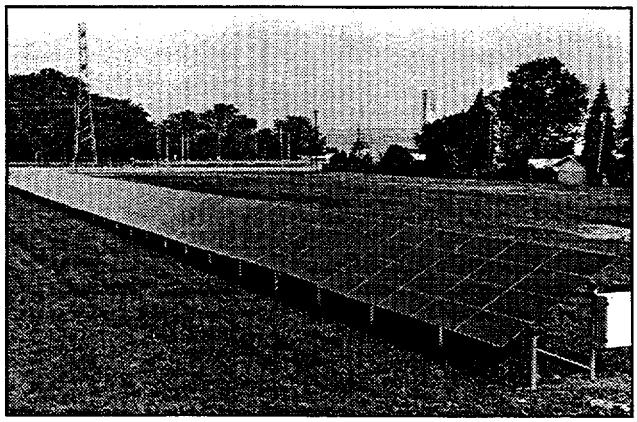

Fig. 3. Solar Cells Inc., has deployed several multikilowatt CdTe arrays. This one is a 10-kW array in Ohio connected to the Toledo Edison utility grid.

CONCLUSIONS

Despite substantial technical progress, many issues obstruct the successful introduction of CIS and CdTe thin films in the marketplace. However, the effort to overcome these technical issues is well under way. New approaches (flexible substrates, non-CdS designs, new processes) and new corporate entries reflect the ongoing technical vitality of the field. Record efficiencies at all levels (cells through modules) are a strong reminder of the potential of these technologies if they can be developed to full commercial success.

ACKNOWLEDGMENTS

This work has been supported by DOE contract No. DE-AC36-83CH10093.

REFERENCES

[1] R.W. Birkmire, H. Hichri, R. Klenk, M. Marudachalam, B.E. McCandless, J.E. Phillips, J.M. Schultz, and W.N. Shafarman, *American Inst. of Physics Conf. Proc.* **353** (13th NREL Photovoltaics Program Review), (1995), 420.

[2] W.E. Devaney,W.S. Chen, J.M. Stewart, and B.J. Stanbery, *American Inst. of Physics Conf. Proc.* **268** (Photovoltaic Advanced Research & Development Project), (1992), 157.

[3] W.N. Shafarman, R. Klenk, and B.E. McCandless, accepted for publication, *J. Appl. Phys.* (May 1996).

[4] K. Ramanathan, private communication.

[5] D. Hariskos, M. Ruckh, U. Rühle, T. Walter, and H.-W. Schock, *Conf. Record 24th IEEE PV Spec. Conf* (1st World Conference), (1994), 91.

[6] C. Ferekides, J. Britt, Y. Ma, and L. Killian, *Conf. Record 23rd IEEE PV Spec. Conf.* (1993), 389.

[7] J.E. Granata, J.R. Sites, G. Contreras-Puente, and A.D. Compaan, this conference.

[8] B. von Roedern, *Proc. 12th European Photovoltaic Solar Energy Conf.* (1994), 1354.

[9] B.E. McCandless, Y. Qu, and R.W. Birkmire, *Conf. Record 24th IEEE PV Spec. Conf* (1st World Conference), (1994), 107.

[10] B. Kroposki, T. Strand, R. Hanson, L. Mrig, T. Zhou, R.C. Powell, and R. Sasala, this conference.

REPORT DOCUMENTATION PAGE

Form Approved
OMB NO. 0704-0188

1. AGENCY USE ONLY (Leave blank)	2. REPORT DATE	3. REPORT TYPE AND DATES COVERED
	May 1996	Technical Report

4. TITLE AND SUBTITLE

NREL Preprints for the 25th IEEE Photovoltaic Specialists Conference

5. FUNDING NUMBERS

TA: PV610107

6. AUTHOR(S)

D. Gwinner, editor

7. PERFORMING ORGANIZATION NAME(S) AND ADDRESS(ES)

National Renewable Energy Laboratory
1617 Cole Blvd.
Golden, CO 80401-3383

8. PERFORMING ORGANIZATION REPORT NUMBER

9. SPONSORING/MONITORING AGENCY NAME(S) AND ADDRESS(ES)

National Renewable Energy Laboratory
1617 Cole Blvd.
Golden, CO 80401-3393

10. SPONSORING/MONITORING AGENCY REPORT NUMBER

TP-410-21091

DE96007880

11. SUPPLEMENTARY NOTES

12a. DISTRIBUTION/AVAILABILITY STATEMENT

12b. DISTRIBUTION CODE

UC-1250

13. ABSTRACT *(Maximum 200 words)*

This document consists of preprints of 40 papers prepared by photovoltaic scientists at the National Renewable Energy Laboratory (NREL) and collaborating researchers and presented at the 25th IEEE Photovoltaic Specialists Conference. The conference was held on May 13-17, 1996, in Washington, D.C. Most of the NREL work described here was funded by the U.S. Department of Energy under contract No. DE-AC36-83CH10093.

14. SUBJECT TERMS

amorphous silicon ; polycrystalline ; thin films ; semiconductors ; crystal growth ; conference proceedings ; IEEE ; photovoltaics ; solar cells

15. NUMBER OF PAGES
172

16. PRICE CODE

17. SECURITY CLASSIFICATION OF REPORT	18. SECURITY CLASSIFICATION OF THIS PAGE	19. SECURITY CLASSIFICATION OF ABSTRACT	20. LIMITATION OF ABSTRACT
Unclassified	Unclassified	Unclassified	UL

NSN 7540-01-280-5500

Standard Form 298 (Rev. 2-89)
Prescribed by ANSI Std. Z39-18
298-102